

Theoretical study of hydrogen storage in alkali- and alkaline-earth graphite intercalate compounds

Charles Wood

A thesis submitted to University College London
for the degree of Doctor of Philosophy

Department of Physics and Astronomy
University College London

July 11, 2013

I, Charles Wood, confirm that the work presented in this thesis is my own. Where previous work has been derived from other sources, I confirm that this has been referred to in the thesis. Any images taken from other sources have also been given due credit.

Acknowledgements

There are many people that have helped me complete this thesis, some too numerous to mention. I will attempt to briefly summarise those of particular importance in no particular order.

My friends from Brockenhurst College who have formed my support network and friendship group for over a decade now. Each and every one has, in some way, helped me complete this Ph.D., whether it's by showing an interest in my studies or directly by sheltering and feeding me (Sam, Aimée, Jim, Vicki, Tom and Chloé especially). I don't know if I'd have been studying this if it was not for our formative years in education together.

My employers over the years of studying that have been supportive and interested in my studies. The interest shown by my friends and colleagues at 580 Ltd., London kept me keen to complete. I wish to especially thank the people of The Silver Hind, Sway for giving me employment (Ross, Ulrike, Andy and Carol) when I most needed it and made working a real pleasure. Turning up to work and chatting with the locals and friends about all matters related (and unrelated) to physics, the universe and everything made me keep my passion for physics. The discussions over that bar, in those short months, will never be forgotten. Thank you again for making my local pub, wherever I may be, a small restaurant in Sway.

My friends who I met at UCL during my first degree gave me the encouragement to continue studying to this level. Without their help I suspect some of my homework sheets may not have made quite the mark they received. Especially I wish to thank Guy Brindley, who without a doubt is the reason I performed so well in my M.Sci. Without his dedication and discipline, exposed so clearly to me in my 2nd year, I would not have had the necessary drive to perform to my potential.

The friends I met while studying my Ph.D. will remain my good friends. Those

people of UCL Physics (particularly F10 and the LCN) showed that studying physics is also good fun. Stephen Harrison and Adam Hawken remained good friends since my first degree and were always available for help when needed. Anna Dejardin, to whom credit belongs for the stunning energy landscape pictures within this thesis, and Rich Spinney were available for vital discussion and social escape whenever necessary.

My family have shown support the whole way through my studies and have never faltered to offer me anything I needed. To them I am extremely grateful for I would not have been able to be studying what I'm studying, where I'm studying it. My Mum and my brother Ewen for housing me for the (unenviable) completing stages of this project without burden or interruption. I hope the completion of this project will inspire him to fulfil his boundless potential for success and pursue his ambition in academia.

I also wish to thank Marta for her enthusiasm that have kept me going when problems seemed insurmountable. She has given me encouragement when I needed it most and to her I owe the motivation to keep pushing-on.

I also, absolutely must, thank Mike Gillan and Neal Skipper. My two supervisors without whom the project would not exist and without their careful guidance would not have the structure it does. For their supervision I can never express my thanks, other than to say my sincere gratitude for this opportunity.

Finally I wish to thank my dad. His words of encouragement when I was just a young boy spurred me on to reach this level. If it wasn't for his talk with me that "you can be a dustman if you want, if you really want; but you have the potential to be something special" I most certainly would not be where I am today, in every respect of my life. His words will never be surpassed in my memory and no father could ever have shown more guidance, more pride and more love for a son. He shall be in my memory always and it is to him that I dedicate this thesis.

To my father,
(17/06/1954 - 21/06/2010).

Abstract

The research project described in the thesis uses atomic-scale computational modelling to investigate the storage of hydrogen in graphite intercalate compounds (GICs). The work is relevant to the energy economy, as hydrogen is a source of clean energy, and can be used efficiently in fuel cells to generate electricity. Storing hydrogen safely has long been a challenge in materials science and, since the proposal of a hydrogen-based transport economy, has attracted great attention. Graphite intercalate compounds offer the possibility of dense storage, because they contain large absorption pores for hydrogen to bind. The absorption mechanisms and patterns in different intercalate compounds are not well understood, and this is the motivation for this work.

Alkali and alkaline-earth metal GICs (A/AE-GICs) were modelled using density functional theory (and benchmarked with quantum chemistry) to investigate their hydrogen storage capabilities and their stability against decomposition into the metal hydride and pure graphite upon hydrogenation. Detailed studies of the calcium-GIC were performed and also a survey of the other A/AE-GICs. The effect of the commonly modelled MC_{14} GIC compared with the experimental MC_{12} stoichiometry has been investigated to bridge the gap between experiment and theory.

The calcium-GIC was found to favourably absorb hydrogen within U.S. Department of Energy targets, but was found to be extremely unstable. Our investigations showed that all AE-GICs are unstable. Heavier A-GICs were found to stably absorb hydrogen at reasonable volumetric densities at the cost of gravimetric densities. The theoretically modelled MC_{14} stoichiometry was found to be fundamentally different from the experimental MC_{12} stoichiometry, with the latter breaking the simple symmetry of the former and offering many more distinct absorption sites and barriers to diffusion. Pair potentials have been built and parametrised to KC_{14} to aid simple modelling of KC_n GICs in, for example, classical molecular dynamics.

Contents

1	Introduction	1
1	Energy and energy storage	1
2	Hydrogen economy	6
2.1	Production	7
2.2	Storage	8
2.3	Use	10
3	Hydrogen storage	11
4	A brief history of graphite intercalates	14
5	Aims of this work	16
2	Background theory	19
1	Introduction	19
	Born-Oppenheimer approximation	21
2	Density functional theory	22
2.1	Hohenberg-Kohn theorems	22
	Variational principle	23
2.2	The Kohn-Sham ansatz and equations	25
2.2.1	Exchange-correlation energy, E_{xc}	28
	Local density approximation (LDA)	29
	Generalised gradient approximation (GGA)	30
2.3	Plane wave basis sets	31
3	Quantum chemistry	32
3.1	Hartree-Fock method	33
	Self-consistent field method	34

CONTENTS

	Localised basis sets	35
3.2	Møller-Plesset perturbation methods	35
3.3	Coupled cluster (CC) methods	37
4	Classical force-fields	38
4.1	Functional forms	38
5	Finite temperature effects	40
3	Hydrogen in calcium graphite	41
1	Introduction	41
2	Predictions of Ca-GICs for H storage	42
2.1	Theoretical predictions	43
2.1.1	Cobian and Íñiguez [1]	43
2.1.2	Kim et al. [2]	45
2.1.3	Yoon et al. [3]	47
2.2	Experimental findings	49
2.2.1	Lovell [4]	49
2.2.2	Srinivas et al. [5]	50
3	Modelled compounds	50
3.1	Graphite	51
	The hexagonal phases	51
	The rhombohedral phase	53
3.2	Calcium graphite (Ca-GICs)	56
3.2.1	The CaC_6 GIC	59
	The hexagonal phases	59
	The rhombohedral phase	60
3.2.2	The CaC_8 and CaC_{14} GICs	66
3.3	Hydrogenated calcium graphite	73
3.3.1	Hydrogenated CaC_6	77
3.3.2	Hydrogenated CaC_8 and CaC_{14}	78
3.3.3	Hydrogenated CaC_n energy landscapes	83
	Hydrogenated CaC_6	83
	Hydrogenated CaC_8	84
	Hydrogenated CaC_{14}	84
3.4	Calcium hydride	92

CONTENTS

4	Conclusions and discussion	94
4	Systematics of H₂ in A- & AE-GICs	101
1	Introduction	101
2	The binding of metal intercalants in GICs	103
2.1	Relaxing the structures of the alkali and alkaline earth GICs	104
2.2	Density of states and Bader analysis	107
3	Hydrogenating GICs	110
4	The binding of H ₂ to metals	115
5	Energetics of the metal hydrides	129
6	Conclusions and discussion	133
5	The dynamics of H₂ in K-GICs	138
1	Introduction	138
2	The differences between KC ₁₄ and KC ₁₂	140
2.1	Comparison of the structures of hydrogenated and unhydrogenated KC ₁₂ and KC ₁₄	141
2.2	Comparison of the energy landscapes of hydrogenated KC ₁₂ and KC ₁₄	144
3	Diffusion of H ₂ in KC ₁₄ and KC ₁₂	145
3.1	Empirical potentials for H ₂ -C and H ₂ -K	148
3.2	H ₂ energy scans through KC ₁₂ and KC ₁₄	149
3.2.1	H ₂ energy scans through KC ₁₄	152
3.2.2	H ₂ energy scans through KC ₁₂	158
4	Conclusions and discussion	163
6	Conclusions and discussion	167
Appendices		
A	Functional variation	170
B	Hartree-Fock method derivation	173
1	The Hartree-Fock equations	174
2	The coulomb and exchange operators	175
2.1	The coulomb operator	176

CONTENTS

2.2	The exchange operator	176
3	Minimising a single Slater determinant	177
C	Coupled cluster method derivation	180
1	The cluster expansion	180
2	The cluster operator	182
D	Allowable stoichimoieties for GICs	186
E	Free atom energies	192
F	Mode of operation of VASP	195
1	Achieving self-consistency	197
	Bibliography	201

List of Figures

1.1	Energy use on a global scale. Energy usage per capita (a) of primary energy before conversion to other end-use fuels. This equals indigenous production plus imports and stock changes, minus exports and fuels given to ships and aircraft used for international transport. Percentage of energy produced from fossil fuels (b). Maps from The World Bank[6] with the legend showing increasing values from light pink to red (white represents no data).	3
1.2	A schematic of the hydrogen economy for a vehicular end-user.	6
1.3	Two fuel cell cars from (a) Honda ^g and (b) Mercedes-Benz ^h . The adaptation from conventional petrol car design to fuel cell design has had little effect to the end-users experience.	11
3.1	The two hexagonal phases of graphite, (a) the fictional $P6/mmm$ phase and (b) the most stable $P6_3/mmc$ phase.	52
3.2	Rhombohedral graphite, space group $R\bar{3}m$, with $A-B-C-A-B-C$ stacking sequence. Again, the unit cell is shown in black.	53
3.3	The difference between the variation of energy per C atom with <i>c</i> -axis separation with the LDA (subfigure (a)) and GGA-PW91 (subfigure (b)) <i>xc</i> -functionals in three phases of graphite stacking: $A-A-A$, $A-B-A-B$ and $A-B-C-A-B-C$. Note the very different ranges in the abscissæ, with the LDA results only between 3-4 Å and the GGA-PW91 results ranging from 3-10 Å. The E_{form}/C values given are corrected for reference to a spin-polarised C atom and given in table 3.2.	57
3.4	The hexagonal phases of CaC_6	60

LIST OF FIGURES

3.5 Rhombohedral $\alpha\beta\gamma$ -stacked $R\bar{3}m$ CaC ₆	61
3.6 Total CaC ₆ unit cell energy plotted against C-C in-plane bond length (a). Only the α stacked phase of CaC ₆ is shown as other stackings gave equivalent results. The strength of the in-plane bond length, and thus its effect on the total energy of the system, is clear from the parabolic shape of the curves shown.	63
3.7 Total CaC ₆ unit cell energy (in three different stackings: α , $\alpha\beta$ and $\alpha\beta\gamma$) as a function of sheet separation (c). The clear minima show the strength of the out-of-plane bonding in CaC ₆	64
3.8 CaC ₈ with (b) the full unit cell shown and (a) projected down the <i>c</i> -axis to show the in-plane structure.	68
3.9 CaC ₁₄ with (b) the full unit cell shown and (a) the unit cell projected down the <i>c</i> -axis to show the unsymmetrical in-plane structure.	69
3.10 The effect on the formation energy (from free spin-polarised ground state atoms) per CaC ₈ unit by in-plane C-C bond length <i>a</i>	70
3.11 The effect on the formation energy (from free spin-polarised ground state atoms) per CaC ₁₄ unit by in-plane C-C bond length <i>a</i>	71
3.12 The reduction in the in-plane C-C bond length, <i>a</i> , with decreasing metal content in the CaC _{<i>n</i>} GICs, approaching the graphite limits (dotted).	72
3.13 The effect on the formation energy (from free spin-polarised ground state atoms) per CaC ₈ unit by the <i>c</i> -axis separation between consecutive sheets of graphite.	74
3.14 The effect on the formation energy (from free spin-polarised ground state atoms) per CaC ₁₄ unit by the <i>c</i> -axis separation between consecutive sheets of graphite.	75
3.15 The three fundamentally different possible orientations of an H ₂ molecule within an arbitrary Ca-GIC, CaC _{<i>n</i>} with H ₂ bond axis (a) parallel to the GIC <i>c</i> -axis producing the transverse orientation, (b) perpendicular to the GIC <i>c</i> -axis for the longitudinal orientation and finally (c) dissociated into two H atoms binding to the intercalant metal. Note that any orientation between (a) and (b) can obviously exist but these represents the extreme opposites of orientation.	76

LIST OF FIGURES

3.16 Equilibrating the <i>c</i> -axes in CaC ₆ with an H ₂ molecule at the global minimum and two H atoms at the global minimum with (a) the LDA and (b) GGA-PW91.	79
3.17 Equilibrating the <i>c</i> -axes in CaC ₈ with an H ₂ molecule at the global minimum and two H atoms at the global minimum with (a) the LDA and (b) GGA-PW91.	80
3.18 Equilibrating the <i>c</i> -axes in CaC ₁₄ with an H ₂ molecule at the global minimum and two H atoms at the global minimum with (a) the LDA and (b) GGA-PW91.	81
3.19 Representative (LDA) energy landscapes for CaC ₆ with (a) an H ₂ molecule in the transverse orientation and (b) two H atoms in symmetrically opposite positions. C positions are represented by black circles and Ca positions by green circles.	85
3.20 Representative (GGA-PW91) energy landscapes for CaC ₆ with (a) an H ₂ molecule in the transverse orientation and (b) two H atoms in symmetrically opposite positions. C positions are represented by black circles and Ca positions by green circles.	86
3.21 Representative (LDA) energy landscapes for CaC ₈ with (a) an H ₂ molecule in the transverse orientation and (b) two H atoms in symmetrically opposite positions. C positions are represented by black circles and Ca positions by green circles.	87
3.22 Representative (GGA-PW91) energy landscapes for CaC ₈ with (a) an H ₂ molecule in the transverse orientation and (b) two H atoms in symmetrically opposite positions. C positions are represented by black circles and Ca positions by green circles.	88
3.23 Representative (LDA) energy landscapes for CaC ₁₄ with (a) an H ₂ molecule in the transverse orientation and (b) two H atoms in symmetrically opposite positions. C positions are represented by black circles and Ca positions by green circles.	90
3.24 Representative (GGA-PW91) energy landscapes for CaC ₁₄ with (a) an H ₂ molecule in the transverse orientation and (b) two H atoms in symmetrically opposite positions. C positions are represented by black circles and Ca positions by green circles.	91

LIST OF FIGURES

3.25 The CaH ₂ unit cell as seen (a) in its entirety with bonds extending outside the unit cell shown, (b) as projected down the \vec{c} -axis and (c) projected down the \vec{b} -axis to show the cell structure most clearly.	92
4.1 The total density of states (DOS) for CaC ₆ (solid line) and the contribution of the Ca <i>d</i> -orbitals (dotted line) for GGA-PW91 calculation.	109
4.2 The symmetry of the chosen stoichiometries leads to only two types of absorption site: red hexagons contain an intercalant, green are empty. Shown for the (a) MC ₆ , (b) MC ₈ and (c) MC ₁₄ stoichiometries.	112
4.3 The two orientations of H ₂ interacting with a metal atom: transverse (right) and longitudinal (left).	116
4.4 Binding curves for the H ₂ -M ⁺ complexes in the transverse orientation with CCSD(T) (a) showing the full binding curve and (b) showing agreement beyond 5 Å between electrostatic prediction and calculated results.	119
4.5 Binding curves for the H ₂ -M ⁺ complexes in the longitudinal orientation with HF with (a) showing the full binding curve and (b) showing agreement beyond 5 Å between electrostatic prediction and calculated results.	120
4.6 Binding curves for the H ₂ -Be ⁺ complex in the (a) transverse and (b) longitudinal configurations. The electrostatic, “predicted”, curves follow equation 4.4 with C^{quad} and α parameters calculated from LDA and GGA-PW91 calculations.	122
4.7 Binding curves for the H ₂ -M ²⁺ complexes in the (a) transverse orientation (CCSD(T) binding energies) and (b) longitudinal orientation (CCSD(T) binding energies).	123
4.8 Unit cells (hydrogen atoms in pink, metal atoms in other colours) of (a) the rock salt structures of the alkali hydrides (LiH, NaH, KH, RbH and CsH), (b) the SiS ₂ structure of BeH ₂ , (c) the rutile TiO ₂ structure of MgH ₂ and (d) the PbCl ₂ structure of CaH ₂ , SrH ₂ and BaH ₂	131
5.1 The unit cells of (a) KC ₁₄ and (b) KC ₁₂ (drawn as 2(KC ₁₂)) as viewed down the <i>c</i> -axis to elucidate the in-plane structure.	141

LIST OF FIGURES

5.2 The long-range in-plane order of (a) the highly symmetric KC ₁₄ and (c) KC ₁₂ (unit cells are outlined in black). The different structures leading to different types of absorption environments, or sites, shown for (b) KC ₁₄ where every empty site is equivalent, and (d) KC ₁₂ where three different types of empty site exist (site A shown in yellow; site B in green and site C in turquoise). Note that similarly coloured sites are equivalent, with red hexagons denoting K sites and green, turquoise and yellow denoting empty sites.	142
5.3 DFT LDA H ₂ energy landscapes for (a) KC ₁₄ and (b) KC ₁₂ . Note the different energy scales, (a) showing between 0 eV and 2.5 eV while (b) shows between 0 eV and 2.0 eV.	146
5.4 DFT GGA-PW91 H ₂ energy landscapes for (a) KC ₁₄ and (b) KC ₁₂ . Note the different energy scales, (a) showing between 0 eV and 1.5 eV while (b) shows between 0 eV and 2.5 eV.	147
5.5 The functional forms of (a) H ₂ -C potentials and the (b) H ₂ -K potentials fitted to DFT data (both LDA and GGA-PW91) from hydrogenated KC ₁₄	150
5.6 The path along which the energy scan in KC ₁₄ is plotted. The unit cell is marked in black with the path starting at “START” and following the arrows finishing at “FINISH”. The single absorption site is marked with 1 and the three important energy barriers are marked A, B and C. K positions are denoted with black filled circles and the graphite lattice is shown.	152
5.7 H ₂ energy scans along the path given in 5.6 comparing DFT with empirical data for (a) LDA and (b) GGA-PW91. Note that “Empirical LDA” and “Empirical GGA-PW91” mean ”Empirical potential fitted to LDA DFT data” and “Empirical potential fitted to DFT-GGA-PW91 data” repectively	154
5.8 Comparison of the jump frequencies (the Boltzmann factors for each jump) for a diffusive jump (red) and a non-diffusive jump (black) of H ₂ at a site 1 in set of sites <i>a</i> in KC ₁₄ (see figure 5.9) with (a) LDA data and (b) GGA-PW91 data. DFT data (solid lines) is compared with empirical data (dashed lines).	156

LIST OF FIGURES

5.9 An H ₂ molecule (filled red circle) located at a site faces six possible routes for diffusion with only three of them likely; two jumps (over barrier A) keep the molecule with the set of sites <i>a</i> (<i>non-diffusive</i> jumps) and one jump (barrier C) takes it to another set of sites <i>b</i> (<i>diffusive</i> jump). The two high barriers, B, are unlikely to be traversed at reasonable temperatures and the dotted path represents an impossible jump.	157
5.10 Energy-error landscapes showing the energy difference between DFT and empirical landscapes for (a) LDA and (b) GGA-PW91 for KC ₁₄	159
5.11 The two paths along which the energy scan in KC ₁₂ is plotted. The unit cell is marked in black with the paths stretching in the direction of the arrows. The three absorption sites are marked 1, 2 and 3 and the five important energy barriers are marked A, B, C, D and E. K positions are denoted with black filled circles and the graphite lattice is shown.	160
5.12 H ₂ energy scans along scan 1 given in 5.11 comparing DFT with empirical data for (a) LDA and (b) GGA-PW91. The initial extremely large barrier is barriers A and B combined with the path passing through a K atom, the subsequent minima is then site 2 followed by barrier C then finishing at site 3.	161
5.13 H ₂ energy scans along scan 2 given in 5.11 comparing DFT with empirical data for (a) LDA and (b) GGA-PW91. The scan starts at site 2, the first small barrier is D then to the minima for site 2, over barrier E until finally finishing at site 1.	162
5.14 Energy-error landscapes between DFT and empirical calculations with (a) showing LDA results and (b) GGA-PW91 results for KC ₁₂	164
D.1 The hexagonal structure. Lattice points at the centre of each hexagon form a triangular lattice, when a basis of two points is added the hexagonal structure above can be obtained.	187
D.2 The three in-plane <i>D</i> ₃ metal lattices (red) on the graphite structure (black). The lattices are slowly expanded until constraint 2 is met. Subfigure (a) and (a) show the cases of simply stretching the metal lattice from different orientations, subfigure (c) shows the effect of stretching and rotating the metal lattice.	189

LIST OF FIGURES

D.3 The four geometrical patterns of the D_6 lattice allowable under both constraints. Note that the triangles represent half the unit cell (with two sides acting as the cell vectors) and that each triangular lattice has a basis of two metal atoms at the lattice point and the centre of the triangle (at $(0, 0, 0)$ and $(1/3, 1/3, 1/3)$ in the basis of the lattice vectors).	191
F.1 Flow diagram of the mode of operation of VASP.	197
F.2 An example of the non-monotonic behaviour of total energy convergence with k -point grid size. The example shows the total unit cell energy for α -stacked CaC_6 using DFT-LDA in VASP (using a fixed plane wave cut-off) plotted against linear size of an $n \times n \times n$ Monkhorst-Pack k -point mesh. Inset shows how the energy difference (ΔE) between successive k -point grid sizes (n) decreases as the mesh is increased.	199
F.3 An example of total energy convergence with plane wave cut-off. The example shows how the unit cell energy of α -stacked CaC_6 converges with increasing plane wave cut-off using DFT-LDA in VASP (using a fixed k -point grid). The inset shows how the difference between each successive plane wave cut-off monotonically decreases allowing extrapolation to the infinite basis set limit.	200

List of Tables

3.1	A summary of the DFT simulation details used for modelling graphite.	54
3.2	A summary of the results from VASP DFT simulations on graphite with both the LDA and the GGA-PW91 <i>xc</i> -functionals compared with experiment[7] for graphite in three registrations: the fictional <i>A-A-A</i> , the hexagonal <i>A-B-A</i> and the rhombohedral <i>A-B-C-A-B-C</i>	58
3.3	A summary of the DFT simulation details used for modelling CaC ₆ in the three stacking regimes of α -, $\alpha\beta$ - and $\alpha\beta\gamma$ -stacking. Where a stacking sequence is not specified this value was used across all simulations.	62
3.4	A summary of the results of relaxing the three phases (α -, $\alpha\beta$ - and $\alpha\beta\gamma$ -stacked) of CaC ₆ with both the LDA and GGA-PW91 <i>xc</i> -functionals compared with experiment[8].	67
3.5	A summary of the results of relaxing the two less dense Ca-GICs of CaC ₈ and CaC ₁₄ with both the LDA and GGA-PW91 <i>xc</i> -functionals. Note that only the CaC ₆ stoichiometry is seen experimentally so comparison with experiment is not feasible but that structural values differ little between CaC ₆ , CaC ₈ and CaC ₁₄ and CaC ₆ can be seen to be in good agreement with experiment (table 3.4).	73
3.6	A summary of the DFT simulation details used for modelling CaC _n +H ₂ and CaC _n +2H in the three stoichiometries with <i>n</i> = 6, 8 and 14.	77
3.7	A summary of the results of hydrogen absorption in the CaC _{<i>n</i>} GICs (with <i>n</i> = 6, 8, 14) both molecularly (in the transverse orientation) and atomically as two H atoms.	82
3.8	A summary of the DFT simulation details used for modelling CaH ₂	93

LIST OF TABLES

3.9	A summary of the results of relaxing CaH ₂ with both the LDA and GGA-PW91 <i>xc</i> -functionals from this work compared with DFT calculations by Li et al. [9] using GGA-PBE, Wolverton and Ozolins [10] using GGA-PW91 and with experiment for CaD ₂ [11].	95
3.10	Selected bond distances (Å) in the CaH ₂ crystal and their comparison with CaD ₂ in experiment.	96
3.11	Binding energies, E_{bind} , of hydrogen in CaC _n GICs with $n = 6, 8, 14$ in atomic absorption (CaC _n +2H) and molecular transverse absorption (CaC _n +H ₂). Negative energies represent favourable binding.	97
3.12	The energies of stability against decomposition into the hydride and pure graphite, ΔE , of all three Ca-GICs from their most stable hydrogenated phase. Note that a negative value implies the hydrogenated GIC is unstable against decomposition in to the products.	99
4.1	The alkali and alkaline earth group metals that are considered in this chapter are highlighted in bold. Electron configurations are given, with number of electrons in parentheses, from the VASP potential files. Note that for Ca, there were two configurations: one for the LDA potential and one for the GGA-PW91 potential. The LDA data are marked with *. For all other elements the details for the LDA and GGA-PW91 potentials are the same.	104
4.2	A summary of the DFT simulation details used for modelling MC _n with M=Li, Be, Na, Mg, K, Ca, Rb, Sr, Cs and Ba; and $n = 6, 8$ and 14. . . .	105
4.3	Formation energies of the alkali and alkaline earth GICs, $E_{\text{form}}(\text{MC}_n)$ (eV unit) from free spin-polarised metal atoms and graphite. Compounds marked with † exhibited no equilibrium <i>c</i> -axis value with GGA-PW91 and the quoted E_{form} is the formation energy at <i>c</i> = 8.00 Å. Values in the table can be compared with values for the formation energy of the pure solid metals ($E_{\text{form}}(\text{M}_{\text{gas}})$) from free atoms. Where values for E_{form} for the metal gas has a larger magnitude than values for the GICs, the GIC is likely unstable against decomposition into graphite and the pure metal.	108
4.4	Equilibrium <i>c</i> -axis values for the MC _n GICs with $n = 6, 8$ and 14 with both the LDA and the GGA-PW91 <i>xc</i> -functionals. Compounds marked with † exhibited no equilibrium <i>c</i> -axis value with GGA-PW91.	109

LIST OF TABLES

4.5 Results of Bader analysis on MC _n structure with n = 6, 8 and 14. Q (M) represents the charge on the intercalate metal and $\overline{Q(C)}$ represents the average charge on a carbon atom from the graphite layer. All charges are given in units of the fundamental charge, e.	111
4.6 Equilibrium c-axis values for the KC ₁₄ , RbC _n and CsC _n (n = 6, 8 and 14) hydrogenated GICs and their relative change (Δc) compared with the unhydrogenated GIC.	114
4.7 Binding energies, E _{bind} , of molecular hydrogen in KC ₁₄ , RbC _n and CsC _n GICs with n = 6, 8, 14. Negative energies represent favourable binding.	115
4.8 The calculated values for the parallel and perpendicular (relative to the H ₂ bond axis) polarisabilities (α in a ₀ ³ units) and quadrupole moments (C ^{quad}) compared with experimental data from the Computational Chemistry Comparison and Benchmark Database[12].	118
4.9 Results for the H ₂ -M ⁺ alkali metal complexes in the transverse orientation. Equilibrium separations, r _{min} , and binding energies, E _{bind} , are given for quantum chemistry calculations (HF and CCSD(T)) and DFT (LDA, GGA-PW91 and GGA-PBE).	125
4.10 Results for the H ₂ -M ⁺ and H ₂ -M ²⁺ alkaline earth metal complexes in the transverse orientation. Equilibrium separations, r _{min} , and binding energies, E _{bind} , are given for quantum chemistry calculations (HF and CCSD(T)) and DFT (LDA, GGA-PW91 and GGA-PBE).	126
4.11 Results for the H ₂ -M ⁺ alkali metal complexes in the longitudinal orientation. Equilibrium separations, r _{min} are between H ₂ centre of mass and metal ion, and binding energies, E _{bind} , are given for quantum chemistry calculations (HF and CCSD(T)) and DFT (LDA, GGA-PW91 and GGA-PBE).	127
4.12 Results for the H ₂ -M ⁺ and H ₂ -M ²⁺ alkaline earth metal complexes in the longitudinal orientation. Equilibrium separations, r _{min} , and binding energies, E _{bind} , are given for quantum chemistry calculations (HF and CCSD(T)) and DFT (LDA, GGA-PW91 and GGA-PBE).	128

LIST OF TABLES

4.13 Results for the H-M ⁺ -H and H-M ²⁺ -H alkaline earth metal complexes. Equilibrium separations, r_{\min} , are between each H atom and the metal ion (each H being equidistant from M), and binding energies, E_{bind} , are given for CCSD(T).	129
4.14 A summary of the DFT simulation details used for modelling the metal hydrides, MH with M=Li,Na,K,Rb and Cs and the metal dihydrides MH ₂ with M=Be,Mg,Ca,Sr and Ba.	130
4.15 Calculated equilibrium lattice parameters and formation energies for the alkali hydrides compared with experiment.	132
4.16 Formation energies per formula unit, E_{form} (eV unit), and lattice parameters (Å unit) for the alkaline earth hydrides.	134
4.17 Stability energies (eV unit), ΔE_{form} , for formation of the GICs from free atoms. Stability is calculated against decomposition of the GIC into the metal in its standard state and pure graphite. N.B. stable GICs have positive values for ΔE_{form}	135
4.18 Stability energies (eV unit), ΔE from equation 4.1, for the alkali and alkaline earth metal GICs. N.B. stable GICs have positive ΔE	137
 5.1 A summary of the DFT simulation details used for modelling KC ₁₄ and KC ₁₂	143
5.2 Structure parameters for unhydrogenated (no H ₂ rows) and hydrogenated (+ H ₂ rows) KC ₁₄ and KC ₁₂ with all three non-equivalent sites shown for K ₁₂	144
5.3 The fitted parameters for the H ₂ -C and H ₂ -K potentials using both LDA and GGA-PW91 <i>xc</i> -functionals.	151
5.4 The barriers to H ₂ diffusion in KC ₁₄	155
5.5 Jump rates, ω , for H ₂ diffusing via the diffusive process (over barrier C) and by the no-diffusive process (either of the A barriers) in KC ₁₄ compared with experimental values for the two jump rates of H ₂ seen in KC ₂₄	158
5.6 The barriers to H ₂ diffusion in KC ₁₂	163
5.7 Stability energies (eV unit), ΔE_{form} , for formation of KC ₁₂ and KC ₁₄ from free atoms. Stability is calculated against decomposition of the GIC into the metal in its standard state and pure graphite. N.B. stable GICs have positive values for ΔE_{form}	165

LIST OF TABLES

B.1 The relationship between chemists' notation (abbreviated as $[i h j]$ and $[ik jl]$) and physicists' Dirac bracket notation (abbreviated as $\langle i h k\rangle$ and $\langle ij kl\rangle$). Note that the chemists' notation groups electrons together (those orbitals with \vec{x}_1 appear on the left, those with \vec{x}_2 on the right) while physicists' notation groups conjugated spin orbitals together.	173
E.1 Differences from the VASP reference state energy of the spin-polarised atomic ground state within DFT using both LDA and GGA-PW91, i.e. $E_{\text{spin-pol}} - E_{\text{ref}}^{\text{VASP}}$	194

Introduction

1 Energy and energy storage

Our current sources of energy are depleting. Energy, as the single most important commodity for civilisation, is often generated from finite resources. Little of our energy supplies are from renewable sources or constant energy sources, such as incident solar radiation or geothermal. Our reliance upon the scarce resources of fossil fuels will, at some point in the future, choke our current quality of life. This will be most noticed in the developed Western world where energy usage per capita is around $17 \times$ that of developing countries^a [6], as can be seen in figure 1.1. It is worth noting that some countries that have an extremely high energy consumption, such as Iceland with 16,842 kilograms of oil equivalent/capita (kgoe/capita)^b (nearly $2.5 \times$ that of the USA) in 2010, developed only 14.7% of their energy from fossil fuels, the rest being generated from renewable sources^c. While Iceland represents a special case due to the abundance of geothermal energy, countries such as these show the way to minimising the effect of fossil fuel shortages upon the population's quality of life. It is clear that some countries simply do not have the renewable resources Iceland has to generate much of their current energy.

1 Energy and energy storage

These countries rely upon importing stored energy or using unsustainable sources.

This work will focus upon hydrogen technologies as a “fuel for the future”. The work will cover *ab initio* modelling of a particular class of hydrogen storage materials based on intercalated graphite. The effective storage of hydrogen is one of the largest technological barriers to the effective use of this technology. In order to contextualise this study a broad general background is necessary.

The necessity for an alternative or supplementary fuel source is evident from every US congressional report on the remaining fossil fuel resources[14]. Using estimates for the 2009 global average rate of energy consumption per capita[6], factoring the percentage obtained from fossil fuels[6], the 2009 world population[15] and the 2010 prediction for the proven remaining global fossil fuel reserves[14] we can make a “back of the envelope” calculation for the remaining years of fossil fuel consumption^d. From these values we see that the current global fossil fuel reserve will be exhausted in 79 years.

It is worth noting that this estimate assumes that the global population remains at its current level; predictions for the economically developed countries support this assumption.

^aThe energy usage per capita of the USA in 2009 was 7,051 kgcoe/capita. In the same year the energy usage in Ethiopia was 402 kgcoe/capita, just under 6 % of the usage per capita in the USA.

^bEnergy given in the industry standard units of kgcoe (kilograms of oil equivalent). This is the approximate amount of energy that can be extracted from 1 kg of crude oil. It has a standardised value of 41,868 kJ/kg[13].

^cIceland’s contribution to its energy needs from fossil fuel sources has been steadily declining since 1960 at an average rate of 1.1 %p.a. (4 × faster than the UK) leading to its 2010 use of fossil fuels per capita being just 2,476 kgcoe/capita c.f. the UK fossil fuel usage of 2,901 kgcoe/capita and the USA usage of 6,098 kgcoe/capita for the same year[6].

^dThe 2009 global average energy usage was 1,791 kgcoe/capita[6]; the 2009 global population was estimated at 6.810 billion[15]; and the 2009 global average fraction of energy obtained from fossil fuels was 81 %[6], giving the total 2009 global fossil fuel consumption of

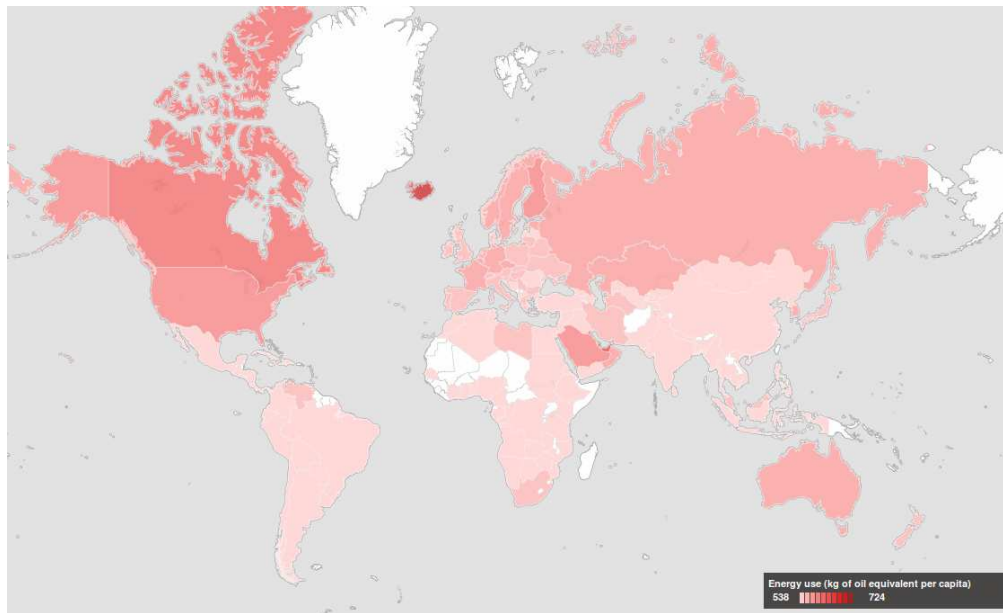
$$1791 \text{ kgcoe/capita} \times 6.810 \text{ billion} \times 81 \% = 9.88 \text{ billion toe},$$

where “toe” refers to metric tons of oil equivalent.

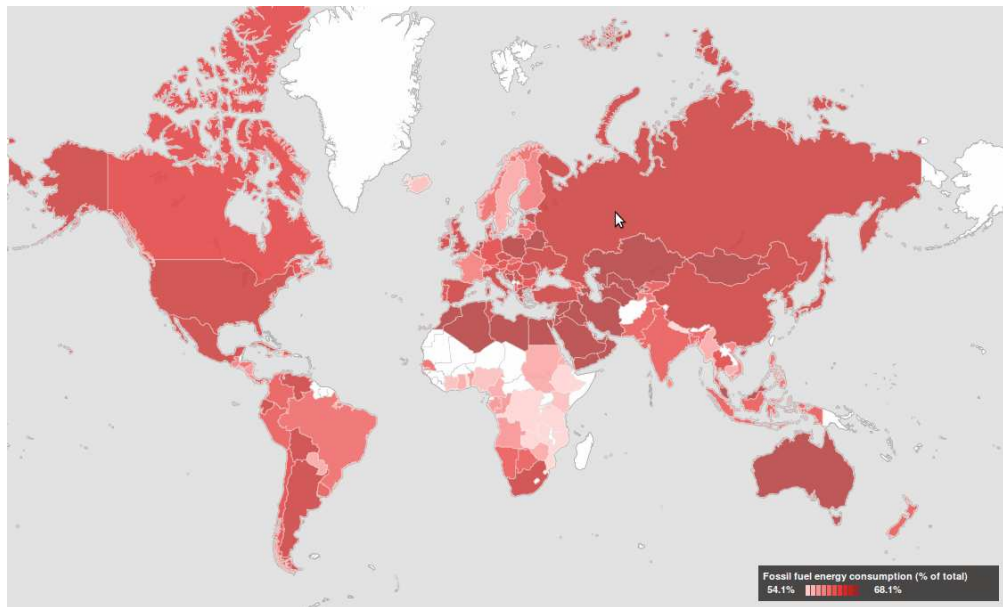
Dividing the 2010 estimated total proved reserves of 5,735 billion boe[14] (where “boe” represents barrels of oil equivalent) and using the conversion factor of 1 toe = 7.4 boe[16] gives the estimated global fossil fuel lifetime,

$$\frac{5735 \text{ billion boe}}{9.88 \text{ billion toe} \times 7.4} = 78.4 \text{ years.}$$

1 Energy and energy storage



(a) Energy usage per capita in 2007-2011 (in kilograms of oil equivalent per capita per annum).



(b) Percentage of energy usage coming from fossil fuels 2007-2011.

Figure 1.1: Energy use on a global scale. Energy usage per capita (a) of primary energy before conversion to other end-use fuels. This equals indigenous production plus imports and stock changes, minus exports and fuels given to ships and aircraft used for international transport. Percentage of energy produced from fossil fuels (b). Maps from The World Bank[6] with the legend showing increasing values from light pink to red (white represents no data).

1 Energy and energy storage

tion, but those for less economically developed countries (LEDCs) predict a rapidly increasing population[17] (the global population increased by 83 million from 2008 to 2009 with over 97 % from LEDCs[15]) causing this assumption to underestimate the remaining resources. This prediction also assumes the global average energy usage remains constant; but as countries develop, the lifestyles of the populace lend themselves to using more energy per capita thus this assumption will also cause an underestimation. This estimate only includes global *proved* fossil fuel reserves. The undiscovered technically recoverable global fossil fuel reserves (global UTTR) could amount to a further 12 %. The UTTR does not take into account economic recovery from these sources. As the demand for energy increases so the price for oil will increase and thus these resources will become economically recoverable, this will have the effect of increasing the estimate for fossil fuel reserve exhaustion. As the price for energy increases upon increasing demand so energy production from other sources, some renewable, will be become economically feasible. The assumption of the amount of energy obtained form fossil fuels should then be an overestimate and lengthen the life span of the remaining fossil fuels.

Taking all the assumptions into account the estimate remains a good approximation as to the life time of current global fossil fuel supplies. With this in mind the drive for another energy source is a challenge for the current generation. Fossil fuels provide an attractive energy solution as they combine energy storage with production; they are in essence energy vectors but only the recovery and processing of the raw material is needed to liberate the stored energy. Other energy sources (such as solar, wind, geothermal, hydro etc.) have to be converted to a type of energy suitable for storage, often to electrical energy that is then transmitted and used or stored as chemical potential energy (e.g. in batteries).

Of course, energy could be stored in any form that can be insulated from the environment. Energy from hydroelectric (non-pumped sources) and winched-mechanical sources store gravitational potential energy. The insulation from the environment simply requires the mass (water or a mass) to be held at a given height. A natural, or man-made, lake performs this for hydroelectric and a lock-pin for winched-mechanical. Other forms of energy storage are much harder to insulate. Thermal energy stored in large concrete blocks requires that the blocks be thermally insulated from the environment requiring expensive lagging. Any deficiencies in the lagging result in a loss of efficiency of the stored energy. Liquid fossil fuels simply require protection from ignition and storage

1 Energy and energy storage

at standard pressure in order to insulate the stored energy. Chemical storage, the most abundant form of stored energy, needs the system to be chemically inert to protect from reactions with the environment that cause an energy leak. Storing electrical energy as chemical potential energy has been highly refined with commercially available lithium-based batteries being almost perfectly insulated from the environment: major battery brands have negligible self-discharge rates, retaining over 97% of their initial charge after a month of being left in open circuit at room temperature[18]. Using hydrogen as an energy vector is a type of chemical energy storage requiring chemical insulation from the environment. A tank free from ignition sources (molecular hydrogen gas not being particularly flammable upon contact with the natural environment[19]) represents a viable storage medium but the stored energy density is low^e without high pressures or low temperatures. More energy-dense gases have been used for energy storage, many of which are naturally more flammable.

The uses to which our stored energy is put are varied, but by far the hardest challenge for a new energy solution is to revolutionise the transport sector. The use of stored energy for mobile applications is the most demanding with the tightest constraints. Potential energy vectors for use in this sector are electrochemical potential storage, methane, alcohols and hydrogen; the last three being used in fuel cell technologies. Methane can be used in coordination with a methane fuel cell employing either in-situ or off-board steam reformation, although other technological barriers are still to be overcome, such as degradation of the electrodes[20], and current operating temperatures are extremely high ($> 500^{\circ}\text{C}$). Alcohols, such as methanol, can be used in direct methanol fuel cells (DMFCs), but these suffer from methanol cross-over, losing fuel to the cathode side[21] reducing apparent efficiency. Electrochemical storage is already commercially available as either the sole energy source in electric vehicles[22] or as a secondary source in hybrid vehicles, such as the now famous Toyota Prius[23]. Hydrogen can be used in hydrogen fuel cells, showing the most promising efficiencies of the fuel cell types[24] for mobile applications.

^eThe stored energy density of hydrogen gas at room temperature and pressure is low given current fuel cell technologies.

2 Hydrogen economy

The concept of a hydrogen economy was first imagined in 1970 at a General Motors Technical Laboratory (Warren, MI, USA) “brainstormer” session when John Bockris announced “we should be living in a Hydrogen Society” and his colleague, Neal Triner, exclaimed “there will be a Hydrogen Economy” [25]. Even as early as 1970 the effects of anthropogenic climate change were being considered.

The concept of a hydrogen economy is a (fairly) simple replacement for the oil economy that exists now. The simple arrangement consists of a hydrogen production from renewable energy sources (originally solar and nuclear), transportation of the energy store in hydrogen over long distances, storage of the hydrogen in large quantities (in cities for example) finally use of the hydrogen either in a fuel cell or burned flamelessly and cleanly in air for space heating. The hydrogen can then produce energy for fixed uses (such as buildings electricity and space heating) and for the mobile sector. A schematic of the hydrogen economy is shown below in figure 1.2.

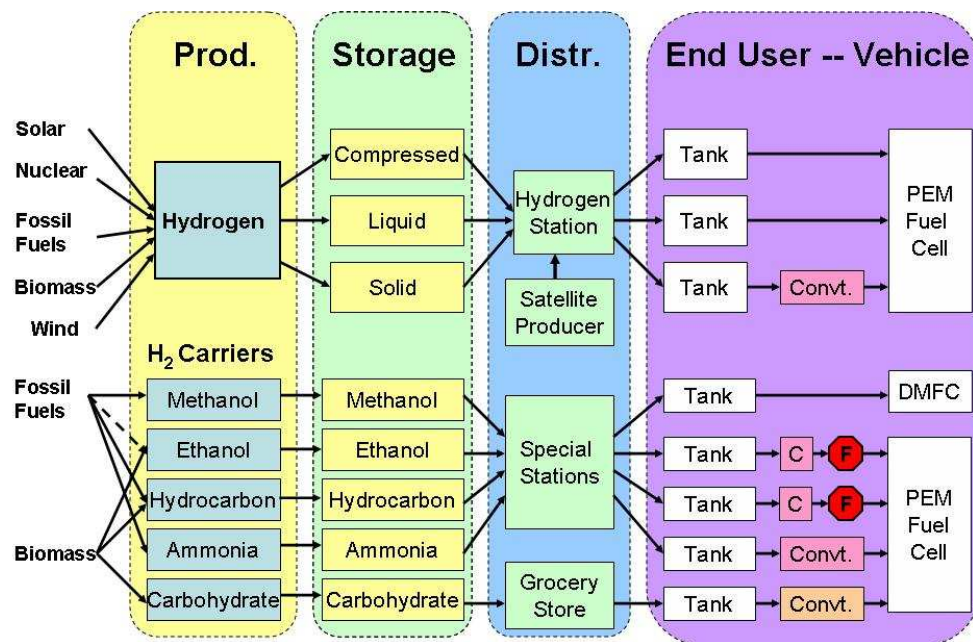


Figure 1.2: A schematic of the hydrogen economy for a vehicular end-user.

Clearly this economy, as with any other, requires a production sector, a storage sector and then eventual uses. These will be briefly discussed in turn.

2 Hydrogen economy

2.1 Production [26]

The main method used to produce hydrogen at the moment is natural gas reformation[27], with $\sim 95\%$ of all the H₂ produced in the USA coming from this method[28]. This method reacts water steam with methane, propane, ethanol or petrol to produce carbon monoxide (and some carbon dioxide) and H₂ gas in “steam-reforming reactions”. The CO gas is then reacted with water in the “water-gas shift reaction” to produce carbon dioxide and H₂. These endothermic reactions require the input of heat in order to proceed.

The use of fossil fuels for hydrogen production, while reducing the greenhouse gas production from direct combustion, is limited in its lifetime by the same reserves that exist for the finite fossil fuel economy. A method of H₂ production from renewable energy sources would be beneficial for the lifetime of the hydrogen economy.

Electrolysis splits the abundant water molecule into oxygen and hydrogen using electric currents. At present the bulk of electricity production is from fossil fuel sources, this conversion from fossil fuel, to a hydrogen store, to electricity via a fuel cell represents a significant loss in efficiency. Electricity production from renewable sources would offer a major benefit to the electrolysis production method. By increasing the temperature of the reaction the efficiency of electrolysis can be improved. Using the waste heat from a nuclear reactor less electrical energy is needed to perform the electrolysis and so reduces the total amount of useful energy used.

The water molecule can also be split solely using high temperatures. Thermochemical water splitting can be achieved using heat from a nuclear reactor or concentrated solar radiation from solar concentrators to split the water molecule. Catalysts can be used to aid the reaction and recycled after use. Photoelectrochemical water splitting can be achieved using a class of semiconductors that absorb sunlight and separate H₂O.

Gasification is a similar process to that of steam reformation: coal or biomass is converted to gas using heat under pressure and in the presence of air and steam. Through a series of chemical reactions the gaseous mixture obtains an increased hydrogen content that can be extracted and purified. Using various carbon capture methods, hydrogen can be produced from coal with near zero greenhouse gas emissions. Using biomass would offer a near zero greenhouse gas production method as biomass absorbs atmospheric carbon and if linked with carbon capture would result in a net decrease in atmospheric CO₂.

2 Hydrogen economy

Biomass can also be used in renewable liquid reforming in the form of alcohols. These can then be easily transported to the end-user where a form of steam reformation can be used to extract hydrogen. If methanol is used this would be best used directly in a methanol fuel cell, as noted earlier.

A natural source of hydrogen can be obtained using the by-products from respiration of certain types of algae and cyanobacteria. In the presence of sunlight they split water into hydrogen and oxygen as a product of their respiration. Some microbes can produce hydrogen directly from biomass. These biological hydrogen producers are being investigated for their potential by companies as well as researchers.

2.2 Storage

Storing hydrogen for any purposes, but especially for the transport sector requires safety as well as efficiency. H₂ gas is flammable in gas mixture concentrations of > 10 % H₂, >~ 30 % air and < 40 % H₂O[29]. The gas mixture will detonate in environments with concentrations of >~ 60 % H₂ and 45 – 80 % air or < 40 % H₂O[29]. The flammability of hydrogen has been well known since its discovery and was brought to popular attention upon the Hindenburg disaster of 1937[30]. While arguments for and against the role of hydrogen in the disaster have been voiced, recent studies (2005) give strong evidence to the role of hydrogen in the fire[31] and strongly disagree with the hypothesis that incendiary paint was to blame[32].

The problem of hydrogen storage is a problem of trying to store the lightest element at reasonable particle densities. The most obvious way to increase the particle density is to reduce the temperature of the gas to ~ 20 K to induce liquefaction. This will result in an overall loss of energy stored in the H₂ in order to reach this extremely low temperature. The technology needed to keep the liquid H₂ at this low temperature will require some vent to allow boil off, our energy store would slowly boil away. Petrol is a form of liquid hydrogen storage, hydrogen is bound to carbon chains and upon combustion these bonds are broken and energy is released. This represents the easiest hydrogen storage medium at present with it being liquid and stable at S.T.P.

The H₂ gas could be compressed to ~ 20 MPa, nearly 200 × atmospheric pressure, in order to increase the particle density. These very high pressures represent a potential hazard if a leak occurs, or a failure of the high pressure tank. In order to safely store a gas at such high pressures a strong and inherently massive tank would be required. This

2 Hydrogen economy

would represent a serious blow to the transport sector that requires gravimetric energy density in order to be feasible. Again, some of the energy stored in H₂ would be lost by compression, approximately 7.2 %. Upon expansion of the gas back to standard pressure one would regain 70 % of this lost energy resulting in a net loss of just 2.2 %[33, 34].

The U.S. Department of Energy (D.o.E.) have set targets[35] for a hydrogen storage medium to meet for it to be suitable for the light-duty transport sector. The most publicised D.o.E. target is the weight fraction target: the hydrogen storage medium must contain 6-7 wt.% hydrogen by mass of loaded material. While hydrogen has nearly 300 % the gravimetric energy density of petrol, liquid hydrogen has just 30 % of the volumetric energy density of petrol. The situation is slightly alleviated by the efficiency of the hydrogen fuel cell over the internal combustion engine, the fuel cell being twice as efficient (60 % efficient) at converting the stored energy to useful work than a conventional spark internal combustion engine (30 % efficient). Ideally the new energy system would have a volumetric energy density equivalent to that of petrol, an extremely challenging task requiring our ideal petrol-replacement H₂ storage medium to be 73 % more densely packed than liquid H₂^f. This assumes there is no weight penalty for this high level of volumetric storage.

Beyond the weight criterion set by the D.o.E. there is also an environmental conditional restraint: the storage medium must be usable at *reasonable* temperatures and pressures. In reality this equates to a temperature range of -40 °C to 85 °C, excluding the use of cryogenic storage, and pressure ranges of < 100 bar, excluding excessive pressure tanks. This is often quoted as requiring the medium to store hydrogen at reasonable

^fThe energy stored (E_{store}) in standard petrol is approximately 34.4 MJ/L with a conventional spark-ignition petrol internal combustion engine (ICE) converting ~ 30 % of this energy to work. Thus a conventional ICE can produce

$$34.4 \text{ MJ/L} \times 30 \% = 10.3 \text{ MJ/L}$$

Current H₂ fuel cells have an efficiency of ~ 60 % thus meaning the H₂ must have $E_{\text{store}} = 10.3 \text{ MJ/L} \div 60 \% = 17.2 \text{ MJ/L}$. Liquid H₂ has $E_{\text{store}} = 10.1 \text{ MJ/L}$. Using the standard reaction in a fuel cell of 2.H₂(g) + O₂(g) → 2.H₂O(l) + 572 kJ, gives the enthalpy of combustion (H_c) for a mole of H₂ to be 286 kJ/mol. We can now define the relative density of this “petrol-like” H₂ c.f. liquid H₂ as

$$\frac{E_{\text{store}} \cdot m(\text{H}_2) \cdot N_A}{H_c \cdot \rho_{\text{liq.}}(\text{H}_2)} = 173 \%,$$

where we have used the liquid H₂ density to be, $\rho_{\text{liq.}}(\text{H}_2) = 0.07 \text{ g/cm}^3$, giving the density of “petrol-like” H₂ to be $\rho_{\text{pet.}}(\text{H}_2) = 0.12 \text{ g/cm}^3$.

2 Hydrogen economy

temperature and pressure with a binding energy in the range of $0.2 - 0.8 \text{ eV}$ per H_2 .

While these D.o.E. targets give focussed goals for research they have not necessarily followed the trends of other technologically-leading countries such as Japan. Japan intends to roll out a high-pressure hydrogen system for the transport sector by 2015[36]. In this system the pressure constraint has been lifted and thus the volumetric density becomes dominant over the gravimetric density. The focus now becomes getting hydrogen to pack more densely in the loaded material than it can in the high pressure tanks absorbing within the D.o.E. range; this material could then be “dropped into” the high pressure tanks allowing the overall pressure to be reduced or the range increased for a given pressure or stored gas.

2.3 Use

Energy stored in hydrogen gas can be released directly by burning it in air. This produces a colourless flame at $\sim 3000^\circ\text{C}$ with only water and heat as by-products. This is the basis of hydrogen rocket fuels[37] and is most efficient method of using the energy stored in hydrogen, especially for space heating in buildings.

The hydrogen based system that gets the most attention is the one based on the hydrogen fuel cell first designed by Grove in 1839[38]. It was first used reliably in NASA’s Gemini V mission in 1965[39] to produce electricity for auxiliary systems and drinking water for the crew. The method simplifies to “reversing” electrolysis — combining hydrogen gas with oxygen gas on a suitable catalyst and forming water and generating a flow of charge.

The efficiency of the hydrogen fuel cell (F.C.) is not limited to the Carnot cycle internal combustion engine (I.C.E.), or the Otto cycle for the four-stroke I.C.E. The efficiency of a fuel cell car projected to 2020, assuming the same level of development in both I.C.E and F.C. systems, is expected to be between $2.2 \times$ and $2.4 \times$ that of an identical I.C.E. car[40]. The efficiency of a fuel cell is strongly linked to the amount of load on the system. At low loadings the system can have efficiencies of 70% but when the power drawn exceeds 10% the efficiency drops to $\sim 50\%$ with the energy lost as heat[41]. In a real system intended for vehicular use this lost heat could potentially be reused in combined heat and power system, effectively increasing the efficiency of the cell again. The actual efficiencies of a total fuel cell system are strongly dependent upon the method of hydrogen storage. A liquid H_2 based storage system would give a total

3 Hydrogen storage

system efficiency of just $\sim 17\%$, while a method of gaseous storage would represent $\sim 22\%$ efficiency. Clearly the focus upon an effective hydrogen storage solution would then improve the efficiency of the whole implemented system.

Currently fuel cell technologies enjoy few commercial applications but are being used in demonstration vehicles and military applications. The German type 212 submarine has nine hydrogen proton exchange membrane (PEM) fuel cells on board for silent cruising generating between 30 kW and 50 kW of power each[42]. A proof-of-principle system has been developed by Birmingham university and implemented in a canal boat called the “Ross Barlow”[43]. Fuel cell buses exist in cities across the world including London, São Paulo, Shanghai, San Francisco and others. Prototype cars have been developed by Honda (shown in figure 1.3(a)), Mercedes (figure 1.3(b)) and Toyota and all show promise with existing systems and use high pressure storage solutions. Fuel cell technologies are now at a stage where they could be implemented, a better storage solution remains the major barrier to this technology.



(a) Honda FCX Clarity car.

(b) Mercedes-Benz F-Cell car.

Figure 1.3: Two fuel cell cars from (a) Honda^g and (b) Mercedes-Benz^h. The adaptation from conventional petrol car design to fuel cell design has had little effect to the end-users experience.

3 Hydrogen storage

More complex hydrogen storage can be achieved using methods beyond compression or liquefaction. H₂ molecules can be physisorbed or chemisorbed into a system and this system then becomes the hydrogen storage medium. Chemisorbed systems include the

^gImage courtesy of www.motorstown.com

^hImage courtesy of www.MotorImpress.com

3 Hydrogen storage

chemical compounds of hydrogen and other elements; physisorbed systems consist of a sorbent to which H₂ molecules, or H atoms, bind weakly.

Research into chemisorbed hydrogen storage solutions has been heavily dominated by metal hydrides, amides, AB₅ compounds and novel reactions. AB₂ metal hydrides, such as MgH₂, have shown excellent promise with hydrogen capacities of 7.7 wt.%. They are limited in the extremely slow kinetics due to strong bonds between the hydrogen and the metal. Improvements to the kinetics of these simple hydrides have been made through nano-structuring[44] and the use of catalysts and transition metal complexes. Doping MgH₂ with transition metals gives a hydrogen fraction of ~ 7 wt.% and releases at 230 – 350 °C[45]. This material is strongly pyrophoric and thus not a good candidate in its raw form. Stabilising it will create stronger bonds that need a heat source of 300 – 350 °C.

Amides, such as LiNH₂, have a weaker M-H bond giving a lower desorption temperature. This greatly improves the kinetics over the stronger AB₂ materials[46, 47]. The amide-to-imide (A.NH₂ to A.NH) reaction has shown promising desorption temperatures in the reaction LiNH₂ + LiH → H₂ + LiNH using a 1 : 1 mixture of lithium hydride and lithium amide. Approximately 200 °C is needed to desorb the material[48] but introduction of a catalyst could improve this further.

Of the AB₅ materials, LiNi₅ is the most widely studied as it has good absorption and desorption kinetics. Unfortunately due to the heavy La and Ni concentrations the uptake is poor, just 1 – 1.5 wt.%[49]. Also a high pressure is needed for desorption. This desorption pressure plateau can be greatly reduced by approximately a factor of 300 by swapping 0 – 20 % of the Ni with Al.

Novel reactions have been considered for potential storage applications. One of the simplest uses ammonia as the storage chemical, having 5.9 wt.% it almost meets the D.o.E. targets. Ammonia can be decomposed at around 300 °C using a catalyst comprising caesium-promoted ruthenium supported on graphite[50]. Ammonia is extremely corrosive however and safe storage would require more technology that would result in an effective decrease in the weight-fraction of stored hydrogen.

Carbohydrate-based reactions have been found to decompose to hydrogen in a reaction based on water, C₆H₁₀O₅ + H₂O → H₂ + CO₂[51]. This compound shows an extremely high storage of 14.8 wt.% and desorption temperature of much less than 100 °C at approximately 1 atm, but the cost of production of the sugars could make it sub-

3 Hydrogen storage

economic.

As previously mentioned, other light molecules such as methane have a high hydrogen storage capacity but are best put to use directly in methane fuel cells rather than converting to hydrogen for use in hydrogen fuel cells.

The physisorbed systems can be broadly split into three categories: macroscopic, mesoscopic and micro/nanoscoptic systems. Glass capillary storage tanks have been developed that have an operating pressure of around 1200 atm, considerably higher than a large capacity tank, and can store approximately 33 wt.% of hydrogen[52]. This system of bundles of glass capillaries offer an advantage of large capacity tanks in that failure in a single capillary represents little loss of hydrogen while failure in many would be extremely unlikely. The risk of using high pressures has now been shifted from the storage vessel to the refuelling rig: the refuelling station needs to supply hydrogen at the extremely high pressures envisaged.

Metal organic frameworks (MOFs) have attracted a lot of attention for mesoscopic physisorbed systems due to their large open structure being able to act as a gaseous sponge. The pores can act as a sieve filtering out unwanted gases and capturing only those of the corresponding size[53]. Using the highly tunable pore sizes[54, 55] a perfect MOF could be made for absorbing H₂[56]. MOF-5 has shown excellent promise adsorbing as much as 4.5 wt.% at 78 K and retaining 1 wt.% of H₂ at room temperature and 20 bar[57]. IRMOF-8 has been shown to store twice as much hydrogen at room temperature, 2 wt.%, and at 100 bar[58] through a method of “spillover”[59] where a metal particle sits on a support and dissociates H₂, the H atoms then pass over the support along a carbon-based bridge into a sorbent and reside in the IRMOF-8 sorbent. Most mesoscopic systems follow this pattern of trapping the H₂ molecules in the gas phase in pores, some with adsorption sites.

Of the nanoscopic systems, the carbon systems are most relevant to this project. DFT predictions of the storage capabilities of carbon nanotubes (CNTs) offer 14 wt.%[60]. Experiments have varied between 4.2 wt.% at room temperature and 100 bar[61], while newer estimates fall in the region of less than 0.1 wt.% at 35 bar[62], up to 67 wt.% at 111 bar[63] for some carbon nanofibers. These levels of hydrogen capacity would represent a packing density of 8 H atoms, or 4 H₂ molecules, per C atom in the nanofiber structure. Ultimately these results were unrepeatable and have been classified as erro-

4 A brief history of graphite intercalates

neous, perhaps due to water contamination[64, 65].

Hydrogenated graphene, single atomic layers of graphite, were predicted to exist in 2007 by Sofo et al. [66]. This was confirmed experimentally in 2009 by Elias et al. [67]. The host graphene structure was found to remain relatively unscathed after annealing at 450 °C. The high temperatures and the delicate manipulation necessary to use this structure make it an unconventional storage medium, although its chemical inertness and plentiful supply make it an interesting candidate[68]. Graphene is not likely to be a major player in the subject of hydrogen storage.

Graphite platelets have been reported to store up to 53 wt.%[63] in experiment, but this has not been verified. It has been found that there is little if any hydrogen uptake in these unactivated graphitic structures[69] with graphite offering no H₂ adsorption. This situation can be altered by changing the interplanar chemistry in graphite by doping with metals — creating graphite intercalate compounds.

4 A brief history of graphite intercalates

Graphite intercalation compounds (GICs) were first synthesised in 1840[70] but were not fully characterised until x-ray methods were developed in the 1930s[71, 72]. GICs are formed by inserting atoms into the empty galleries of the graphite host. *Intercalated* atoms can be inserted into every empty gallery (forming a stage-I GIC) or every m -th empty gallery (forming a stage- m GIC), leaving m layers of graphite between each intercalant layer. The in-plane density of the intercalated metal atoms can also be tuned giving an in-plane intercalate-to-carbon ratio (A:C) given by $p : 1$, producing a stage- m GIC with a stoichiometry of MC _{$p \times m$} . Upon intercalation the separation and registration of the graphite layers is altered dependent upon the stage and stoichiometry of the GIC. The differing interaction between different intercalants and the graphite host, and the induced change in *c*-axis separation of the host, creates a different interplanar chemistry for each GIC. Beyond atoms, molecules can also be intercalated into graphite allowing a huge range of *c*-axis separations to be produced. Molecules as large as the C₆₀ Buckminsterfullerene have been intercalated into graphite[73]. By changing the *c*-axis separation the effective pore size can be altered, and optimised for the molecule to be absorbed in the GIC. Absorption of another species other than the intercalant would result in the formation of a tertiary GIC, though this nomenclature is rarely used for weakly bound secondary intercalants. An extensive review by Dresselhaus and

4 A brief history of graphite intercalates

Dresselhaus [74] exists for these materials and gives an excellent full description of many types of GICs.

Graphite intercalates of potassium and caesium were found to be superconducting in 1965[75] at very low temperatures, but recently calcium GICs have been found to have a high T_c of 11.5 K[76]. GICs offer a realistic commercial hydrogen storage solution with the finely tunable inter-plane chemistry and economically as they are relative easy and cheap to construct[77, 78]. GICs have been shown to be robust with some going through a phase change at ambient temperature but only with pressures in excess of 75 kbar[79].

Some species have exhibited surprising difficulty to intercalate. Sodium has been a difficult candidate to intercalate[80] and requires high pressures[81–83] to produce compounds with anything but extremely high-stage GICs[84], while species with the same valency (such as Li and K) and Ca with a comparable ionic radius ($r_{\text{ionic}}(\text{Na}) = 1.02 \times r_{\text{ionic}}(\text{Ca})$) have been intercalated using normal methods. Intercalate compounds of magnesium and beryllium have also resisted manufacture (noted in [85]) despite presenting similar arguments as for those of sodium.

Graphite intercalate compounds have been studied for hydrogen storage for 40 years[86] but is still attracting attention with recent studies adding to our understanding of the interaction of these materials with hydrogen. Of particular interest is the left-hand-side of the periodic table: the alkali and alkaline-earth metal GICs. Heavy alkali-GICs have been shown to be successful absorbers of hydrogen with the potassium GIC attracting a lot of attention. Stage-I KC_8 has been shown to absorb hydrogen directly at 77 K forming $\text{KC}_8\text{H}_{0.67}$ [87]; if KH is intercalated directly then the concentration can be increased to $\text{KC}_8\text{H}_{0.8}$ [88]. Stage-I RbC_8 absorbs little hydrogen at 77 K with a ratio of intercalated-metal to hydrogen of just 1 : 0.05; this situation is greatly improved upon application of 100 bar of pressure and the GIC forms $\text{RbC}_8\text{H}_{0.67}$ [89]. The stage-II compounds of KC_{24} , CsC_{24} and RbC_{24} have been shown to absorb more than two H_2 molecules per metal atom at less than 200 K[86].

Higher stage GICs, such as the stage-II KC_{24} , CsC_{24} and RbC_{24} compounds, show molecularly absorption with more than two H_2 molecules per metal atom at less than 200 K[86]. Of the light-alkali GICs only the Li-GIC has been synthesised and has been shown to decompose upon hydrogenation[88, 90].

The behaviour of decomposition of the Li-GIC is also displayed by the Ca-GIC. The

5 Aims of this work

Ca-GIC was predicted[1] to have a high hydrogen capacity, and offer a better fractional weight uptake against the heavier alkaline-earth GICs, but subsequent experiments by Srinivas et al. [91] have shown it to be unstable in the same manner as the Li-GIC. The lighter Mg- and Be-GICs have also been predicted[1] to have good hydrogen uptake and offer 6 - 7 wt.% of hydrogen but have yet to been synthesised.

5 Aims of this work

This work compliments the experimental work of Neal Skipper's group at University College London. In 2000 Skipper et al. [92] created the ternary methylamine K-GIC. The hydrogen content per unit cell of this $KC_{24}(CH_3NH_2)_3$ material was 3.6 wt.%. The superconductivity of CaC_6 and YbC_6 and their relatively high transition temperature was discovered in 2005 by Weller et al. [76]. Lovell et al. [93] produced findings on KC_{24} for hydrogen storage using neutron scattering experimental techniques to probe the dynamics of hydrogen in these systems. The following year in 2007 Lovell [4] fully described the phase transition visible upon hydrogenating KC_8 which was included in the same year in the thesis by Lovell et al. [87]. In 2008 the dynamics of hydrogenating KC_{24} was studied again by Lovell et al. [94] to understand the limiting processes that prohibit the complete saturation of hydrogen in the compound and lead to the quantum delocalisation of hydrogen to explain the results. The hydrogenation of CaC_6 was examined in 2009 leading to three papers by Srinivas et al. [91][5, 95]. The findings showed that Ca-GICs are extremely unstable when hydrogenated, a topic that is extended in this work. In 2007 Professor Skipper embarked on a industrial project with two former students of his, Dr Lovell and Dr Kurban, and collaborators at Rutherford Appleton Laboratory, Didcot, to produce safe, low-cost hydrogen storage materials. This material was originally based on hydrogenated K-GICs encapsulated in plastic that act as a partially permeable membrane for the passage of hydrogen but a barrier to air. The technology has now moved onto other chemical hydrides that may be pyrophoric in air but safe once encapsulated.

This strong background opened the path to modelling hydrogen in GICs to corroborate experimental findings and attempt to elucidate on some of the open questions. The energetics of hydrogen storage will be the main theme of this work which will look for the mechanisms of H_2 binding in GICs. Predictions for the H_2 absorption will be made for the alkali and alkaline-earth metal GICs (A-/AE-GICs). Also the of stability

5 Aims of this work

of the hydrogenated GIC, which has not been theoretically examined previously, will be calculated for a large group of GICs, including all the A- and AE-GICs in various stoichiometries. Patterns will be derived from these results and predictions made as to the likely stability of some GICs.

This work will attempt to make predictions for the hydrogen storage capabilities of the alkali and alkaline-earth GICs. The focus will be to understand the fundamental interactions that govern a successful hydrogen storage GIC and thus allow its design. Density functional theory (DFT) will be heavily employed in order to study the interaction of hydrogen with the bulk crystalline GICs and these calculations will be benchmarked against high-accuracy quantum chemistry (QC) techniques. QC methods will also be used to decompose the H₂-metal interaction into the important components. Where possible the results and predictions will be compared with experiment.

The K-GIC was extensively covered as detailed information, both experimental and theoretical, exists for the hydrogenated compound. The importance of symmetry in the K-GIC will be explored to link the unexplained hydrogen diffusion results of Purewal [96] with theory. Simple classical pair-potentials parametrised to the K-GIC will allow the rapid simulation of hydrogen diffusion in this material.

A brief summary of what is to appear in the following pages will be necessary here. Chapter 2 will introduce the theory behind the main methods used in this work. §2 goes through a derivation of DFT with proofs of the two Hohenberg-Kohn theorems and a statement of the variational principle. A derivation of the Kohn-Sham equations appears in §2.2 followed by a description of the two main exchange-correlation functionals in use: the local density approximation and the generalised gradient approximation, finishing with a description of plane-wave basis sets. §3 goes through a qualitative description of the quantum chemistry methods used, including Hartree-Fock in §3.1 with the self-consistent field method and a description of localised basis sets. Post Hartree-Fock methods, such as Møller-Plesset second order perturbation theory appearing in §3.2 and coupled cluster methods in §3.3, complete the chapter.

The next chapter, 3, contains the results of calculations performed on the Ca-GIC. The chapter outlines the work that has gone prior, §2, with a summary of the theoretical predictions given in §2.1 followed by a summary of the experimental results in §2.2. The characterisation and the results for the compounds modelled in this chapter come next

5 Aims of this work

with graphite appearing first in §3.1 in its three possible phases. The results for the Ca-GIC come next in §3.2 with the three possible registrations of CaC_6 given before the results for CaC_8 and CaC_{14} in the α -stacked phase. Results for the energetics of hydrogen absorption in the three stoichiometries of GICs appears in §3.3 with detailed discussion of hydrogen energy landscapes for all three in §3.3.3. Results from calculations on the CaH_2 crystal are present in §3.4 with comparison to experiment. Finally this chapter is concluded and the results for the individual compounds brought together in §4.

Chapter 4 deals with the systematics of hydrogen absorption in all the alkali and alkaline-earth metal GICs. The stability of the A-/AE-GICs themselves is examined in §2 with reasons given as to the difficulty of synthesising some compounds. Calculations for hydrogen in these compounds are reported in §3. The fundamental interaction governing hydrogen absorption in these GICs, the $\text{H}_2\text{-M}$ interaction, is reported with QC results in §4. The DFT results of relaxing the hydrides are given §5 with the final conclusions given in §6.

The final results chapter, 5, details the results of calculations upon the two different and widely used stoichiometries of KC_{14} and KC_{12} . These two compounds are used to model the experimental stage-II KC_{24} GIC that shows good reversible hydrogen uptake. The chapter starts, in §1, with an introduction to the modelling work and its comparison with experiment that has gone before. The two structures, both hydrogenated and unhydrogenated, are compared and contrasted in §2. While KC_{14} is commonly used to fit experimental H_2 diffusion data in stage-II KC_{24} §3 will show that the model is too simplistic; the KC_{12} structure adds a slight complexity to the compound that allows a much better fit to experiment. Parametrised potentials for the $\text{H}_2\text{-K}$ and $\text{H}_2\text{-C}$ interactions are given in §3.1 and compared to DFT calculations. A Detailed study of the barriers to diffusion in these two similar compounds appears in this chapter.

Finally the conclusions from the whole project are brought together in chapter 6. This chapter is brief and highlights the major findings of this work.

Chapter 2

Background theory

1 Introduction

The two main methods used in this work, density functional theory (DFT) and quantum chemistry (QC) are both methods for solving the many-body Schrödinger equation of 2.4. For extended systems studied in condensed matter physics DFT is frequently employed, even though it is less accurate than QC methods, since QC methods are computationally more expensive, and their computational requirements increase very rapidly with system size. On the other hand, QC methods are often employed on small isolated systems to obtain accurate results. The majority of this work deals with large periodic arrangements of atoms, such as the graphite intercalates and metal hydrides modelled in chapters 3, 4 and 5, and DFT will be our most commonly used technique. QC will be used on small clusters, such as the H₂-metal complexes of chapter 4, to benchmark the DFT results. Calculations on extended systems using DFT generally employ plane-wave basis sets, as will be done here. Localised Gaussian basis sets will be used for the isolated H₂-metal systems. Finally, we shall also use classical forcefields. For this, two classical Lennard-Jones-type potentials have been built. This type of simulation involves only two-body potentials and is computationally extremely cheap. Once the potentials have been parametrised correctly, they can be used for rapid classical molecular dynamics simulations to compute quantities such as diffusion coefficients.

This chapter will start with §2, which will describe the details of the main theoretical method used to solve the Schrödinger equation: DFT. A derivation will be presented as well as the main parameters affecting the quality of results. §3 will qualitatively describe

1 Introduction

the QC methods used in this work including Hartree-Fock (HF) and the highly accurate post-HF coupled cluster (CC) technique. A derivation of the Hartree-Fock method is present in Appendix B and the coupled cluster method derivation is given in Appendix C. A short overview of the method of classical force-fields will be given in §4.

The Schrödinger equation in 2.1 is the archetypal quantum mechanical equation and is the quantum mechanical analogue of Newton's second law, the classical equation of motion $\mathbf{F} = m\mathbf{a}$. It describes how the state of a system specified by wave function Ψ evolves in time,

$$\hat{\mathbf{H}}\Psi = i\hbar \frac{\partial}{\partial t}\Psi. \quad (2.1)$$

The ground-state wavefunction Ψ_0 is the stationary-state solution,

$$\hat{\mathbf{H}}|\Psi_0\rangle = E_0|\Psi_0\rangle, \quad (2.2)$$

having the lowest energy E_0 . When dealing with systems of atoms, more precisely nuclei and electrons, the wave function will be a function of the set of n nuclear coordinates, $\{\vec{R}_n\}$ and the set of N electronic coordinates, which depend upon position, \vec{r}_i , and spin, σ_i , of each electron, thus the set $\{\vec{x}_N\} = \{(\vec{r}_N, \sigma_N)\}$. The stationary state solution to the Schrödinger equation above can then be written $\hat{\mathbf{H}}\Psi_0(\{\vec{R}_n\}, \{\vec{x}_N\}) = E_0\Psi_0(\{\vec{R}_n\}, \{\vec{x}_N\})$. This Hamiltonian can then be split into five terms. The first two terms representing the kinetic energies of the system and the last three terms representing the potential energies of the system, in this case the electrostatic energies of the system. For a system consisting of N electrons with mass m_e and n nuclei (of which the ν -th species has a mass M_ν) in S.I. units we get

$$\begin{aligned} \hat{\mathbf{H}} = & \underbrace{-\frac{\hbar^2}{2m_e} \sum_{i=1}^N \nabla_i^2 - \frac{\hbar^2}{2} \sum_{\nu=1}^n \frac{\nabla_\nu^2}{M_\nu}}_{\text{kinetic energy terms}} \\ & \underbrace{-\frac{e^2}{4\pi\epsilon_0} \sum_{i\neq\nu} \frac{Z_\nu}{r_{i\nu}} + \frac{1}{2} \frac{e^2}{4\pi\epsilon_0} \sum_{\mu\neq\nu} \frac{Z_\mu Z_\nu}{R_{\mu\nu}} + \frac{1}{2} \frac{e^2}{4\pi\epsilon_0} \sum_{i\neq j} \frac{1}{r_{ij}}}_{\text{potential (electrostatic) terms}}, \end{aligned} \quad (2.3)$$

where ∇ is the differential operator $\nabla = (\partial/\partial x, \partial/\partial y, \partial/\partial z)$ and ∇^2 is the Laplacian; e is the charge on the electron; Z_ν is the charge on nucleus ν ; $r_{i\nu}$ is the distance between electron i and nucleus ν ; $R_{\mu\nu}$ is the distance between nuclei ν and μ ; and r_{ij} is the distance between electrons i and j .

1 Introduction

Born-Oppenheimer approximation This multi-body problem cannot be solved exactly but can be simplified using the Born-Oppenheimer approximation. The knowledge that the nuclei of a system are always much more massive than an electron, over 1800 times heavier for the lightest element, allows us to make the approximation that, within the characteristic time scale of the electrons, the nuclei remain stationary. This assertion allows the second term of 2.3, the nuclei kinetic energy term, to be expunged; the third term, the electron-nuclear interaction term, becomes a constant electrostatic field that the electrons move in; and the fourth, nuclear-nuclear interaction, term becomes an additive constant. This approximation would assert that at any given instant the electrons are in their instantaneous ground state for any given arrangement of nuclei.

The wave function given in the Schrödinger equation in 2.2 now depends upon the set of electronic coordinates as before, $\{\vec{x}_N\}$, but only *parametrically* upon the set of nuclear coordinates, $\{\vec{R}_n\}$. Thus, under the Born-Oppenheimer approximation, the wave function can be separated into the wave function of the electrons, Ψ^{elec} , and the wave function of the nuclei, Ψ^{nuc} , thus $\Psi(\{\vec{R}_n\}, \{\vec{x}_N\}) = \Psi^{\text{elec}}(\{\vec{x}_N\}; \{\vec{R}_n\}) \Psi^{\text{nuc}}(\{\vec{R}_n\})$. The resulting *reduced electronic* problem still cannot be solved exactly for $N > 1$ and requires approximation methods to solve the steady state *electronic* Schrödinger equation, now given by

$$\hat{\mathbf{H}}_e \Psi_0^{\text{elec}}(\{\vec{x}_N\}; \{\vec{R}_n\}) = E_0^{\text{elec}} \Psi_0^{\text{elec}}(\{\vec{x}_N\}; \{\vec{R}_n\}), \quad (2.4)$$

using the reduced electronic Hamiltonian ($\hat{\mathbf{H}}_e$) to recover the total electronic ground state energy of the system (E_0^{elec}). As this work will always be dealing with the electronic problem, the subscript “*e*” will remain on the Hamiltonian but the superscript “elec” will be dropped from E_0 and the electronic energy of the system will be denoted E and the electronic ground state energy as E_0 . The final term in 2.3 is the electron-electron repulsive term and needs to be fully included in order to accurately solve for the energy eigenvalues. Both density functional theory (§2) and quantum chemistry (§3) split this difficult term into more manageable terms to express the exchange and correlation energies.

The wave-function holds all the information about the underlying system but cannot be observed directly. To gain insight into it we look at the square of the norm of the wave function, the probability density, e.g. the probability of finding the particle within a volume element V centred at $\vec{r} = (x, y, z)$ at time t would be $P(\vec{r}, t) = \int_V |\Psi(\vec{r}, t)|^2 d\vec{r}$.

2 Density functional theory

The quantum chemistry methods described in §3 rely on approximating the actual wave functions involved in the problem as the basic variable, while the density functional theory method of §2 exploits the close relationship between the wave function and position probability density and uses the particle density as the basic variable.

2 Density functional theory

Density functional theory (DFT) is a method for solving the many-body Schrödinger equation of 2.2 to calculate the ground state energy E_0 of the system of nuclei and electrons. The many-body problem is reduced using the Born-Oppenheimer approximation, seen earlier, so that we have to treat the energetics of a system of electrons in the static field of the nuclei. The electronic Hamiltonian, $\hat{\mathbf{H}}_e$, can be separated into the electron kinetic energy operator ($\hat{\mathbf{T}}_e$), the electron-electron interaction energy operator ($\hat{\mathbf{U}}_{ee}$) and the electron-nuclear potential energy interaction operator ($\hat{\mathbf{V}}$),

$$\hat{\mathbf{H}}_e = \hat{\mathbf{T}}_e + \hat{\mathbf{U}}_{ee} + \hat{\mathbf{V}}. \quad (2.5)$$

The key to this method is the mapping of the problem from an abstract wave function based approach, as will be seen in QC later (§3), to a more tangible particle density approach. The two Hohenberg-Kohn theorems[97] allow the complicated many-body wave-function to be mapped to a single particle electron density function dependent upon only a single position, $n(\vec{r})$.

2.1 Hohenberg-Kohn theorems

Hohenberg-Kohn theorem 1. *For a system of interacting particles within an external potential, $v_{\text{ext}}(\vec{r})$, the external potential is fully determined (to within an additive constant) by the ground state particle density $n_0(\vec{r})$.*

Proof. This *reductio ad absurdum* proof is proven for the case of a non-degenerate ground state wave function and in the absence of an external vector field, such as a magnetic field. The proofs have been generalised to include the effects of magnetic fields[98] and degeneracy[99].

This proof assumes there exist two external potentials, $v_{\text{ext}}(\vec{r})$ and $v'_{\text{ext}}(\vec{r})$, that differ by more than an additive constant such that they are distinct. We define two operators, $\hat{\mathbf{V}}$ and $\hat{\mathbf{V}'}$, for these potentials of the form $\hat{\mathbf{V}} = \sum_i v_{\text{ext}}(\vec{r}_i)$. If these potentials differed

2 Density functional theory

by just an additive constant the primed system would be a copy of the unprimed system with the energy levels shifted.

Let us assume we have two systems that differ by only the external potentials (i.e. the kinetic and electron-electron interaction terms are equal) giving rise to two Hamiltonians,

$$\hat{\mathbf{H}}_e = \hat{\mathbf{T}}_e + \hat{\mathbf{U}}_{ee} + \hat{\mathbf{V}} \quad (2.6)$$

$$\text{and } \hat{\mathbf{H}}'_e = \hat{\mathbf{T}}_e + \hat{\mathbf{U}}_{ee} + \hat{\mathbf{V}}'. \quad (2.7)$$

Let us now assume the two potentials result in the same ground state particle density $n_0(\vec{r})$. We will complete this proof using the variational principle.

Variational principle The variational principle asserts that using any arbitrary wave function that is *not* the ground state wave function of the system will always result in an energy higher than (or in the case of degenerate ground states, equal to) the ground state energy for the system, thus

$$\langle \Psi | \hat{\mathbf{H}}_e | \Psi \rangle = E \geq E_0 = \langle \Psi_0 | \hat{\mathbf{H}}_e | \Psi_0 \rangle, \quad (2.8)$$

where the subscript zero, Ψ_0 and E_0 , refers to the ground state properties of the system with Hamiltonian $\hat{\mathbf{H}}$ and Ψ is an arbitrary wave function that is not the ground state wave function of the system.

Calculating the expectation values of the Hamiltonians of each of our systems, $\langle \hat{\mathbf{H}}_e \rangle = \langle \Psi | \hat{\mathbf{H}}_e | \Psi \rangle = E$ and $\langle \hat{\mathbf{H}}'_e \rangle = \langle \Psi' | \hat{\mathbf{H}}'_e | \Psi' \rangle = E'$, will thus always give a higher energy unless the ground state wave function of the system is used. Note that the earlier assertion that the ground states of our two systems (the primed and unprimed systems) are unique, i.e. non-degenerate, results in the inequality becoming a *strictly more than* inequality, i.e. $\geq \rightarrow >$ under the non-degenerate scheme in 2.8. If we now define two non-degenerate ground state wave functions for the primed and unprimed systems as Ψ'_0 and Ψ_0 respectively, then we can state that

$$E'_0 = \langle \Psi'_0 | \hat{\mathbf{H}}'_e | \Psi'_0 \rangle < \langle \Psi_0 | \hat{\mathbf{H}}'_e | \Psi_0 \rangle, \quad (2.9)$$

noting that the wave function Ψ_0 is not the ground state wave function of the primed system.

Using the Hamiltonian of the primed system from 2.7 and adding then subtracting

2 Density functional theory

the potential operator of the unprimed system, $\hat{\mathbf{V}}$, we get

$$\begin{aligned}\hat{\mathbf{H}}'_e &= \underbrace{\hat{\mathbf{T}}_e + \hat{\mathbf{U}}_{ee} + \hat{\mathbf{V}}}_{\hat{\mathbf{H}}_e} + (\hat{\mathbf{V}}' - \hat{\mathbf{V}}) \\ &= \hat{\mathbf{H}}_e + (\hat{\mathbf{V}}' - \hat{\mathbf{V}}).\end{aligned}\quad (2.10)$$

We can now substitute this result 2.10 into the right hand side of 2.9,

$$\begin{aligned}E'_0 &< \langle \Psi_0 | \hat{\mathbf{H}}_e + (\hat{\mathbf{V}}' - \hat{\mathbf{V}}) | \Psi_0 \rangle \\ &= E_0 + \langle \Psi_0 | (\hat{\mathbf{V}}' - \hat{\mathbf{V}}) | \Psi_0 \rangle \\ \therefore E'_0 &< E_0 + \langle \Psi_0 | (\hat{\mathbf{V}}' - \hat{\mathbf{V}}) | \Psi_0 \rangle,\end{aligned}\quad (2.11)$$

where we have noted that $E_0 = \langle \Psi_0 | \hat{\mathbf{H}}_e | \Psi_0 \rangle$.

We can rewrite 2.11 as

$$E'_0 < E_0 + \int (v'_{\text{ext}}(\vec{r}) - v_{\text{ext}}(\vec{r})) n_0(\vec{r}) d\vec{r}. \quad (2.12)$$

We can, of course, rerun the argument from equation 2.9 using the unprimed system and arrive at a similar equation, namely

$$E_0 < E'_0 + \int (v_{\text{ext}}(\vec{r}) - v'_{\text{ext}}(\vec{r})) n'_0(\vec{r}) d\vec{r}. \quad (2.13)$$

Adding these two results, 2.12 and 2.13, we arrive at the crux of this proof,

$$E_0 + E'_0 < E'_0 + E_0 + \int (v'_{\text{ext}}(\vec{r}) - v_{\text{ext}}(\vec{r})) (n_0(\vec{r}) - n'_0(\vec{r})) d\vec{r}. \quad (2.14)$$

We asserted that the two potentials $v'_{\text{ext}}(\vec{r})$ and $v_{\text{ext}}(\vec{r})$ were distinctly different. Therefore if the two systems have the same ground state particle density, $n'_0(\vec{r}) = n_0(\vec{r})$, then we arrive at the absurd claim that the sum of the total ground state energies of the two systems is strictly less than itself, $E_0 + E'_0 < E'_0 + E_0$.

Thus we conclude that for two systems with external potentials that differ by more than an additive constant they must have different non-degenerate ground states. This gives us a one-to-one mapping between the ground state particle density and the external potential,

$$n_0(\vec{r}) \mapsto v_{\text{ext}}(\vec{r}). \quad (2.15)$$

Now the Hamiltonian is fully determined, to within a constant shift of the energy levels of the system, *the ground and all excited states of the system are also fully determined*. Finally, we can thus assert that *all* properties of the system are fully determined by the ground state particle density $n_0(\vec{r})$.

□

2 Density functional theory

The total energy, E , of the system is a *functional* of the Hamiltonian and thus the external potential. Using the relation in 2.15 we can now say the energy is a functional of the particle density, i.e. $E[v_{\text{ext}}(\vec{r})] \mapsto E[n(\vec{r})]$. Using the second Hohenberg-Kohn theorem we can relate the ground state energy, E_0 , to the ground state particle density.

Hohenberg-Kohn theorem 2. *The exact ground state energy, E_0 , of the system is the global minimum of the energy functional with respect to the particle density ($E[n(\vec{r})]$), subject to the constraints of keeping the total number of particles (N) and the external potential ($v_{\text{ext}}(\vec{r})$) fixed. The density at this global minimum, subject to the constraints, is then the ground state particle density $n_0(\vec{r})$.*

Proof. This proof involves just one system. We invoke the variational principle of 2.8 again and state that (for the case of a non-degenerate ground state) the true ground state energy, $E_0 = \langle \Psi_0 | \hat{\mathbf{H}}_e | \Psi_0 \rangle$, of a system will always be lower than the energy obtained with some arbitrary wave function, Ψ , that is not the ground state (Ψ_0) of the system, i.e.

$$E_0 = \langle \Psi_0 | \hat{\mathbf{H}}_e | \Psi_0 \rangle < \langle \Psi | \hat{\mathbf{H}}_e | \Psi \rangle. \quad (2.16)$$

If we now split the Hamiltonian operator, defined in 2.5, into two parts: an operator, $\hat{\mathbf{B}}$, consisting of the $\hat{\mathbf{T}}_e$ and $\hat{\mathbf{U}}_{ee}$ terms and a part consisting of the external potential $\hat{\mathbf{V}}$ term. We now take the expectation value of the Hamiltonian and define the universal functional $F[n(\vec{r})]$ to be the expectation value of $\hat{\mathbf{B}}$ that is the same for all systems, and note that $n(\vec{r})$ is the particle density corresponding to the arbitrary wave function Ψ . Expanding 2.16 using these definitions leads to

$$\begin{aligned} E_0 &< \left\langle \Psi \left| \underbrace{\hat{\mathbf{T}}_e + \hat{\mathbf{U}}_{ee}}_{\hat{\mathbf{B}}} + \hat{\mathbf{V}} \right| \Psi \right\rangle \\ &\implies E_0 < \langle \Psi | \hat{\mathbf{B}} | \Psi \rangle + \langle \Psi | \hat{\mathbf{V}} | \Psi \rangle \\ &\implies E_0 < F[n(\vec{r})] + \int v_{\text{ext}}(\vec{r}) n(\vec{r}) d\vec{r}. \end{aligned} \quad (2.17)$$

As we search through all the possible particle densities the lowest value of the right hand side of 2.17 is E_0 and will be obtained when the particle density is the ground state particle density, $n(\vec{r}) = n_0(\vec{r})$. □

2.2 The Kohn-Sham ansatz and equations

The Hohenberg-Kohn theorems above show that the ground state particle density can be used as a basic variable in solving the Schrödinger equation. In order to create a method

2 Density functional theory

to find the solution we implement the method derived by Kohn and Sham [100]. The Kohn-Sham ansatz states that there exists a system of non-interacting particles that has the same ground state particle density as the equivalent interacting system. This allows the difficult interacting system to be replaced with an auxiliary system of *non-interacting* particles, that is (in principle) soluble. In order to arrive at the Kohn-Sham equations we shall run two systems sequentially: a system of non-interacting particles and one of interacting particles (in this case, of electrons).

Beginning with the case for non-interacting particles, we define the Hamiltonian operator to be

$$\text{Non-interacting system: } \hat{\mathbf{H}}_e^{\text{non-int}} = \hat{\mathbf{H}}_0 + \hat{\mathbf{V}}_{\text{ext}}, \quad (2.18)$$

where $\hat{\mathbf{H}}_e$ is the electronic Hamiltonian; $\hat{\mathbf{H}}_0$ is the non-interacting homogeneous gas Hamiltonian; and $\hat{\mathbf{V}}_{\text{ext}}$ is the total interaction energy of the particles with the external potential.

Using the Hohenberg-Kohn theorems we define the total energy of the system as a functional of the density. At this stage we can now bring in the same total energy functional for the interacting system. Both energy functionals then appear as

$$\text{Non-interacting system: } E_{\text{non-int}}[n] = T_s[n] + \int v_{\text{ext}}(\vec{r}) n(\vec{r}) d\vec{r}, \quad (2.19)$$

$$\text{Interacting system: } E_{\text{int}}[n] = T_s[n] + \int v_{\text{ext}}(\vec{r}) n(\vec{r}) d\vec{r} \quad (2.20)$$

$$+ \frac{1}{2} \int \frac{n(\vec{r}) n(\vec{r}')}{|\vec{r} - \vec{r}'|} d\vec{r} d\vec{r}' + E_{xc}[n]. \quad (2.21)$$

The interacting system has been attributed with the same kinetic energy functional as for the non-interacting case ($T_s[n]$) with the contribution to the electron motion due to their interaction (correlation) and the quantum mechanical effects of particle exchange pushed to the exchange-correlation energy. It also has the additional terms of the Coulomb self interaction term, the Hartree Energy functional, representing the interaction energy of the charge distribution with itself,

$$E_{\text{Hartree}}[n] = \frac{1}{2} \int \frac{n(\vec{r}) n(\vec{r}')}{|\vec{r} - \vec{r}'|} d\vec{r} d\vec{r}', \quad (2.22)$$

and the exchange correlation energy functional (E_{xc}). At this stage the formalism is correct, with all the many-body difficulty pushed to the exchange correlation term.

To find the ground state energy of the systems we wish to minimise the total energy functionals with respect to the particle density, $\delta E / \delta n(\vec{r})$. We must ensure that the particle

2 Density functional theory

number remains fixed ($N = \int n(\vec{r}) d\vec{r}$) which leads to a constrained minimisation. The method of Lagrange undetermined multipliers is used and gives the Lagrange functions for the two systems to be,

$$\text{Non-interacting system: } \Lambda_{\text{non-int}}[n] = T_s[n] + \int v_{\text{ext}}(\vec{r}) n(\vec{r}) d\vec{r} - \mu N, \quad (2.23)$$

$$\begin{aligned} \text{Interacting system: } \Lambda_{\text{int}}[n] &= T_s[n] + \int v_{\text{ext}}(\vec{r}) n(\vec{r}) d\vec{r} + E_{\text{Hartree}}[n] \\ &\quad + E_{xc}[n] - \mu N. \end{aligned} \quad (2.24) \quad (2.25)$$

We now minimise with respect to the particle density and set to zero to find the minimum energy,

$$\text{Non-interacting system: } \frac{\delta \Lambda_{\text{non-int}}}{\delta n(\vec{r})} = 0 \Rightarrow \frac{\delta T_s}{\delta n(\vec{r})} + v_{\text{ext}}(\vec{r}) = \mu, \quad (2.26)$$

$$\text{Interacting system: } \frac{\delta \Lambda_{\text{int}}}{\delta n(\vec{r})} = 0 \Rightarrow \frac{\delta T_s}{\delta n(\vec{r})} + v_{\text{ext}}(\vec{r}) \quad (2.27)$$

$$+ \frac{\delta E_{\text{Hartree}}}{\delta n} + \frac{\delta E_{xc}}{\delta n} = \mu. \quad (2.28)$$

The Hartree potential is defined as

$$v_{\text{Hartree}}(\vec{r}) = \frac{\delta E_{\text{Hartree}}}{\delta n(\vec{r})} \quad (2.29)$$

$$= \frac{\delta}{\delta n(\vec{r})} \left[\frac{1}{2} \int \frac{n(\vec{r}) n(\vec{r}')}{|\vec{r} - \vec{r}'|} d^3 r d^3 r' \right] \quad (2.30)$$

$$= \int \frac{n(\vec{r}')}{|\vec{r} - \vec{r}'|} d\vec{r}', \quad (2.31)$$

and the exchange-correlation potential as

$$v_{xc}(\vec{r}) = \frac{\delta E_{xc}}{\delta n}. \quad (2.32)$$

Now by grouping the Hartree potential, exchange-correlation potential and the external potential of the interacting system into one effective potential,

$$v_{\text{eff}}(\vec{r}) = v_{\text{Hartree}}(\vec{r}) + v_{xc}(\vec{r}) + v_{\text{ext}}(\vec{r}), \quad (2.33)$$

we arrive at the two systems being indistinguishable if the external potential of the non-interacting system is chosen to be equivalent to the effective potential of the interacting system,

$$\text{Non-interacting system: } \frac{\delta T_s}{\delta n(\vec{r})} + v_{\text{ext}}(\vec{r}) = \mu, \quad (2.34)$$

$$\text{Interacting system: } \frac{\delta T_s}{\delta n(\vec{r})} + v_{\text{eff}}(\vec{r}) = \mu. \quad (2.35)$$

2 Density functional theory

We can now construct the Kohn-Sham Schrödinger-like equation for the interacting case that looks equivalent to the non-interacting case with the external potential swapped for the effective potential,

$$\text{Non-interacting system: } \left[-\frac{\hbar^2}{2m_e} \nabla^2 + v_{\text{ext}}(\vec{r}) \right] \phi_i(\vec{r}) = \varepsilon_i \phi_i(\vec{r}), \quad (2.36)$$

$$\text{Interacting system: } \left[-\frac{\hbar^2}{2m_e} \nabla^2 + v_{\text{eff}}(\vec{r}) \right] \phi_i(\vec{r}) = \varepsilon_i \phi_i(\vec{r}), \quad (2.37)$$

where we wish to minimise the energy with respect to the Kohn-Sham orbitals, $\phi_i(\vec{r})$, to find the ground state energy. Since the effective potential, $v_{\text{eff}}(\vec{r})$, depends directly upon the particle density and thus indirectly upon the Kohn-Sham orbitals we must solve this self-consistently. Equation 2.37 is often written as two equations by being split into

$$(\hat{\mathbf{H}}_{\text{KS}} - \varepsilon_i) \phi_i(\vec{r}) = 0, \quad (2.38)$$

with the Kohn-Sham Hamiltonian given as

$$\hat{\mathbf{H}}_{\text{KS}}(\vec{r}) = -\frac{\hbar^2}{2m_e} \nabla^2 + v_{\text{KS}}(\vec{r}), \quad (2.39)$$

where the Kohn-Sham potential is simply the effective potential that gives the minimum ground state energy. These three equations (2.33, 2.38 and 2.39) form the Kohn-Sham equations and solved self-consistently allow the evaluation of the total ground state energy and particle density.

We have ended up with our many-body interacting system described in terms of a set single independent-particle orbitals, $\{\phi_i(\vec{r})\}$. It is worth noting at this stage that individual single particle energies, ε_i , and individual single particle orbitals ϕ_i do not have any physical significance as individual particle energies or orbitals. The description of the system as a set of independent particles is incorrect, it is only using the complete set of these that the total energy and particle density is correct. Surprisingly, however, plotting of these orbitals can yield results that are close to the band structures of real materials in some systems.

2.2.1 Exchange-correlation energy, E_{xc}

At this stage the formulation is exact and if exact potentials were known for equation 2.33 that representing the energy functionals, specifically for the exchange-correlation (xc) energy functional $E_{xc}[n(\vec{r})]$, then the resulting energy and particle density would be exact within the chosen basis. Note that for the result to be exact a complete, infinite,

2 Density functional theory

basis set would be required. All the potentials in 2.33 are well-defined except for the xc -potential.

The electronic exchange-correlation energy is the energy difference between the interacting system and the auxiliary system of non-interacting particles used as a model in the Kohn-Sham scheme. This can be described as the sum of the energy difference between the kinetic energy of the interacting electrons (the true kinetic energy, $\langle \hat{\mathbf{T}}_e \rangle$) and the kinetic energy of the non-interacting system (the Kohn-Sham kinetic energy, T_s); and the energy difference between the interaction of the electrons in the physical system ($\langle \hat{\mathbf{U}}_{ee} \rangle$) and the Hartree self-interaction energy E_{Hartree} . So it can be expressed as,

$$E_{xc} [n] = \langle \hat{\mathbf{T}}_e \rangle - T_s [n] + \langle \hat{\mathbf{U}}_{ee} \rangle - E_{\text{Hartree}} [n]. \quad (2.40)$$

It is the approximation to this functional that greatly affects the accuracy of DFT calculations. Much effort has been expended to create functionals that are both accurate and transferable. The simplest assumption is to take the exchange-correlation energy from the homogeneous electron gas with a particle density equal to that of the system of interest: the *local density approximation*. The next stage is to adapt this homogeneous electron gas to include smooth changes in the electron density from place-to-place: the *generalised gradient approximation*.

Local density approximation (LDA) The first and simplest approximation to the exchange-correlation functional is to use that of jellium, the uniform electron gas. The assumption starts by creating an amount of exchange correlation energy within a volume element at \vec{r} in the jellium given by $\delta\mathcal{E}_{xc}^{\text{LDA}} (n(\vec{r}))$. Since jellium is defined to have a homogeneous particle density, n is no longer dependent upon \vec{r} and thus the amount of xc -energy within this volume element is also independent of position,

$$\delta\mathcal{E}_{xc}^{\text{LDA}} (n(\vec{r})) \mapsto \delta\mathcal{E}_{xc}^{\text{LDA}} (n). \quad (2.41)$$

This is the essence of the local density approximation: the density of exchange correlation energy within a volume element located at \vec{r} is dependent only upon the local particle density within the volume element.

To use this in our physical system to approximate the xc -energy, we simply multiply this element of xc -energy from jellium with the density at the position \vec{r} in our system, given by $n(\vec{r})$, thus

$$\delta E_{xc}^{\text{LDA}} [n(\vec{r})] = \delta\mathcal{E}_{xc}^{\text{LDA}} (n) \cdot n(\vec{r}), \quad (2.42)$$

2 Density functional theory

where $\delta E_{xc}^{\text{LDA}}[n(\vec{r})]$ is the LDA *xc*-energy within the volume element located at \vec{r} within our system.

We integrate this expression to find the total LDA exchange-correlation energy in our system, $E_{xc}^{\text{LDA}}[n(\vec{r})]$,

$$E_{xc}^{\text{LDA}}[n(\vec{r})] = \int \delta E_{xc}^{\text{LDA}}[n(\vec{r})] d\vec{r} = \int (\delta \mathcal{E}_{xc}^{\text{LDA}}(n) \cdot n(\vec{r})) d\vec{r}. \quad (2.43)$$

In this approximation it can be seen that the exchange-correlation energy is dependent only upon the local particle density. No consideration is given as to how the particle density changes outside the volume element. This initial approximation, while simple in construction, allowed the first DFT calculations to be performed with remarkable success for systems with slowly varying particle densities. Using the LDA method is computationally cheap allowing large calculations to be well approximated before more accurate methods are implemented.

The next stage of approximation to this energy functional is to consider how the *xc*-energy within a volume element is affected in the presence of a gradient in the particle density.

Generalised gradient approximation (GGA) While the computationally cheap LDA method requires just the local value of the particle density in order to evaluate the *xc*-energy at that point; the GGA requires the local value and the gradient of the local particle density at each point to be known. This increases computational costs but also shows a marked improvement on systems with more complex particle densities.

The approximation to the exchange-correlation energy within a volume element at the position \vec{r} at a local particle density of $n(\vec{r})$ is now $\delta \mathcal{E}_{xc}^{\text{GGA}}(n(\vec{r}), \nabla n(\vec{r}))$ within a non-uniform electron gas. Note that $\delta \mathcal{E}_{xc}^{\text{GGA}}$ cannot be simplified to be local-density-dependent only. It is usually denoted by a function, f , split into a spin-up part (\uparrow) and a spin-down part (\downarrow), notated as $f(n_{\uparrow}(\vec{r}), n_{\downarrow}(\vec{r}), \nabla n_{\uparrow}(\vec{r}), \nabla n_{\downarrow}(\vec{r}))$. We then integrate this expression to obtain the GGA approximation to the total *xc*-energy of our real system with particle density $n(\vec{r})$,

$$E_{xc}^{\text{GGA}}[n(\vec{r})] = \int f(n_{\uparrow}(\vec{r}), n_{\downarrow}(\vec{r}), \nabla n_{\uparrow}(\vec{r}), \nabla n_{\downarrow}(\vec{r})) d\vec{r}. \quad (2.44)$$

The effect of using the GGA over the LDA is a general improvement on covalently bonded systems at the expense of a moderately increased simulation time.

2.3 Plane wave basis sets

The solution to the electronic Schrödinger equation of 2.4 requires a description of the wave function inherent to the system of interest. The approximation to the true wave function is performed by expanding it on an infinite basis set. Use of an infinite basis set is impossible for real-world calculations and so a smaller finite subset of this is used. Two types of basis set are frequently used for this expansion: a basis set of plane waves (inherently non-local and will be used for most of the work in chapters 3, 4 and 5 when DFT is employed) and a basis set comprising Gaussian functions (a set of local functions employed in QC calculations in chapter 4).

The expansion of the true electronic wave function (dependent upon the electronic spin-vector $\vec{x} = (\vec{r}, \sigma)$), $\Psi(\vec{x})$, by an incomplete set of basis functions, $\{\phi_n(\vec{x})\}$, is thus the approximation

$$\Psi(\vec{x}) = \lim_{n \rightarrow \infty} \sum_i^n a_i \phi_i(\vec{x}), \quad (2.45)$$

$$\Psi(\vec{x}) \approx \sum_i^n a_i \phi_i(\vec{x}) \quad (\forall n < \infty), \quad (2.46)$$

where a_i is the i -th expansion coefficient of the i -th basis function, ϕ_i ; just as in the expansion of a vector on an orthonormal basis ($\hat{\mathbf{e}}_i$), $\vec{v} = \sum_i a_i \hat{\mathbf{e}}_i$.

A basis set of plane waves has $\phi(\vec{r}) = e^{i(\vec{k} \cdot \vec{r})}$, where \vec{k} is the wave vector and \vec{r} the position vector as usual. Using a plane wave for the members of the basis set works well for periodic crystals as these functions are naturally periodic. Electrons within metallic systems, and valence electrons in materials, will often have a wave function similar to the free electron plane wave.

For a crystal system exhibiting a periodic nature, i.e. with a periodic potential created by the nuclei, Bloch's theorem can be utilised to separate the electronic wave function into a plane wave-like part and a periodic function, $f_{j,\vec{k}}(\vec{r})$, absorbing the information of the crystal lattice,

$$\phi_{j,\vec{k}}(\vec{r}) = e^{i(\vec{k} \cdot \vec{r})} f_{j,\vec{k}}(\vec{r}). \quad (2.47)$$

The problem of solving the infinite crystal has been reduced from solving the case of an infinite number of electrons interacting with an infinite number of nuclei to solving the electrons interacting with the nuclei within the unit cell (one period of the periodic potential of the nuclei). The periodic function $f_{j,\vec{k}}(\vec{r})$ can now be expanded into a sum

of plane waves,

$$f_{j\vec{k}}(\vec{r}) = \sum_{\vec{G}} a_{j,\vec{G}} e^{i(\vec{G}\cdot\vec{r})}, \quad (2.48)$$

where \vec{G} are the reciprocal lattice vectors, defined as the Fourier transform of the unit cell lattice vectors \vec{l} , as $\vec{G} \cdot \vec{l} = 2\pi m$ ($\forall \vec{l}$), where m is an integer. This expansion can now be included in 2.47 and the two wave-like parts combined to give

$$\phi_{j,\vec{k}}(\vec{r}) = \sum_{\vec{G}} a_{j,(\vec{G}+\vec{k})} e^{i(\vec{G}+\vec{k})\cdot\vec{r}}, \quad (2.49)$$

producing a wave function expressed in terms of an infinite sum of reciprocal lattice vectors within the first Brillouin zone, \vec{k} . Each plane wave in the sum can be ascribed an energy of $E = \hbar^2 |\vec{k} + \vec{G}|^2 / 2m_e$, where m_e is the mass of the electron. We can now use this energy to curtail the sum to exclude plane waves above an energy E_{cut} , the *plane wave cut off*. The slowly varying, lower energy, plane waves contribute most to the electronic energy and as we increase the cut-off so the approximation will smoothly approach the true electronic function ϕ . This smooth approach of the total energy to the infinite basis set limit allows this limit to be extrapolated from modest basis sets.

3 Quantum chemistry

Quantum chemistry (QC) methods, as distinct from the solid state methods employing DFT, focus on a wave function-based approach to solving the electronic Schrödinger equation of 2.4. In this method the wave functions of individual electrons in the system are used as a basic variable. Both DFT and QC accuracy depend highly upon the completeness of the basis set and upon a system specific choice: how much complexity to introduce to the electron-electron interaction term.

In DFT the choice of *xc*-functional determines how much complexity is introduced into the $\hat{\mathbf{U}}_{ee}$ term in the Hamiltonian 2.5 with LDA offering the simplest approximation and GGA offering the next step of complexity. More complicated functionals also exist for complicated systems and result in high accuracy calculations. In QC the choice of increasing complexity of the electron-electron interaction term starts with the basic Hartree-Fock (HF) approach and leads onto post-HF methods that model electron correlation more fully. In some systems it is known that GGA improves little over the computationally cheaper LDA *xc*-functional. In QC the considerably more computationally expensive post-HF methods, such as CCSD(T), may not improve much over

3 Quantum chemistry

other perturbative methods for the electron correlation, or even the extremely cheap HF approach, for some systems.

The principles of QC again rely upon the variational principle of equation 2.8. The wave function Ψ is given an appropriate first guess then iteratively corrected until the energy of the system cannot be lowered any further. This lowest-energy solution is then the ground state energy of the system. E_0 , with the corresponding wave function giving the ground state wave function Ψ_0 .

3.1 Hartree-Fock method

A full derivation of the Hartree-Fock method following Szabo and Ostlund [101] is given in appendix B (page 173) and as such only a qualitative description shall be given here to illuminate the main differences between DFT and HF.

Again the electronic energy, E , of the system in question is given by the expectation value of the electronic Hamiltonian, $\hat{\mathbf{H}}_e$, with respect to the wave function Ψ . By the variational principle this energy will only (for systems with a non-degenerate ground state wave function) give the ground state energy, E_0 , when the ground state wave function, Ψ_0 , is used, i.e.

$$E = \langle \Psi | \hat{\mathbf{H}}_e | \Psi \rangle > E_0 = \langle \Psi_0 | \hat{\mathbf{H}}_e | \Psi_0 \rangle. \quad (2.50)$$

By using a wave function that respects the rules of anti-symmetry of fermions, a Slater determinant, we have a method that necessarily considers electron exchange directly as it is built-in. A Slater determinant is formed by filling a square matrix with single-electron spin-orbitals, χ_a , and taking the determinant,

$$|\Psi(\vec{x}_1, \vec{x}_2, \dots, \vec{x}_N)\rangle = \frac{1}{\sqrt{N!}} \begin{vmatrix} \chi_1(\vec{x}_1) & \chi_2(\vec{x}_1) & \cdots & \chi_N(\vec{x}_1) \\ \chi_1(\vec{x}_2) & \chi_2(\vec{x}_2) & \cdots & \chi_N(\vec{x}_2) \\ \vdots & \vdots & \ddots & \vdots \\ \chi_1(\vec{x}_N) & \chi_2(\vec{x}_N) & \cdots & \chi_N(\vec{x}_N) \end{vmatrix} = |\chi_1 \chi_2 \cdots \chi_N\rangle, \quad (2.51)$$

where, again, \vec{x}_i is the electronic spin-vector of electron i , $\vec{x}_i = (\vec{r}_i, \sigma_i)$.

The Pauli-exclusion principle, a result of the antisymmetry principle, is respected in this form of wave function (exchanging any two electrons results in exchanging two columns of the determinant and thus flips the sign of the wave function) and as such the position of electrons of equal spin is correlated in a sense that they cannot be

3 Quantum chemistry

equal (two columns of the determinant would become equal and the determinant, and thus the wave function, would vanish). Beyond this, electron correlation is not directly employed; a *mean field* approach is implemented. This mean field approximation is the biggest approximation of this method and assumes an electron in the system moves in an average field created by the other ($N - 1$) electrons.

The initial guess for the wave function, using a Slater determinant, is varied using a more general form of the variationl principle: *functional variation*. This is discussed more fully in Appendix A on page 170. This method is used to vary the components of the Slater determinant, the single electron spin-orbitals, until the energy is lowered through the self-consistent field method.

Self-consistent field method This iterative loop to lower the energy depends upon the variability of the Slater determinant and this flexibility arises from the choice of the set of spin orbitals, $\{\chi_N\}$. The process of minimising the energy in 2.50 by varying the choice of spin orbitals in the Slater determinant leads to the eigenvalue equation,

$$f(i)\chi(\vec{x}_i) = \varepsilon\chi(\vec{x}_i), \quad (2.52)$$

the Hartree-Fock equation, where $f(i)$ is the *Fock operator* (not to be confused with the GGA functional seen in DFT earlier). The Fock operator is given as,

$$f(i) = h(i) + v_{\text{HF}}(i) = \left[-\frac{1}{2}\nabla_i^2 - \sum_{\nu=1}^n \frac{Z_\nu}{r_{i\nu}} + v_{\text{HF}}(i) \right], \quad (2.53)$$

where $h(i)$ is the “non-interacting” single particle Hamiltonian of electron i (i.e. only includes kinetic and electron-nuclear interaction terms) with ∇_i^2 the Laplacian for electron i ; $r_{i\nu}$ the distance between electron i and nucleus ν ; Z_ν the charge on nucleus ν ; and $v_{\text{HF}}(i)$ the Hartree-Fock average potential felt by electron i .

The mean-field $v_{\text{HF}}(i)$ deals with the electron-electron interaction in an average way. In this sense, electron correlation is not directly accounted for. Instead it specifies the strength of the coulomb field at position \vec{r}_i of electron with spin σ_i (i.e. the spin-vector \vec{x}_i) averaged over the rest of the electrons in all other occupied orbitals.

It can now be seen that an iterative method is necessary to solve this cyclic-structured equation as the Fock operator of 2.53 depends upon the mean-field $v_{\text{HF}}(i)$ of the electrons which depends upon the set of occupied spin orbitals $\{\chi_N\}$, and thus the left hand side of 2.52 is dependent upon the right hand side. The self-consistent field method is employed to solve the Hartree-Fock equation of 2.52 to find the set of spin-orbitals $\{\chi_N\}$, which

3 Quantum chemistry

are then put back into the field in the Fock operator in order to solve the Hartree-Fock equation again.

Localised basis sets Localised basis sets, such as Slater type orbitals (STOs), are used to approximate atomic wave functions when quantum chemistry methods are used in this work for clusters of atoms modelled without periodic boundary conditions. These offer the most precise description of actual atomic orbitals and have the form $\phi_{\text{STO}} = e^{-\zeta r}$. With the many integrations required to perform calculations these basis sets are extremely expensive. To overcome this computational expense they are often approximated by Gaussian functions of the form $\phi_{\text{Gauss}} = e^{-\alpha r^2}$, which integrate to another Gaussian function greatly simplifying the integrations. A Slater orbital can be well approximated by a sum of Gaussian functions with little loss of accuracy.

In this work Gaussian orbitals made by Dunning will be used as the basis sets. These are described by the number of Gaussian functions used to approximate valence orbitals, valence double zeta (VDZ), valence triple zeta (VTZ) etc. The main advantage of Dunning-type basis sets over others are that they approach the complete basis set limit exponentially with increasing basis set size. Thus, the deviation from the complete basis set limit for a given finite basis set can be reasonably approximated.

3.2 Møller-Plesset perturbation methods

A brief introduction to the most commonly used post-HF method, Møller-Plesset second order perturbation theory, MP2, is necessary. The method uses Rayleigh-Schrödinger perturbation theory to perturb the Hartree-Fock Hamiltonian to include increasing orders of electron interaction.

The zeroth-order Hartree-Fock Hamiltonian, which shall be denoted $\hat{\mathbf{H}}_0$, is the sum of the N single-electron Fock operators and includes the kinetic energy term for individual electrons, a nuclear-electron interaction term and a mean field term,

$$\hat{\mathbf{H}}_0 = \sum_i^N f(i) = \sum_i^N \left[-\frac{1}{2} \nabla_i^2 - \sum_\nu^n \frac{Z_\nu}{r_{i\nu}} + v_{\text{HF}}(i) \right]. \quad (2.54)$$

The final term, $v_{\text{HF}}(i)$, includes no direct electron correlation as it limits the electron-electron interaction to an electron interacting with the average field created by the remaining electrons. The first correction to this approximation is to then perturb this Hamiltonian with a perturbation Hamiltonian, $\hat{\mathbf{H}}_{\text{pert.}}$, that includes the electrostatic

3 Quantum chemistry

interaction between pairs of electrons. This perturbation first removes this average-field term and replaces it with a direct electron-electron interaction, $1/r_{ij}$,

$$\hat{\mathbf{H}}_{\text{pert.}} = \sum_{i < j} \frac{1}{r_{ij}} - v_{\text{HF}}(i). \quad (2.55)$$

We then include a perturbation parameter, λ , to allow the transition from the unperturbed (Hartree-Fock) system to the fully perturbed form,

$$\hat{\mathbf{H}}_{\text{MP}} = \hat{\mathbf{H}}_0 + \lambda \hat{\mathbf{H}}_{\text{pert.}}, \quad (2.56)$$

where $\hat{\mathbf{H}}_{\text{MP}}$ is the full Hamiltonian of the system to be used in the Schrödinger equation.

Writing the Schrödinger equation using $\hat{\mathbf{H}}_{\text{MP}}$ and given that the perturbation $\hat{\mathbf{H}}_{\text{pert.}}$ is small, we can expand both the wave function and the eigenvalue energy as a power series in λ ,

$$\hat{\mathbf{H}}_{\text{MP}} \Psi = E \Psi, \quad (2.57)$$

$$(\hat{\mathbf{H}}_0 + \lambda \hat{\mathbf{H}}_{\text{pert.}}) \Psi = E \Psi, \quad (2.58)$$

$$(\hat{\mathbf{H}}_0 + \lambda \hat{\mathbf{H}}_{\text{pert.}}) \left(\lim_{n \rightarrow \infty} \sum_i^n \lambda^i \Psi^{(i)} \right) = \left(\lim_{n \rightarrow \infty} \sum_i^n \lambda^i E^{(i)} \right) \left(\lim_{n \rightarrow \infty} \sum_i^n \lambda^i \Psi^{(i)} \right), \quad (2.59)$$

where the summations are the power series expansions of Ψ and E ; $\Psi^{(i)}$ refers to the i -th term in the expansion of Ψ and $E^{(i)}$ the i -th term in the series expansion of E . A value for the k -th order energy is thus given by summing up terms in the expansion less than k , $E_{\text{MP}k} = E^{(0)} + E^{(1)} + E^{(2)} + \dots + E^{(k)}$; and similarly for the k -th order wave function.

We can now equate powers in λ and obtain ever increasing corrections to the system energy. The zeroth-order term gives the sum of occupied orbital energies, where ϵ_i is the energy of the i -th occupied orbital; the first-order term plus the zeroth-order term gives the Hartree-Fock energy, E_{HF} . The first correction to the Hartree-Fock energy does not come until the second-order term, equating powers of λ^2 ,

$$E_{\text{MP}0} = E^{(0)} = \sum_i \epsilon_i, \quad (2.60)$$

$$E_{\text{MP}1} = E^{(0)} + E^{(1)} = E_{\text{HF}}, \quad (2.61)$$

$$E_{\text{MP}2} = E^{(0)} + E^{(1)} + E^{(2)} \quad (2.62)$$

$$= E_{\text{HF}} + \sum_{a < b; r < s} \frac{\left| \langle \Psi_0^{(0)} \left| \frac{1}{r_{12}} \right| \Psi_{ab}^{rs} \rangle \right|^2}{\epsilon_a + \epsilon_b - \epsilon_r - \epsilon_s}, \quad (2.63)$$

3 Quantum chemistry

where Ψ_{ab}^{rs} is the wave function that has electrons promoted from occupied orbitals a and b to unoccupied virtual orbitals r and s .

This method starts to include the major features of electron correlation but is only the first correction to the HF energy. An infinite sum of MP terms would be required to get the exact MP energy for the system. As the order of summation increases beyond MP2 to MP3 and MP4 the method becomes increasingly expensive and other methods, such as coupled cluster techniques, give better results for less expense. In this work the coupled cluster methods will be used rather than the MP techniques.

3.3 Coupled cluster (CC) methods

One post-HF method that begins to incorporate the most important aspects of electron correlation is the *coupled cluster* techniques. Clusters of electrons are considered consisting of two or more electrons and the single-electron orbitals that formed the Slater determinant from the HF method, $\{\chi_N\}$, are modified following the consideration of electron interactions (as can be seen in the derivation in appendix C, also single-electron “clusters” are considered in order to allow the single-electron orbitals to relax).

Electron clusters are considered up to a certain size for a given coupled cluster technique, e.g. CCSD would include single- and double-electron clusters, CCSDT would explicitly include all those clusters of CCSD and triple-electron clusters. A cluster operator, $\hat{\mathbf{T}}$, is defined to produce all the cluster functions, $f_{ij\dots}$, that modify the single-electron orbitals. The method used in this work is the coupled cluster method including single and double excitations and perturbatively includes triple excitations, denoted as CCSD(T). Triple excitations are not modelled explicitly as the cluster operator $\hat{\mathbf{T}}$ is truncated at the level of double-electron excitations (i.e. $\hat{\mathbf{T}} = \hat{\mathbf{T}}_1 + \hat{\mathbf{T}}_2$), but instead are approximated using the perturbation terms formed from the cross-terms of the single-electron cluster operator, $\hat{\mathbf{T}}_1$, and the double-electron cluster operator, $\hat{\mathbf{T}}_2$.

The CCSD(T) method generally tends to overestimate the contribution from the triple-electron clusters and underestimate those from the quadruple-electron clusters, thus causing a favourable cancellation of errors. CC methods are preferred over truncated configuration interaction (CI) methods as the former is *size consistent* while the latter is not. Size consistency is the requirement that if a system is made of N non-interacting monomers then the energy of the supermolecule ($E_{\text{supermolecule}}$) is simply $E_{\text{supermolecule}} =$

$N \times E_{\text{monomer}}$. This is important when considering the interactions of §4, generating the full interaction curve between $\text{M}^+ \text{-H}_2$, where a size consistent method will give the energy of the system at a great separation, $r \rightarrow \infty$, as the sum of the energies of the metal ion and the free H_2 molecule. Only full-CI is size consistent, any truncated form is not, while *all* CC methods respect this requirement. When comparing systems of different numbers of electrons *size extensivity* is important. Size extensivity requires that the energy scales with the total number of electrons in the system. Again, CI methods are not size extensive while CC methods are. The resulting high quality results from CCSD(T) mean it is often referred to as the *gold standard* of quantum chemical calculations.

4 Classical force-fields

In this work classical force-fields will be used to replicate DFT results for hydrogenated K-GICs in chapter 5. Force-fields are extremely computationally cheap and can be used to quickly evaluate potential energies and thus forces for use in dynamic simulations. The functional form of the force-field needs to be decided upon and then the subsequent parameters fitted from data (either experimental or computational). In this work two forms of pair potential are used and are based on the Lennard-Jones type interaction.

4.1 Functional forms

The Lennard-Jones (LJ) type interaction qualitatively describes the interaction between two atoms extremely well. It is composed of a strongly repulsive part ($1/r^{12}$), which models the hard sphere repulsion at close approach between atoms, and a long-range attractive part ($-1/r^6$) that envelopes all the bonding processes. The LJ potential energy between two interacting elements (atoms, molecules or particles etc.) separated by a distance r is given by

$$V_{\text{LJ}}(r) = 4\epsilon \left[\left(\frac{\sigma}{r}\right)^{12} - \left(\frac{\sigma}{r}\right)^6 \right], \quad (2.64)$$

where ϵ is the depth of the potential well (the potential energy of the two part system at equilibrium); and σ is the separation at which the potential energy vanishes, leading to the separation at minimum potential energy being $r_{\min} = 2^{1/6}\sigma$.

In this work the LJ form shall be used to model the favourable interaction between hydrogen and intercalants using different exponents creating an $n - m$ potential of the

form,

$$V_{n-m}(r) = 4\epsilon \left[\left(\frac{\sigma}{r}\right)^n - \left(\frac{\sigma}{r}\right)^m \right], \quad (2.65)$$

and a purely repulsive form of potential shall be used for the hydrogen and carbon interaction based on the repulsive part of the LJ potential,

$$V_{\text{repuls.}}(r) = 4\epsilon \left(\frac{\sigma}{r}\right)^k. \quad (2.66)$$

In both V_{n-m} and $V_{\text{repuls.}}$ adjustment of the exponents (n and m ; and k , respectively) allows the strength of repulsion and attraction to be calmed relative to standard LJ potentials. These simple pair-potentials can have the ϵ and σ parameters fitted to DFT data for each choice of exponents to find the best fit.

Total energy calculations are then calculated by summing all contributions to the energy from every pair interaction within a cut-off radius r_{cut} . This creates a truncated potential that goes discontinuously to zero at r_{cut} . To avoid discontinuities in the energy landscape using these potentials the potential is *cut and shifted* such that at r_{cut} the potential goes to zero, thus

$$V_{n-m}^{\text{trunc.}}(r) = V_{n-m}(r) - V_{n-m}(r_{\text{cut}}), \quad (2.67)$$

$$V_{n-m}^{\text{trunc.}}(r) = 4\epsilon \left[\left\{ \left(\frac{\sigma}{r}\right)^n - \left(\frac{\sigma}{r_{\text{cut}}}\right)^n \right\} - \left\{ \left(\frac{\sigma}{r}\right)^m - \left(\frac{\sigma}{r_{\text{cut}}}\right)^m \right\} \right] \text{ for } 0 < r < r_{\text{cut}} \quad (2.68)$$

$$= 0 \text{ for } r > r_{\text{cut}}. \quad (2.69)$$

Finally, while this form ensures no discontinuities in the energy landscape, there do exist discontinuities in the force at r_{cut} as the gradient of $V_{n-m}^{\text{trunc.}}$ is not continuous. To avoid this we introduce the final form of the $n - m$ pair potential, the *force corrected truncated n - m* potential using the force correction method

$$V_{n-m}^{\text{F corr.}}(r) = V_{n-m}^{\text{trunc.}}(r) - \frac{dV(r_{\text{cut}})}{dr}(r - r_{\text{cut}}). \quad (2.70)$$

Using this form of $n - m$ potential it is possible to build a continuous energy landscape and ensure that calculations of the force remain continuous.

The details of the fitting of these potentials to DFT data and their success will be given in chapter 5.

5 Finite temperature effects

When considering the stability of these hydrogenated materials we are considering whether a reaction pathway is possible or not. Without modelling each step in the pathway to decomposition of a hydrogenated GIC to pure graphite and the metal hydride we can only consider the initial and final states of the system. Throughout this work the initial and final enthalpies shall be compared to see if a reaction is favourable or unfavourable with the enthalpy difference defined as

$$\Delta E = E(\text{final}) - E(\text{initial}), \quad (2.71)$$

giving a negative value for a favourable reaction and positive for an unfavourable reaction. Noting that the energies involved are always negative, i.e. defining ΔE as the difference in the magnitudes of the energies results in the more normal relationship of $\Delta E > 0$ being favourable and $\Delta E < 0$ giving an unfavourable reaction.

Comparison of the enthalpies yields only part of the story when deciding if the reaction is favourable or not. In order to accurately determine whether a process will spontaneously occur at a given temperature one needs to consider a quantity that takes into account both the enthalpy and the entropy, the *free energy*. The change in the Helmholtz free energy tells us whether a process is favourable or not and is defined as

$$\Delta H = \Delta E - T\Delta S, \quad (2.72)$$

where ΔE is the change in energy due to the process; T is the temperature of the system; and ΔS is the change in the entropy of the process.

Full inclusion of the entropy change during the processes considered here would be very elaborate and so is neglected throughout. As a rough estimate as to which term dominates 2.72 we can consider thermal energies at a temperature T to $\sim k_B T$, which as $T = 500$ K is ~ 0.05 eV. This is an order of magnitude smaller than the stability energies and absorption energies considered later in this project and so it is clear that the change in the free energy is dominated by the change in energy during the process.

This allows the static 0 K calculations for the energies given here to be a good guide to the processes at finite temperatures.

Chapter 3

Hydrogen in calcium graphite

1 Introduction

The graphite intercalate compound made with calcium has been considered for potential hydrogen storage after the recent work of Cobian and Íñiguez [1] suggested the material could provide excellent hydrogen binding sites and prove to be a high density hydrogen storage material. The predictions did not consider the stability of the material upon hydrogenation against decomposition into pure graphite and calcium hydride. Experiments performed in 2009 by Srinivas et al. [91] showed this to be a vitally important question for the viability of such a material.

In this chapter the energy difference between the three compounds of importance, the Ca-GIC, graphite and CaH_2 , will define whether the GIC is stable against decomposition. If this energy difference,

$$[E(\text{CaH}_2) + E(\text{Graphite})] - E(\text{hydrogenated Ca-GIC}),$$

is negative then the hydrogenated Ca-GIC is unstable against decomposition into the products on the left, calcium hydride and graphite. This approach will only work if the energies compared are the actual ground state energies of the system; this requires finding the global minimum of each component in the equation.

The plan of this chapter is to first review the predictions of hydrogen storage in Ca-GICs in §2. This will cover a review of theoretical calculations, on page 43, and experimental work, on page 49, on the GIC in question and related GICs. The next section, 3, will detail the compounds that were modelled and the methods used to do so, as well as covering the solutions to the problems outlined above. Crystal data and details

2 Predictions of Ca-GICs for H storage

of the energetics of the compounds will be found in this section. In the final section, 4, will be found the conclusions that can be draw from these calculations and a discussion of them. This section will include comparing the energies obtained, and comparison of the results with the necessary targets and a consideration of the thermodynamics required. It will also discuss the likely sources of errors and the accuracy of the obtained results.

To hydrogenate a GIC in experiment the compound is exposed to hydrogen gas for some period of time and then the excess gas removed and the material tested for successful absorption. In this setup the gas can condense upon, or adsorb, to the surface of the compound if the apparatus is cooled sufficiently. This is avoided at all costs so that only hydrogen uptake due to absorption into the pores of the material, in the case into the galleries of the GICs, is considered. The hydrogen must then diffuse from outside the material into the bulk and arrange within the galleries. In this chapter the diffusion from outside of the GIC is not considered, only the arrangement once within the bulk of the material is discussed.

The plan of this chapter is to first review the predictions of hydrogen storage in Ca-GICs in §2. This will cover a review of theoretical calculations, on page 43, and experimental work, on page 49, on the GIC in question and related GICs. The next section, 3, will detail the compounds that were modelled and the methods used to do so, as well as covering the solutions to the problems outlined above. Crystal data and details of the energetics of the compounds will be found in this section. In the final section, 4, will be found the conclusions that can be draw from these calculations and a discussion of them. This section will include comparing the energies obtained, and comparison of the results with the necessary targets and a consideration of the thermodynamics required. It will also discuss the likely sources of errors and the accuracy of the obtained results.

2 Predictions of Ca-GICs for hydrogen storage from the literature

Here will be given a review of the expected results of hydrogenating the Ca-GIC based on theoretical calculations and experiments.

2.1 Theoretical predictions

This section will cover the large survey on these materials by Cobian and Íñiguez [1] which covered hydrogen absorption by Ca-GICs, among other intercalate compounds. Next the work of Kim et al. [2] on Ca-hydrogen complexes being intercalated into host structures, such as graphite, will be discussed. Finally the report of expected large hydrogen capacities on Ca-decorated Buckminster-Fullerenes (C_{60} , “Bucky balls” or simply fullerenes) by Yoon et al. [3]. All of these papers will offer results that can be compared and contrasted with those found later in this chapter.

2.1.1 Cobian and Íñiguez [1]

In 2008 Cobian and Íñiguez released a paper that performed a systematic theoretical study of hydrogen absorption in metal intercalated graphite. The authors used DFT within the Vienna *ab initio* Simulation Package (VASP) to model their systems, which covered binary graphite intercalates of alkali metals, alkaline-earth metals and some transition metals. This thorough work made some predictions about the binding energies one could expect from the GICs upon hydrogenation and about the maximum hydrogen capacity of each material. A plane-wave basis within the projector augmented wave (PAW) scheme was employed, as is standard in VASP, with a plane-wave cut off of 400 eV, k -point sampling grids was considered converged. The authors chose to use the local density approximation (LDA) for the exchange-correlation functional (*xc*-functional) and, where it was felt necessary, ratified these results with the Perdew-Burke-Ernzerhof generalised gradient approximation (GGA-PBE). As such, the energies quoted here will be LDA energies. It should be noted that, in strongly bound systems especially, the LDA tends to over-bind resulting in reduced bond lengths and increasing bonding energies relative to GGA.

Concentrating on the results for the Ca-GIC, the authors studied CaC_4 and CaC_6 , with the less dense GIC being the one observed experimentally. They found the *c*-axis separation to be 4.51 Å with a charge transfer from the Ca metal to the graphite sheets. The previously empty metal *p*-orbitals became occupied upon intercalation suggesting their important role in binding of the metal to graphite. Upon hydrogenation this situation changes greatly.

In what follows, when referring to the order of intercalated hydrogen molecules, their ordinal number is per metal atom, i.e. the second H_2 would refer to the GIC system

2 Predictions of Ca-GICs for H storage

having two H₂'s (four H atoms) per metal atom. The first intercalated H₂ molecule dissociates in both stoichiometries and each hydrogen atom chemically binds to the Ca metal. The total binding energy of this first pair of H atoms is favourable giving -0.41 eV in CaC₆ and -0.43 eV for the CaC₄ system. This represents a binding energy per H atom of -0.21 eV and -0.22 eV respectively. The strong Ca-H interactions result in a concomitant weakening of the metals bond with the graphite layers: the Ca-C bond. This causes the interlayer, *c*-axis, separation to increase from 4.51 Å to 5.09 Å.

The introduction of second H₂ molecule is not energetically favourable with a binding energy of +0.24 eV for CaC₆ and +0.15 eV for CaC₄. The authors found the lowest energy solution in this case to have no dissociated H₂ but to have two extremely elongated H₂ molecules with an H-H bond length increasing from 0.74 Å for a free H₂ molecule to 0.86 Å. This pair of H₂ molecules exhibits a weaker Ca-H interaction and as such the material deflates to a *c*-axis separation of 4.66 Å, a reduction of 0.43 Å from the case of one dissociated H₂ and a slight increase of 0.15 Å on the unhydrogenated material. This shows the Ca-C bond is affected very little by the presence of the two H₂ molecules.

The introduction of the third H₂ molecule is favourable relative to the second with a binding energy of -0.34 eV in CaC₆ and -0.24 eV in CaC₄. The lowest energy solution in this case was found to have one dissociated H₂ bonding chemically to the Ca ion and two H₂ molecules interacting weakly with it. The strong interaction of the two H atoms, coupled with the interaction of the other two H₂ molecules, with the Ca ion strongly affects the Ca-graphite bond and the material's *c*-axis swells by 53 % to 6.91 Å compared with the unhydrogenated material.

The fourth H₂ has little interaction with the system, having a non-favourable interaction of +0.02 eV in CaC₆ and a favourable binding of just -0.02 eV with CaC₆. This remains molecular and adds to the previous arrangement giving one dissociated H₂ binding chemically to Ca and three H₂ molecules binding weakly to the metal ion.

As the hydrogen loading is increased, it was found that the graphite sheets back-donate to the Ca ion some of the charge originally given to them. The charge on the ion thus decreases as hydrogen is loaded. The first H₂ molecule thus sees the most electronegative environment and this would prompt its dissociation. The ion then drags charge from the H₂ σ -orbitals causing their elongation. There was no back donation from the metal to the H₂ σ^* -orbitals observed. The donation of charge from the H₂ σ -orbital to the empty metal orbitals with no back donation to the anti-bonding σ^* -orbital

2 Predictions of Ca-GICs for H storage

is consistent with the interaction of H_2 and Mg^{2+} as noted by Lochan and Head-Gordon [102].

These results show that the tightly bound hydrogen thus has a much smaller effective diameter than free H_2 allowing a tighter packing. These calculations show that CaC_6 has a mass fraction of hydrogen of 6.7 wt% (weight-percent) with CaC_4 exhibiting 8.4 wt%. These mass-fractions are well above the DoE targets and, with the computed binding energies, would provide hydrogen storage and delivery within the DoE specifications. This makes the Ca-GICs a particularly interesting material.

2.1.2 Kim et al. [2]

In 2009 a paper was released that cast doubt upon the previous predictions for a Ca based H absorbent. Kim et al. published a theoretical paper investigating the H absorption capabilities of light alkali and alkaline-earth materials. The paper examined the interaction of H_2 with the naked ions in various valence states to elucidate the nature of the H_2 binding. The paper reports two sets of calculations: one with DFT on the larger systems and one set using quantum chemistry (QC) methods for the isolated $H_2\text{-}M$ systems.

The DFT calculations were performed with both the LDA and GGA-PBE exchange-correlation functionals with some systems being modelled using the B3LYP functional. The results reported used the LDA *xc*-functional, while the results were tested against GGA-PBE. The GGA-PBE results systematically under-bound relative to the LDA results, but followed the same trend, and were omitted from the paper. It is known that in systems where weak bonding occurs the LDA will over-bind the systems, presenting more promising results than could actually be obtained.

They also replicated the results with two QC methods: Møller-Plesset second order perturbation theory (MP2) and coupled-cluster with single and double excitations (CCSD). These QC calculations used the split-valence basis set of Pople, specifically the triple-zeta basis with both diffuse functions and polarisation functions added to light and heavy atoms, 6-311++G(d,p).

Charge neutral atoms were observed to only bond H_2 weakly by physisorption as the metal's *s*-electrons formed a repulsive cloud allowing a closest approach of approximately the van der Waals radius. Thus to obtain bonding the metal must be oxidised. It was noted that while all alkali and alkaline-earth metals have no bound *d*-orbitals, that is

2 Predictions of Ca-GICs for H storage

they are unoccupied and above the Fermi energy, Ca has the lowest *d*-orbitals sitting just 0.06 eV above the vacuum energy. When the metal becomes oxidised, as it is upon intercalation, the *d*-orbitals become bound and local. This is necessary for H₂ to bind to the metal.

For the Ca²⁺-H₂ system, the introduction of the first H₂ was found to be favourable giving a binding energy of -0.387 eV with MP2, -0.380 eV with CCSD and -0.463 eV with DFT using the B3LYP *xc*-functional. These are markedly higher than those energies obtained for the singly-ionised K⁺ ion, which gave just -0.056 eV for both MP2 and DFT with B3LYP and -0.054 eV with CCSD. These values compare well with the experimentally observed value of -0.063 eV for the addition of the first H₂ and -0.059 eV for the absorption of a second H₂ reported by Bushnell et al. [103].

The H₂ absorption energy upon additional hydrogen loading varies little, decreasing slowly with just a 0.012 eV reduction in the binding energy per additional H₂ up to the sixth H₂ and a final absorption energy of 0.218 eV for the eighth H₂ added per Ca²⁺. This leads to the astonishing prediction that one doubly-ionised Ca ion can absorb up to eight H₂ molecules within the DoE absorption targets. This extremely close packing results in an H₂-H₂ distance of just 2.1 Å for H₂ bound to the same cluster and 2.7 Å for the H₂-H₂ closest separation for H₂ molecules bound to neighbouring Ca clusters, compared with the liquid average distance of 4 Å. It was noted that as H₂ molecules are added to the system the *d*-electrons start to accumulate on the Ca²⁺ metal. This pattern was also observed for Mg²⁺.

The authors then search for a medium within which this Ca²⁺-8.H₂ cluster can exist and posit a pillared Ca-GIC as a potential solution. The CaC₆ GIC is ruled out as the small 4.4 Å *c*-axis separation would be far too small to incorporate the cluster. The *c*-axis would need to be dilated to around 7.5 Å to allow the clusters to fit in the GIC. This would require an addition of 2.59 eV per Ca to do this, this is much more than the gains received by H₂ binding. To this end the Ca-GIC would have to be pillared to this large *c*-axis before the clusters could be incorporated, perhaps by organic molecules. Once this has been achieved the GIC could then be able to accommodate the Ca-H₂ clusters and exhibit the high H₂ content reported.

The proposed GIC would have the, unfathomable, stoichiometry of CaC_{10.5} and the Ca would have a hexagonal close-packed structure. This would give the strongest interaction between the Ca and the graphene sheets of *E* (Ca-C) = 0.90 eV per Ca ion

2 Predictions of Ca-GICs for H storage

and a *c*-axis separation of 7.8 Å when modelled with VASP using the LDA *xc*-functional. It is important to note than only Ca^{2+} can accommodate eight H_2 molecules around it and thus reach 8.8 wt% in the $\text{CaC}_{10.5}$ GIC (excluding the necessary pillars to expand the graphite).

The authors suggestion that “Such complexes could easily be incorporated into existing porous materials such as metal-organic frameworks, carbon nanotubes or graphite” are unfortunately unsubstantiated other for metal-organic frameworks (MOFs) [57]. The conclusion that the first hydrogen molecule would remain molecular in the strongly ionic region of the Ca^{2+} in a graphite host is in contradiction with the predictions of dissociation given above by Cobian and Íñiguez [1]. Although the authors suggest and interesting strategy different to that outlined by Cobian and Íñiguez; they suggest creating the $\text{Ca}-\text{H}_2$ complex first and then intercalating it. This would prove very tricky, although the recent work by Gupta et al. [73] on intercalating a C_{60} Buckminster-fullerene into graphite would imply that ever larger structures could possibly be intercalated. The role of the Ca *d*-orbitals in the H_2 binding could be interfereed with if they are involved with the bonding of the metal to the graphite planes upon intercalation. This could limit the possible maximum number of absorbed H_2 molecules when the cluster is in the graphite host.

2.1.3 Yoon et al. [3]

The other interesting proposition for Ca-decorated graphite structures for hydrogen storage is that of Ca-decorated C_{60} fullerenes. This material being obviously relevant for comparing results reported in this chapter. This was investigated by Yoon et al. using DFT within VASP to get a theoretical picture of this potential hydrogen storage medium. The authors investigate the binding of light alkaline-earth metals to C_{60} , namely beryllium, magnesium, calcium and strontium. They find that while Be and Mg bind only weakly to the fullerene structure, Ca and Sr bind strongly. This strong binding is attributed to a charge transfer mechanism involving the metal *d*-orbitals. This charge redistribution then acts a large hydrogen attractor. The alkaline-earth group are selected as they lie between the weakly H_2 -binding alkali metals [58] and the overly strong H_2 -binding transition metals that tend to cluster together on the fullerene surface and dissociate H_2 molecules [104].

The authors used DFT within VASP and the GGA *xc*-functional due to Perdew and

2 Predictions of Ca-GICs for H storage

Wang (GGA-PW91) and where appropriate compared these results with the LDA *xc*-functional. The PAW scheme was implemented, as is usual in VASP, with a plane-wave cut off of 400 eV. The fullerene-metal clusters were modelled in large boxes with a side length upwards of 22 Å.

It was found that while Be and Mg bind weakly, just 60 meV per metal atom through a van der Waals interaction above a C-C single bond, Ca and Sr bind strongly, 1.3 eV per metal atom, above a hexagon centre. This is around half the binding energy of a typical transition metal such as titanium. They note this structure should remain stable at room temperature. For the Be and Mg cases, it was found that there was little depletion of the metal *s*-electrons, presumably due to the high ionisation potential, and only a rigid shift down of the C₆₀ highest occupied (HOMO) and the lowest unoccupied molecular orbitals (LUMO). Also the partial density of states (pDOS) shows little variation over the free metal atom and free C₆₀, with both Be and Mg having *s*-orbitals just below the Fermi energy, E_f , and *p*-orbitals ~ 3 eV above it.

The Ca and Sr cases show a greater difference in the pDOS, with both the HOMO and LUMO of C₆₀ shifted below E_f and significantly broadened. Low lying metal *d*-orbitals are observed to become occupied and hybridisation occurs between C₆₀ π - and π^* -orbitals and metal *d*-orbitals. The metals become ionised, losing both electrons from the *s*-orbitals to the fullerene.

Hydrogen molecules were then brought to the MC₆₀ structure consisting of just one metal atom bound to the fullerene. For Ca and Sr up to five H₂ molecules were found to bind with binding energies staying approximately constant for each successive H₂ added. For Ca H₂ binding energies remained just above -0.2 eV with GGA-PW91 and around -0.4 eV with LDA, note that LDA severely overbinds. For Sr the H₂ binding energy is constant just under -0.2 eV.

The authors then focus on the Ca-decorated fullerene for hydrogen storage as it possesses similar binding characteristics as Sr but higher gravimetric densities. Coating the fullerene in a monolayer of Ca producing Ca₃₂C₆₀, the authors then introduce 92 H₂ molecules and allow the system to relax. This relaxed system gives an average H₂ binding energy of ~ -0.4 eV with LDA and ~ -0.2 eV per molecule with GGA-PW91.

The statement that "...it is conceivable that more hydrogen molecules are likely to be accommodated onto the system" would seem optimistic noting the difficulty in binding a second layer of H₂ molecules to a saturated substrate. The resultant material,

2 Predictions of Ca-GICs for H storage

$H_{92}\text{-Ca}_{32}\text{C}_{60}$, would have a gravimetric hydrogen density of 8.4 wt%. While our results here will compare well with the expected binding energy of an H_2 molecule, the overall conclusions will be drastically different.

It is clear from these calculations that Ca-decorated graphitic structures offer an exciting area for investigation, particularly those of Ca-GICs. These predictions not only give excellent binding energies but also target-meeting gravimetric densities. Missing from these reports though is consideration on the process of hydrogenation. Many of them consider just the final material, while some consider the possibility of metal clustering, few examine the process of introducing a H_2 molecule to the highly oxidised metal and the tendency for a strongly bound hydride to form.

2.2 Experimental findings

This section gives an overview of the experimental work that occurred after the predictions above and provided contrasting results from those expected. First the thesis by Lovell [4] is examined for the work performed on the hydrogenation of the Ca-GIC. The extensive thesis covers many other GICs with a strong focus on the K-GIC and this will be reviewed in the appropriate sections of the present work. These form the basis of the investigation later in this chapter. Finally, the definitive work by Srinivas et al. [5] shows categorically the result of attempting to absorb H_2 into Ca-GIC.

2.2.1 Lovell [4]

While the main focus of the thesis by Lovell was on the K-GIC for hydrogen storage, other GICs were investigated. It was considered that perhaps CaC_6 would undergo a phase transition, upon hydrogenation, similar to that seen in KC_8 . The phase transition seen in KC_8 under hydrogenation is characterised by a formation of a three layer intercalate structure: graphite-potassium-hydrogen-potassium-graphite (C-K-H-K-C) [87], also noted by Enoki et al. [88]. This compound exhibited a large 8.53 Å *c*-axis separation (between two graphite sheets), showing the new three layer structure. Within the galleries K remained positively charged and H gained a negative charge. When the CaC_6 compound was investigated using neutron diffraction the expected transition was not observed. Unexpected peaks did appear in the spectrum and were attributed to calcium carbide (CaC_2) formation and not due to any formation of a hydride within the sample.

It was noted, however, that the hydrogen uptake was not reversible as it had been for

3 Modelled compounds

the K-GICs. For the less dense K-GIC, KC_{24} , it was expected that up to six H_2 molecules would bind to every K site, but instead only two could due to *quantum delocalisation* [94]. This result may have made the prediction that the Ca-GIC, particularly in low concentrations, might show a lower-than-expected hydrogen uptake.

2.2.2 Srinivas et al. [5]

Finally, the recent work published by Srinivas et al. [5, 91] definitively showed that a Ca-GIC phase does not survive hydrogenation longer than 30 minutes at $500^\circ C$ and 10 bar. After just 15 minutes it was observed that the x-ray diffraction (XRD) peaks of CaC_6 has nearly vanished (and had done so after just 30 minutes) leaving behind only rapidly growing calcium hydride (CaH_2) peaks and pristine graphite peaks. After 15 minutes two unexplained very weak peaks appear around $\sim 11^\circ$ and $\sim 16^\circ$, which could potentially be a Ca-metal phase, that then disappears after 45 minutes of hydrogen exposure.

This process of deintercalation upon hydrogenation was also noted for LiC_6 by Enoki et al. [88] in 1990 and by Ishida et al. [90] in 2008. XRD experiments [90] show that lithium hydride (LiH) phases appear in LiC_6 and LiC_{12} upon hydrogenation at around $450^\circ C$ but could be desorbed at $500^\circ C$ leaving a lithium carbide, LiC , compound. No such reversibility was observed the Ca-GIC.

Despite the Li-GIC being an alkali-GIC and the Ca-GIC being an alkaline-earth-GIC they exhibit similar hydrogen exposure characteristics, with the Ca-GIC binding hydrogen more strongly. The authors note that the stability of the material can be considered an effect of the ratio of the metal to graphite charge transfer and the enthalpy of formation of the metal hydride. This is an idea that shall be greatly expanded in this chapter.

3 Modelled compounds

This section will contain the results from modelling the compounds of graphite, with its associated difficulties, calcium graphite, hydrogenated calcium graphite and calcium hydride. Comparisons with experiment, where possible, will be made as well as comparison to other theoretical work. The basis of this section is to accurately calculate the formation enthalpies of the compounds necessary for the reaction,



3 Modelled compounds

where CaC_n is the Ca-GIC in a given stoichiometry; C_n is graphite; and CaH_2 is calcium hydride.

To show this reaction is strongly “one way” we need to compare the values for the enthalpies of formation for all the reactants and products in this reaction.

To this end, all compounds were modelled using DFT within VASP. They used the PAW scheme with various plane-wave cutoffs that ensured total energies were converged, with specific values given where appropriate. Both the LDA and GGA-PW91 *xc*-functionals were used for comparison within DFT. A discussion of the effect of each is given in §4 of this chapter. Appropriate *k*-point meshes were used that, again, gave highly converged results.

Graphite is discussed first in §3.1 along with the difficulties in using DFT to model this compound. The Ca-GIC comes in §3.2 in various stoichiometries. Calcium Hydride follows in §3.4 with the difficulties of it’s complex structure. Finally the task of relaxing hydrogen inside the various Ca-GICs is reported in §3.3.

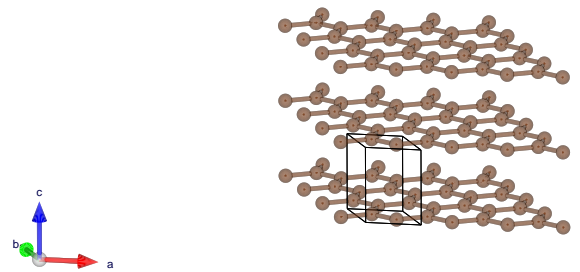
3.1 Graphite

Graphite is an allotrope of carbon made of off-set stacked sheets of graphene, hexagonally (sp^2 -) bonded carbon, with a C–C bond length of $a = 1.42 \text{ \AA}$. This forms a lamellar arrangement of graphene sheets with successive sheets shifted in-plane relative to the sheet below making either the *A-B-A-B*, hexagonal, stacking arrangement with $P6_3/mmc$ space group or the *A-B-C-A-B-C*, rhombohedral, arrangement with $R\bar{3}m$ space group, each with a graphene sheet separation of $\sim 3.36 \text{ \AA}$ [7]. Another possibility that is not experimentally observed is the *A-A-A* registration with space group $P6/mmm$, this was investigated due to its importance for intercalated graphite. Figure 3.1(b) shows the more thermodynamically stable[7] hexagonal phase of graphite, with the less stable rhombohedral phase shown in figure 3.2.

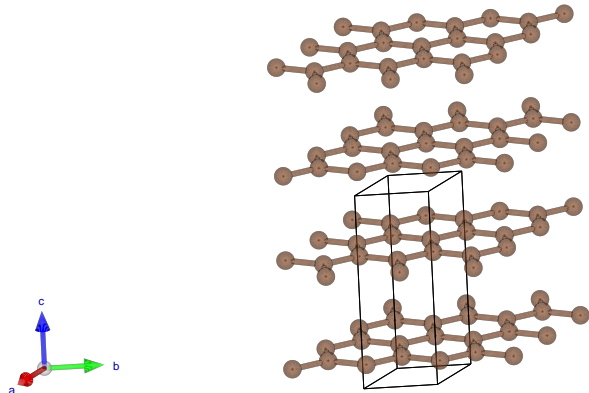
The hexagonal phases The $P6/mmm$ phase is not observed in nature and is a curiosity to see the importance of the shifted registrations in graphite while the $P6_3/mmc$ is the most stable form of graphite. The phases have hexagonal unit cells with 120° between the two in plane unit vectors, \vec{a} and \vec{b} , and 90° between these two and the third vector, \vec{c} . The length of the two in-plane vectors is a factor of the in-plane C-C bond length, a , $|\vec{a}| = |\vec{b}| = \sqrt{3}a$. The out-of-plane vector is defined as multiples of the repeat distance between successive layers, c . The unit cells are shown in figure 3.1 with (a)

3 Modelled compounds

showing the $P6/mmm$ phase and (b) showing the $P6_3/mmc$ phase.



(a) $P6/mmm$ phase.



(b) $P6_3/mmc$ phase.

Figure 3.1: The two hexagonal phases of graphite, (a) the fictional $P6/mmm$ phase and (b) the most stable $P6_3/mmc$ phase.

The atomic basis for the $P6/mmm$ phase has two carbon atoms at the Wyckoff 2(*c*) positions of $(1/3, 2/3, 0)$ and the reflected position of $(2/3, 1/3, 0)$. The $P6_3/mmc$ has an atomic basis of four atoms: two occupying the symmetric Wyckoff 2(*b*) positions at $(0, 0, 1/4)$ and the negative of this position: $(0, 0, 3/4)$; and two more occupying the equally symmetric Wyckoff 2(*c*) positions at $(1/3, 2/3, 1/4)$ and the negative of this position: $(2/3, 1/3, 3/4)$.

3 Modelled compounds

The rhombohedral phase The $R\bar{3}m$ phase of graphite has a rhombohedral set of lattice vectors, with none being in the plane of the graphite sheets. The vectors have a length, in terms of the C-C bond length a and the sheet separation c , of $|\vec{a}| = |\vec{b}| = |\vec{c}| = \sqrt{a^2 + c^2}$. Being a rhombohedral unit cell, all three vectors have equal angles between them of $\alpha = \beta = \gamma = \arccos\left(\frac{c^2 - \frac{1}{2}a^2}{a^2 + c^2}\right)$. Using the same parameters for a and c as given above we get that $|\vec{a}| = 3.65 \text{ \AA}$ and $\alpha = 39.40^\circ$. The unit cell and extended structure is shown in figure 3.2.

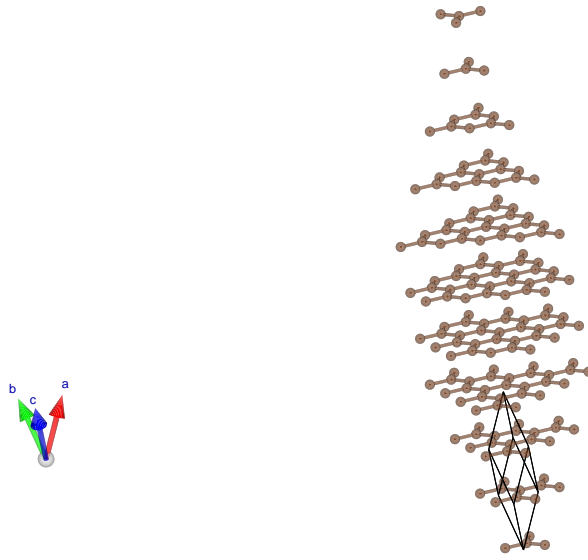


Figure 3.2: Rhombohedral graphite, space group $R\bar{3}m$, with $A-B-C-A-B-C$ stacking sequence. Again, the unit cell is shown in black.

The atomic basis for this phase is given by a single C atom at the Wyckoff 2(c) position $(1/3, 1/3, 1/3)$, and the negative position $(-1/3, -1/3, -1/3)$, with $x = 1/3$.

The difficulty with modelling graphite is with the weak interlayer bonds. While the sheets of graphite are strongly bound in-plane by hybridised sp^2 -bonds, sheets are bound to each other with weak van der Waals bonds. These van der Waals bonds are notoriously hard to model with DFT using standard xc -functionals such as the LDA and the GGAs. In principle, DFT includes the affect of van der Waals dispersive bonding but these two functionals fail to capture it accurately[105]. The fictitious structure was modelled for intrigue for determination of the importance of shifted registrations, while the other two phases were modelled for comparison with known results.

3 Modelled compounds

Simulation detail	Value
Calculation type	DFT
<i>xc</i> -functionals	LDA and GGA-PW91
Program	VASP
Basis	Plane wave within PAW scheme
Basis cut-off	800 eV
<i>k</i> -point grid	$8 \times 8 \times 8$ Monkhorst-Pack
Atomic basis	Fixed

Table 3.1: A summary of the DFT simulation details used for modelling graphite.

The relaxation of the structure to find the ground state was fairly simple. The *c*-axis parameter was held fixed at the experimental value of $c = 3.36\text{ \AA}$ and the C-C bond length was varied from $a = 1.35 - 1.50\text{ \AA}$ in steps of 0.005 \AA and a static DFT simulation in VASP was performed for each value. The binding energies per carbon atom (E/C) were then plotted and the minimum was taken as the equilibrium parameter. This equilibrium value for a was then taken and held fixed while static calculations were run for different *c*-axis values. For the LDA results 100 simulations were run with the sheet separation ranging from $c = 3.00 - 4.00\text{ \AA}$ in steps of 0.01 \AA . For the GGA-PW91 results the sheet separation was varied from $c = 3.0 - 10.0\text{ \AA}$ in steps of 0.5 \AA . It was expected that this functional would not produce smooth binding as was expected from the LDA functional. These results were then plotted (as can be seen in figure 3.3) and the minimum energy was taken as the equilibrium *c*-axis separation.

A plane wave basis using the projector augmented wave (PAW) method was used with a cutoff of 800 eV . A Monkhorst-Pack *k*-point grid of $8 \times 8 \times 8$ was implemented, both choices ensured all energies were satisfactorily converged. Total external pressures and forces were kept low at the final equilibrium structures. The atomic basis within each unit cell was kept fixed and periodic boundary conditions were implemented. A summary of the simulation parameters is given in table 3.1.

Both the LDA and GGA-PW91 functionals produce bound solutions for the variation of the C-C in-plane bond length, with LDA overbinding as is typical. The binding energy per C atom of the hexagonal *A-B-A* and the rhombohedral *A-B-C-A-B-C* structures differ from the artificial *A-A-A* structure by 16 meV , while only differing from each

3 Modelled compounds

other by 0.3 meV with both functionals. All three structures give the same in-plane C-C bond length for LDA of $a = 1.410 \text{ \AA}$ and $a = 1.425 \text{ \AA}$ for GGA-PW91. These compare well with the experimental C-C bond length of $a = 1.42 \text{ \AA}$ [7]. The smaller equilibrium a value given by LDA is indicative of this functional's tendency to overbind, evidenced by the stronger binding energy per C atom of 0.92 eV in all three phases compared with GGA-PW91.

For the equilibrium c -axis parameter, the story is very different. While the LDA results offer a typical binding curve reminiscent of a Lennard-Jones type interaction, the GGA-PW91 results offer a binding curve that monotonically decreases with increasing c -axis separation. When scrutinising the energy per C atom variation with c -axis separation we start to see the slight favourability of the hexagonal graphite phase over the rhombohedral phase.

The GGA is shown to produce little or no binding between the layers within graphite while LDA is shown to make a reasonable approximation of the interplane separation[106]. The nature of the van der Waals interaction means that electron correlation plays a very important role, it being a bonding due to the correlated motion of electrons, and something that is hard to model with either of these functionals. In calculations performed[107] on silicon LDA was shown to give reasonable parameters for the binding due to luck: the xc -functional tends to offer values of the exchange energy that are too large and values of the correlation energy that are too small, resulting in a cancellation of errors[107]. It is this cancellation of errors that leads to binding between the layers in graphite but for the wrong reasons.

The LDA results (figure 3.3(a)) for the binding energy per C atom variation with c -axis separation show that the $A\text{-}B\text{-}A$ and rhombohedral $A\text{-}B\text{-}C\text{-}A\text{-}B\text{-}C$ structures are more energetically favourable than the inverted $A\text{-}A\text{-}A$ phase by 11 meV. While the hexagonal phase gives a more favourable binding energy per C atom by just 0.34 meV. The $A\text{-}A\text{-}A$ phase giving an equilibrium c -axis separation of 3.61 \AA , while both the hexagonal and rhombohedral phases gives 3.31 \AA . The values for the c -axis parameter obtained with LDA are in good agreement with the experimental value of $c = 3.36 \text{ \AA}$ [7].

The GGA-PW91 results show a somewhat less intuitive pattern, as can be seen in figure 3.3(b). Only the hexagonal phase shows a minimum at $\sim 6 \text{ \AA}$, wildly different from the LDA results and in very poor agreement with experiment. Both the rhombohedral

3 Modelled compounds

and $A\text{-}A\text{-}A$ structures follow the same pattern of a sharp decrease in the binding energy per C atom from $3 - 4 \text{ \AA}$ and then a long plateau from $4 - \sim 8 \text{ \AA}$ before falling off indefinitely beyond 10 \AA with no sign of an energy minimum. This poor reproduction of the real situation in graphite was expected from previous work, as mentioned earlier. When the energy per C atom in graphite within the GGA-PW91 regime is needed later, the value at the experimental c -axis separation will be quoted. This will be noted where appropriate.

A summary of the results for graphite calculations and the comparison to experiment is given in table 3.2 where the E_{form}/C values refer to the formation energy of graphite per carbon atom from a free ground state spin-polarised carbon atom, i.e. they are the values corrected from VASP (see appendix E on page 192 for an explanation of this).

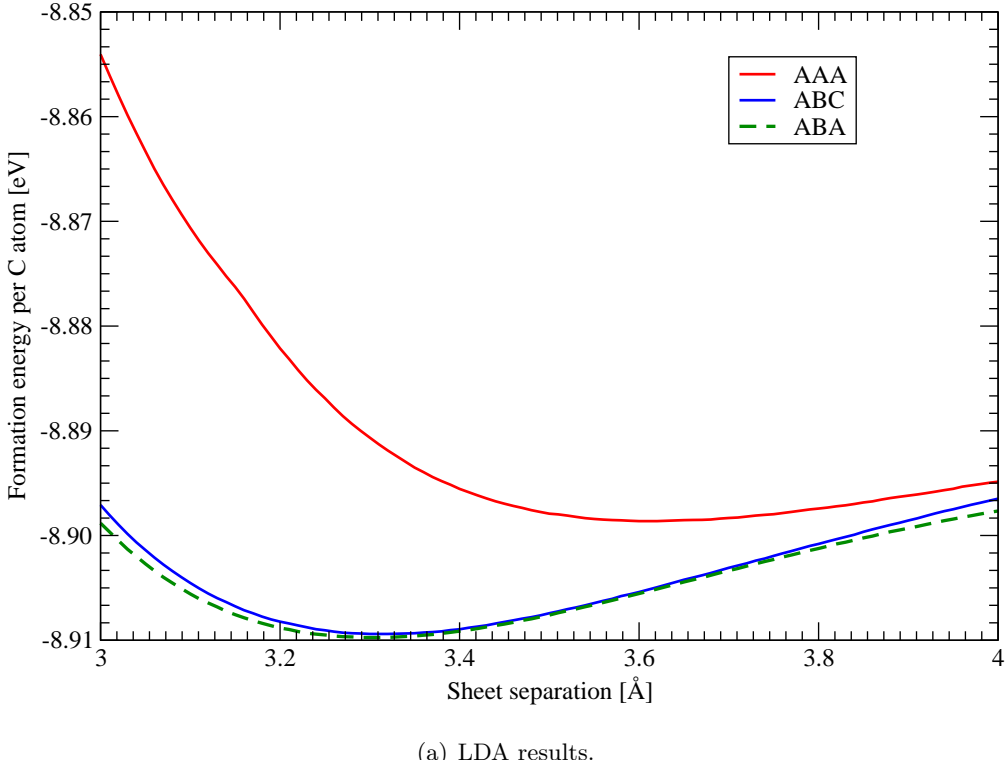
3.2 Calcium graphite (Ca-GICs)

Calcium intercalated graphite, the real focus of this chapter, is one of many graphite intercalation compounds and is made by inserting layers of Ca atoms between the sheets of graphite. By having the previously empty galleries of graphite filled, the chemistry in these interlayer spaces changes. Upon intercalation, the Ca atoms donate their valence $2s$ electrons to the graphite layers, charging the layers negatively and obtaining a positive charge themselves[108]. Some back-donation onto the Ca metal high orbital angular momentum electron states occurs reducing the positive charge of the metal[3, 109]. The graphite layers shift registration such that they lie coincident to each other in the c -axis, forming $A\text{-}A\text{-}A$ stacking[8]. The intercalated Ca atoms form a regular triangular lattice underneath graphite hexagon centres.

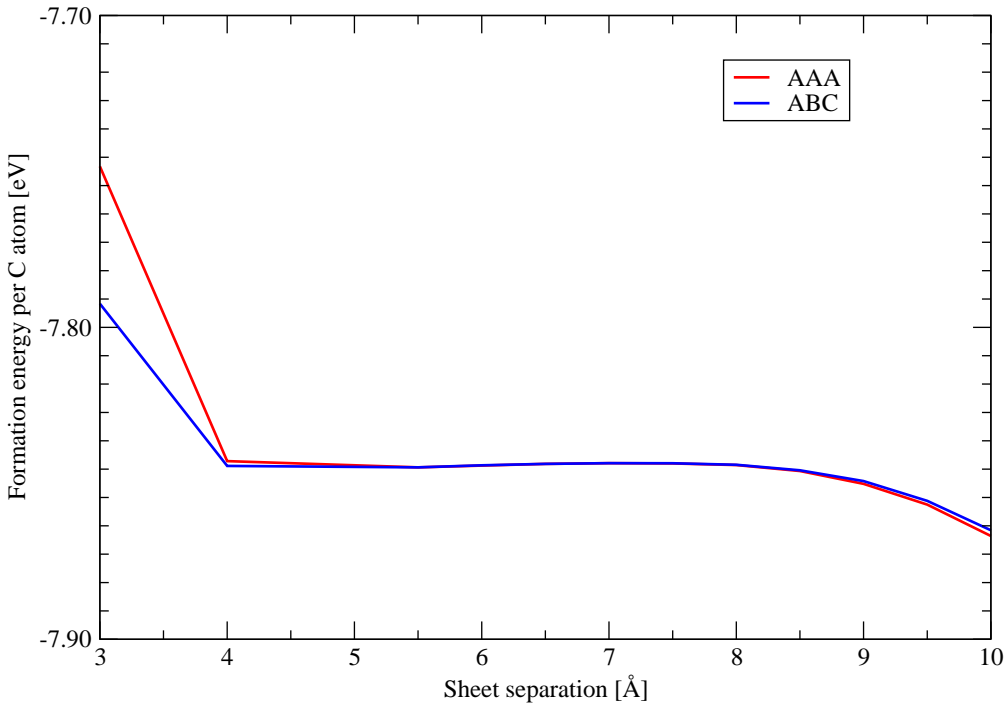
The in-plane triangular lattice of the intercalated metal can have three different forms of registration out-of-the-plane: $\alpha\text{-}\alpha\text{-}\alpha$ where each successive layer of metal atoms lies coincident with the layer below belonging to the $P6/mmm$ space group; $\alpha\text{-}\beta\text{-}\alpha\text{-}\beta$ where each successive layer is staggered relative to the layer below producing a $P6_3/mmc$ space group structure; and $\alpha\text{-}\beta\text{-}\gamma\text{-}\alpha\text{-}\beta\text{-}\gamma$ forming a rhombohedral structure having the space group $R\bar{3}m$. These three space groups are the same was were seen for graphite above in §3.1. Of course the full structure list would include the graphite $A\text{-}A\text{-}A$ registrations,

^aNote that since GGA-PW91 gives nonsensical values for the interplane binding of graphite, these values of the binding energy per C atom are taken from the structure at the experimental c -axis separation of $c = 3.36 \text{ \AA}$ and using the relaxed C-C bond length of $a = 1.425 \text{ \AA}$.

3 Modelled compounds



(a) LDA results.



(b) GGA-PW91 results.

Figure 3.3: The difference between the variation of energy per C atom with *c*-axis separation with the LDA (subfigure (a)) and GGA-PW91 (subfigure (b)) *xc*-functionals in three phases of graphite stacking: *A-A-A*, *A-B-A-B* and *A-B-C-A-B-C*. Note the very different ranges in the abscissæ, with the LDA results only between 3-4 Å and the GGA-PW91 results ranging from 3-10 Å. The E_{form}/C values given are corrected for reference to a spin-polarised C atom and given in table 3.2.

	<i>a</i> (Å)			<i>c</i> (Å)			E _{form} /C (eV)	
	LDA	GGA-PW91	Expt.	LDA	GGA-PW91	Expt.	LDA	GGA-PW91
<i>A-A-A</i>	1.410	1.425	N/A	3.61	N/A	N/A	-8.899	-7.815 ^a
<i>A-B-A</i>	1.410	1.425	N/A	3.31	N/A	N/A	-8.910	-7.831 ^a
c <i>A-B-C</i>	1.410	1.425	1.42	3.31	N/A	3.36	-8.909	-7.831 ^a

Table 3.2: A summary of the results from VASP DFT simulations on graphite with both the LDA and the GGA-PW91 *xc*-functionals compared with experiment[7] for graphite in three registrations: the fictional *A-A-A*, the hexagonal *A-B-A* and the rhombohedral *A-B-C-A-B-C*.

3 Modelled compounds

producing registrations like $A\text{-}\alpha\text{-}A\text{-}\beta\text{-}A\text{-}\gamma\text{-}A\text{-}\alpha\text{-}A\text{-}\beta\text{-}A\text{-}\gamma$, but for clarity these are not written here.

Experimentally only the stage-I rhombohedral, $R\bar{3}m$ $\alpha\text{-}\beta\text{-}\gamma\text{-}\alpha\text{-}\beta\text{-}\gamma$, stacking sequence is observed in CaC_6 [8]. All three stoichiometries were modelled in order to examine what differences exist with the simulations between the three stacking sequences. Other GICs are known to crystallise into the other two stacking sequences, LiC_6 forms $P6/mmm$ $\alpha\text{-}\alpha\text{-}\alpha$ stacking[110], while SrC_6 , BaC_6 , EuC_6 , SmC_6 and YbC_6 are thought to exhibit the $P6_3/mmc$ $\alpha\text{-}\beta\text{-}\alpha\text{-}\beta$ stacking[111–113].

Beyond the stacking sequence of the intercalated layers a GIC can also have varying metal densities relative to C. This is achieved by expanding the regular triangular lattice of the metal atoms until each lattice point is coincident with a graphite hexagon centre. If we make the ascertain that the only stoichiometries allowable are those that have a homogeneous arrangement of metal atoms coincident below graphite hexagon centres then the allowable values for n in the stage- m GIC formula MC_n are,

$$n = \begin{cases} 2m(k(k+2)+1) \\ 6m(k(k+2)+1) \\ 2m(k(k-1)+1) \end{cases}, \quad (3.2)$$

where k is any natural number $0, 1, 2, 3, \dots$ and m represents the staging index of the number, i.e. it counts the number of graphite layers between successive intercalant layers. These relations are derived diagrammatically in appendix D on page 186.

The graphite intercalation compound of Ca is only observed experimentally to be in the CaC_6 stoichiometry[8]. The other less dense stoichiometries of CaC_8 and CaC_{14} were investigated in §3.2.2 to see if the free space in the galleries of the GIC contributed significantly to the hydrogen sorption properties.

3.2.1 The CaC_6 GIC

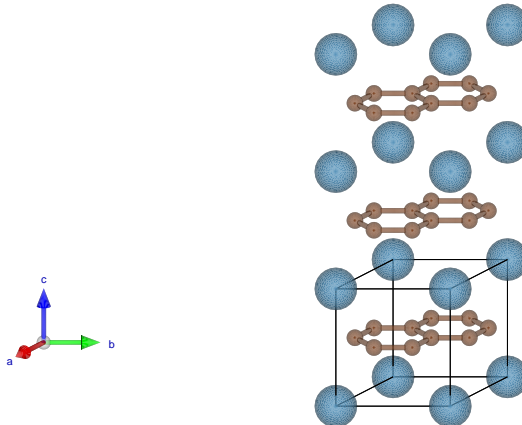
The hexagonal phases Two hexagonal phases exist for CaC_6 , as they did for graphite: the $P6/mmm$ phase with α -stacking, shown in figure 3.4(a), and the $P6_3/mmc$ phase with $\alpha\beta$ -stacking, shown in figure 3.4(b). Both have similar unit cell vectors as were seen for the equivalent graphite phases.

The α -stacked phase has an atomic basis of six C atoms occupying the Wyckoff 6 (k) positions of $(x, 0, 1/2)$, $(0, x, 1/2)$ and $(x, x, 1/2)$ and their respective negative positions $(-x, 0, 1/2)$, $(0, -x, 1/2)$ and $(-x, -x, 1/2)$, with $x = 1/3$. The single Ca occupies the 1 (a)

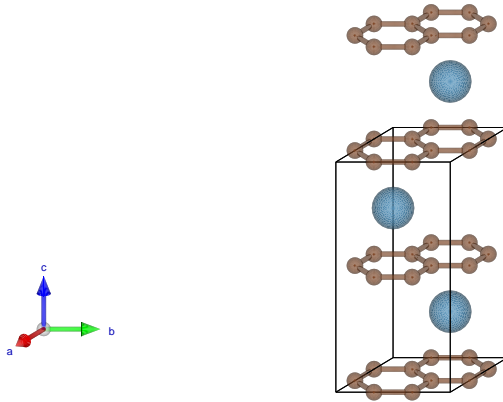
3 Modelled compounds

(0, 0, 0) site.

The $\alpha\beta$ -stacked phase has an atomic basis of twelve C atoms occupying the Wyckoff 12(i) positions which have the positions $(x, 0, 0)$, $(0, x, 0)$ and $(x, x, 0)$, their respective negative positions $(-x, 0, 0)$, $(0, -x, 0)$ and $(-x, -x, 0)$, and the same positions for the graphite layer above $(x, 0, 1/2)$, $(0, x, 1/2)$ and $(x, x, 1/2)$, their respective negative positions $(-x, 0, 1/2)$, $(0, -x, 1/2)$ and $(-x, -x, 1/2)$, with the same value as for x as for the α -stacking phase of $x = 1/3$. The two Ca atoms occupy the 2(c) sites of $(1/3, 2/3, 1/4)$ and its negative $(2/3, 1/3, 3/4)$.



(a) The α -stacked phase.



(b) The $\alpha\beta$ -stacked phase.

Figure 3.4: The hexagonal phases of CaC_6 .

The rhombohedral phase The $R\bar{3}m$ phase of CaC_6 with $\alpha\beta\gamma$ -stacking (shown in figure 3.5) is the only one observed experimentally and has a rhombohedral unit cell much like that of rhombohedral graphite on page 52 which comprises three lattice vectors

3 Modelled compounds

of equal length $|\vec{a}| = |\vec{b}| = |\vec{c}| = \sqrt{3a^2 + c^2}$ that form an equal angle between each one of $\alpha = \beta = \gamma = \arccos \frac{c^2 - \frac{3}{2}a^2}{3a^2 + c^2}$. Mind the α , β , γ designation is for the angle between the \vec{b} - and \vec{c} -vectors; the \vec{a} - and \vec{c} -vectors; and the \vec{a} - and \vec{b} -vectors respectively *not* the designation of successive intercalant layers when denoting the stacking sequence.

The phase has an atomic basis of six C atoms occupying the Wyckoff 6(g) positions of $(x, -x, 1/2)$, $(1/2, x, -x)$ and $(-x, 1/2, x)$ with their respective negative positions $(-x, x, 1/2)$, $(1/2, -x, x)$ and $(x, 1/2, -x)$, with $x = 1/6$. The Ca atom occupies the Wyckoff 1(a) position of $(0, 0, 0)$.

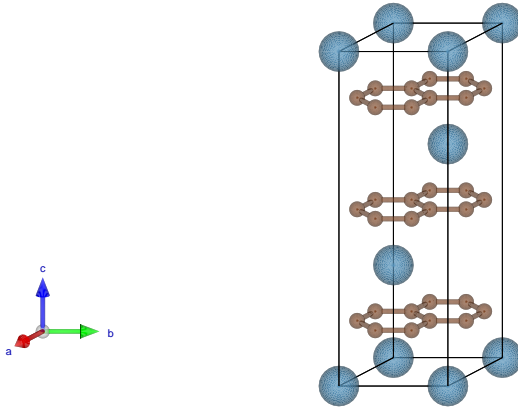


Figure 3.5: Rhombohedral $\alpha\beta\gamma$ -stacked $R\bar{3}m$ CaC_6 .

All three phases (α -, $\alpha\beta$ - and $\alpha\beta\gamma$ -stacked) of CaC_6 were modelled in VASP using DFT to ascertain the importance of the different registrations. The simulations were performed using both the LDA and GGA-PW91 xc -functionals with large plane-wave basis sets within the PAW scheme with cut-offs of 600 eV for $\alpha\beta$ - and $\alpha\beta\gamma$ -stacked systems and 800 eV for α -stacked CaC_6 . All systems had Monkhorst-Pack k -point grids that ensured convergence of the total energy. For α -stacked systems high-accuracy k -point grids of $7 \times 7 \times 7$ were used. For the $\alpha\beta$ - and $\alpha\beta\gamma$ -stacked cases lower grids of $5 \times 5 \times 5$ were deemed acceptable. A summary of the simulation parameters is given in table 3.3.

In order to arrive at the ground state of the models within the computation the unit cell was varied in two ways separately. Firstly, the in-plane vectors (and for this the hexagonal form of the $\alpha\beta\gamma$ -stacked CaC_6 was used) were varied to find the equilibrium

3 Modelled compounds

Simulation detail	Value
Calculation type	DFT
<i>xc</i> -functionals	LDA and GGA-PW91
Program	VASP
Basis	Plane wave within PAW scheme
Basis cut-off	600 eV for $\alpha\beta$ and $\alpha\beta\gamma$ 800 eV for α
<i>k</i> -point grid	$5 \times 5 \times 5$ for $\alpha\beta$ and $\alpha\beta\gamma$ $7 \times 7 \times 7$ for α
Atomic basis	Fixed

Table 3.3: A summary of the DFT simulation details used for modelling CaC₆ in the three stacking regimes of α -, $\alpha\beta$ - and $\alpha\beta\gamma$ -stacking. Where a stacking sequence is not specified this value was used across all simulations.

in-plane structure. The in-plane C-C bond length a was varied between 1.400 – 1.450 Å in steps of 0.005 Å for all three stacking sequences with the *c*-axis vector held fixed at an appropriate near-equilibrium value of 4.50 Å. The formation energies per CaC₆ unit for the α -stacked case are shown in figure 3.6, with the LDA results shown in (a) and the GGA-PW91 results shown in (b).

Once the optimum value of a was found the out-of-plane *c*-vector was varied between 4.30 – 4.40 Å in steps of 0.01 Å for α -stacking; between 4 – 5 Å in steps of 0.05 Å for $\alpha\beta$ -stacking; and between 3.5 – 5.5 Å in steps of 0.1 Å for $\alpha\beta\gamma$ -stacking. Once relaxed in the *c*-axis the in-plane pressure and energy was checked to ensure the relaxed value of a had not changed. It was found that a was rigidly found to change little during the *c*-axis relaxations. The symmetric atomic basis given by the Wyckoff positions above was used during the relaxation of the unit cell. Once the relaxed cell was formed the atomic basis was allowed to relax using the automatic algorithm in VASP and found not to change from the symmetric Wyckoff positions. The results of the *c*-axis relaxation for all three stacking sequences are shown in figure 3.7 with the LDA results in (a) and the GGA-PW91 results in (b).

The variation of formation energy per CaC₆ unit followed a similar pattern as for graphite above, with a strong parabolic type potential for both *xc*-functionals. The

3 Modelled compounds

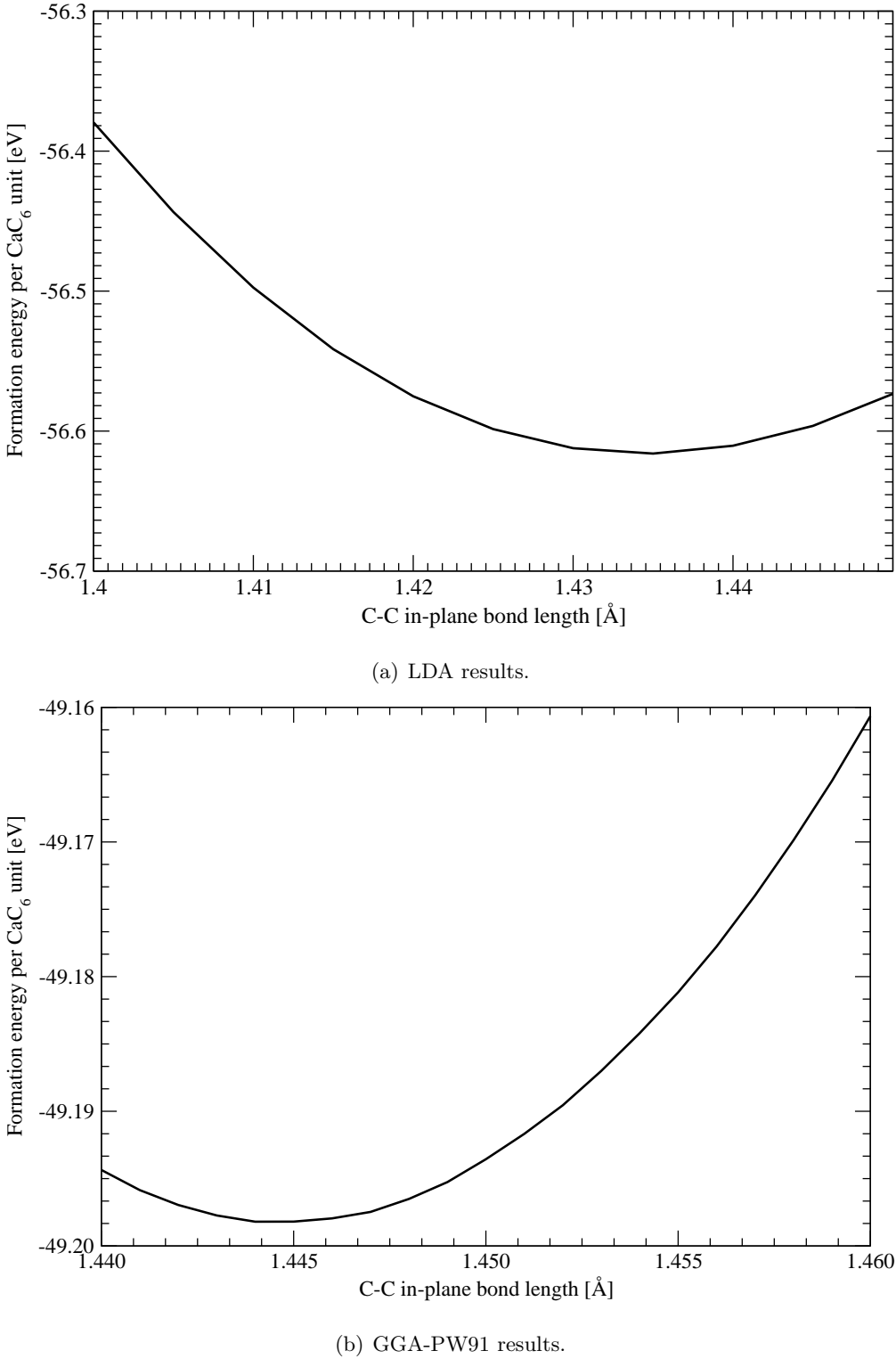


Figure 3.6: Total CaC_6 unit cell energy plotted against C-C in-plane bond length (a). Only the α stacked phase of CaC_6 is shown as other stackings gave equivalent results. The strength of the in-plane bond length, and thus its effect on the total energy of the system, is clear from the parabolic shape of the curves shown.

3 Modelled compounds

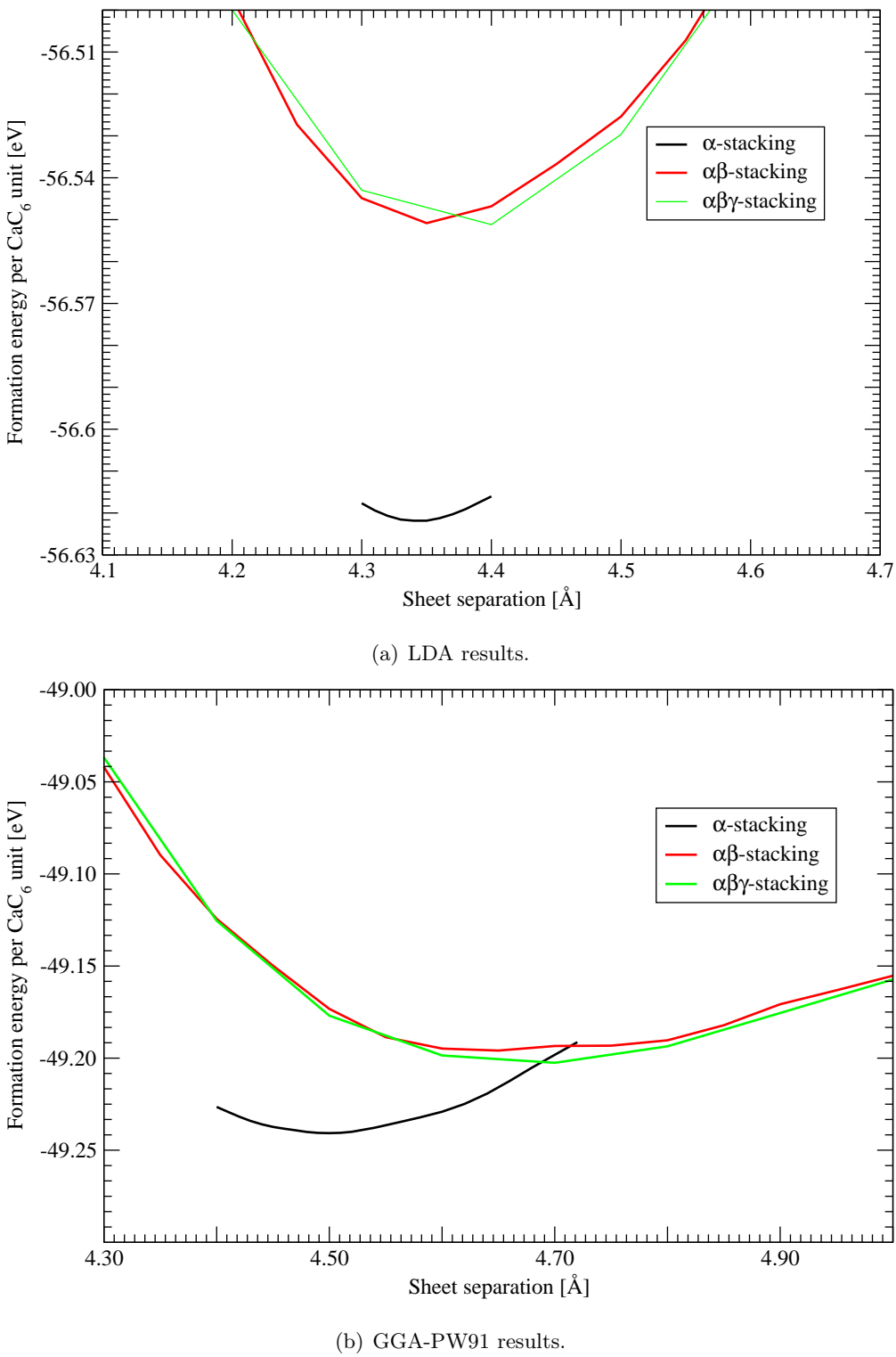


Figure 3.7: Total CaC_6 unit cell energy (in three different stackings: α , $\alpha\beta$ and $\alpha\beta\gamma$) as a function of sheet separation (c). The clear minima show the strength of the out-of-plane bonding in CaC_6 .

3 Modelled compounds

equilibrium value for the C-C in-plane bond can be seen to have increased from $a = 1.410 \text{ \AA}$ in graphite to $a = 1.435 \text{ \AA}$ in CaC_6 with the LDA, a small increase of just 1.8%; and from $a = 1.425 \text{ \AA}$ in graphite to $a = 1.444 \text{ \AA}$ in CaC_6 with GGA-PW91, another very small increase of just 1.3%. We can see that the value of a in CaC_6 is rigidly bound to these values as just a small change will require a relatively large amount of energy, a change of just 0.01 \AA in a requires $\sim 20 \text{ meV}$ in LDA and $\sim 10 \text{ meV}$ in GGA-PW91. While the values of energy required to make these changes of a sound small it is worth noting that they will only deliver a 0.7% change in the C-C bond length. All three phases exhibited similar values for the a parameter of between 1.434-1.435 \AA for LDA and between 1.444-1.450 \AA for GGA-PW91.

The agreement with experiment for the equilibrium a value of CaC_6 is worth remark. The experimental value is found to be 1.444 \AA by Emery et al. [8] for the only observed $\alpha\beta\gamma$ -phase. This is in perfect agreement with the higher accuracy calculations performed on the α -stacked phase here with no difference between the value for GGA-PW91 and LDA typically overbinding by just 0.6%. The other phases agree well with this value also.

The addition of Ca atoms intercalated between the layers of graphite has a profound effect on the interlayer binding and thus the equilibrium c -axis separation. The sheets of graphite are no longer bound to each other by weak dispersive van der Waals bonds that are hard for the xc -functionals to model, especially for GGA-PW91, but are now bound by strong covalent bonds to the intercalated atoms. As noted the atoms become charged between the sheets and donate their charge to the graphite layers (potentially one reason for the slight increase in the in-plane a parameter of CaC_6 compared with graphite). This strong binding is well modelled within DFT under both xc functionals and we see that the comparison with experiment is very good.

The variation of the formation energy per CaC_6 unit ($E_{\text{form}}/\text{CaC}_6$) with c -axis separation between successive sheets shows a typical Lennard-Jones type interaction between the sheets: a strong repulsion at close separation and a long-tail attraction beyond the equilibrium value of c . The intercalation of Ca atoms into graphite results in an expansion along the c -axis of 31% with LDA in good agreement with the experimental expansion of an increase of 35%[7, 8]. A value for the increase of the c -axis with GGA-PW91 is not feasible. The minima are almost parabolic by nature but noticeably softer than the variation of the in-plane a -parameter. A change of $\sim 0.1 \text{ \AA}$ in the c -axis in any

3 Modelled compounds

phase can be achieved with the addition of just ~ 20 meV in LDA and ~ 10 meV with GGA-PW91. Again, the difference in these two figures typifies the tendency of LDA to overbind systems. With the shape of the c -axis binding curve it is always slightly easier to expand the c -axis than to compress it, approximately 5 meV easier with LDA and 3 meV easier with GGA-PW91. This implies that under uniform pressure the CaC₆ would tend to compress along the c -axis rather than the in-plane a -axis.

The agreement with experiment for the c -axis separations is very good also, with GGA-PW91 performing better than LDA. The experimental value of 4.524 Å is in excellent agreement with the more accurate α -stacked GGA-PW91 result of 4.50 Å and good agreement with the other two phases with LDA again overbinding by 0.12 Å. The results of the relaxation and the comparison with experiment is shown in table 3.4.

3.2.2 The CaC₈ and CaC₁₄ GICs

Looking at the results from the previous section it is clear that the stacking sequence need not play an important part in the following work. The structural parameters are so similar that it was considered unnecessary to triple the number of models needed to gain an insight into the physical nature of these systems under hydrogenation and as stand-alone systems. For this reason the following lower density CaC₈ and CaC₁₄ GICs were only modelled in the hexagonal $P6/mmm$ α -stacked phase.

The CaC₈ structure has an atomic basis of eight C atoms with two occupying the Wyckoff 2 (d) positions of $(1/3, 2/3, 1/2)$ and the mirrored position of $(2/3, 1/3, 1/2)$. The other six C atoms occupy the 6 (m) of $(x, 2x, 1/2)$, $(x, -x, 1/2)$ and $(2x, x, 1/2)$ with their respective mirrored positions $(-x, -2x, 1/2)$, $(-x, x, 1/2)$ and $(-2x, -x, 1/2)$, with $x = 1/6$. The Ca atom occupies the Wyckoff 1 (a) position, $(0, 0, 0)$. The structure is shown in figure 3.8 with the in-plane unit cell (the unit cell as viewed down the c -axis) shown in (a).

The CaC₁₄ GIC belongs to the same unit cell type but has a very different basis of atoms. The atomic basis requires symmetry to be removed, placing the unit cell in the triclinic $P1$ group with no symmetric positions whatsoever, but can be understood within this $P6/mmm$ system. The Ca atom occupies the Wyckoff 1 (a) position as usual. Of the fourteen C atoms, two occupy the 2 (d) positions of $(2/3, 1/3, 1/2)$ and the mirrored position of $(1/3, 2/3, 1/2)$. The other twelve C atoms occupy half the 12 (q) positions, namely $(px, py, 1/2)$, $(-py, px - py, 1/2)$, $(-px + py, -px, 1/2)$ and their mirrored

	<i>a</i> (Å)			<i>c</i> (Å)			E _{form} /CaC ₆ (eV)	
	LDA	GGA-PW91	Expt.	LDA	GGA-PW91	Expt.	LDA	GGA-PW91
α	1.435	1.444	N/A	4.34	4.50	N/A	-56.622	-49.241
$\alpha\beta$	1.435	1.450	N/A	4.35	4.65	N/A	-56.551	-49.196
$\alpha\beta\gamma$	1.434	1.450	1.444	4.40	4.70	4.524	-56.551	-49.203

Table 3.4: A summary of the results of relaxing the three phases (α -, $\alpha\beta$ - and $\alpha\beta\gamma$ -stacked) of CaC₆ with both the LDA and GGA-PW91 *xc*-functionals compared with experiment[8].

3 Modelled compounds

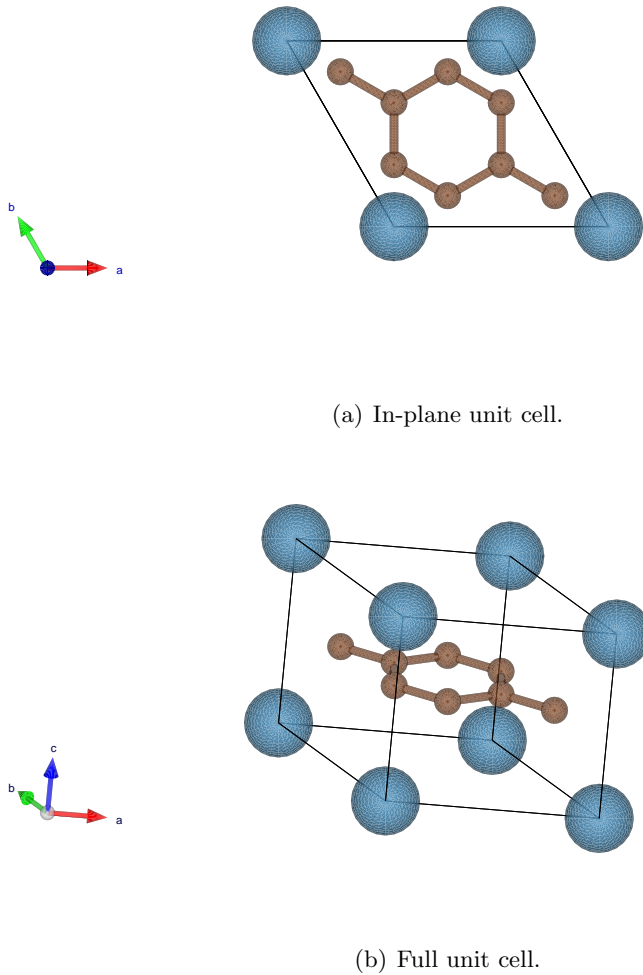
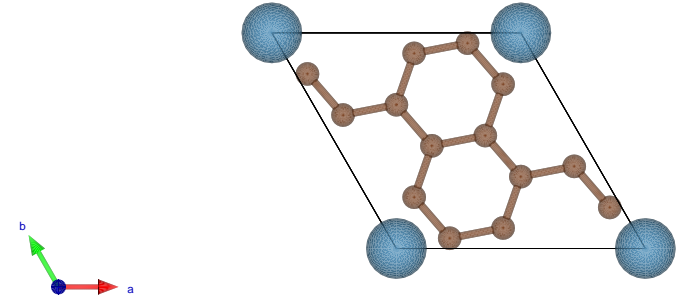


Figure 3.8: CaC₈ with (b) the full unit cell shown and (a) projected down the *c*-axis to show the in-plane structure.

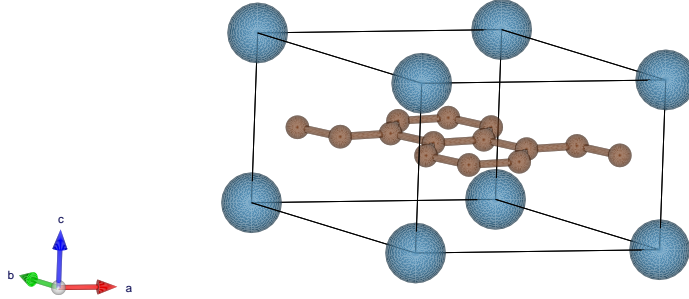
positions of $(-px, -py, 1/2)$, $(py, -px + py, 1/2)$, $(px - py, px, 1/2)$ with $p = 1$ and 2 and $x = 5/21$ and $y = 1/21$. The other six Wyckoff 12(*q*) positions are unoccupied. This unit cell is shown in figure 3.9 with the projection along the *c*-axis, (a), elucidating the unsymmetrical in-plane nature of the atomic basis.

Relaxations of these lower density GICs were performed in the same way as for CaC₆ with the unit cell varied in-plane first to find the equilibrium *a* value, then out-of-the-plane to find the equilibrium *c*-axis separation. The variation of the corrected formation energy per CaC_{*n*} unit from free atoms in their ground state with the in-plane C-C bond length, *a*, is shown in figure 3.10 for CaC₈ with the LDA bonding curve shown in (a)

3 Modelled compounds



(a) In-plane unit cell.



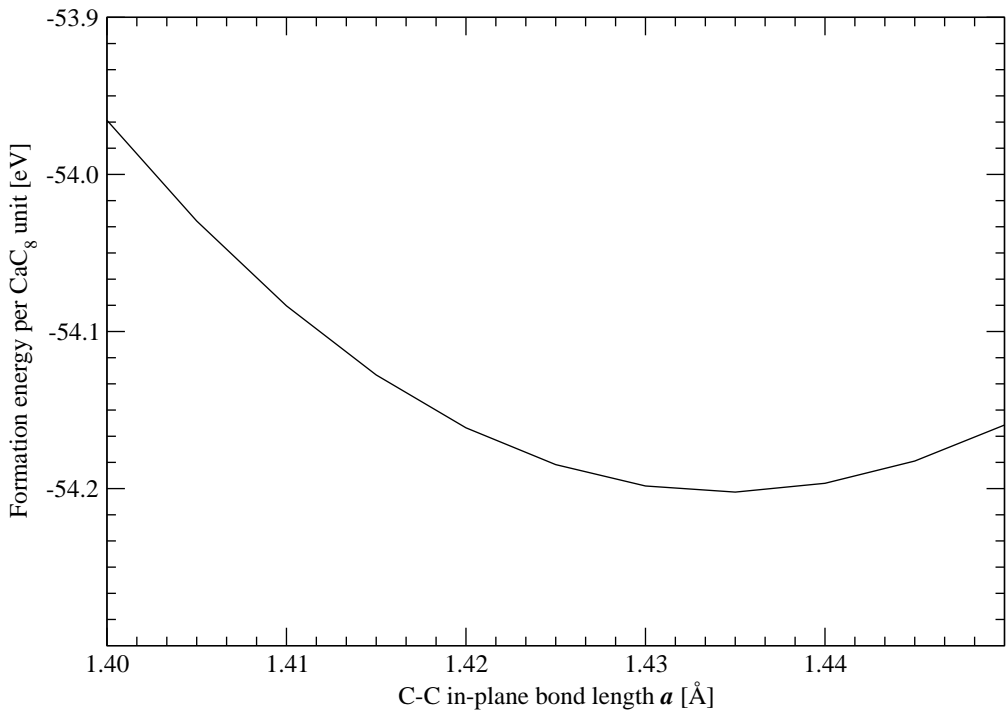
(b) Full unit cell.

Figure 3.9: CaC_{14} with (b) the full unit cell shown and (a) the unit cell projected down the c -axis to show the unsymmetrical in-plane structure.

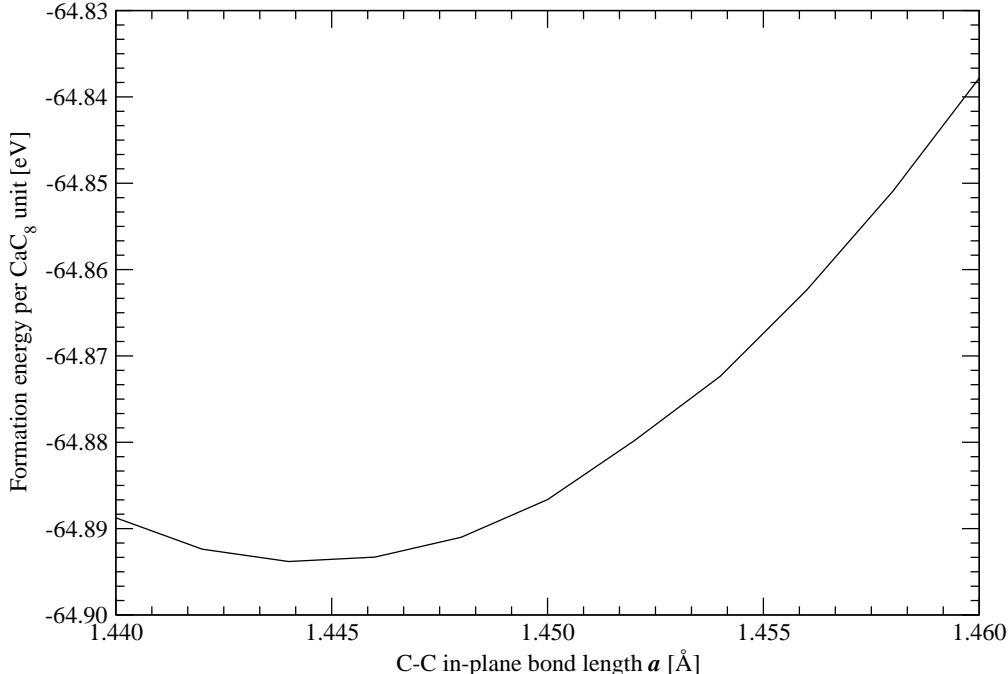
and the GGA-PW91 data shown in (b). Figure 3.11 the case of CaC_{14} with again (a) showing LDA and (b) showing the GGA-PW91 results.

We can see from figures 3.10 and 3.11 that the in-plane C-C bond length is tightly bound to the equilibrium value of 1.435 \AA in LDA and 1.444 \AA for GGA-PW91 for the CaC_8 stoichiometry and 1.424 \AA for LDA and 1.436 \AA for GGA-PW91 for CaC_{14} . There appears very little change from the CaC_6 (in the α -stacked $P6/mmm$ phase for comparison) value for a compared with CaC_8 for both LDA and GGA-PW91, whereas the value is 0.011 \AA and 0.008 \AA smaller in CaC_{14} in LDA and GGA-PW91 respectively.

3 Modelled compounds



(a) CaC_8 LDA results.



(b) CaC_8 GGA-PW91 results.

Figure 3.10: The effect on the formation energy (from free spin-polarised ground state atoms) per CaC_8 unit by in-plane C-C bond length a .

3 Modelled compounds

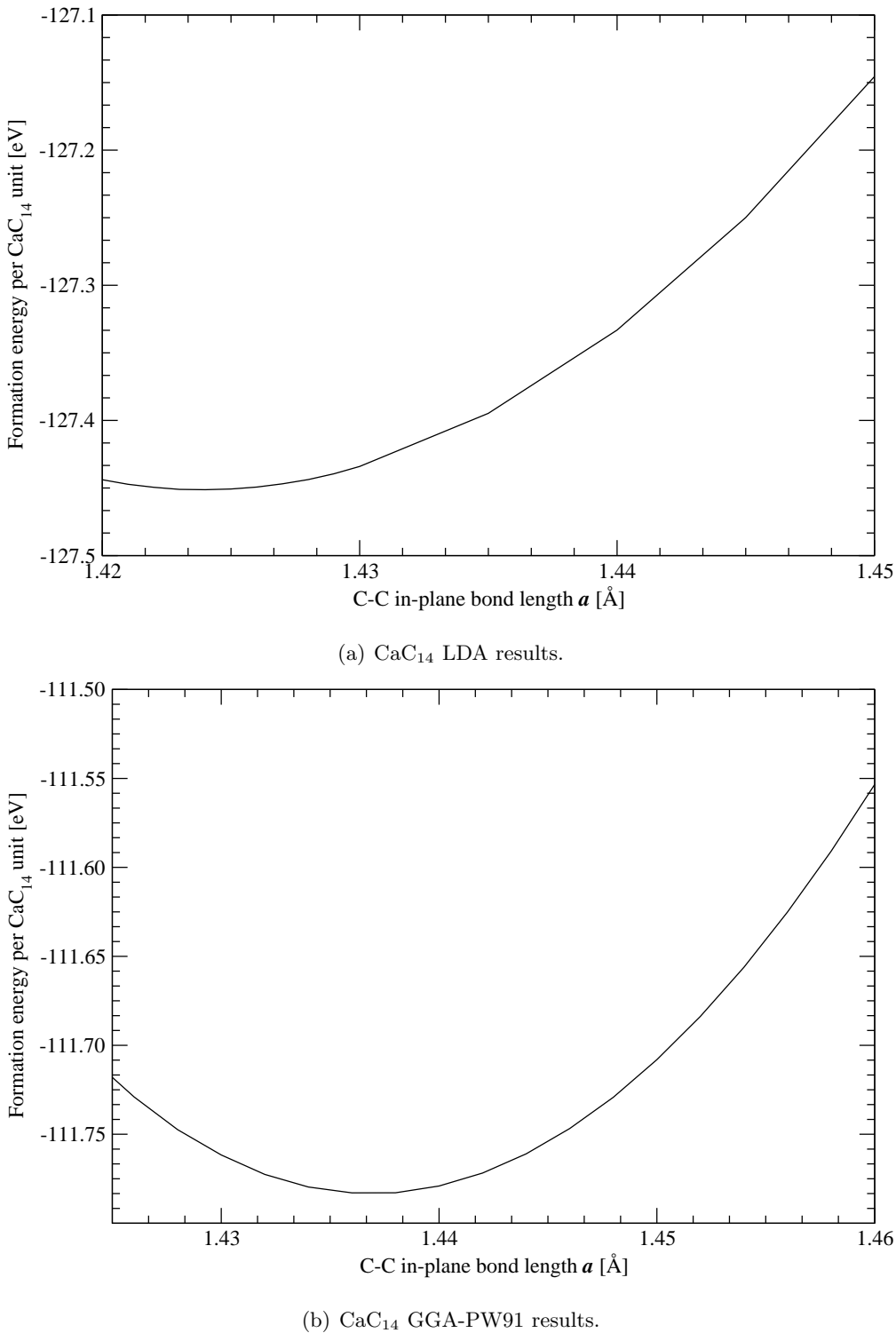


Figure 3.11: The effect on the formation energy (from free spin-polarised ground state atoms) per CaC_{14} unit by in-plane C-C bond length a .

3 Modelled compounds

This corroborates the idea that as you decrease metal density in the GIC so you decrease the charge transfer from the metal to the graphite sheets and thus the C-C bonds increase in strength (approaching the graphite limit), shown in figure 3.12. These two compounds exhibit similar binding strength in the plane and higher than CaC_6 with the GGA-PW91 functional (ignoring the tendency of LDA to over-bind covalent systems such as those in the plane of graphite). To stretch or contract the C-C bond by just 0.01 Å (representing a $\sim 0.7\%$ change in a) in CaC_6 required $\sim 3.3 \text{ meV/C}$ with LDA and $\sim 2.3 \text{ meV/C}$ with GGA-PW91. The less dense CaC_8 material required less energy per carbon atom with LDA, $\sim 2.5 \text{ meV/C}$, and more with GGA-PW91 $\sim 2.7 \text{ meV/C}$ to distort the a value by the same amount. CaC_{14} required considerably more than either with LDA, needing $\sim 4 \text{ meV/C}$ and roughly the same as the other compounds with GGA-PW91, $\sim 2.6 \text{ meV/C}$ to distort the a -parameter by 0.01 Å. It is worth noting that to achieve the same change in a in pure graphite, $\sim 2.5 \text{ meV/C}$ is required with LDA and $\sim 4.6 \text{ meV/C}$ with GGA-PW91. While it would be thought that graphite would be the hardest to stretch or contract in-plane, it appears this is only true for the GGA-PW91 xc -functional, it also exhibit the smallest a value of any GICs implying a strong in-plane bond as noted above.

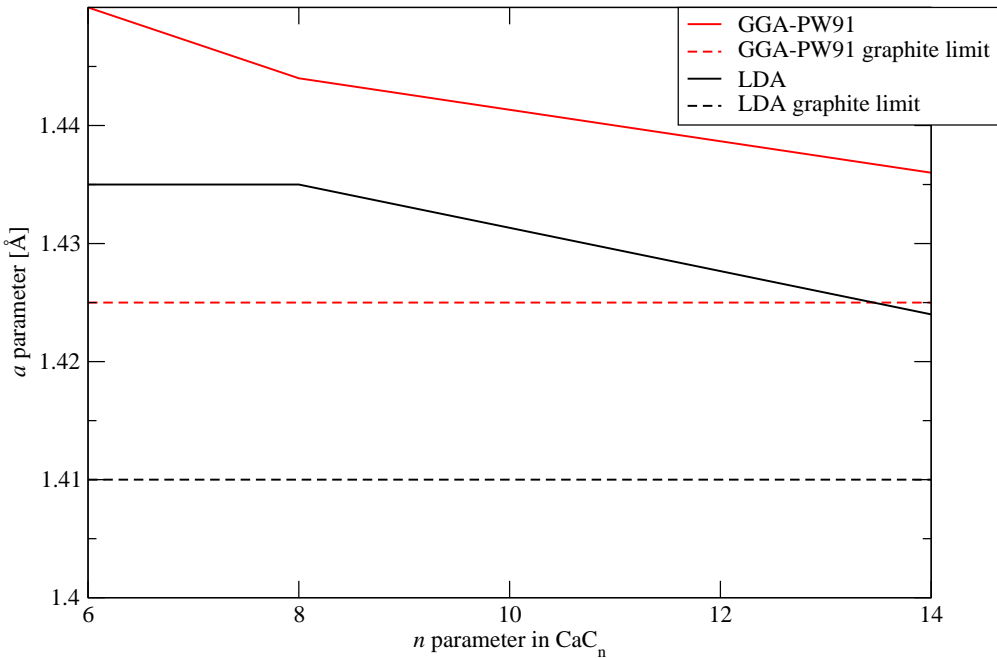


Figure 3.12: The reduction in the in-plane C-C bond length, a , with decreasing metal content in the CaC_n GICs, approaching the graphite limits (dotted).

3 Modelled compounds

The c -axis relaxations take on a similar appearance as to those in the case of CaC₆. Figure 3.13 and 3.14 show the variation of the formation energy per CaC _{n} unit for CaC₈ and CaC₁₄ respectively, with both LDA and GGA-PW91 shown. The graphs show that the c -axis equilibrium values differ little from CaC₆ with CaC₈ giving 4.31 Å and 4.45 Å and CaC₁₄ giving 4.28 Å and 4.45 Å with LDA and GGA-PW91 respectively, approximately just 1 % smaller than $P6/mmm$ α -stacked CaC₆ in all cases. The strength of the c -axis bonding is comparable to CaC₆ also, requiring ~ 20 meV to expand or contract CaC₈ or CaC₁₄ by 0.01 Å in the c -axis in both LDA and GGA-PW91.

A summary of the structural parameters of both CaC₈ and CaC₁₄ and the formation energy from free atoms in their spin-polarised ground state (a close comparison to the formation energy from the atomic gas), E_{form}/CaC _{n} , is shown in table 3.5.

	a (Å)		c (Å)		E _{form} /CaC _{n} (eV)	
	LDA	GGA-PW91	LDA	GGA-PW91	LDA	GGA-PW91
CaC ₈	1.435	1.444	4.31	4.45	-74.389	-64.898
CaC ₁₄	1.424	1.436	4.28	4.45	-127.482	-111.789

Table 3.5: A summary of the results of relaxing the two less dense Ca-GICs of CaC₈ and CaC₁₄ with both the LDA and GGA-PW91 xc -functionals. Note that only the CaC₆ stoichiometry is seen experimentally so comparison with experiment is not feasible but that structural values differ little between CaC₆, CaC₈ and CaC₁₄ and CaC₆ can be seen to be in good agreement with experiment (table 3.4).

3.3 Hydrogenated calcium graphite

Once in the Ca-GIC a molecule of H₂ can arrange itself in many ways: parallel to the c -axis, figure 3.15(a) (and thus perpendicular to the graphite sheets), perpendicular to the c -axis, figure 3.15(b) (and thus parallel to the graphite sheets), any angle in between these two cases, or dissociated into two H atoms, figure 3.15(c). After this the position relative to a charged metal intercalant acting as a binding site needs to be found.

In order to fairly represent H₂ absorption into the Ca-GICs the c -axis was relaxed around an H₂ in all three scenarios show in 3.15. The a parameter (the in-plane C-C bond and thus the in-plane lattice parameter) was unchanged from the empty GIC case in all cases. The H₂ molecules (of two H atoms) were placed at a local minimum within the each GIC and the c -axis varied until the ground state structure in this arrangement

3 Modelled compounds

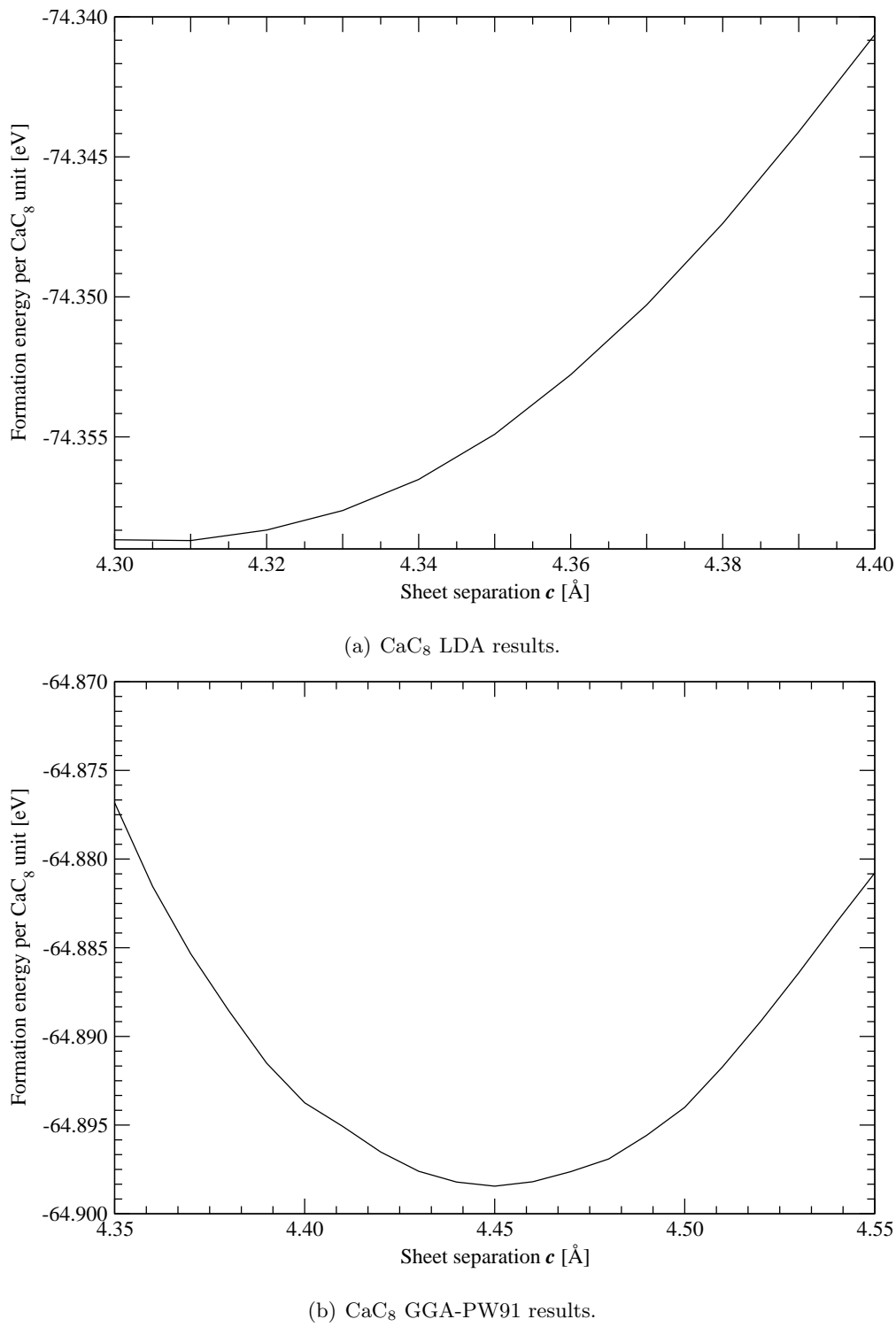


Figure 3.13: The effect on the formation energy (from free spin-polarised ground state atoms) per CaC_8 unit by the c -axis separation between consecutive sheets of graphite.

3 Modelled compounds

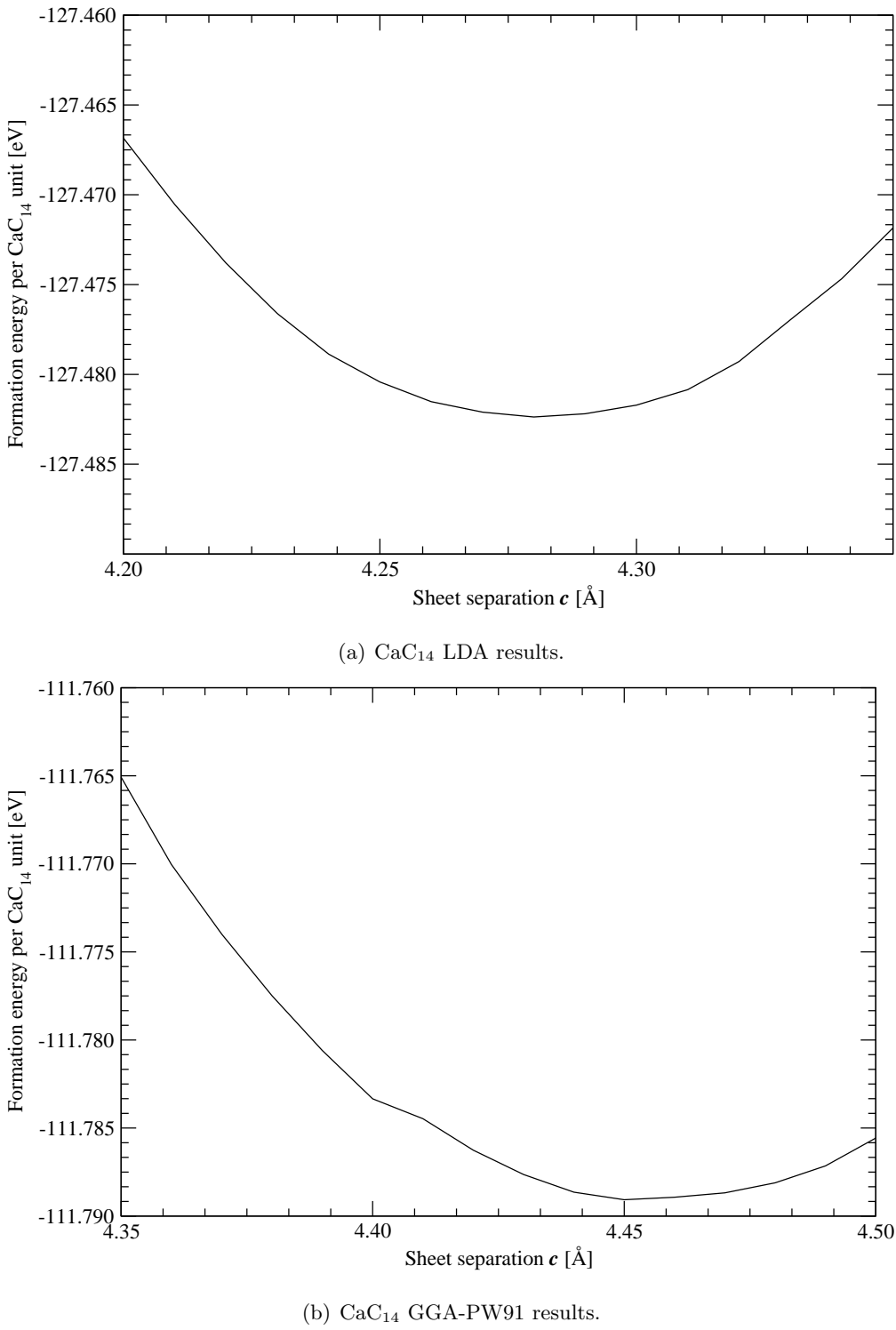
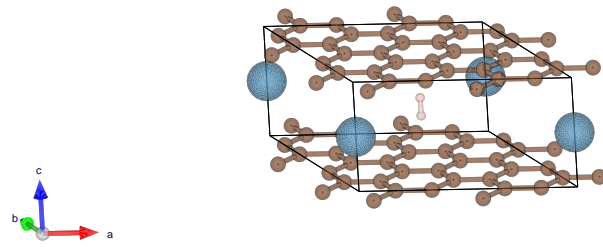
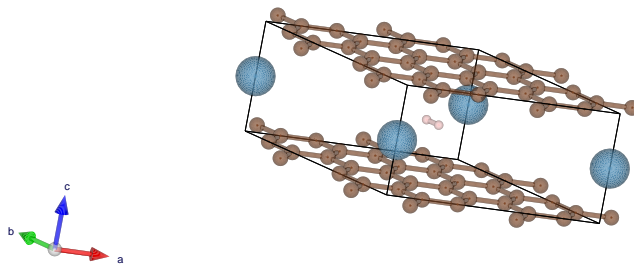


Figure 3.14: The effect on the formation energy (from free spin-polarised ground state atoms) per CaC_{14} unit by the c -axis separation between consecutive sheets of graphite.

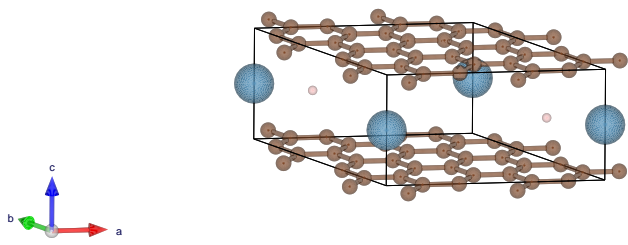
3 Modelled compounds



(a) H₂ parallel to the *c*-axis; the transverse orientation.



(b) H₂ perpendicular to the *c*-axis; the longitudinal orientation.



(c) H₂ dissociated into two H atoms; the dissociated case.

Figure 3.15: The three fundamentally different possible orientations of an H₂ molecule within an arbitrary Ca-GIC, CaC_{*n*} with H₂ bond axis (a) parallel to the GIC *c*-axis producing the transverse orientation, (b) perpendicular to the GIC *c*-axis for the longitudinal orientation and finally (c) dissociated into two H atoms binding to the intercalant metal. Note that any orientation between (a) and (b) can obviously exist but these represent the extreme opposites of orientation.

3 Modelled compounds

Simulation detail	Value
Calculation type	DFT
<i>xc</i> -functionals	LDA and GGA-PW91
Program	VASP
Basis	Plane wave within PAW scheme
Basis cut-off	800 eV
<i>k</i> -point grid	$8 \times 8 \times 8$
Atomic basis	Fixed and manually changed

Table 3.6: A summary of the DFT simulation details used for modelling $\text{CaC}_n + \text{H}_2$ and $\text{CaC}_n + 2\text{H}$ in the three stoichiometries with $n = 6, 8$ and 14 .

was found. The H_2 was then moved around the structure to inspect the energy landscape such that that global minimum could be found. The process was repeated until all global minima in all three stoichiometries using both *xc*-functionals for all three forms of H_2 (of two H) orientations given above were found. In all cases the longitudinal orientation (3.15(b)) was found to be highest in energy and thus less favourable than the other cases. As such it is omitted in the following discussion.

All calculations were performed on the α -stacked *P6/mmm* phase of Ca-GICs as little difference was seen between the phases. Calculations were performed within VASP using a plane-wave basis within the PAW scheme. The simulation details are shown in table 3.6 showing a plane wave cut off of 800 eV and a Monkhorst-Pack *k*-point grid of $8 \times 8 \times 8$ which together gave converged results for the energy. All energy landscapes were created using a triangular lattice within the unit cell resulting in 50 sampling points for the stoichiometries of CaC_6 and CaC_8 and 84 points for CaC_{14} . A smooth map was generated by linearly interpolating between adjacent points and then colour mapped such that dark blue represents an energy minima (a preferred absorption site) and dark red an energy maxima (a strong repulsion due to Ca ions or C atoms). Lighter blue, or white, tends to represent energy barriers.

3.3.1 Hydrogenated CaC_6

Following the work of Cobian and Íñiguez [1] it was expected that the most energetically favourable absorption in CaC_6 would be the dissociated case rather than molecular absorption. The binding curves for varying the GIC *c*-axis around both transverse H_2

3 Modelled compounds

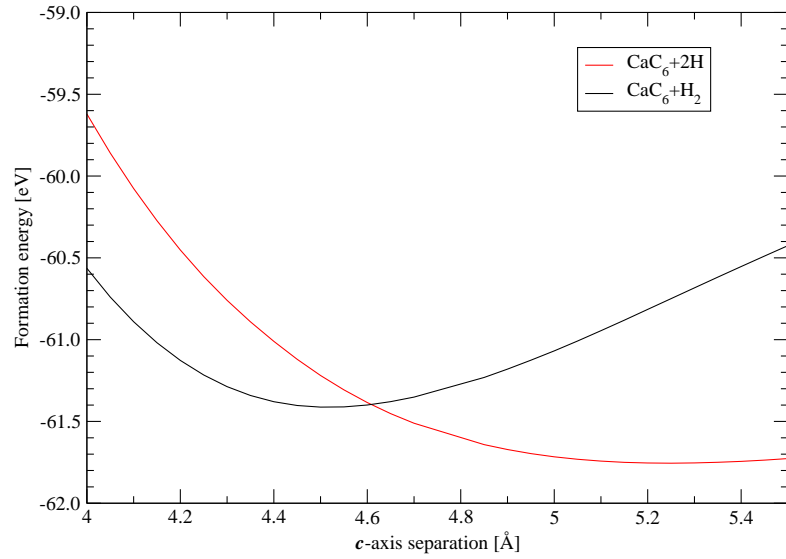
and around two H atoms in the global minimum is shown for LDA in figure 3.16(a) and for GGA-PW91 in 3.16(b). The formation energy from spin-polarised free atoms is given as the ordinate. It is clear in both cases that while there is an energetic penalty for expanding the GIC *c*-axis well beyond the CaC₆ equilibrium value, there is a large energy gain in dissociating the H₂ molecule. The large increase in the *c*-axis separation upon dissociation relative to un-hydrogenated CaC₆ in the *P6/mmm* phase of 21 % with LDA and 34 % with GGA-PW91 shows the strong Ca-H binding and concomitant weakening of the Ca-C bonds. The H₂ absorption energy is 0.34 eV lower, in the dissociated case than the case of molecular absorption, with LDA and 0.94 eV with GGA-PW91. The equilibrium *c*-axis separation for the case of molecular absorption is 4.50 Å with LDA and 4.70 Å with GGA-PW91, whereas in the dissociated case they are 5.25 Å and 6.05 Å with LDA and GGA-PW91 respectively. The LDA clearly over-binds this case versus the generalised gradient *xc*-functional and we can see from the graph in figure 3.16(b) that GGA-PW91 struggles to contain the dissociated system as noted from the very shallow bonding curve beyond *c*_{equil.}.

3.3.2 Hydrogenated CaC₈ and CaC₁₄

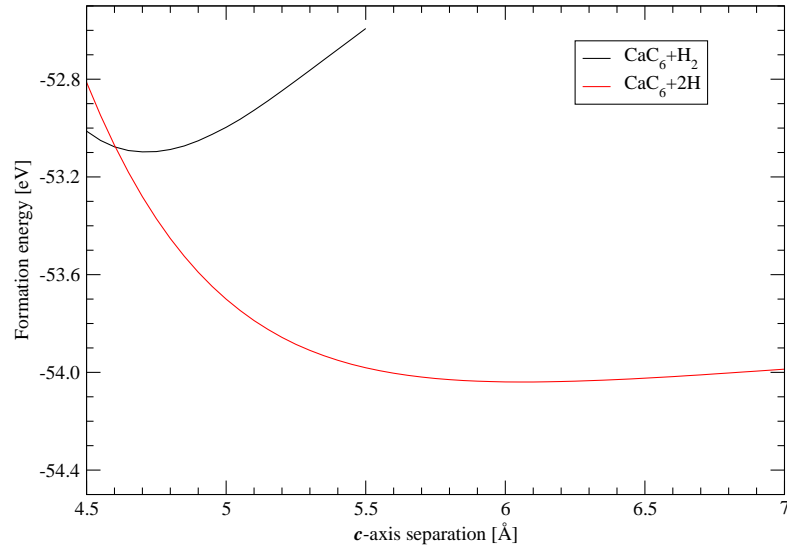
The case for the less densely packed GICs of CaC₈ and CaC₁₄ is different to that of CaC₆. In this regime the most favourable absorption is of the H₂ molecule. Figure 3.17 shows the variation of the formation energy of CaC₈ when loaded with H₂ in the global minimum compared with two H atoms in the global minimum; (a) shows the results from the LDA *xc*-functional and (b) shows results from the results from the using GGA-PW91. Again, the formation energy from spin-polarised free atoms is given as the ordinate. We can see that with both functionals the molecular absorption is more energetically favourable by 1.3 eV with LDA and 1.1 eV with GGA-PW91. The slight *c*-axis expansion of CaC₈ upon absorption of an H₂ molecule can also be clearly seen, 3 % in LDA and 4 % with GGA-PW91. The weakening of the Ca-C bonds, in the dissociated case, due to the formation of Ca-H bonds is again noticeable by the large 14% increase in the *c*-axis relative to the unloaded CaC₈ material with LDA and 31 % for GGA-PW91.

The same qualitative result appears upon the analysis of hydrogenation of CaC₁₄ shown in 3.18, with molecular absorption being favoured over atomic H absorption. The equilibration of the *c*-axis for LDA is shown in 3.18(a) and for GGA-PW91 in 3.18(b). The expansion of the *c*-axis upon molecular absorption is slightly more pronounced than

3 Modelled compounds



(a) LDA *c*-axis equilibration.



(b) GGA-PW91 *c*-axis equilibration.

Figure 3.16: Equilibrating the *c*-axes in CaC_6 with an H_2 molecule at the global minimum and two H atoms at the global minimum with (a) the LDA and (b) GGA-PW91.

3 Modelled compounds

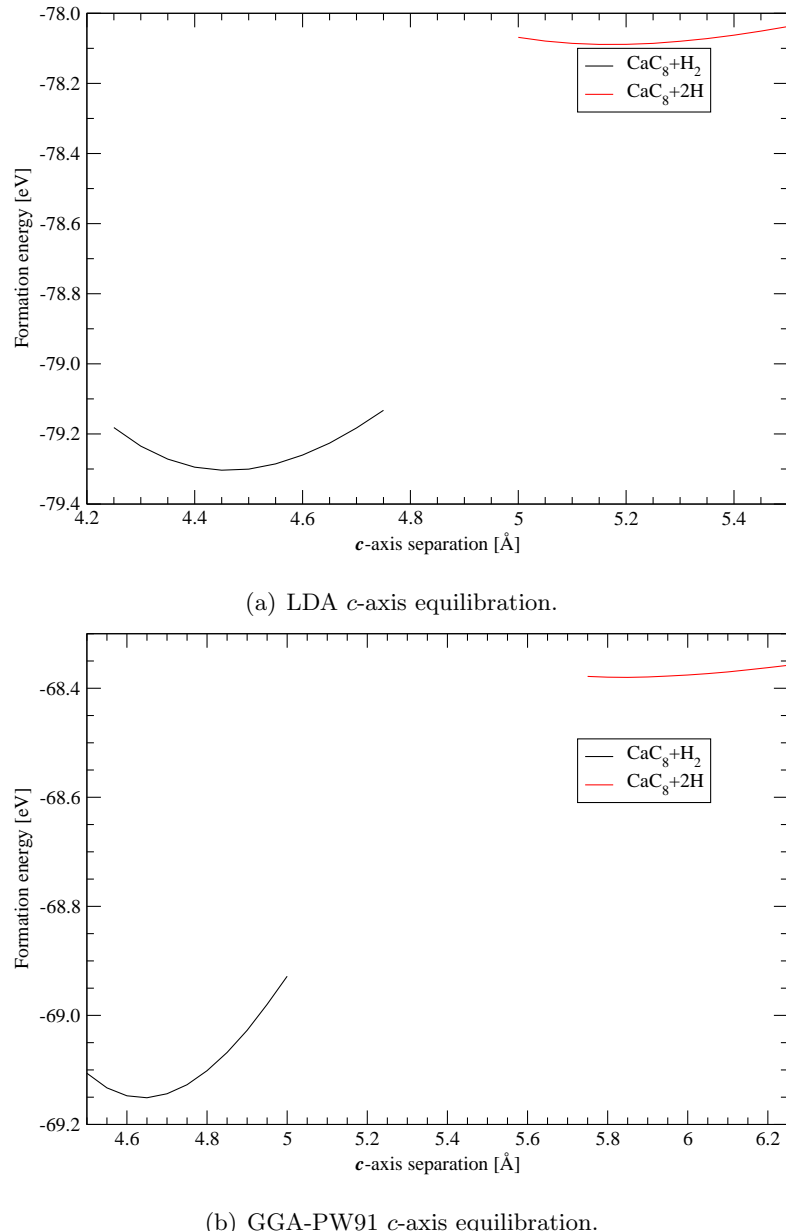
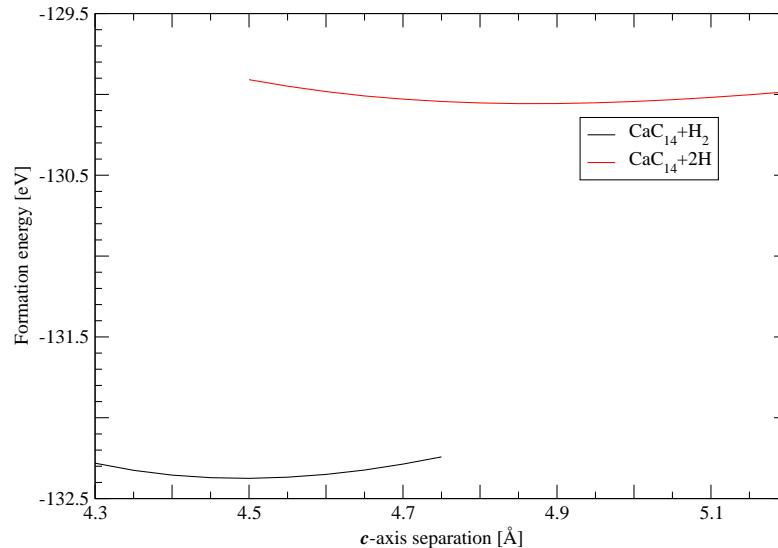


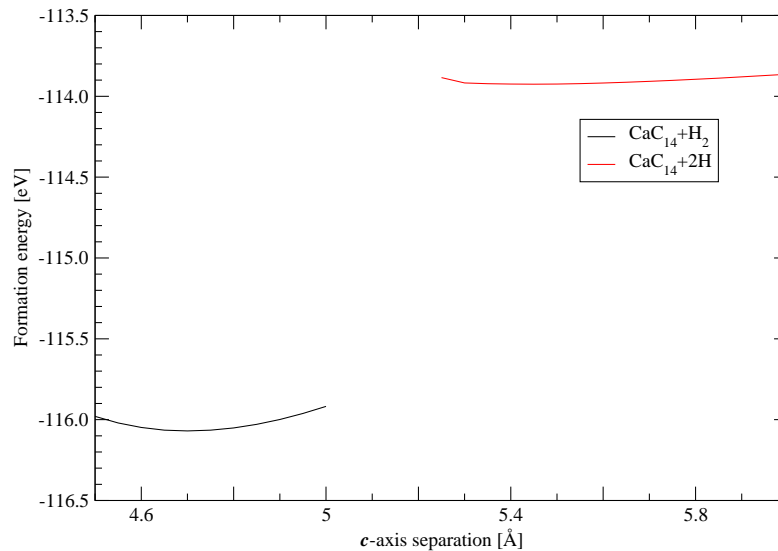
Figure 3.17: Equilibrating the *c*-axes in CaC_8 with an H_2 molecule at the global minimum and two H atoms at the global minimum with (a) the LDA and (b) GGA-PW91.

3 Modelled compounds

for the case of CaC_8 , although still small at just 5 % with LDA and 6 % with GGA-PW91. Again, the weakened Ca-C bonds in the dissociated regime are clear from the 13 % increase in the *c*-axis with LDA and 22 % with GGA-PW91.



(a) LDA *c*-axis equilibration.



(b) GGA-PW91 *c*-axis equilibration.

Figure 3.18: Equilibrating the *c*-axes in CaC_{14} with an H_2 molecule at the global minimum and two H atoms at the global minimum with (a) the LDA and (b) GGA-PW91.

Values for the equilibrium *c*-axis for each of the CaC_n GICs (with $n = 6, 8, 14$) in the molecular absorption and atomic absorption of hydrogen regime with total formation energies from spin-polarised free atoms are given in table 3.7.

LDA			GGA-PW91		
	c (Å)	$E_{\text{form}}/\text{hydrogenated CaC}_n$ (Å)		c (Å)	$E_{\text{form}}/\text{hydrogenated CaC}_n$ (Å)
CaC₆					
+H ₂	4.50	-61.413		4.70	-53.010
+2H	5.25	-61.755		6.05	-54.040
CaC₈					
+H ₂	4.45	-79.339		4.65	-69.151
+2H	5.15	-78.088		5.85	-68.380
CaC₁₄					
+H ₂	4.50	-132.391		4.70	-116.070
+2H	4.85	-130.057		5.45	-113.925

Table 3.7: A summary of the results of hydrogen absorption in the CaC_n GICs (with $n = 6, 8, 14$) both molecularly (in the transverse orientation) and atomically as two H atoms.

3 Modelled compounds

3.3.3 Hydrogenated CaC_n energy landscapes

The landscapes that follow are shown projected down the c -axis of the GIC and thus the plane of the graphite sheets are shown in the plane of the page. For these representative cases the molecule was fixed at half way down the c -axis (as the with the global energy minimum of the hydrogenated compound) and the c -axis fixed at its equilibrium value as the molecule was permuted around the unit cell. For the dissociated case the projection is again down the c -axis and the energy at a point represents an H atom at that location and the other at the symmetrically opposite location on the other side of the unit cell, i.e. for a position given (in fractional coordinates of the lattice vectors) at (p, q, r) the second H atom would appear at $((1 - p), (1 - q), (1 - r))$. Where these two positions were equal the second H atom was placed in as similar position as possible, e.g. for $(1/2, 1/2, 1/2)$ the second H atom was placed at $(0, 1/2, 1/2)$. C positions are represented by black circles and Ca positions by green circles. It should be noted that the intercalant Ca atoms in all cases are surrounded by a red area in the following landscapes as they present strong repellers in all cases for both H_2 and individual H atoms.

Hydrogenated CaC_6 Representative energy landscapes for hydrogenated CaC_6 are shown in figure 3.19 (with the LDA functional) and 3.20 (for the GGA-PW91 functional) for H_2 in the transverse orientation and for the dissociated case of two H atoms.

In both LDA and GGA-PW91 the minima for H_2 absorption appears more diffuse and softer than for individual H atoms; it even appears as if it has a lower minimum energy but this is an artefact of plotting not of the landscape itself. It is clear however that atomic absorption is strongly bound allowing little freedom for the diffusion of the H atoms through the material.

Steep energy barriers of $\sim 1\text{ eV}$ with LDA and $\sim 1.2\text{ eV}$ with GGA-PW91 exist between sites (passing under a C-C bond) for the case of atomic absorption. These are the barriers necessary for H to cross to diffuse from the global minimum below the centre of an empty C hexagon through the material.

Conversely, for the less favourable case of molecular hydrogen absorption the barrier heights to diffusion are much lower, at just $\sim 0.3\text{ eV}$ for both LDA and GGA-PW91. This does not take into account a reorientation of an H_2 molecule to cross an energy barrier and assumes that the bond axis remains parallel to the GIC c -axis, i.e. in the transverse orientation. It would be expected that the molecule may "flatten" out over

3 Modelled compounds

an energy barrier into the longitudinal configuration in order to maximise the distance between H and C atoms. This would have the effect of lowering these molecular diffusion barriers somewhat.

Hydrogenated CaC₈ Representative energy landscapes are shown in 3.21 (LDA) and 3.22 (GGA-PW91) for the case (a) of H₂ in CaC₈ and (b) for two H atoms in CaC₈. The same process as for the CaC₆ energy landscapes was used here.

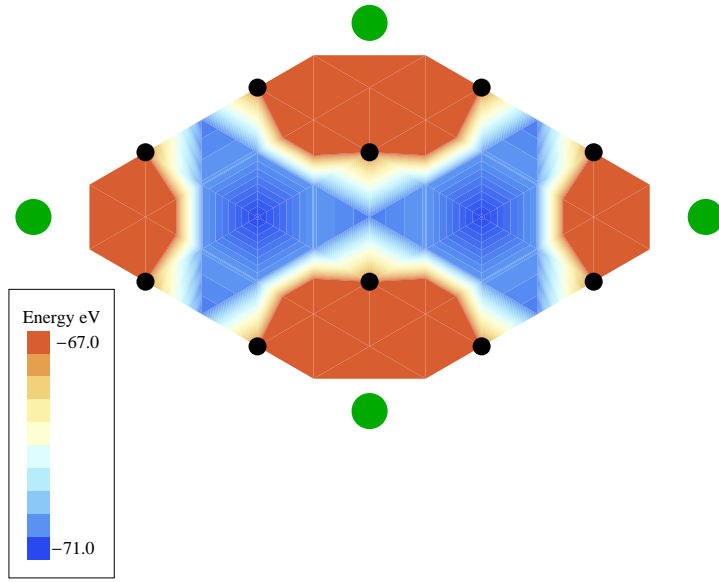
In the case of hydrogen absorption in CaC₈ we see that a similar situation occurs with confinement of H atoms in the dissociated case as was seen in CaC₆. Strong localised attractors exist below the centre of C hexagons with little spatial extent for this less favourable absorption process. For an H atom to diffuse from site-to-site in CaC₈ it would have to hop the barrier caused by the C-C bond above and below it. This barrier is much lower than for the CaC₆ case, being 0.4 eV in LDA and 0.6 eV in GGA-PW91.

For the more energetically favourable case of molecular absorption in the CaC₈+H₂ energy landscapes we energy minima again exist underneath C hexagons and the space directly beneath C atoms themselves represent strong barriers to absorption (visible in the bright white part of the landscapes around the C atoms). These sites show more spatial extent than for the dissociated case allowing potentially slightly more freedom for the H₂ molecule to wander within the confines of one site. Diffusion for an H₂ molecule between sites requires only small barriers, relative to H₂ diffusion in CaC₆, to be crossed of ~ 0.2 eV with both LDA and GGA-PW91.

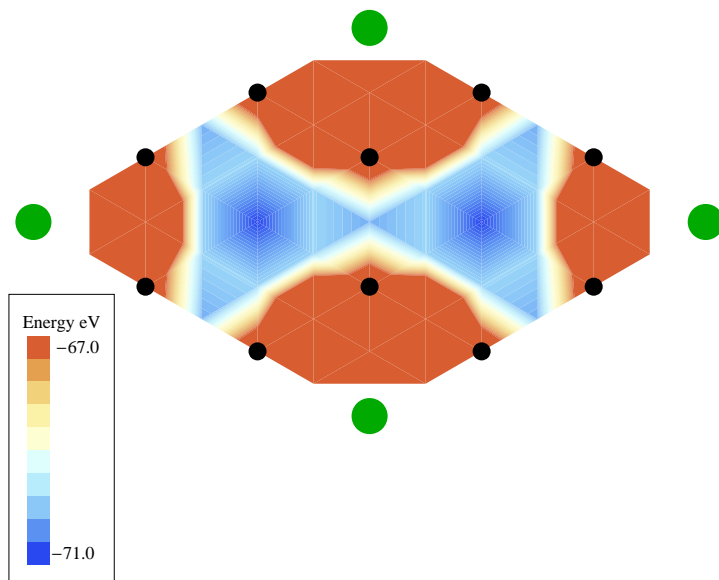
Hydrogenated CaC₁₄ Hydrogen energy landscapes for this material are shown in figure 3.23 for LDA and figure 3.24 for GGA-PW91. Note that, unlike the other cases of CaC₆ and CaC₈, the graphite lattice is rotated at $\sim 10^\circ$ relative to the lattice vectors.

The energy landscapes of hydrogenated CaC₁₄ represent the most stark difference between molecular and atomic absorption. We can see that in the less favourable case of atomic H absorption we have long spatially extended minima from beneath the centre of C hexagons across the hexagon. While some of this is an artefact from the sampling method and linear interpolation employed, it is worth noting that the global minimum for absorption is not below a graphite hexagon centre. This position would no longer be perfectly symmetric between nearest neighbour Ca atoms and so does not benefit from equal bonding to each. Instead the energy minimum is found before the graphite centre closer to the Ca, at a distance of 2.4 Å from the Ca intercalant. Again, the strong

3 Modelled compounds

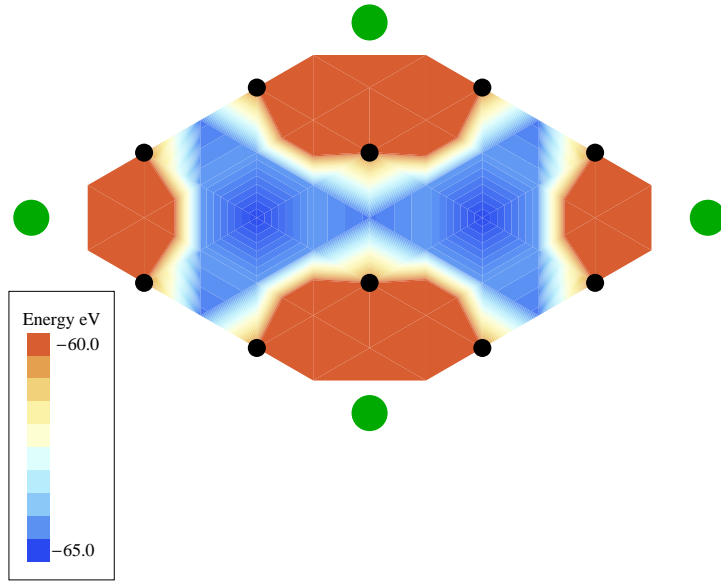


(a) LDA $\text{CaC}_6 + \text{H}_2$ (transverse).

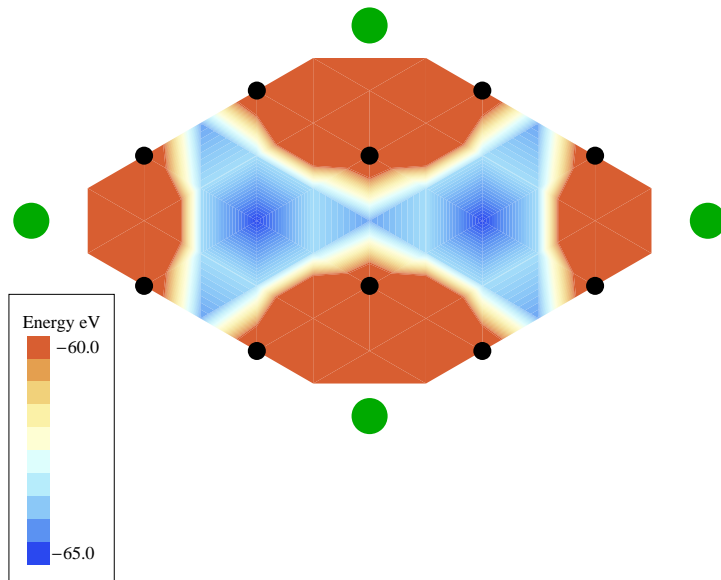


(b) LDA $\text{CaC}_6 + 2\text{H}$.

Figure 3.19: Representative (LDA) energy landscapes for CaC_6 with (a) an H_2 molecule in the transverse orientation and (b) two H atoms in symmetrically opposite positions. C positions are represented by black circles and Ca positions by green circles.



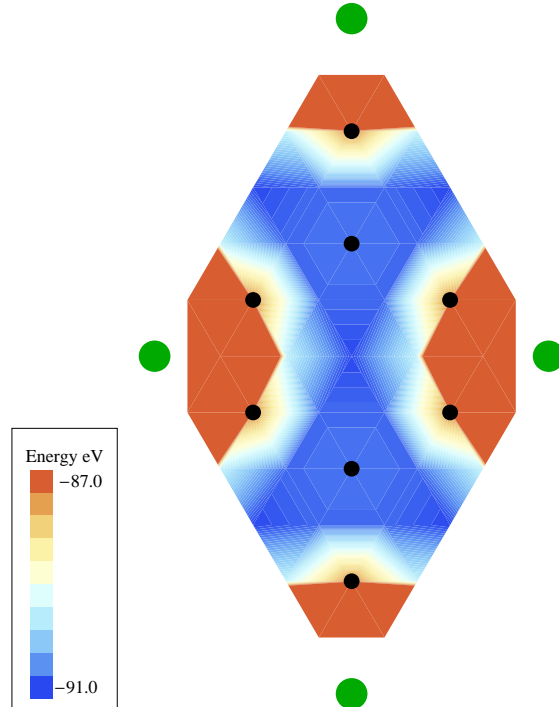
(a) GGA-PW91 CaC₆+H₂ (transverse).



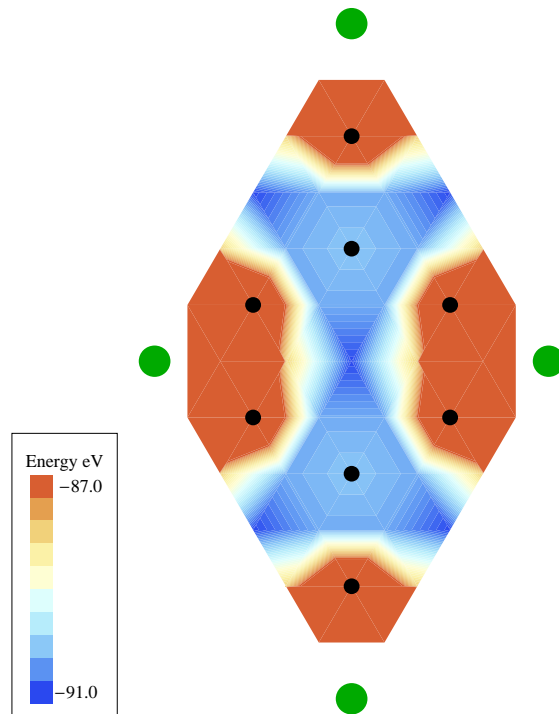
(b) PW91 CaC₆+2H.

Figure 3.20: Representative (GGA-PW91) energy landscapes for CaC₆ with (a) an H₂ molecule in the transverse orientation and (b) two H atoms in symmetrically opposite positions. C positions are represented by black circles and Ca positions by green circles.

3 Modelled compounds



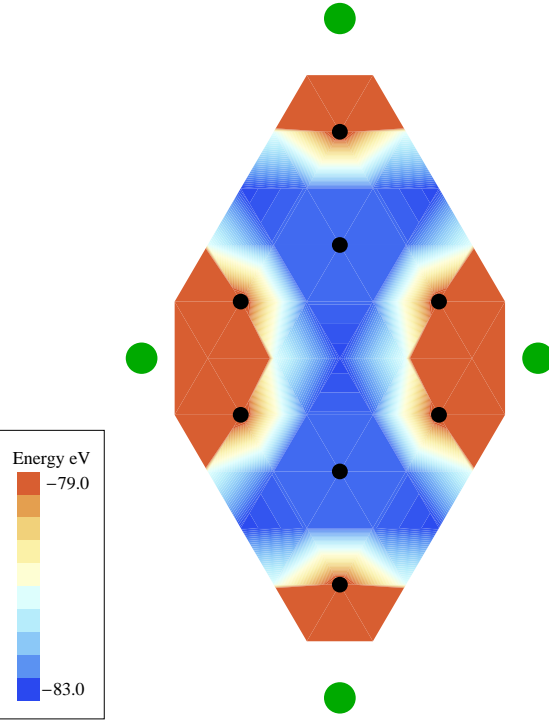
(a) LDA $\text{CaC}_8 + \text{H}_2$ (transverse).



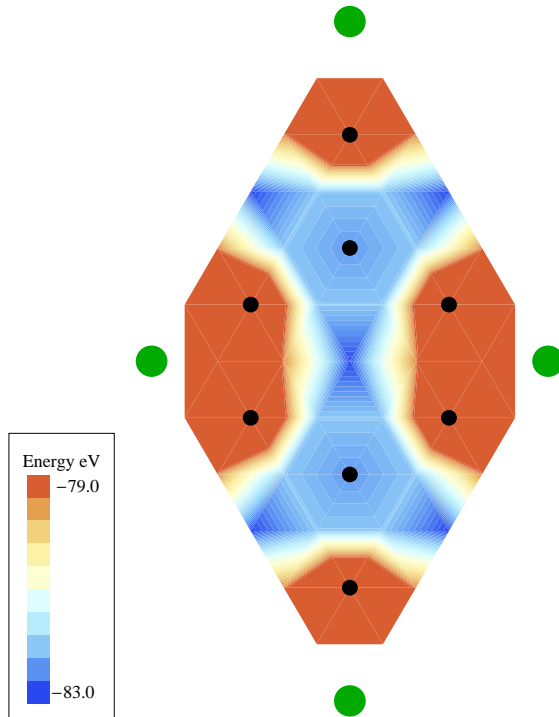
(b) LDA $\text{CaC}_8 + 2\text{H}$.

Figure 3.21: Representative (LDA) energy landscapes for CaC_8 with (a) an H_2 molecule in the transverse orientation and (b) two H atoms in symmetrically opposite positions. C positions are represented by black circles and Ca positions by green circles.

3 Modelled compounds



(a) GGA-PW91 $\text{CaC}_8 + \text{H}_2$ (transverse).



(b) PW91 $\text{CaC}_8 + 2\text{H}$.

Figure 3.22: Representative (GGA-PW91) energy landscapes for CaC_8 with (a) an H_2 molecule in the transverse orientation and (b) two H atoms in symmetrically opposite positions. C positions are represented by black circles and Ca positions by green circles.

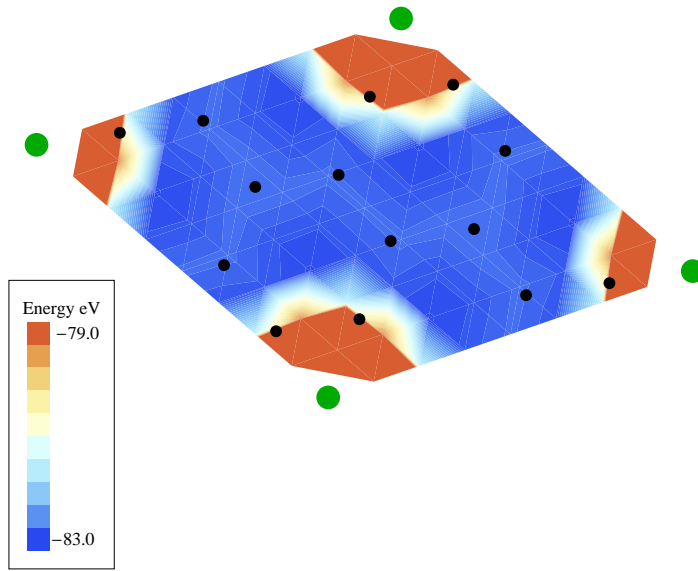
3 Modelled compounds

repulsion of the C atoms to the H atoms is clearly visible in the high white peaks in the energy landscape under the C atoms. Extremely large barriers exist for H diffusion, other than the artificial channels that are artefacts of the sampling method, of 1.3 eV in LDA and 1.4 eV for GGA-PW91.

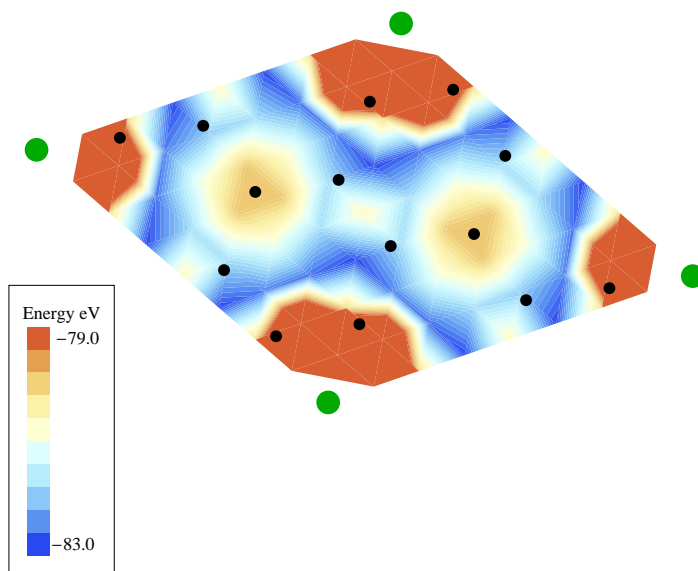
The favourable absorption case of the $\text{CaC}_{14} + \text{H}_2$ landscape is very different. This is the first case where H_2 diffusion looks extremely possible. Absorption sites are located almost at the centre of absorption sites and represent soft minima in the energy landscape. Barriers to diffusion are clearly visible and trace the C-C bonds existing above and below them forming an hexagonal grid of energy barriers. C atoms not directly near an intercalant Ca atom offer a small rise in the landscape but not the strong repellers of previous GICs. By inspecting the barriers around a particular absorption site, of which the unit cell shows six, we see that the barriers are of similar height, 0.25 eV and 0.23 eV with LDA and 0.13 eV and 0.11 eV with GGA-PW91. These six absorption sites can be grouped into two sets of 3 sites to form two sets of sites, set *A* and set *B*. In fractional coordinates of the lattice vectors, the set *A* consists of the absorption sites at the three positions $A = \{(3/8, 1/4, 1/2), (3/4, 1/8, 1/2), (7/8, 5/8, 1/2)\}$. The second set *B* of absorption sites comprises the rotated positions given in *A*, thus if a member of *A* is given as (r_a, r_b, r_c) then the corresponding member of *B* would be $((1 - r_a), (1 - r_b), (1 - r_c))$.

The reason for splitting these sites into two sets now becomes clear. When an H_2 molecule resides at a site that is a member of *A* it faces three equal barriers. Of these, crossing one of two barriers will take the molecule to another member of the set *A* and only one barrier offers changing to a member of the set *B*. Given even barrier heights and under normal conditions the random diffusing H_2 molecule has a 67% chance of remaining within the same set of absorption sites, thus remaining localised, and a 33% chance of changing from one set to another, thus diffusing. The “set-changing” barrier is the one located at the centre of the unit cell. Further detailed discussion of these energy landscapes and their implication upon hydrogen absorption and diffusion is saved for §4.

The question raised in the introduction is whether the hydrogenated Ca-GICs are stable against decomposition into pure graphite and CaH_2 . Having modelled the materials necessary to investigate hydrogen absorption in Ca-GICs we now focus upon the possible decomposition products.

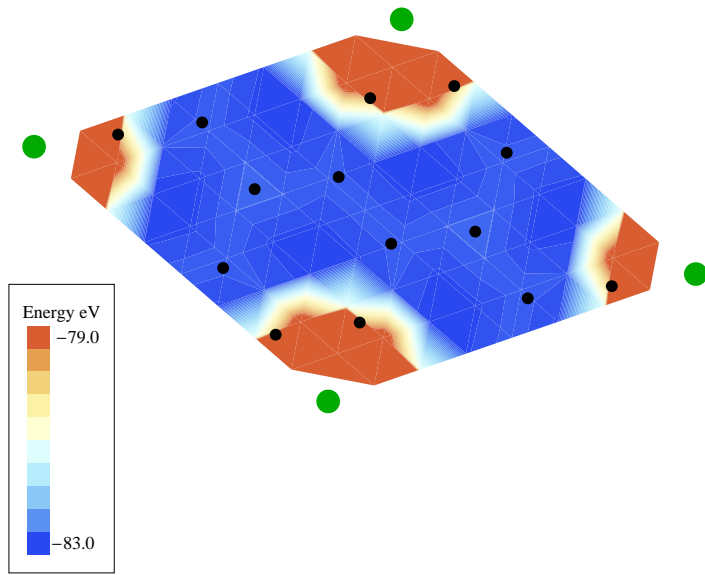


(a) LDA $\text{CaC}_{14} + \text{H}_2$ (transverse).

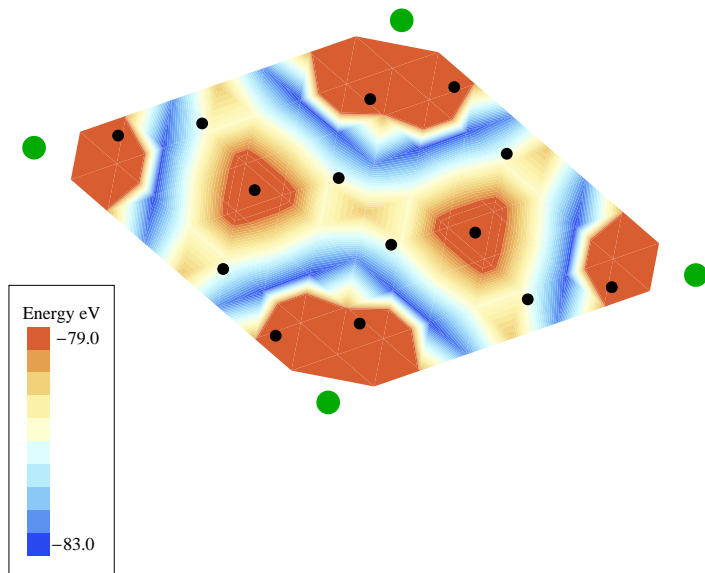


(b) LDA $\text{CaC}_{14} + 2\text{H}$.

Figure 3.23: Representative (LDA) energy landscapes for CaC_{14} with (a) an H_2 molecule in the transverse orientation and (b) two H atoms in symmetrically opposite positions. C positions are represented by black circles and Ca positions by green circles.



(a) GGA-PW91 $\text{CaC}_{14} + \text{H}_2$ (transverse).



(b) PW91 $\text{CaC}_{14} + 2\text{H}$.

Figure 3.24: Representative (GGA-PW91) energy landscapes for CaC_{14} with (a) an H_2 molecule in the transverse orientation and (b) two H atoms in symmetrically opposite positions. C positions are represented by black circles and Ca positions by green circles.

3 Modelled compounds

3.4 Calcium hydride

The calcium hydride crystal has a complicated structure when visualised, as can be seen in figure 3.25, but has an orthorhombic (with three unequal length lattice vectors, $|\vec{a}| \neq |\vec{b}| \neq |\vec{c}|$, and with $\alpha = \beta = \gamma = 90^\circ$) unit cell of the *Pnma* symmetry group. The structure is better understood by considering it as one CaH_2 unit sitting on the Wyckoff 4(c) positions of $(x, 1/4, z)$, $(x + 1/2, 1/4, -z + 1/2)$ and the mirrored positions of $(-x, 3/4, -z)$ and $(-x + 1/2, 3/4, z + 1/2)$ respectively. This produces equivalent Ca sites and two inequivalent H sites labelled H1 and H2. Each H1 is coordinated by eight other H atoms and four Ca atoms, each H2 by ten other H atoms and five Ca atoms, such that each Ca is coordinated with nine H atoms.

The unit cell is shown with bonds extending beyond it in 3.25(a) and projected down the \vec{c} -axis in (b) and most elucidating, projected down the \vec{b} -axis in (c).

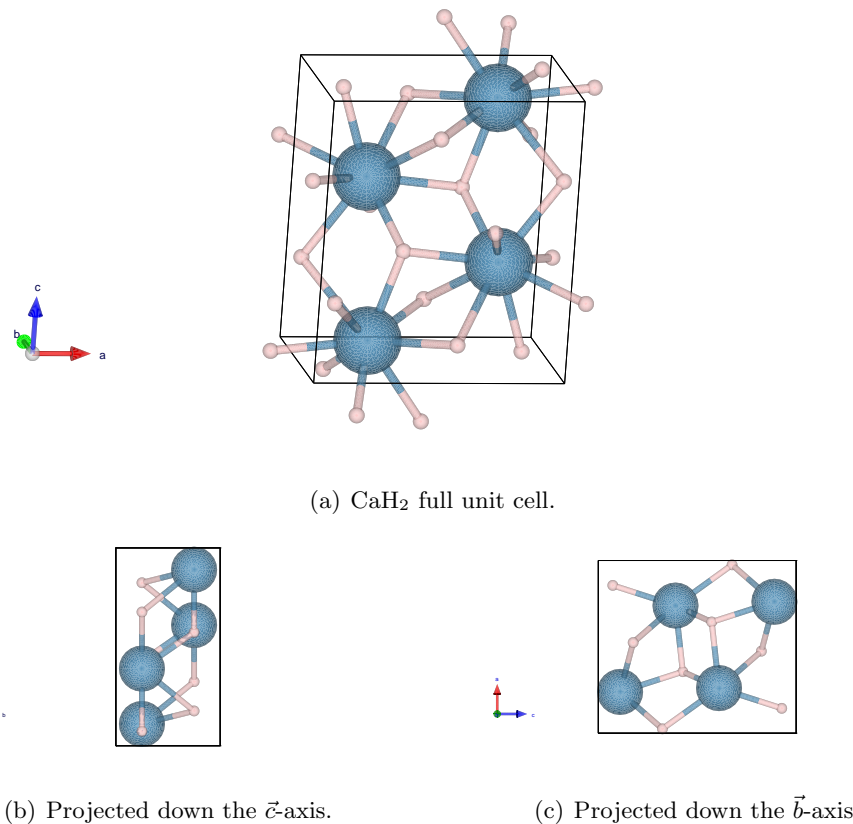


Figure 3.25: The CaH_2 unit cell as seen (a) in its entirety with bonds extending outside the unit cell shown, (b) as projected down the \vec{c} -axis and (c) projected down the \vec{b} -axis to show the cell structure most clearly.

3 Modelled compounds

Simulation detail	Value
Calculation type	DFT
<i>xc</i> -functionals	LDA and GGA-PW91
Program	VASP
Basis	Plane wave within PAW scheme
Basis cut-off	700 ev
<i>k</i> -point grid	$7 \times 7 \times 7$
Atomic basis	Free to relax with quasi-Netwon method

Table 3.8: A summary of the DFT simulation details used for modelling CaH₂.

The structure was modelled in VASP using DFT and both *xc*-functionals considered throughout: LDA and GGA-PW91. A plane-wave basis within the PAW scheme with a cutoff of 700 eV was employed after convergence tests showed the total energy of the cell to be converged. A Monkhorst-Pack *k*-point grid of $7 \times 7 \times 7$ was used after giving well converged results in testing. Within each unit cell relaxation the atomic basis was free to relax to its nearest local minimum using the automatic quasi-Newton routine within VASP. Since the structure was considered to be very close to the local minimum this variable metric method was chosen. The method uses the accurate calculated forces to determine a search direction and relaxes the atomic basis relative to these forces. A summary of these parameters is given in table 3.8.

Relaxing the system was done manually to ensure the correct structure was approached. Using the structure given by Wu et al. [11] the unit cell was relaxed with both LDA and GGA-PW91 by varying the volume of the cell while maintaining the shape of the cell, i.e. the ratios of the lattice vectors $|\vec{a}|/|\vec{b}|$, $|\vec{a}|/|\vec{c}|$ and $|\vec{b}|/|\vec{c}|$ were fixed while the volume varied. During each relaxation the atomic basis was allowed to relax to the nearest local minim and a negligible change of the basis was observed, enforcing that the correct original structure was chosen. Once the volume giving the lowest total energy was found the cell shape was changed by varying all three lattice vector ratios independently by 1% both increasing and decreasing. When a new cell shape reported a lower energy the process was repeated from this cell shape and the shape fixed while the volume varied again. Once no further energy reductions could be made by changing either the shape or volume of the cell the final structure was taken as the equilibrium unit cell.

4 Conclusions and discussion

The calculated parameters are shown in table 3.9 and are compared with other DFT calculations. Calculations by Li et al. [9] were performed within linear response DFT for phonon calculations within the Quantum-ESPRESSO package. A plane-wave pseudopotential method was used, rather than the PAW scheme implemented in VASP, with the GGA-PBE *xc*-functional. A plane-wave cut-off of 952 eV was used with a *k*-point grid of $3 \times 6 \times 3$. The atomic basis was allowed to relax during the cell relaxation. The DFT calculations by Wolverton and Ozolins [10] were performed in VASP with the GGA-PW91 *xc*-functional with a PAW plane-wave basis with a cut-off of 875 eV and a *k*-point mesh of $4 \times 4 \times 4$ or better. The automatic conjugate-gradient relaxation method was used and both the cell vectors and atomic basis was allowed to change until total energy changes were < 1 meV. The high-resolution neutron powder diffraction experiment was performed on CaD₂ by Wu et al. [11] and shows excellent agreement with all calculated parameters. All three GGA-PW91 values for the cell parameters and all *x*- and *z*-values for the atomic basis of Ca, H1 and H2 are within 0.3 % of the 9 K experimental data. The three LDA values for the cell parameters are all ~ 0.3 Å too small, showing the tendency for this functional to overbind systems, while most of the *x*- and *z*-values for the atomic basis are within 1 %.

Some selected atomic distances within CaH₂ are shown in table 3.10 and compared with experiment again [11] to underline the accurate representation of this crystal within DFT.

4 Conclusions and discussion

It is now possible to calculate the binding energy of hydrogen to these three stoichiometries of CaC_{*n*} with *n* = 6, 8 and 14. The binding energy of hydrogen in the material shall be defined as the energy required to bring hydrogen in its standard state (as the H₂ molecule) from a vacuum and place it within the relaxed GIC. For this only three formation energies are needed: the formation energy of the H₂ molecule, *E*_{form}(H₂) (given in appendix E), the formation energy of CaC_{*n*}, *E*_{form}(CaC_{*n*}), and the formation energy of the hydrogenated GIC *E*_{form}(Hydrogenated CaC_{*n*}). Mind that “formation energies” here refers to formation energies of the materials from spin-polarised free atoms. Thus the hydrogen binding energy, *E*_{bind}, is given,

$$E_{\text{bind}} = E_{\text{form}}(\text{Hydrogenated CaC}_n) - [E_{\text{form}}(\text{CaC}_n) + E_{\text{form}}(\text{H}_2)], \quad (3.3)$$

	Calculated 0 K (without zero point energies)		Theory 0 K		Experimental CaD ₂	
	LDA	GGA-PW91	(ref. [9])	(ref. [10])	(ref. [11])	
			GGA-PBE	GGA-PW91	9 K	298 K
Unit cell parameters						
	$ \vec{a} $ (Å)	5.722	5.908	5.9673	5.884	5.92852(5)
	$ \vec{b} $ (Å)	3.466	3.570	3.6062	3.568	3.57774(3)
	$ \vec{c} $ (Å)	6.569	6.770	6.8384	6.756	6.78956(6)
	V (Å ³)	130.3	142.8	147.156	141.836	144.011(1)
	E _{form} /CaH ₂	-9.400	-8.256			145.362(2)
Ca (4c)						
95	x	0.239	0.239	0.2400	0.240	0.2387(1)
	z	0.112	0.110	0.1099	0.109	0.1102(1)
H1 (Calc.) / D1 (Exp.) (4c)						
	x	0.355	0.356	0.3557	0.355	0.3558(1)
	z	0.428	0.427	0.4265	0.427	0.4276(1)
H2 (Calc.) / D2 (Exp.) (4c)						
	x	0.974	0.975	0.9754	N/A	0.9750(1)
	z	0.681	0.676	0.6765	N/A	0.6756(1)
						0.6759(1)

Table 3.9: A summary of the results of relaxing CaH₂ with both the LDA and GGA-PW91 *xc*-functionals from this work compared with DFT calculations by Li et al. [9] using GGA-PBE, Wolverton and Ozolins [10] using GGA-PW91 and with experiment for CaD₂ [11].

4 Conclusions and discussion

	Calculated 0 K		Experimental ref. [11]	
	LDA	GGA-PW91	9 K	298 K
Ca1-H1	2.18299	2.25580	2.2639(12)	2.2662(15)
Ca1-H1	2.17770	2.24327	2.2477(7)	2.2555(9)
Ca1-H1	3.17770	2.24327	2.2477(7)	2.2555(9)
Ca1-H1	2.21401	2.27897	2.2841(11)	2.3002(15)
Ca1-H2	2.43034	2.49848	2.5055(9)	2.5152(11)
Ca1-H2	2.43034	2.49848	2.5055(9)	2.5152(11)
Ca1-H2	2.51724	2.62262	2.6307(9)	2.6426(12)
Ca1-H2	2.51724	2.62262	2.6307(9)	2.6426(12)
Ca1-H2	2.34947	2.38635	2.3936(11)	2.3893(14)
H1-H1	2.56807	2.65852	2.6624(12)	2.6809(15)
H1-H1	2.56807	2.65852	2.6624(12)	2.6809(15)
H1-H2	3.24160	2.81346	2.8162(11)	2.8286(14)
H1-H2	2.57856	2.65691	2.6708(8)	2.6777(10)
H1-H2	2.57856	2.65691	2.6708(8)	2.6777(10)
H1-H2	2.65826	2.73773	2.7457(9)	2.7487(11)
H1-H2	2.65827	2.73773	2.7457(9)	2.7487(11)
H1-H2	2.65261	2.77376	2.7855(10)	2.7940(13)
H2-H2	2.40138	2.99746	2.9952(12)	3.0074(15)
H2-H2	2.40138	2.99746	2.9952(12)	3.0074(15)
H2-H2	3.46418	3.11706	3.1319(5)	3.1402(6)
H2-H2	3.46419	3.11705	3.1319(5)	3.1402(6)

Table 3.10: Selected bond distances (\AA) in the CaH_2 crystal and their comparison with CaD_2 in experiment.

4 Conclusions and discussion

where E_{bind} will be negative for favourable absorption and positive for unfavourable.

The binding energies of hydrogen in both molecular and atomic absorption are given in table 3.11 for all three stoichiometries.

	E_{bind} (eV)	
	LDA	GGA-PW91
CaC ₆		
+H ₂	0.11	0.79
+2H	-0.23	-0.24
CaC ₈		
+H ₂	-0.05	0.31
+2H	1.20	1.08
CaC ₁₄		
+H ₂	-0.01	0.28
+2H	2.33	2.42

Table 3.11: Binding energies, E_{bind} , of hydrogen in CaC_n GICs with $n = 6, 8, 14$ in atomic absorption (CaC_n+2H) and molecular transverse absorption (CaC_n+H₂). Negative energies represent favourable binding.

While the H₂ molecule was never found to dissociate in simulations, these barriers being much too large, it was found that in the case of CaC₆ atomic absorption of hydrogen is much favoured over molecular by 0.34 eV with LDA and 1.03 eV with GGA-PW91, and is energetically favourable. For the less dense Ca-GICs hydrogen absorption is only slightly, if ever, energetically favourable, as can be seen from the negligible binding energies only given by the over-binding LDA *xc*-functional. Without knowledge of the barriers to absorption these cases could still absorb hydrogen as was noted earlier. It is clear that in the GICs with more free space, CaC₈ and CaC₁₄, molecular absorption is favoured over atomic by over 0.7 eV in each case. This can be attributed to the relative large size of the H₂ molecule being larger than the available “pores”, “sites”, in the more dense GIC but being allowable in the less dense GICs; once the system has a chance to gain the energy from an H₂ bond it becomes favourable to do so.

LDA gave a favourable binding of H₂ in CaC₈ and CaC₁₄ while GGA-PW91 did not. This is due to the LDA, uncharacteristically, *underbinding* the free H₂ molecule. The bond length was found to be extended relative to the expected value and this

4 Conclusions and discussion

consequently gave a lower value for $E_{\text{form}}(\text{H}_2)$, which then thus pushes the LDA E_{bind} negative due to equation 3.3 relative to GGA-PW91.

For the case of molecular absorption in CaC_8 there was only a 3 meV difference in binding energy between the transverse configuration and the longitudinal configuration (parallel and perpendicular to the GIC *c*-axis) of the H_2 molecule. A qualitative comparison with the K-GIC KC_8 corroborates these results. Inelastic neutron scattering experiments by Lovell et al. [94] on the hydrogenated KC_8 material show preferential molecular absorption at a site equivalent to that found here for the case of CaC_8 . The authors also perform DFT calculations and find that the difference between the transverse and longitudinal configurations to be of just a few meV, in agreement with what was noted here.

The LDA binding energies for atomic H absorption in CaC_6 reported here are in quantitative agreement with those given in [1] when the same plane-wave cut-off and *k*-point grid is implemented.

In considering whether this material would be suitable for a hydrogen storage material we now calculate the stability energy, ΔE . This is the energy released upon decomposition of the hydrogenated Ca-GIC into the hydride, CaH_2 , and pure graphite. By subtracting the formation energy of the hydrogenated material from the formation energies of the hydride, $E_{\text{form}}(\text{CaH}_2)$, and pure graphite, $E_{\text{form}}(\text{C}_n)$, thus

$$\Delta E = [E_{\text{form}}(\text{CaH}_2) + E_{\text{form}}(\text{C}_n)] - E_{\text{form}}(\text{Hydrogenated CaC}_n), \quad (3.4)$$

will give a negative ΔE if the hydrogen-loaded GIC is unstable against decomposition into the hydride and graphite products.

The decomposition energies are given in table 3.12 for all three GICs in just the minimum energy configuration, thus only the CaC_6+2H material is considered for the case of CaC_6 and only $\text{CaC}_{8,14}+\text{H}_2$ is considered for CaC_8 and CaC_{14} .

We can see from table 3.12 that the Ca-GICs are strongly unstable with respect to decomposition into CaH_2 and pure graphite with 1.1 – 1.8 eV released upon decomposition. This explains the experimental work by Srinivas et al. [91] which showed that after hydrogenating the CaC_6 sample no hydrogenated phase was observed and only the complete deintercalation of the Ca-GIC was seen leaving pure graphite and CaH_2 .

The high level of symmetry of this class of materials is immediately evident from

4 Conclusions and discussion

	ΔE (eV)	
	LDA	GGA-PW91
$\text{CaC}_6 + 2\text{H}$	-1.11	-1.20
$\text{CaC}_8 + \text{H}_2$	-1.38	-1.75
$\text{CaC}_{14} + \text{H}_2$	-1.75	-1.82

Table 3.12: The energies of stability against decomposition into the hydride and pure graphite, ΔE , of all three Ca-GICs from their most stable hydrogenated phase. Note that a negative value implies the hydrogenated GIC is unstable against decomposition in to the products.

the energy landscapes shown in §3.3.3. It is also immediately evident that for the three stoichiometries (CaC_6 , CaC_8 and CaC_{14}) belonging to the first geometric pattern (the first equation D.2) in appendix D, only two distinct environments exist for and H_2 molecule. The similar statement can be said for the case of two H atoms but an extra degree of freedom exists with the second H atom. The environments in question are best viewed from down the *c*-axis of the GIC and are formed by the hexagonal C arrangement. In these materials there exist only two distinct hexagonal environments: one occupied by an intercalant atom and one empty of an intercalant atom. All hexagonal sites within these materials falls into one of these two categories and within each categories all sites exhibit identical environments.

These results completely confirm earlier predictions[1] that CaC_6 does favourably absorb hydrogen within the DoE binding energy range of $0.2 - 0.8$ eV. In considering the possible errors in this work it is well known that DFT can suffer from errors in the formation energy of a few tenths of an electron-volt. With a maximum difference of ~ 0.3 eV between LDA and GGA-PW91 values of ΔE our results would tend to suggest the true value lies in this range. A study by Pozzo and Alfè [114] on the energetics showed that DFT errors can be as large as 0.5 eV, but that LDA and GGA-PW91 tend to bracket the true value. Even errors as large as 0.5 eV would not affect the conclusion here. We are left in no doubt that the reaction is strongly exothermic with a decomposition energy of at least 1.0 eV.

While the thermodynamic instability with respect to decomposition is evident it does not necessarily tell us that decomposition will occur at a given temperature; this process may be kinetically hindered. The experiment [91] shows that at room temperature the

4 Conclusions and discussion

process is unhindered and suggests an activation energy of ~ 0.9 eV for the rate limiting step. The full computational search for decomposition pathways is beyond the scope of this work.

The results here raise the interesting question as to what defines a stable hydrogen storage media. While it is known that the Li- and Ca-GICs are unstable the K-GIC appears to be stable with many experiments existing on the hydrogenated material[93, 94, 115, 116]. The formation energy of the metal hydride, E_{form} (MH_2), is thought to be the dominant energy controlling the stability of hydrogenated GICs. The double charge of Ca in CaH_2 relative to the single charge of K in the KH crystal is likely to increase the formation energy and push the hydrogenated GIC to be unstable. These results have been published in a paper by the author[117]. A study of the stabilities of the alkali- and alkaline-earth metal GICs is saved for the next chapter.

Chapter 4

The systematics of H₂ in alkali and alkaline earth metal intercalated graphite

1 Introduction

It is known that GICs formed with some alkali and alkaline earth metals absorb molecular hydrogen. Alkali GICs of potassium[4, 96], caesium[93, 96, 118, 119] and rubidium[93, 120] have been shown to absorb hydrogen[121], while lithium GICs have been shown to decompose[90] as well as, of course, the alkaline earth GIC of Calcium (shown in the previous chapter 3).

Following on from the previous chapter these chapter attempts to find what other alkali and alkaline earth GICs are unstable against decomposition into the metal hydride and pure graphite upon hydrogenation and also if any patterns exist in the energetics of these materials.

The complicated task of locating the H₂ ground state absorption site in these materials, outlined in §3.3, can be neglected when looking into the energetics of stability. As was seen in the previous chapter, decomposition energies, ΔE , were large (larger than 1 eV, see table 3.12 on page 99) compared with the favourable hydrogen binding energies, E_{bind} (smaller than -0.25 eV, see table 3.11 on page 97). This large difference implies that equation 4.1 can be approximated by exchanging the term for the formation energy of the hydrogenated GIC, E_{form} (Hydrogenated MC_n), with the formation energy of the GIC, E_{form} (MC_n). Thus we can arrive at an approximation for the expression for the

1 Introduction

stability energy, ΔE , of

$$\begin{aligned}\Delta E &= [E_{\text{form}}(\text{MH}_m) + E_{\text{form}}(\text{C}_n)] - E_{\text{form}}(\text{Hydrogenated MC}_n), \\ &= [E_{\text{form}}(\text{MH}_m) + E_{\text{form}}(\text{C}_n)] - [E_{\text{form}}(\text{MC}_n) + E_{\text{bind}}(\text{H}_2) + E_{\text{form}}(\text{H}_2)], \\ \text{and assuming } E_{\text{bind}} \text{ small, then} \\ \Rightarrow \Delta E &\approx [E_{\text{form}}(\text{MH}_m) + E_{\text{form}}(\text{C}_n)] - [E_{\text{form}}(\text{MC}_n) + E_{\text{form}}(\text{H}_2)].\end{aligned}\quad (4.1)$$

Since the DoE states that E_{bind} must be in the range of $0.2 - 0.8 \text{ eV}$, if the values for ΔE are larger than $\sim 1 \text{ eV}$ then the binding energy of hydrogen necessary to stabilise the material would mean that the material would fall outside of the DoE targets.

By making this approximation, the lengthy process of finding the global energy minimum for the hydrogenated GICs can be ignored. The modelling of the hydrogenated GICs no longer needs to be considered under this approximation that means the difficulty of considering H_2 orientation and absorption sites can be ignored. This being said, the interesting cases of hydrogenating RbC_n , CsC_n and KC_n were considered explicitly. The lowest energy configurations from the previous chapter in §3.3 were taken as starting points for energy minima searches and the final H_2 configurations corresponding to the global minima of these GICs differed little from the starting configurations. As we shown in the previous chapter, the absorption of molecular hydrogen was considered only.

The plan for this chapter is to investigate the reactants in the decomposition reaction,



by considering the energetics of each component. First the binding of the metal in each GIC will be studied in §2. This will include the relaxed structures and formation energies from free atoms. There will be a discussion as to the stability of the GICs themselves against decomposition into graphite and the pure metal. Energetic reasons will be given as to the viability of making some alkali and alkaline-earth GICs. The following section, 3, will look at the binding of hydrogen in the GICs. The effects of metal density within the GIC, characterised by the $M : C$ ratio, and the charge on the intercalated metal atom upon hydrogen absorption will be discussed. Values for the hydrogen binding energies will only be considered for the alkali metal GICs; following the work on CaC_n from the previous chapter alkaline earth metal GICs are likely to be excessively unstable. §4 will investigate the binding mechanisms of the H_2 molecule to free metal ions. This will elucidate the mechanisms for binding of an H_2 molecule to a partially charged

2 The binding of metal intercalants in GICs

metal intercalant in a GIC. The DFT binding energies of metal-hydrogen complexes will be compared with highly accurate quantum chemistry (CCSD(T)) binding energies in order that the DFT predictions be benchmarked. §5 will give details as to the work performed on modelling the metal hydrides. Structures and formation energies will be compared with experiment and Madelung-type patterns will be drawn from the results. Finally, §6 will discuss the importance of these calculations and show patterns for the stability energies, ΔE as one descends the alkali and alkaline earth metal groups. The conclusions to this general survey of hydrogenating alkali and alkaline earth metal GICs will be drawn in this final section.

2 The binding of metal intercalants in GICs

The investigation of metal binding with graphite to form GICs was motivated by the work of the previous chapter, being a major part of the energetics of stability of intercalate compounds under hydrogenation. An intriguing issue lingered from the previous study on hydrogenating the Ca-GICs, some of the metals within the alkali and alkaline earth groups have not been possible to intercalate into graphite. Of particular interest are the GICs of beryllium and magnesium, that do not form GICs. Sodium has proven difficult to intercalate despite having an ionic radius extremely close to that of Ca and a valence charge structure equal to that of Li and K, all three of which intercalate. These reasons gave the driving force to survey the metal binding in the alkali and alkaline earth metal GICs.

The focus of this work is, of course, upon viable hydrogen storage media. As such, not all members of the alkali and alkaline earth metal groups were investigated here. Notably, francium is absent from the discussion, despite belonging to the favourable (as shall be seen) alkali metal group. There would be no way of creating a viable hydrogen storage medium using the element. It is highly radioactive, decaying via beta decay, with the most stable isotope having a half life of just 21 minutes[122]. To add to the problems of using francium, it is vanishingly scarce on Earth, with estimates that there may be as little as 30 g present in the whole of the Earth's crust[123] and the largest laboratory sources reaching just a few hundred thousand atoms[124]. At the end of the alkaline earth metal series, radium has also been omitted from this discussion. Radium has a long and famous history with its discovery by Curie et al. [125] in 1898. It is not present here due to its high radioactivity making it unsuitable as a storage medium,

2 The binding of metal intercalants in GICs

				atomic # atomic mass	Symbol	e^- config.	(# of e^-)
1 1.008	H						
3 6.941	Li	$s1p0$	(1)	4 9.012	Be	$s2p0$	(4)
11 22.990	Na	$s1p0$	(9)	12 24.305	Mg	$p6s2$	(8)
19 39.098	K	$3s3p4s1d$	(9)	20 40.078	Ca	$(p6^*) s2d0.01$	$(8^*/2)$
37 85.468	Rb	$4s4p5s$	(9)	38 87.62	Sr	$3s3p4s$	(10)
55 132.905	Cs	$5s5p6s$	(9)	56 137.327	Ba	$s2p6s2$	(10)
87 (223)	Fr			88 (226)	Ra		

Table 4.1: The alkali and alkaline earth group metals that are considered in this chapter are highlighted in bold. Electron configurations are given, with number of electrons in parentheses, from the VASP potential files. Note that for Ca, there were two configurations: one for the LDA potential and one for the GGA-PW91 potential. The LDA data are marked with *. For all other elements the details for the LDA and GGA-PW91 potentials are the same.

emitting a spectrum of α , β and γ radiation[126] (the α pathway being the dominant decay mode of Ra-226, and the other decay modes arising from the short lived daughter products).

The section of the periodic table that is considered is shown in table 4.1 in bold. Average atomic weights are given where possible, estimations given in parentheses where they are not. The electron configuration and electron number is given and taken from the potential files used in VASP.

2.1 Relaxing the structures of the alkali and alkaline earth GICs

The structure of these GICs were relaxed in much the same way as for the Ca-GICs in the previous chapter. The structures were modelled in the hexagonal α -stacked $P6/mmm$ phase for all three stoichiometries, i.e. MC_6 , MC_8 and MC_{14} . While it is known that some of the more diffuse GICs, notably that of CsC_{24} and KC_{24} , are stage-II compounds[4] we have noted previously that this makes little difference to the energetic study in these simulations (c.f. table 3.4 in §3.2.1). The formation energy of the GICs in this section is defined as the energy change per metal atom when a metal atom from the gas phase is inserted between the sheets of graphite, then the system allowed to relax.

The GICs of MC_n with $n = 6, 8$ and 14 were modelled in VASP with a basis of plane waves in the PAW scheme using a cut-off of 800 eV. A Monkhorst-Pack k -point grid of

Simulation detail	Value
Calculation type	DFT
<i>xc</i> -functionals	LDA and GGA-PW91
Program	VASP
Basis	Plane wave within PAW scheme
Basis cut-off	800 eV
<i>k</i> -point grid	$8 \times 8 \times 8$
Atomic basis	Fixed

Table 4.2: A summary of the DFT simulation details used for modelling MC_n with $\text{M}=\text{Li}, \text{Be}, \text{Na}, \text{Mg}, \text{K}, \text{Ca}, \text{Rb}, \text{Sr}, \text{Cs}$ and Ba ; and $n = 6, 8$ and 14 .

$8 \times 8 \times 8$ was used for all GIC calculations and together with the choice of PW cut-off resulted in unit cell energies being converged to within 0.1 eV per unit cell (better than 20 meV per C atom). Both the LDA and GGA-PW91 *xc*-functionals were used and the details of the included orbitals and valence electrons are given in table 4.1. As with the Ca-GICs in §3.2 the atomic basis was fixed as the unit cell was relaxed in-the-plane to give an equilibrium *a*-value while the *c*-axis was held fixed at a reasonable value; the cell was then relaxed in the *c*-axis using the fixed equilibrium in-plane *a*-value. The in-plane value was checked to ensure no change had occurred during the *c*-axis relaxation. In the final configuration the atomic basis was allowed to change and no difference was observed from the fixed-basis calculation. A summary of the simulation details is given in table 4.2.

The C-C in-plane bond length, *a*, of every GIC changed little from that of graphite, with slight increases in all cases of no more than 2 % with LDA and GGA-PW91.

Our results show that in the alkali GICs the typical magnitude of $E_{\text{form}}(\text{MC}_n)$ is between 1 and 2 eV, with GGA-PW91 tending to underbind the MC_6 and MC_8 systems but overbinding the MC_{14} GICs relative to LDA. In general $E_{\text{form}}(\text{MC}_n)$ tends to get stronger (more negative) with decreasing metal concentration for GGA-PW91 and for the heavier alkali GICs (K, Rb, Cs) with LDA. In the alkaline earth GICs $E_{\text{form}}(\text{MC}_n)$ is very small for Be and Mg (in agreement with calculations performed by Yoon et al. [3] on $\text{Be}-\text{C}_{60}$ and $\text{Mg}-\text{C}_{60}$), but much larger (in the range 2-3 eV) for Ca, Sr and Ba with GGA-PW91 tending to underbind relative to LDA for these GICs. For the alkaline-earth GICs $|E_{\text{form}}(\text{MC}_n)|$ always decreases with lower $M : C$ ratio with both LDA and

2 The binding of metal intercalants in GICs

GGA-PW91 (with the exception of the two unbound Mg and Be GICs in GGA-PW91).

It is interesting to compare the computed energies with the cohesive energies of the pure solid metals relative to free atoms, $E_{\text{form}}(\text{M}_{\text{gas}})$, and we include experimental values of these cohesive energies in the table (4.3). It is immediately clear that the very weak binding of Be and Mg in the GIC is much too small to stabilise the GIC against decomposition into graphite and the solid metal. For Ca, Sr and Ba $E_{\text{form}}(\text{MC}_n)$ is considerably larger than necessary to stabilise it. All the alkali GICs are stable, except for Na, which borders stability depending upon the stoichiometry. This appears to explain why the Na-GIC is very hard to make in anything but low Na concentrations[80] or at normal concentrations under high pressure[81–84].

The variation of E_{form} along both the alkali and alkaline earth series is not straightforward. On going from Li to Na, $|E_{\text{form}}|$ decreases strongly, but then increases again with K and remains fairly constant after that. In the alkaline earth series, after the large jump from Mg to Ca, $|E_{\text{form}}|$ remains almost constant in the rest of the series. These features will be related to the electronic states later. In general, the dependence of E_{form} on stoichiometry is fairly weak, but the GGA-PW91 values for the alkali GICs are not consistent with this rule, showing a significant increase with $M : C$ ratio in the alkali metals.

The c lattice parameter is considerably greater than that of pure graphite in all cases except Li. The very large values of c for Be and Mg are clearly related to their very small E_{form} values. The GGA-PW91 results for these two GICs are marked with † to indicate that they exhibit no equilibrium c -axis separation; the total energy decreased monotonically with increasing sheet separation. Equilibrium c -axis values are given in table 4.4. Agreement with experiment[96] is very reasonable with KC_{24} exhibiting 5.4 Å c -axis in experiment, CsC_{24} showing 5.9 Å in experiment. Experiments performed by Lovell et al. [87] on KC_8 report a c -axis separation of 5.35 Å in excellent agreement with GGA-PW91 results.

The formation energy per formula unit ($E_{\text{form}}(\text{MC}_n)$) of the relaxed structures of all the alkali and alkaline earth GICs in three stoichiometries are given in table 4.3. The formation energy is given from spin polarised free metal atoms and graphite for each of the GICs in each of the stoichiometries using both LDA and GGA-PW91. This amounts to the energy needed to form one unit cell of the GIC from the free metal atom and pure

graphite. For reference, the experimental formation energy of the neutral atomic gas, $E_{\text{form}}(\text{M}_{\text{gas}})$, is given[127].

2.2 Density of states and Bader analysis

The large jump in binding between the unbound Mg-GICs and the strongly bound Ca-GICs can be understood by the presence of Ca *d*-orbitals shifting below the Fermi Energy and broadening as they hybridise with C orbitals; a mechanism that is absent in Mg-GICs. All the GICs below the *d*-orbital boundary (K, Rb, Cs, Ca, Sr and Ba) show evidence of the metal *d*-orbitals falling below the Fermi level and thus becoming involved in binding of the metal in the GIC. This is shown in figure 4.1 where the total density of states (DOS) is shown for CaC_6 with the contribution from the Ca *d*-orbitals. The calculated total DOS for CaC_6 agrees well with that calculated by Machado [128]. This shift in metal *d*-orbitals below the Fermi level and the subsequent broadening is also seen in Ca and Sr absorption onto C_{60} [3] where this donation/back-donation mechanism has been noted (the metal donates its *s* electrons to the fullerene which then back-donates to the low lying, shifted, empty metal *d* orbitals). Deng et al. [129] also note the importance of Ca *d*-orbitals in the binding of CaC_6 .

Bader analysis was performed upon the GICs to find the partial charges of the intercalant atoms. In Bader analysis the charge density of the material is divided into regions surrounded by zero-flux surfaces, i.e. surfaces obeying $\nabla\rho(r_s) \cdot \vec{n}(r_s) = 0$ where r_s is a point on the surface $S(r_s)$, $\vec{n}(r_s)$ is the unit vector normal to the surface. Each volume contained with each surface often surrounds an atomic nucleus (this was the case in all cases presented here). The charge inside this volume can then be integrated to get the total charge attributable to each atom.

We can see from table 4.5 that that the alkali GICs donate between 0.6 and 0.9 electrons to the graphite sheets, giving the C atoms an average charge of -0.06 and -0.1 depending upon stoichiometry. In all cases as the $M : C$ ratio increases (the GIC becomes less dense) the charge on the metal atom increases while the average charge on a C atom decreases. The alkaline earth GICs donate between 1.0 and 1.5 electrons to the graphite sheets (with the noticeable exception of Be and Mg), noticeably increasing

^aFormation energies taken from JANAF Thermochemical Tables[127] at 0K and are formation energies relative to free atoms in the gas phase.

Compound	$M_{\text{gas}}^{\text{a}}$	LDA			GGA-PW91		
		MC ₆	MC ₈	MC ₁₄	MC ₆	MC ₈	MC ₁₄
Li	1.635	-2.190	-2.178	-2.110	-1.806	-1.867	-1.995
Na	1.115	-1.248	-1.214	-1.173	-1.031	-1.100	-1.398
K	0.932	-1.520	-1.559	-1.562	-1.166	-1.327	-1.733
Rb	0.852	-1.444	-1.516	-1.526	-1.075	-1.255	-1.697
Cs	0.809	-1.585	-1.695	-1.683	-1.124	-1.381	-1.806
Be	3.314	-0.315	-0.154	0.063	-0.311 [†]	-0.308 [†]	-0.415 [†]
Mg	1.512	-0.491	-0.221	0.071	-0.452 [†]	-0.329 [†]	-0.678 [†]
Ca	1.838	-3.137	-3.045	-2.683	-2.302	-2.313	-2.264
Sr	1.704	-2.846	-2.697	-2.036	-2.118	-2.089	-2.040
Ba	1.863	-3.431	-3.314	-2.841	-2.667	-2.655	-2.576

Table 4.3: Formation energies of the alkali and alkaline earth GICs, $E_{\text{form}}(\text{MC}_n)$ (eV unit) from free spin-polarised metal atoms and graphite. Compounds marked with [†] exhibited no equilibrium *c*-axis value with GGA-PW91 and the quoted E_{form} is the formation energy at $c = 8.00 \text{ \AA}$. Values in the table can be compared with values for the formation energy of the pure solid metals ($E_{\text{form}}(M_{\text{gas}})$) from free atoms. Where values for E_{form} for the metal gas has a larger magnitude than values for the GICs, the GIC is likely unstable against decomposition into graphite and the pure metal.

2 The binding of metal intercalants in GICs

Compound	LDA			GGA-PW91		
	MC ₆	MC ₈	MC ₁₄	MC ₆	MC ₈	MC ₁₄
Li	3.50	3.55	3.55	3.80	3.80	3.90
Na	4.60	4.40	4.45	4.80	4.65	4.75
K	5.20	5.15	5.20	5.40	5.40	5.50
Rb	5.50	5.50	5.55	5.80	5.85	5.80
Cs	5.80	5.90	5.90	6.10	6.10	6.20
Be	5.90	6.10	6.00	8.00 [†]	8.00 [†]	8.00 [†]
Mg	6.50	6.20	6.60	8.00 [†]	8.00 [†]	8.00 [†]
Ca	4.34	4.31	4.28	4.50	4.45	4.45
Sr	4.80	4.75	4.35	5.00	4.90	4.40
Ba	5.30	5.20	5.10	5.40	5.30	5.30

Table 4.4: Equilibrium c -axis values for the MC _{n} GICs with $n = 6, 8$ and 14 with both the LDA and the GGA-PW91 xc -functionals. Compounds marked with \dagger exhibited no equilibrium c -axis value with GGA-PW91.

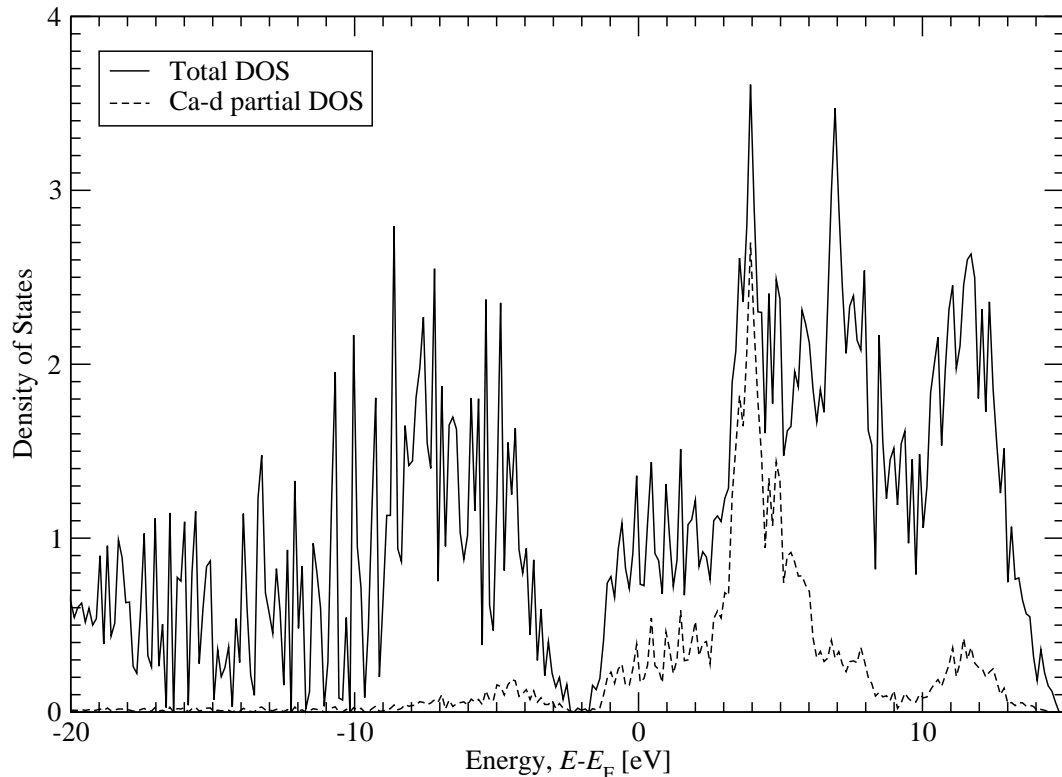


Figure 4.1: The total density of states (DOS) for CaC₆ (solid line) and the contribution of the Ca d -orbitals (dotted line) for GGA-PW91 calculation.

3 Hydrogenating GICs

the electrostatic bonding between the metal and the graphite sheet. The average charge of a C atom in the AE-GICs is generally between -0.1 and -0.2 electrons, markedly higher than in the alkali GICs. The Be and Mg GICs appear to break the pattern of the other alkaline earth GICs by donating between 0.1 and 0.3 electrons with LDA and less than 0.1 with GGA-PW91. This clearly correlates with the weak binding of these GICs, showing that charge transfer is an important mechanism in GIC binding. The values for the charge on the metal intercalate in LiC_6 and MC_8 with $\text{M}=\text{Li}, \text{Na}, \text{K}, \text{Rb}$ and Cs agree well with those calculated by Hartwigsen et al. [130]. We notice that the LDA and GGA-PW91 values for the donated charge by the metal atom are very similar with LDA values tending to be slightly lower.

3 Hydrogenating GICs

The binding of H_2 molecules was investigated within a select few of the stage-I alkali GICs: KC_{14} , RbC_n and CsC_n in the three stoichiometries of $n = 6, 8$, and 14 . The lighter alkali GICs of LiC_n were ignored for their known instability upon hydrogenation as noted in chapter 3 and the Na-GICs excluded due to the extreme difficulty in their synthesis; while all alkali earth GICs were not considered due to the overwhelming instability found in Ca-GICs in chapter 3. Within the stoichiometries examined in this chapter (MC_n with $n = 6, 8$, and 14) only two absorption environments exist: (1) below a graphite hexagon containing an intercalant and (2) below a graphite hexagon without an intercalant, as shown in figure 4.2. Following the experimental observation that the H_2 molecules preferentially absorb with the H_2 bond axis parallel to the GIC c -axis in stage-II KC_{24} [94] and that the same was found in Ca-GICs[117], only this orientation was considered for these GICs. While it is known that hydrogen preferentially absorbs atomically in the high concentration GICs such as KC_8 [87] and the same was predicted in CaC_6 [1, 117] only molecular absorption was considered here for all GICs, as confirmed by experiments upon KC_{24} , CsC_{24} and RbC_{24} [96]. The complicated structures formed by atomic absorption in KC_8 and the decomposition of CaC_6 prohibited their accurate modelling. Stage-II GICs were not considered as no hydrogen absorption has been observed in the empty galleries of high stage GICs[131], typified by no absorption seen in pure graphite[132].

Absorption sites were investigated by placing an H_2 molecule vertically (with its bond axis aligned to the GIC c -axis) in the centre of one of the equivalent empty (green

Compound	LDA						GGA-PW91					
	MC ₆		MC ₈		MC ₁₄		MC ₆		MC ₈		MC ₁₄	
	$Q(M)$	$\overline{Q(C)}$	$Q(M)$	$\overline{Q(C)}$	$Q(M)$	$\overline{Q(C)}$	$Q(M)$	$\overline{Q(C)}$	$Q(M)$	$\overline{Q(C)}$	$Q(M)$	$\overline{Q(C)}$
Li	+0.79	-0.13	+0.80	-0.10	+0.80	-0.06	+0.84	-0.14	+0.84	-0.10	+0.85	-0.06
Na	+0.78	-0.13	+0.80	-0.10	+0.82	-0.06	+0.80	-0.13	+0.84	-0.10	+0.85	-0.06
K	+0.72	-0.12	+0.77	-0.10	+0.83	-0.06	+0.73	-0.12	+0.82	-0.10	+0.87	-0.06
Rb	+0.66	-0.11	+0.74	-0.09	+0.85	-0.06	+0.66	-0.11	+0.64	-0.08	+0.87	-0.06
Cs	+0.64	-0.11	+0.68	-0.08	+0.85	-0.06	+0.63	-0.11	+0.70	-0.09	+0.87	-0.06
Be	+0.14	-0.02	+0.10	-0.01	+0.11	-0.01	+0.02	± 0.00	+0.03	± 0.00	+0.03	± 0.00
Mg	+0.23	-0.04	+0.34	-0.04	+0.20	-0.01	+0.10	-0.02	+0.06	-0.01	+0.07	-0.01
Ca	+1.27	-0.21	+1.33	-0.17	+1.36	-0.10	+1.23	-0.21	+1.31	-0.16	+1.34	-0.10
Sr	+1.14	-0.19	+1.32	-0.16	+1.38	-0.10	+1.12	-0.19	+1.35	-0.17	+1.42	-0.10
Ba	+1.03	-0.17	+1.17	-0.15	+1.39	-0.10	+0.92	-0.15	+1.18	-0.15	+1.44	-0.10

Table 4.5: Results of Bader analysis on MC_n structure with $n = 6, 8$ and 14 . $Q(M)$ represents the charge on the intercalate metal and $\overline{Q(C)}$ represents the average charge on a carbon atom from the graphite layer. All charges are given in units of the fundamental charge, e .

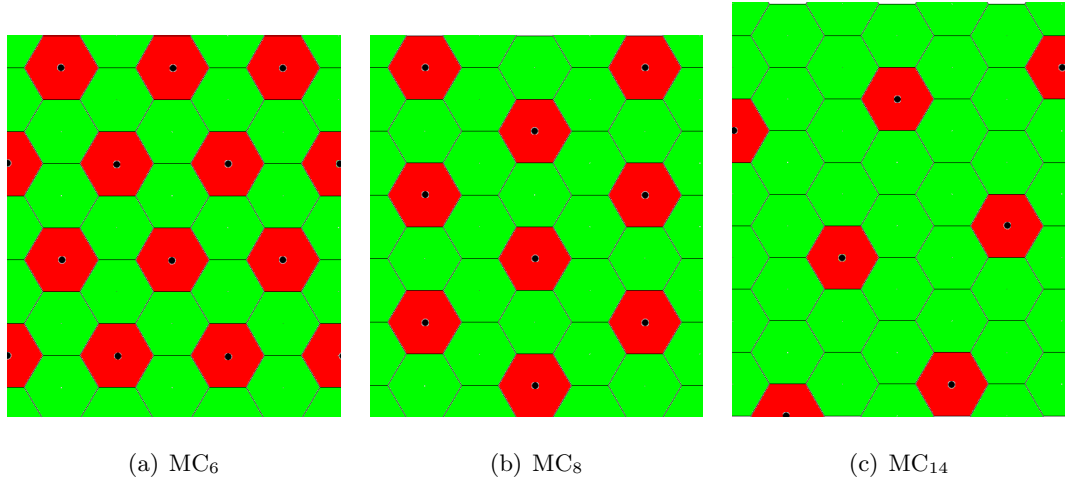


Figure 4.2: The symmetry of the chosen stoichiometries leads to only two types of absorption site: red hexagons contain an intercalant, green are empty. Shown for the (a) MC₆, (b) MC₈ and (c) MC₁₄ stoichiometries.

in 4.2) hexagons in each of the stage-I GICs leading to configuration of one H₂ molecule per metal intercalant. The H₂ bond was held fixed at its equilibrium value of 0.74 Å while the GIC was relaxed in-plane to find the equilibrium *a*-value while the *c*-axis was held fixed at an appropriate value; the in-plane lattice vectors were then held fixed using the equilibrium *a* value while the *c*-axis was relaxed. Again, after the final relaxation the in-plane lattice vectors were checked to see if any change had taken place and none had in all cases. Once the unit cell had been equilibrated the GIC basis was allowed to vary and no change from the symmetric configuration was observed. The H₂ molecule was then relaxed and little change in its position was seen; it remained centred in the *c*-axis of the GIC nearly centred below a graphite hexagon. The H₂ bond length was observed to expand by ∼3 % in the less dense MC₁₄ GICs.

Results from the structural relaxations of the hydrogenated GICs showed that C-C in-plane bonds varied little upon hydrogenation increasing less than 1 % for high metal density GICs and this bond stretch decreasing with decreasing metal content, with MC₁₄ GICs showing no change in *a*-value with either LDA or GGA-PW91. Changes in the *c*-axis upon hydrogenation were not as systematic, although all changes were generally less than 4.5 %. Experiments show that the *c*-axis of KC₂₄ expands to 5.6 Å upon hydrogenation[96], in excellent agreement with GGA-PW91 results. Little or no *c*-axis expansion was seen in RbC₂₄ or CsC₂₄ compounds in experiment[96], with CsC₂₄ remaining at the unhydrogenated separation of 5.9 Å in excellent agreement with LDA.

3 Hydrogenating GICs

The equilibrium c -axis values for the hydrogenated GICs, along with the relative change with respect to the unhydrogenated GIC ($\Delta c = c(\text{H}_2 + \text{MC}_n)/c(\text{MC}_n)$, with $c(\text{MC}_n)$ values taken from table 4.4) are shown in table 4.6.

DFT calculations were performed in VASP and used the same format as for the unhydrogenated material (see table 4.2, page 105 for details).

The binding energy for H_2 in the GIC (E_{bind}) was calculated by subtracting the energy of an isolated H_2 ($E(\text{H}_2)$) and the relaxed GIC ($E(\text{MC}_n)$) from the energy of the hydrogenated GIC ($E(\text{H}_2 + \text{MC}_n)$), giving a generalised form of equation 3.3

$$E_{\text{bind}} = E(\text{H}_2 + \text{MC}_n) - [E(\text{H}_2) + E(\text{MC}_n)], \quad (4.3)$$

resulting in a negative binding energy for favourable binding. The calculated binding energies for the KC_{14} , RbC_n and CsC_n GICs with $n = 6, 8$ and 14 are compared with experimental results for the isosteric heats of absorption from Purewal [96] for the stage-II compounds MC_{24} in table 4.7.

We can see that the calculated values bracket the experimental values for E_{bind} , with the exception of the K-GIC. The LDA value for KC_{14} is extremely close to the experimental value for stage-II KC_{24} , with GGA-PW91 overestimating the binding by ~ 0.3 eV. For RbC_{14} and CsC_{14} the two calculated values bracket the experimental value for the stage-II RbC_{24} and CsC_{24} GICs, with the GGA-PW91 value underestimating E_{bind} by 0.09 eV ($\sim 60\%$) and LDA over estimating by 0.1 eV ($\sim 75\%$) in both cases.

It also clear that from the table that E_{bind} gets stronger (more negative) as the metal concentration is lowered with the Cs-GICs crossing the boundary of unfavourable absorption to favourable absorption at an $M : C$ ratio of $1 : 14$. This follows from the increasing negativity of the intercalant atom as the metal concentration is lowered, clearly showing that there is a stronger absorption the more negative the intercalant. Although this does not explain the pattern of H_2 binding in its entirety as in the MC_{14} stoichiometry all these GICs have the same intercalant charge while having varying H_2 binding energies. Potentially another factor affecting H_2 absorption is pore size within these GICs. The H_2 molecule preferentially absorbs into GICs that offer enough space for the molecule (the MC_6 and MC_8 absorption sites are all bounded on two sides of the hexagon by an intercalant occupied hexagon, only the MC_{14} absorption sites offer more space, see figure 4.2). It can also be seen that the RbC_{14} and CsC_{14} GICs have values for E_{bind} that lie near the DoE target range (0.2-0.8 eV per H unit).

Compound	LDA						GGA-PW91					
	MC ₆		MC ₈		MC ₁₄		MC ₆		MC ₈		MC ₁₄	
	<i>c</i> [Å]	Δc [%]	<i>c</i> [Å]	Δc [%]	<i>c</i> [Å]	Δc [%]	<i>c</i> [Å]	Δc [%]	<i>c</i> [Å]	Δc [%]	<i>c</i> [Å]	Δc [%]
K	—	—	—	—	5.2	± 0.0	—	—	—	—	5.7	3.6
Rb	5.7	3.6	5.5	± 0.0	5.8	4.5	5.8	± 0.0	5.7	-2.6	6.0	3.4
Cs	5.6	-3.4	5.8	-1.7	5.9	± 0.0	5.9	-3.3	5.9	-3.3	6.3	1.6

Table 4.6: Equilibrium *c*-axis values for the KC₁₄, RbC_{*n*} and CsC_{*n*} (*n* = 6, 8 and 14) hydrogenated GICs and their relative change (Δc) compared with the unhydrogenated GIC.

4 The binding of H₂ to metals

Compound	LDA			GGA-PW91			Experiment[96]	
	MC ₆	MC ₈	MC ₁₄	MC ₆	MC ₈	MC ₁₄	Compound	
K	–	–	–0.10	–	–	–0.37	KC ₂₄	–0.095
Rb	+0.05	–0.08	–0.23	+0.41	+0.25	–0.05	RbC ₂₄	–0.131
Cs	+0.40	+0.29	–0.27	+0.83	+0.64	–0.06	CsC ₂₄	–0.154

Table 4.7: Binding energies, E_{bind} , of molecular hydrogen in KC₁₄, RbC_n and CsC_n GICs with $n = 6, 8, 14$. Negative energies represent favourable binding.

4 The binding of H₂ to metals

Calculations were performed on the interaction between H₂ and isolated charged metal atoms to benchmark the results for H₂ binding in GICs, alongside calculations for two H atoms interacting with charged metal ions. Both quantum chemistry (Hartreee-Fock and coupled cluster methods) and DFT were used to calculate binding curves for 2H and H₂ in two orientations: transverse (with the H₂ bond axis perpendicular to the H₂-M line) and longitudinal (with the H₂ bond axis parallel to the H₂-M line), both shown in figure 4.3. The isolated metal atoms were charged +1 for all alkali and alkaline earth metals and +2 for the alkaline earth metals. No appreciable interaction was seen between the H₂ molecule and neutral metals atoms.

Basis set superposition error (BSSE) is an error that occurs when incomplete basis sets are used for two elements of a quantum chemical calculation using localised basis sets (such as the Gaussian-type orbitals used here). As the two atoms approach the two sets of orbitals for each overlap, so each atom “borrows” orbitals from the other increasing the size of its own basis set. This increase in the basis set causes a fictitious reduction in the energy.

This type of error is important in calculations such as those presented here as energies are being compared for atoms at large and small separations. This error would be eliminated using complete (infinite) basis sets but can be managed using finite basis sets. The two main methods of BSSE elimination, the chemical Hamiltonian approach where projections in the Hamiltonian that allow this orbital mixing are removed *a priori* and the counterpoise method which repeats all the calculations using the mixed basis sets (introducing empty orbitals to each atom) and subtracting the energy from the uncorrected energy *a posteriori*, will not be considered necessary as contributions from

4 The binding of H₂ to metals

BSSE will be small. In this work basis set completeness was tested for each calculation by running tests using Dunning's valence triple zeta Gaussian basis sets (VTZ), VQZ basis sets and V5Z basis sets. The interaction energy (difference in the energy of the system at a separation of $r = \infty$ and $r = r_{\min}$) for each basis set was compared and the little change was observed between the two largest basis sets (VQZ and V5Z). This shows that BSSE was not a major contribution to the energetics as fictitious binding due to BSSE would show as a reduction in binding as a larger basis set was used for each atom. Basis set completeness for each system was also tested and the basis sets used were considered near-complete.

For some of the alkali and alkaline earth metals the interaction of atomic hydrogen was investigated: two H atoms were placed either side of the charged metal atom and brought closer from a large distance such that the H atoms remained equidistant from the metal ion. This was done for Be, Mg and Ca for the +1 and +2 charge state of the metal atom. Difficulties in implementing the basis sets in the available version of MOLPRO restricted the study to the lighter elements.



Figure 4.3: The two orientations of H₂ interacting with a metal atom: transverse (right) and longitudinal (left).

MOLPRO[133–146] was used to perform the QC and DFT calculations using augmented valence quadruple zeta (AVQZ) Gaussian basis sets from the MOLPRO library where possible and from the Basis Set Exchange[147, 148] (<https://bse.pnl.gov/bse/portal>) where not. The completeness of the basis sets was tested and AVQZ basis sets resulted in DFT and QC calculations being fully converged.

Molecular H₂ binding to charged metal atoms is likely to be dominated (in the long distance) by charge-quadrupole and charge-induced dipole interactions[103, 149–151]. The neutral H₂ molecule would feel no zero-order change in energy due to the electric field created by the charged metal ion. The first moment of the charge distribution in

4 The binding of H₂ to metals

the H₂ molecule is the quadrupole moment; the charge distribution in the H₂ molecule has no natural dipole moment without the presence of an external electric field. The charge-quadrupole interaction is directly proportional to the field strength by C^{quad} and there exist two components to the quadrupole moment tensor, attributed to orientation of the H₂ bond axis within the electric field: the parallel component ($C_{\parallel}^{\text{quad}}$) and the perpendicular component (C_{\perp}^{quad}). The interaction falls off as $1/r^3$ and is the first dominant moment in the multipole expansion.

The next dominant interaction is caused by the induction of a dipole on the H₂ molecule in the presence of the electric field created by the charged metal ion. In the regime of small electric fields (such as these at long distances) the charge centre of the negative charge cloud (created by the electrons) is displaced from the charge centre of positive charges (the protons) by an amount that is proportional to the strength of the inducing electric field, denoted the dipole polarisability α . Due to the geometry of H₂ we expect the polarisability to be a function of orientation of the H₂ bond axis within the inducing electric field, characterised by two forms of the polarisability: the parallel polarisability (α_{\parallel}) and the perpendicular polarisability (α_{\perp}) with $\alpha_{\parallel} \sim 1.5\alpha_{\perp}$ and both positive. The induced dipole interaction falls away as $1/r^4$ and is the next dominant term in the electrostatic interaction between a charged metal atom and H₂.

This leads to the expression, in atomic coordinates (i.e. r in a_0 , q in e , E in Hartrees), to describe the electrostatic interaction energy (the change in energy, ΔE , due to interaction) of H₂ with a charge, q , at a distance, r , in the limit of a small electric field (e.g. long distances)

$$\Delta E = \frac{C^{\text{quad}} q}{2r^3} - \frac{\alpha q^2}{2r^4}. \quad (4.4)$$

It can be seen that at very long distances the charge-quadrupole interaction will dominate the charge-induction interaction. The components of the quadrupole moment tensor have opposite sign depending upon orientation with $C_{\parallel}^{\text{quad}} > 0$ and $C_{\perp}^{\text{quad}} < 0$. This causes the charge-quadrupole and charge-induction terms to work together to reduce the energy (favourable interaction) in the transverse configuration and work oppositely in the longitudinal configuration.

Polarisabilities and components of the quadrupole moment tensor were calculated using HF and DFT (using LDA and GGA-PW91) using the augmented valence quintuple zeta Dunning Gaussian-type basis set (AV5Z). Calculations for HF contain all the information necessary to calculate these properties of H₂ without requiring the more ac-

4 The binding of H₂ to metals

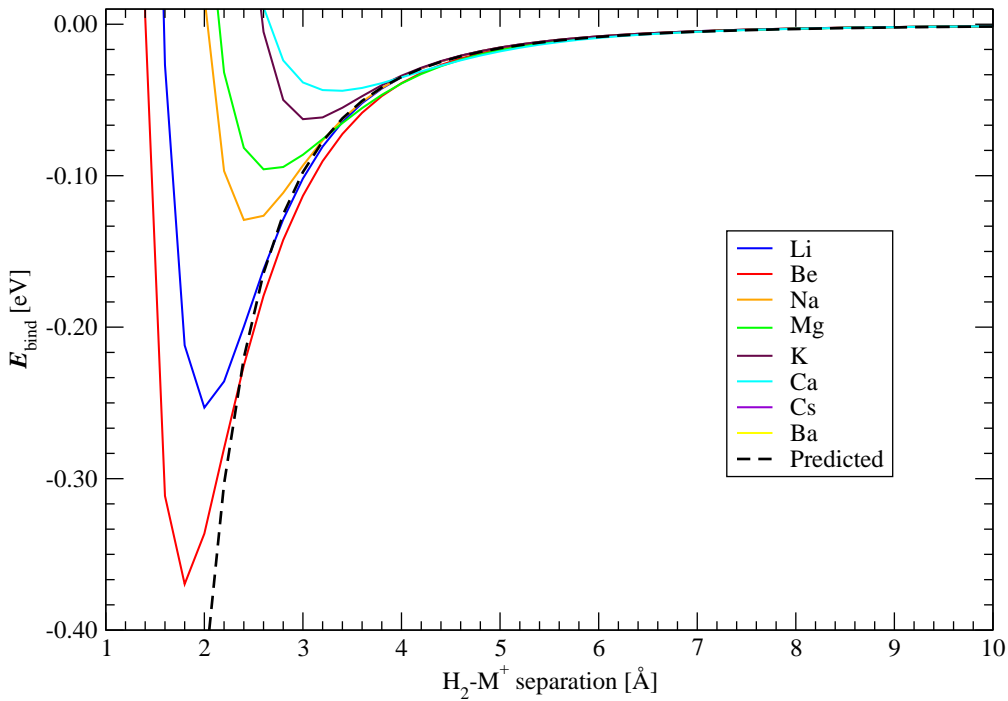
curate CCSD(T) method. Calculations were performed by placing the H₂ molecule in a varying electric field both parallel and perpendicular to the H₂ bond axis to get both polarisabilities. Components of the quadrupole moment tensor were calculated by placing two point charges equidistant from the H₂ centre of mass at a distance of 15 a₀ (7.94 Å) in both the parallel and perpendicular configurations and the value of the point charges varied equally. Data for both were fitted independently to recover the polarisabilities and quadrupole moment components. Values for the quadrupole moment components and the polarisabilities from calculations are given in table 4.8.

Property	DFT			Experimental[12]
	LDA	GGA-PW91	HF	
α_{\parallel}	7.913	6.880	6.440	6.35
α_{\perp}	4.903	4.752	4.590	4.56
$C_{\parallel}^{\text{quad}}$	0.8672	0.8557	0.9831	
C_{\perp}^{quad}	-0.4401	-0.4339	-0.4958	

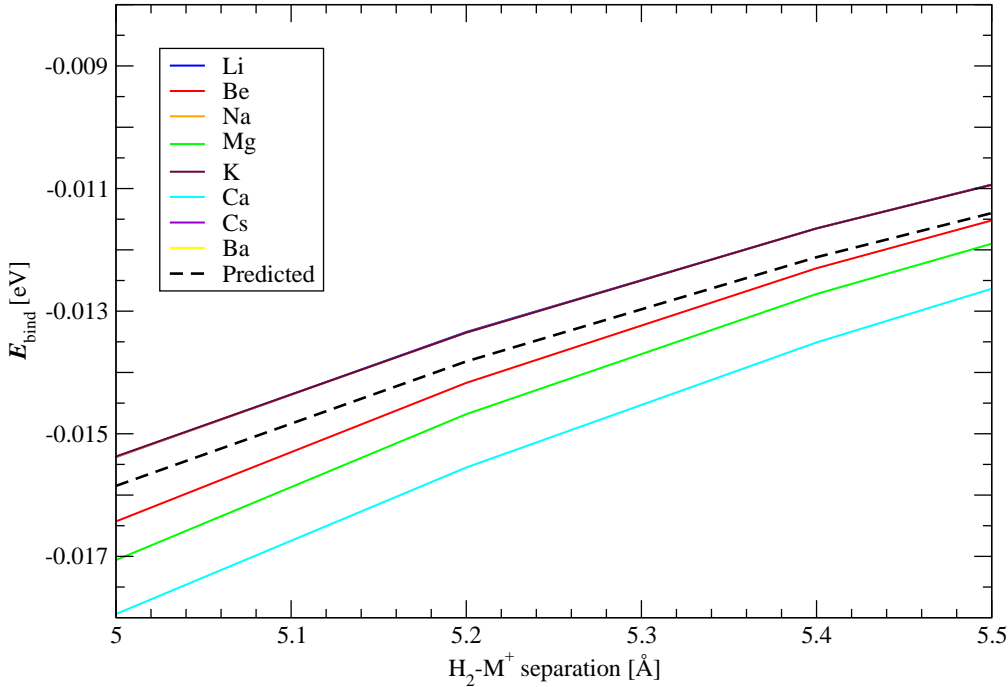
Table 4.8: The calculated values for the parallel and perpendicular (relative to the H₂ bond axis) polarisabilities (α in a₀³ units) and quadrupole moments (C^{quad}) compared with experimental data from the Computational Chemistry Comparison and Benchmark Database[12].

Binding curves for the H₂-M⁺ systems with M=Li-Cs and M=Be-Ba are shown in figures 4.4 showing the transverse orientation and 4.5 showing the longitudinal orientation. Coupled cluster with single, double and perturbative triple excitations (CCSD(T)) offered little improvement over Hartree-Fock (HF) calculations with the former shown for the transverse orientation and the latter for the longitudinal orientation (the difficulty of successfully implementing CCSD(T) at close approach for the heavy metals in the +1 state in the longitudinal configuration means only HF data are reported in this instance). The electrostatic interaction at long distances from equation 4.4 is shown in both graphs as the “predicted”, dashed line. The dominance of the unfavourable charge-quadrupole interaction can be seen in 4.5(a) at distances of $r > 3.5$ Å. The agreement between the purely electrostatic interaction and the simulation results is excellent beyond 5 Å in both the transverse orientation and in the longitudinal configuration.

Example binding curves for the H₂-Be⁺ complex are shown in figure 4.6 using DFT with the LDA, GGA-PW91 and GGA-PBE *xc*-functionals with (a) showing the trans-

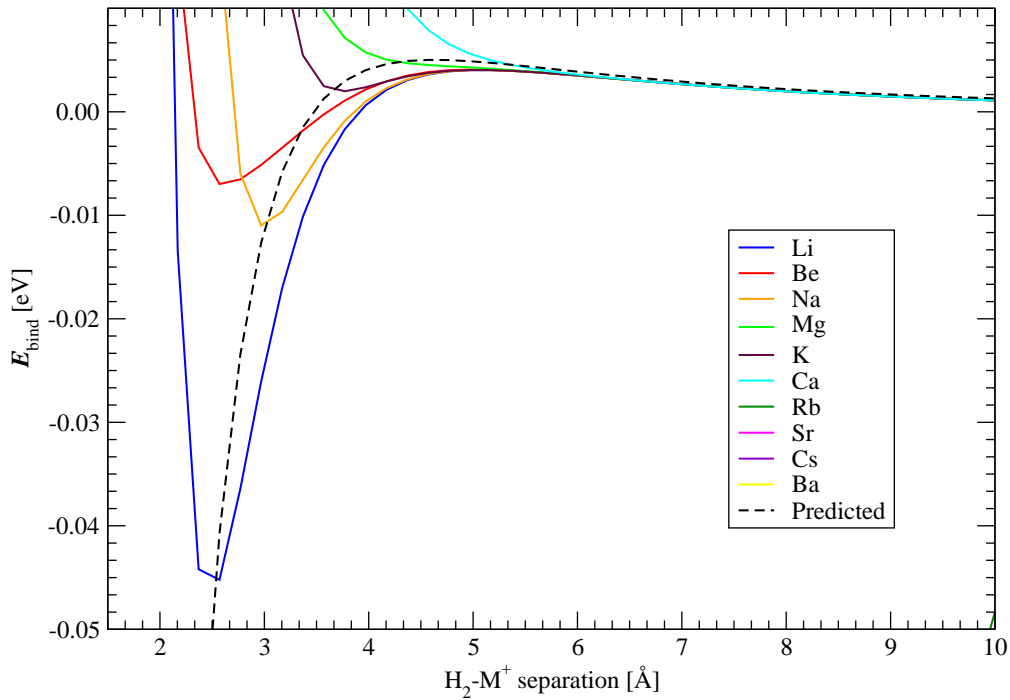


(a) Full binding curve, transverse orientation, CCSD(T).

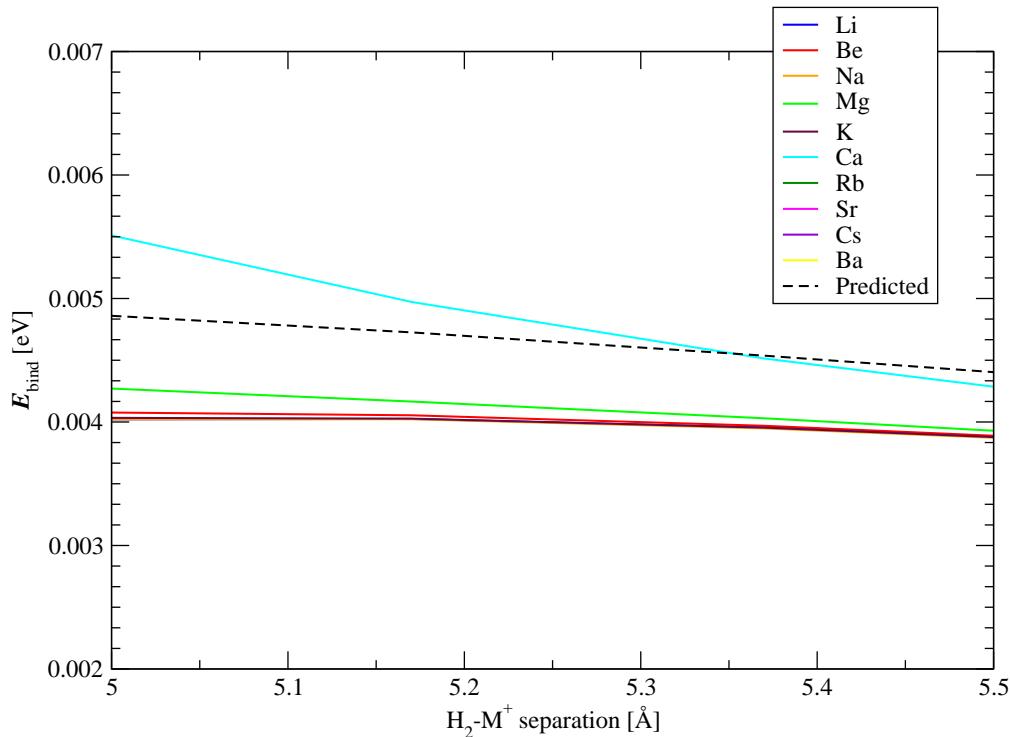


(b) Zoom in of (a), CCSD(T).

Figure 4.4: Binding curves for the H₂-M⁺ complexes in the transverse orientation with CCSD(T) (a) showing the full binding curve and (b) showing agreement beyond 5 Å between electrostatic prediction and calculated results.



(a) Full binding curve, longitudinal orientation, HF.



(b) Zoom in of (a), CCSD(T).

Figure 4.5: Binding curves for the H₂-M⁺ complexes in the longitudinal orientation with HF with (a) showing the full binding curve and (b) showing agreement beyond 5 Å between electrostatic prediction and calculated results.

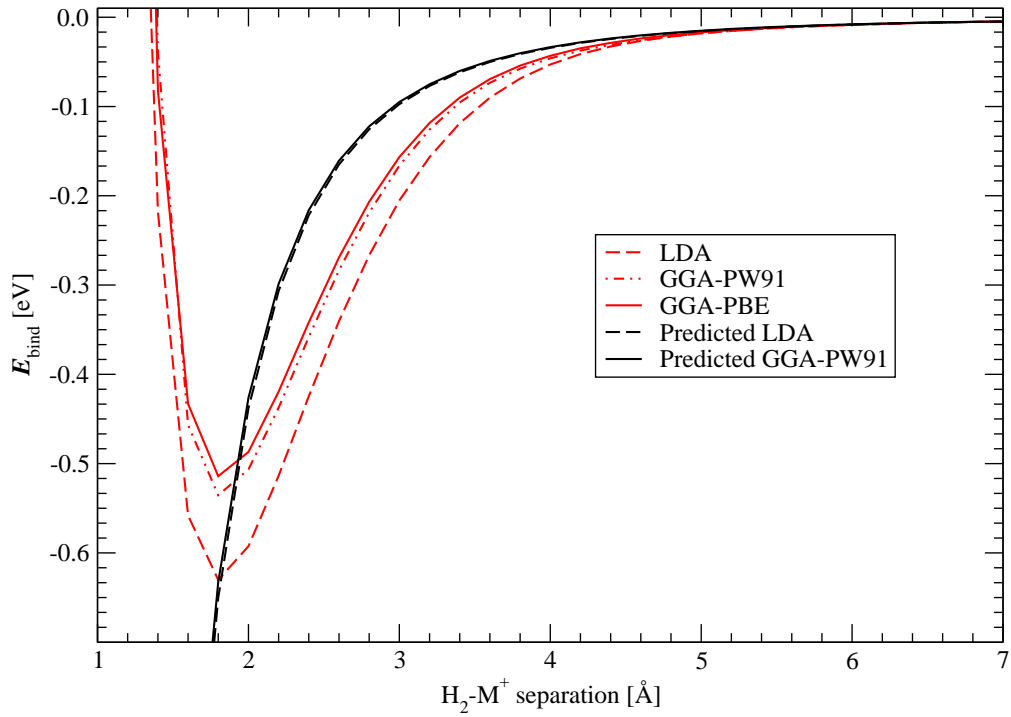
verse configuration and (b) the longitudinal configuration. Electrostatic interaction predictions are given as “predicted” using values for the quadrupole moments and dipole polarisability from LDA and GGA-PW91 functionals. It is clear that LDA tends to over-bind the complexes in all cases with the two GGA functionals producing similar results.

Binding curves for the CCSD(T) interaction energy of the H₂-M²⁺ complexes are shown in figure 4.7. Again the energy change, ΔE , from the electrostatic contribution from the charge-quadrupole and charge-induced dipole interactions is plotted with a dashed line. We can see that the higher electric field created by doubling the charge on the metal atom makes this approximation to the bonding breakdown earlier and only becomes valid after 5 Å in the transverse orientation and 6 Å in the longitudinal configuration. It is evident that the equilibrium binding energies are considerably higher in the H₂-M²⁺ than the H₂-M⁺ systems. The equilibrium separation is noticeably closer in all cases also.

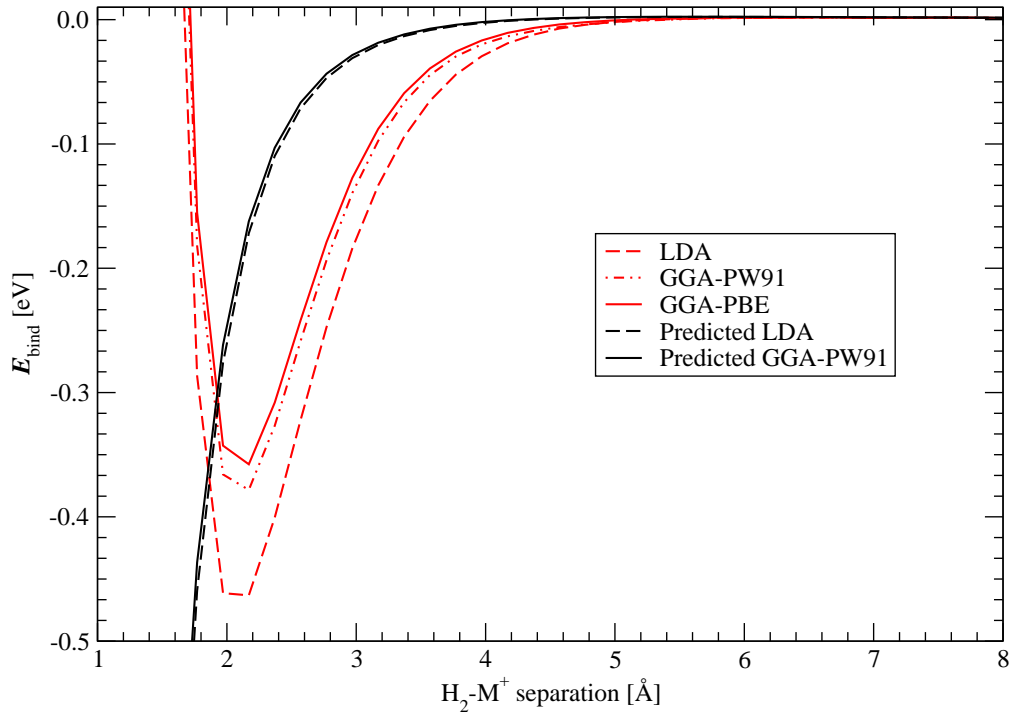
Results from the relaxations of the hydrogen-metal complexes in both charge states (+1 and +2) are given in tables 4.9, 4.10, 4.11 and 4.12 including the equilibrium hydrogen-metal separation r_{\min} (given between the H₂ centre of mass and the metal ion in the longitudinal configuration, tables 4.11 and 4.12) and binding energies of the hydrogen-metal complexes E_{bind} . Table 4.9 gives results for the H₂-alkali metal complexes in the +1 charge state in the transverse orientation; table 4.10 gives results for the same orientation for the H₂-alkaline earth metal complexes in the +1 and +2 charge states. Tables 4.11 and 4.12 give the results for the H₂-alkali metal and H₂-alkaline earth metal complexes in the longitudinal configuration (the latter given for both charge states).

Calculated results for M*-H₂ binding in the transverse configuration with M* = Li⁺, Na⁺, and Mg²⁺ using HF and CCSD(T) with the correlation consistent polarised valence triple zeta (cc-pVTZ) basis set from Lochan and Head-Gordon [102] agree well with the findings in tables 4.9 and 4.10. Lochan and Head-Gordon [102] gives HF E_{bind} (CCSD(T) in parentheses) to be 0.248 eV (0.249 eV), 0.130 eV (0.133 eV) and 0.937 eV (0.957 eV) respectively for M* = Li⁺, Na⁺, and Mg²⁺. Equilibrium separations, r_{\min} , are given as 2.089 Å, 2.471 Å and 2.034 Å respectively. These values are in excellent agreement with those calculated here.

Calculated MP4 results from Barbatti et al. [152] using the 6 – 311G (d,p) basis sets

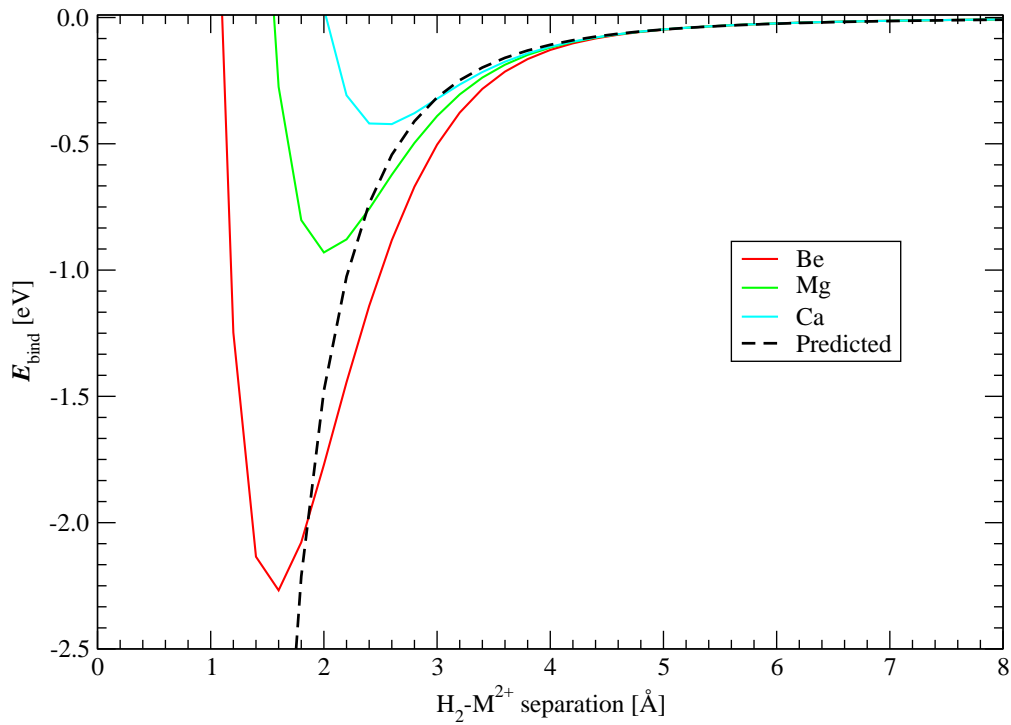


(a) Transverse orientation.

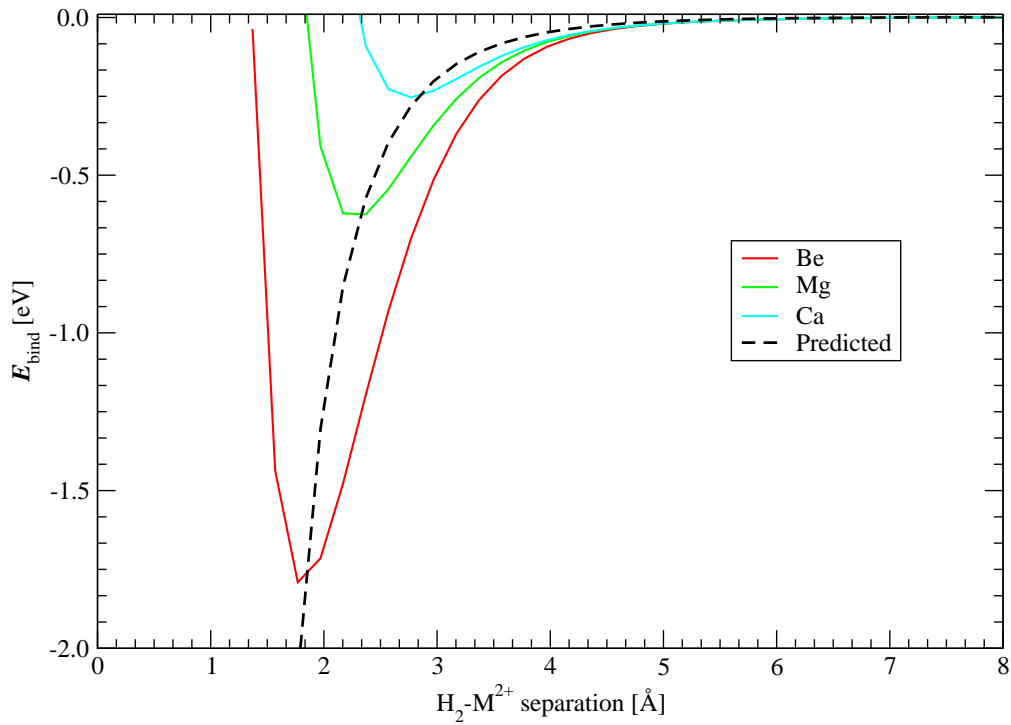


(b) Longitudinal orientation.

Figure 4.6: Binding curves for the H₂-Be⁺ complex in the (a) transverse and (b) longitudinal configurations. The electrostatic, “predicted”, curves follow equation 4.4 with C^{quad} and α parameters calculated from LDA and GGA-PW91 calculations.



(a) Transverse orientation, CCSD(T).



(b) Longitudinal orientation, CCSD(T).

Figure 4.7: Binding curves for the H₂-M²⁺ complexes in the (a) transverse orientation (CCSD(T) binding energies) and (b) longitudinal orientation (CCSD(T) binding energies).

4 The binding of H₂ to metals

for M* = Li⁺, Na⁺ and K⁺ also agree well with values from table 4.9. E_{bind} values are given as 0.257 eV, 0.129 eV and 0.051 eV respectively, agreeing well with results presented here.

We can see from table 4.9 that both QC methods give very similar E_{bind} and identical r_{\min} , showing that CCSD(T) offers no more information about the energetics. DFT values always over-bind, with LDA over-binding the most and the two GGAs offering similar results, also seen from the shorter r_{\min} for DFT-LDA, relative to the QC methods. Errors are typically 0.3 – 0.5 eV between DFT GGA and CCSD(T). Large differences exist between the binding energy of H₂ with K, Rb and Cs in the transverse orientation in the +1 state and the binding energies of H₂ in the diffuse GICs made with these atoms seen in table 4.7. The stronger binding seen in the +1 complexes is clearly related to the higher charge, the partial charge of the intercalant being markedly less than +1.

For the alkaline-earth metals seen in table 4.10 it is noticeable that the HF results consistently under-bind relative to CCSD(T). DFT results show large differences from CCSD(T) for the +1 charge state, always over-binding with LDA showing the strongest binding. Again, r_{\min} values show this tendency of LDA to over-bind the systems. DFT errors for E_{bind} differ by as much as 0.2 eV for Be while getting much closer to CCSD(T) values for Mg and Ca. For the +2 systems DFT-GGA and CCSD(T) report similar values for Mg and Ca showing that DFT appears to operate more effectively for the systems stripped of valence electrons.

In the longitudinal configuration for the alkali metal complexes (table 4.11) it is much the same pattern as before: DFT over-binds relative to QC results (with HF and CCSD(T) reporting similar values for E_{bind}) with DFT-LDA over-binding more than DFT-GGA. DFT still exhibits large errors relative to CCSD(T).

In table 4.12 is it clear that DFT is over-binding systems considerably, sometimes producing binding when none is observed with CCSD(T). Errors as large as 0.2 eV can be seen even though values for r_{\min} match closely between QC and DFT. Clearly DFT struggles to deal with these systems when only one valence electron is present on the metal atom.

Table 4.13 shows the results of two individual H atoms binding to an alkaline earth metal ion in either the +1 or +2 charge state. Binding energies between atomic hydrogen and these metal species (Be, Mg and Ca) are appreciably higher than in the molecular cases but conversely to the molecular case increasing the charge appears not to increase

Atom	Charge	E_{bind} eV						r_{min} Å					
		QC		DFT				QC		DFT			
		HF	CCSD(T)	LDA	GGA-PW91	GGA-PBE	HF	CCSD(T)	LDA	GGA-PW91	GGA-PBE		
Li	+1	-0.256	-0.253	-0.327	-0.318	-0.302	2.0	2.0	2.0	2.0	2.0		
Na	+1	-0.131	-0.129	-0.218	-0.193	-0.178	2.4	2.4	2.2	2.4	2.4		
K	+1	-0.066	-0.063	-0.139	-0.103	-0.093	3.0	3.0	2.8	2.8	3.0		
Rb	+1	-	-	-0.016	-0.013	-0.013	-	-	4.8	5.4	5.8		
Cs	+1	-	-	-0.066	-0.050	-0.042	-	-	3.4	3.6	3.6		

Table 4.9: Results for the H₂-M⁺ alkali metal complexes in the transverse orientation. Equilibrium separations, r_{min} , and binding energies, E_{bind} , are given for quantum chemistry calculations (HF and CCSD(T)) and DFT (LDA, GGA-PW91 and GGA-PBE).

Atom	Charge	E_{bind} eV						r_{\min} Å					
		QC			DFT			QC			DFT		
		HF	CCSD(T)	LDA	GGA-PW91	GGA-PBE	HF	CCSD(T)	LDA	GGA-PW91	GGA-PBE		
Be	+1	-0.250	-0.370	-0.630	-0.535	-0.514	1.8	1.8	1.8	1.8	1.8		
	+2	-2.188	-2.268	-	-	-	1.6	1.6	-	-	-		
Mg	+1	-0.054	-0.096	-0.240	-0.168	-0.152	3.0	2.6	2.4	2.6	2.6		
	+2	-0.930	-0.930	-0.907	-0.909	-	2.0	2.0	2.3	2.5	-		
Ca	+1	-0.023	-0.044	-0.207	-0.148	-0.128	3.8	3.4	2.6	2.6	2.8		
	+2	-0.427	-0.422	-0.666	-0.488	-	2.6	2.6	2.0	2.0	-		
Sr	+1	-	-	-0.070	-0.046	-0.036	-	-	3.6	3.8	3.8		
	+2	-	-	-	-	-	-	-	-	-	-		
Ba	+1	-	-	-	-	-	-	-	-	-	-		
	+2	-	-	-	-	-	-	-	-	-	-		

Table 4.10: Results for the H₂-M⁺ and H₂-M²⁺ alkaline earth metal complexes in the transverse orientation. Equilibrium separations, r_{\min} , and binding energies, E_{bind} , are given for quantum chemistry calculations (HF and CCSD(T)) and DFT (LDA, GGA-PW91 and GGA-PBE).

Atom	Charge	E_{bind} eV						r_{\min} Å					
		QC			DFT			QC			DFT		
		HF	CCSD(T)	LDA	GGA-PW91	GGA-PBE	HF	CCSD(T)	LDA	GGA-PW91	GGA-PBE		
Li	+1	-0.045	-0.058	-0.125	-0.127	-0.112	2.6	2.4	2.4	2.4	2.4		
Na	+1	-0.011	-0.017	-0.091	-0.078	-0.064	3.0	3.0	2.6	2.8	2.8		
K	+1	-	-0.001	-0.057	-0.033	-0.024	-	3.8	3.0	3.2	3.2		
Rb	+1	-	-	-0.032	-0.020	-0.015	-	-	4.4	4.8	5.0		
Cs	+1	-	-	-0.058	-0.039	-0.032	-	-	3.4	3.8	3.8		

127

Table 4.11: Results for the H₂-M⁺ alkali metal complexes in the longitudinal orientation. Equilibrium separations, r_{\min} are between H₂ centre of mass and metal ion, and binding energies, E_{bind} , are given for quantum chemistry calculations (HF and CCSD(T)) and DFT (LDA, GGA-PW91 and GGA-PBE).

Atom	Charge	E_{bind} eV						r_{min} Å					
		QC		DFT				QC		DFT			
		HF	CCSD(T)	LDA	GGA-PW91	GGA-PBE	HF	CCSD(T)	LDA	GGA-PW91	GGA-PBE		
Be	+1	-0.007	-0.138	-0.463	-0.378	-0.358	2.6	2.2	2.2	2.2	2.2		
	+2	-1.650	-	-	-	-	1.8	-	-	-	-		
Mg	+1	± 0.000	-0.017	-0.172	-0.106	-0.091	-	3.0	2.6	2.8	2.8		
	+2	-0.590	-0.624	-	-	-	2.4	2.4	-	-	-		
Ca	+1	± 0.000	-0.003	-0.116	-0.059	-0.047	-	4.2	3.0	3.2	3.2		
	+2	-0.238	-0.253	-	-	-	2.8	2.8	-	-	-		

Table 4.12: Results for the H₂-M⁺ and H₂-M²⁺ alkaline earth metal complexes in the longitudinal orientation. Equilibrium separations, r_{min} , and binding energies, E_{bind} , are given for quantum chemistry calculations (HF and CCSD(T)) and DFT (LDA, GGA-PW91 and GGA-PBE).

5 Energetics of the metal hydrides

the binding between the species and 2H. Binding energies of the magnitude reported in table 4.13 are of no use for hydrogen storage as they will offer significant hindering when trying to extract the hydrogen and are well outside the 0.2 – 0.8 eV DoE range.

Atom	Charge	E_{bind} eV	r_{min} Å
Be	+1	-6.833	1.4
	+2	-1.672	1.8
Mg	+1	-4.772	1.8
	+2	-0.733	2.2
Ca	+1	-4.096	2.2
	+2	-1.418	2.6

Table 4.13: Results for the H-M⁺-H and H-M²⁺-H alkaline earth metal complexes. Equilibrium separations, r_{min} , are between each H atom and the metal ion (each H being equidistant from M), and binding energies, E_{bind} , are given for CCSD(T).

5 Energetics of the metal hydrides

This section shall present the findings of relaxing the metal hydride structures. Calculations were performed within VASP using plane wave basis sets within the PAW scheme. Plane wave cut-offs and Monkhorst-Pack k -point grids were used such that all total energies were converged to within 0.05 eV. Both the LDA and GGA-PW91 xc -functionals were used. A summary of the simulation details are given in table 4.14.

Structures for the metal hydride crystals (shown in figure 4.8) were relaxed by taking the known structures from literature, varying the cell volume to find the minimum energy volume. The cell shape was then varied by $\pm 1\%$ along each lattice vector while maintaining the cell volume. When a lower energy structure was found the volume was relaxed again and the shape varied in the same manner again. Once the lowest energy volume and shape had been found the atomic basis was allowed to relax and no variation was seen from the fixed atomic basis.

The structures of the alkali metal hydrides are well known to have the rock salt structure, two interleaved face centred cubic lattices with space group $Fm\bar{3}m$ with one species occupying the four Wyckoff 4(a) positions and the other species occupying the four 4(b) sites shown in figure 4.8(a). The structure is fully defined by the lattice

5 Energetics of the metal hydrides

Simulation detail	Value
Calculation type	DFT
<i>xc</i> -functionals	LDA and GGA-PW91
Program	VASP
Basis	Plane wave within PAW scheme
Basis cut-off	600 eV
<i>k</i> -point grid	$5 \times 5 \times 5$
Atomic basis	Fixed

Table 4.14: A summary of the DFT simulation details used for modelling the metal hydrides, MH with M=Li,Na,K,Rb and Cs and the metal dihydrides MH₂ with M=Be,Mg,Ca,Sr and Ba.

parameter a that defines the length of the three equal lattice vectors $\vec{a} = (a, 0, 0)$, $\vec{b} = (0, a, 0)$ and $\vec{c} = (0, 0, a)$.

The alkaline earth metal hydrides do not possess the same structure with the two lighter hydrides of BeH₂ and MgH₂ having different structures from each other and the remaining hydrides. For many years the BeH₂ crystal structure was unknown and presumed to be amorphous. Studies now agree that it has the SiS₂ structure[153, 154] consisting of an orthorhombic unit cell with the *Ibam* space group shown in 4.8(b). The MgH₂ crystal is well known to have the rutile structure of TiO₂ having a tetragonal unit cell with the *P4₂/mnm* space group shown in 4.8(c). The remaining alkaline earth hydrides of CaH₂, SrH₂ and BaH₂ all have the PbCl₂ structure with an orthorhombic unit cell of *Pnma* space group shown in 4.8(d).

The BeH₂ crystal consists of twelve BeH₂ units with two distinct Be atoms (four Be(1) atoms occupying the Wyckoff 4 (*a*) sites and eight Be(2) occupying the 8 (*j*) sites) and two distinct H atoms (eight H(1) occupying the 8 (*j*) sites and 16 H(2) occupying the 16 (*k*) Wyckoff sites). Parameters for the Wyckoff positions were taken from Smith et al. [153] with the Be(1) positions fixed by symmetry and $x(\text{Be}(2)) = 0.1253$, $y(\text{Be}(2)) = 0.1699$, $x(\text{H}(1)) = 0.2823$, $y(\text{H}(1)) = 0.3055$, $x(\text{H}(2)) = 0.1949$, $y(\text{H}(1)) = 0.0895$ and $z(\text{H}(1)) = 0.1515$. After relaxations these values did not change appreciably.

The rutile structure of MgH₂ has two equal length lattice vectors allowing the unit cell to be fully defined by the length of one, $|a|$, and the ratio of the other lattice vector $|a|/|c|$. The unit cell consists of two Mg atoms occupying the Wyckoff 2 (*a*) sites and four H atoms at the 4 (*f*) sites defined as $(\pm x, \pm x, 0)$ and $(1/2 \pm x, 1/2 \mp x, 1/2)$. The value

5 Energetics of the metal hydrides

for x was taken from Pozzo and Alfè [114] as $x = 0.304$ and no variation was seen after relaxation.

The structures of CaH_2 , SrH_2 and BaH_2 all have unit cells consisting of four MH_2 units at the Wyckoff 4(c) positions of $(\pm x, \pm 1/4, \pm z)$ and $(1/2 \pm x, \pm 1/4, 1/2 \mp z)$. The structure is then fully defined by the x and z parameters and the size of the three lattice vectors $|a|$, $|b|$ and $|c|$. The x and z parameters were taken from Gridani et al. [155] for SrH_2 , Bronger et al. [156] for BaH_2 and are reported in chapter 3 for CaH_2 ; little change was seen after relaxations.

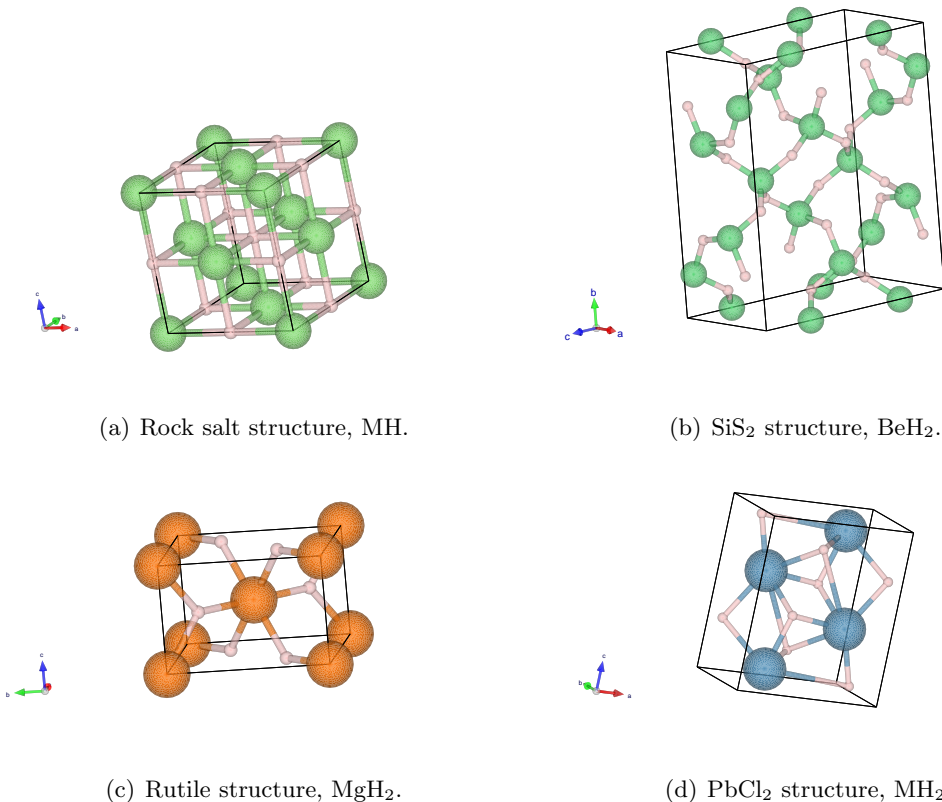


Figure 4.8: Unit cells (hydrogen atoms in pink, metal atoms in other colours) of (a) the rock salt structures of the alkali hydrides (LiH , NaH , KH , RbH and CsH), (b) the SiS_2 structure of BeH_2 , (c) the rutile TiO_2 structure of MgH_2 and (d) the PbCl_2 structure of CaH_2 , SrH_2 and BaH_2 .

The lattice parameters, a , and the formation energies (from spin-polarised free atoms) of the alkali metal hydrides are compared with experiment and shown in table 4.15. We notice that GGA-PW91 calculated values for the lattice parameters agree very well with experimental values with LDA being noticeably worse and $\sim 3\%$ smaller. The calculated values for the formation energy always bracket the experimental value (only

5 Energetics of the metal hydrides

E_{form} of LiH breaks this rule with the GGA-PW91 value giving almost the experimental value). The formation energy decreases monotonically as we pass down the series as the lattice parameter increases. This can be understood using the Madelung concept for the electrostatic lattice energy of an ionic crystal, the cohesive energy of a crystal is then directly proportional to the charge on the ions, the Madelung constant and inversely proportional to the lattice constant.

Compound	Lattice parameter, $a \text{ \AA}$			Formation energy, $E_{\text{form}} \text{ eV}$		
	DFT			DFT		
	LDA	GGA-PW91	Expt.	LDA	GGA-PW91	Expt.
LiH	3.90	4.00	4.061	-5.35	-4.77	-4.76 ^a
NaH	4.70	4.85	4.89	-4.28	-3.80	-3.89 ^a
KH	5.45	5.70	5.70	-4.12	-3.60	-3.77 ^a
RbH	5.80	6.05		-3.94	-3.43	-3.62 ^b
CsH	6.10	6.40	6.388	-3.70	-3.37	-3.59 ^b

Table 4.15: Calculated equilibrium lattice parameters and formation energies for the alkali hydrides compared with experiment.

The cohesive energy of the alkaline earth hydrides and the lattice parameters are compared with experiment and given in table 4.16. Lattice parameters calculated using LDA show a typical overbinding of less than 4% in all cases. Values calculated using GGA-PW91 show excellent agreement with experiment with differences of less than 1% for all cases with the exception of the BeH₂ crystal and c for BaH₂ both exhibiting difference of $\sim 2\%$. The calculated values for E_{form} bracket the experimental values with LDA tending to overbind and GGA-PW91 underbinding. GGA-PW91 performing noticeably better being within 2% in all cases, except for the BeH₂ crystal where GGA-PW91 overbinds by 5.5%. The values given here bracket the extremely accurate diffusion Monte Carlo results of Pozzo and Alfè [114] for the cohesive energy of MgH₂. The binding energies follow a similar Madelung-type pattern as you descend the series. E_{form} per formula unit decreases as the volume per formula unit increases, producing a nearly flat negative correlation. The notable exception to this pattern is the unusual structure

^aFormation energies taken from the Chase [127] at 0 K and are relative to free atoms in the gas phase.

^bFormation energies given at 25 °C. E_{form} for the MH crystals taken from Gunn [157] and E_{form} of the monatomic gas taken from Chase [127] both at 25 °C.

6 Conclusions and discussion

of BeH_2 which has a dense structure with just each BeH_2 unit occupying 40 % of an MgH_2 unit. The cube of the volume then gives a good standardised length to predict the strength of the formation energy following, $|E_{\text{form}}| \propto 1/\sqrt[3]{V_{\text{f.u.}}}$.

Metal hydrides have long been considered for hydrogen storage for many reasons, not least the high hydrogen capacities and ease of manufacture. The extremely high cohesive energies reported in tables 4.15 and 4.16 make the alkali and alkaline earth metal hydrides unlikely candidates for hydrogen storage. The slow kinetics of desorption will likely hinder a useful hydrogen storage medium, despite the high gravimetric storage densities. Work is currently being undertaken to improve the kinetics of MgH_2 [45, 165].

6 Conclusions and discussion

We are now in the position to make predictions as to the stability of GICs against decomposition into the metal and graphite and stability against decomposition into pure graphite and the metal hydride under hydrogenation. By subtracting (values taken from table 4.3) the formation energy of the GIC, $E_{\text{form}}(\text{MC}_n)$, from the formation energy of the metal, $E_{\text{form}}(\text{M}_{\text{gas}})$, we get the stability energy of the formation of the GIC, ΔE_{form} . This value will show which GICs are favourable to make from free atoms in the gas phase and which GICs preferentially form pure graphite and the metal in its standard state. Note that both $E_{\text{form}}(\text{MC}_n)$ and $E_{\text{form}}(\text{M}_{\text{gas}})$ are formation energies from free atoms. Stability energies for the formation of the GICs are given in table 4.17.

We can see in table 4.17 that the Na-GICs border on stability with LDA reporting stable GICs and GGA-PW91 reporting unstable GICs. Calculated values show that the Na-GICs become less unstable at low metal concentrations with NaC_{14} being stable in both LDA and GGA-PW91. This is in good agreement with the very low concentration GICs made by Asher and Wilson [80] where Na-GICs were made with an in-plane sto-

^cValues taken from Smith et al. [153].

^dFormation energy given at 25 °C. E_{form} for BeH_2 crystal taken from Hector et al. [158], citing Senin et al. [159], and E_{form} for the monatomic gas taken from Chase [127] both at 25 °C.

^eValues taken from Bortz et al. [160].

^fValues taken from Chase [127].

^gValues taken from Wu et al. [11] at 9 K.

^hFormation energy given at 25 °C. E_{form} of MH_2 taken from Hector et al. [158], citing Mueller et al. [161], and E_{form} of the monatomic gas taken from Chase [127] both at 25 °C.

ⁱValues taken from El Gridiani and El Mouhtadi [162], citing Sichla and Jacobs [163].

^jValues taken from Snyder et al. [164].

Compound	Lattice parameters [Å]									E_{form} [eV]		
	<i>a</i>			<i>b</i>			<i>c</i>					
	LDA	GGA-PW91	Expt.	LDA	GGA-PW91	Expt.	LDA	GGA-PW91	Expt.	LDA	GGA-PW91	Expt.
BeH ₂	4.20	4.25	4.160 ^c	9.17	9.28	9.082 ^c	7.78	7.87	7.707 ^c	-9.47	-8.48	-8.03 ^d
MgH ₂	4.45	4.50	4.501 ^e	4.45	4.50	4.501 ^e	2.98	3.01	3.011 ^e	-7.59	-6.68	-6.69 ^f
CaH ₂	5.72	5.91	5.929 ^g	3.47	3.57	3.578 ^g	6.57	6.77	6.790 ^g	-9.40	-8.25	-8.28 ^h
SrH ₂	6.21	6.36	6.364 ⁱ	3.47	3.57	3.578 ⁱ	6.57	6.77	6.790 ⁱ	-9.40	-8.25	-8.28 ^h
BaH ₂	6.65	6.80	6.792 ^j	4.08	4.18	4.168 ^j	7.87	8.05	7.858 ^j	-9.04	-8.01	-8.11 ^h

Table 4.16: Formation energies per formula unit, E_{form} (eV unit), and lattice parameters (Å unit) for the alkaline earth hydrides.

6 Conclusions and discussion

ichiometry of NaC_8 giving a total stoichiometry of $\sim\text{NaC}_{64}$. The large energetic cost in making the lighter alkali GICs does not necessarily hinder their formation. Insurmountable barriers may exist under the extremes of temperature and pressure[81–83, 166] that allow the GIC to exist, as evidenced by experiments forming NaC_2 under 40 – 45 kbar of pressure and more than 650 °C. The alkali GICs of K, Rb and Cs show more stable structures at low metal concentrations while the Li-GICs appear to be most stable at high metal concentrations with LDA and low concentrations with GGA-PW91.

For the alkaline earth metals we can see that the Be and Mg-GICs are strongly unstable upon formation with Be-GICs showing ~ 3 eV instability with both LDA and GGA-PW91, showing slight favourability in high metal concentrations. The Mg-GICs also report large instability with ΔE_{form} values being ~ 1 eV. The AE-GICs from Ca to Ba prove to be stable with both LDA and GGA-PW91 giving ΔE_{form} values of more than 0.3 eV. These results are in good agreement with DFT calculations performed by Cobian and Íñiguez [1].

Compound	LDA			GGA-PW91		
	$n = 6$	$n = 8$	$n = 14$	$n = 6$	$n = 8$	$n = 14$
LiC_n	+0.56	+0.54	+0.48	+0.17	+0.23	+0.36
NaC_n	+0.13	+0.10	+0.06	-0.08	-0.02	+0.28
KC_n	+0.59	+0.63	+0.63	+0.23	+0.40	+0.47
RbC_n	+0.59	+0.66	+0.67	+0.22	+0.40	+0.85
CsC_n	+0.78	+0.89	+0.87	+0.32	+0.57	+1.00
BeC_n	-3.00	-3.16	-3.38	-3.00	-3.00	-2.90
MgC_n	-1.06	-1.18	-0.84	-1.06	-1.18	-0.83
CaC_n	+1.30	+1.21	+0.85	+0.46	+0.48	+0.43
SrC_n	+1.14	+0.99	+0.33	+0.41	+0.39	+0.34
BaC_n	+1.57	+1.45	+0.98	+0.80	+0.79	+0.71

Table 4.17: Stability energies (eV unit), ΔE_{form} , for formation of the GICs from free atoms. Stability is calculated against decomposition of the GIC into the metal in its standard state and pure graphite. N.B. stable GICs have positive values for ΔE_{form} .

The stability of these GICs under hydrogenation can now be ascertained using the expression in 4.1. Table 4.18 shows the stability energies of the GICs studied using equation 4.1, which gives a positive ΔE for GICs stable under hydrogenation. We can see

6 Conclusions and discussion

that of the alkali GICs Li, Na and low concentration K-GICs are all unstable under hydrogenation consistent with experiments for LiC_6 [88]. High concentration K-GICs such as KC_8 have been shown to be stable under hydrogenation but form a K bilayer either side of the H layer in the GIC gallery forming a layering pattern of *C-K-H-K-C*[87]. The structure for which these stability energies are given is for a single H_2 molecule per metal atom located in the same plane as the intercalant, this is the situation when stage-II KC_{24} absorbs hydrogen[94] and our calculations correctly predict stability (with LDA showing instability and GGA-PW91 predicting stability) for this material (c.f. KC_{14} for comparison to the experimental structure). The lower concentration Rb-GICs are predicted to be stable and all GICs of Cs are predicted to be stable under hydrogenation. Combining this with the favourable absorption energies of the low concentration Rb and Cs-GICs (see table 4.7) the calculations predict these to be both stable GICs and stable under hydrogenation with favourable absorption energies. This is in excellent agreement with experiment[96].

The alkaline earth GICs are all predicted to be unstable with both LDA and GGA-PW91 upon hydrogenation, in agreement with experiments performed on CaC_6 [5]. The stability values given for the Ca-GICs here differ from those given in chapter 3 because the same approximation used for the other GICs was used here for direct comparison; in chapter 3 stability energies are given relative to the hydrogenated material itself. The binding energy of the alkaline-earth metal hydrides is far stronger than for the alkali hydrides and pushes these GICs to be extremely unstable.

The presence of *d*-orbitals below the Fermi level in the K, Rb, Cs, Ca, Sr and Ba GICs implicate them in GIC binding and help to explain the large jump in binding noticed across the *d*-orbital boundary. This increases the binding energy of these GICs and helps to stabilise the alkali GICs against decomposition into pure graphite and the metal. This is also helped by the decreasing binding energy of the hydrides as you descend the group.

Calculations performed on $\text{H}_2\text{-M}^+$ and $\text{H}_2\text{-M}^{2+}$ show that DFT tends to overestimate the binding compared with CCSD(T) making the GICs appear more stable than they

^aThe stability energies reported here for CaC_n are those following the pattern of the other GICs and hence are different from those in chapter 3 by the binding energy of hydrogen.

6 Conclusions and discussion

Compound	LDA			GGA-PW91		
	$n = 6$	$n = 8$	$n = 14$	$n = 6$	$n = 8$	$n = 14$
LiC_n	-1.42	-1.45	-1.59	-1.38	-1.25	-1.00
NaC_n	-1.16	-1.23	-1.31	-0.96	-0.82	-0.23
KC_n	-0.29	-0.21	-0.20	-0.31	+0.01	+0.82
RbC_n	-0.08	-0.15	+0.08	-0.15	+0.25	+1.10
CsC_n	+0.40	+0.29	-0.27	+0.83	+0.64	-0.06
BeC_n	-8.50	-8.82	-9.26	-7.29	-7.30	-7.09
MgC_n	-4.38	-4.92	-5.54	-3.35	-3.59	-2.90
CaC_n^{a}	-1.36	-1.45	-1.81	-1.40	-1.38	-1.43
SrC_n	-2.46	-2.98	-3.32	-2.38	-3.42	-2.50
BaC_n	-1.41	-1.64	-2.59	-1.56	-1.59	-1.74

Table 4.18: Stability energies (eV unit), ΔE from equation 4.1, for the alkali and alkaline earth metal GICs. N.B. stable GICs have positive ΔE .

are. These calculations confirm that the H_2 molecule preferentially binds in the transverse orientation exploiting the favourable induction and charge-quadrupole interactions, despite the relative reduction in the charge-induced dipole interaction.

The potential errors arise from the accuracy of DFT for modelling these systems. The predictions of DFT for binding calculations involving the H_2 molecule have been discussed in §4 when compared with CCSD(T) values. Work by Pozzo and Alfe [114] on the MgH_2 crystal shows that DFT tends to bracket the true formation energy, found by diffusion Monte Carlo and in excellent agreement with experiment, with LDA overbinding and GGA-PW91 underbinding. The largest errors were found to be 0.5 eV in these calculations, considerably smaller than the exothermic decomposition energies found in this work of more than 1 eV in unstable cases. Errors of this magnitude would not affect the results reported here.

Chapter 5

The dynamics of H₂ in K-GICs

1 Introduction

The hydrogenation of K-GICs has been an intense source of research for over 40 years[167]. Stage-I KC₈ is known to go through a phase transformation upon hydrogenation into stage-II KC₈H_{0.67} with a tri-layer K-H-K intercalant layer[87]. The less dense K-GIC of stage-II KC₂₄ can adsorb hydrogen without going through a metal to non-metal phase transition[93]. Attempts to use theoretical models to understand hydrogen dynamics within stage-II KC₂₄ have focussed on using the simpler in-plane structure of KC₁₄, rather than the experimental KC₁₂ in-plane structure[94, 96]. While the simpler KC₁₄ structure yields a total stoichiometry, KC₂₈, close to that of the experimental KC₂₄ it will be shown that this structure is too symmetric to explain the experimental observations of hydrogen dynamics, such as those of Purewal [96].

Lovell [4] found that neutron scattering experimental results performed on hydrogenated KC₂₄ could best be described by the presence of multiple absorption sites. The measured isotherms disputed this as they exhibited no multiple site filling; bumps in the absorption isotherm due to different sites having different enthalpies of absorption were not seen. It was concluded that KC₂₄ showed only one site, or more accurately one enthalpy of absorption (usually attributed to the presence of one site). It is then discussed that an alternative explanation, using the ideas from Lindsell [168], could help explain the experimental data. Having various homogeneous sites the peak-splitting seen in the neutron scattering data could be explained if the absorption sites were very similar. To fulfil this idea a “non-ordered incommensurate structure with discrete site degeneracy of only three of four would have to be invoked”[4]. It was noted that the

1 Introduction

in-plane structure of such a compound would be hard to solve and increase the time of simulations drastically. This lead to a paper by the authors the following year [94] stating that a quantum delocalisation of H₂ around the three equivalent sites (due to symmetry) in KC₁₄ best described the results from hydrogenating KC₂₄.

Purewal [96] found that H₂ diffusion in KC₂₄ had two distinct time scales inferring that two distinct diffusion processes were occurring; the slower process having a residency time $\sim 50 \times$ longer than the fast process at 55 K. The slow diffusion process was thought to be due to the presence of a strong H₂ attractor, as is seen in the metal hydrides, but the process must be non-dissociative. The quasi elastic neutron scattering results could not be well described by a simple jump diffusion model based on KC₁₄. KC₂₄ was found to have three distinct H₂ absorption sites (found by probing the rotational hindering of the molecules due to the energetic structure of the site) at low H₂ concentrations of KC₂₄ (H₂)_{0.25–0.5} and five distinct sites at higher concentrations of KC₂₄ (H₂)₁. It was noted that a close packed structure that fitted the experimental structure data best possessed many absorption sites while KC₁₄ had only one type of site. Using a simple hindered rotor model, assuming a single fixed absorption site in an unchanging crystal field and neglecting H₂-H₂ interactions, the experimental data could not be accurately fit.

This chapter will study the adsorption of molecular hydrogen in the less dense stage-I K-GICs, KC₁₄ and KC₁₂ using DFT and empirical potentials. The extra freedom found by breaking the highly symmetric KC₁₄ structure in favour of the KC₁₂ structure will be discussed in §2 where the two structures will be compared and the difference in the energy landscape shall be evaluated. The different structures found by relaxing KC₁₂ and KC₁₄ will also be reported along with the structural changes upon hydrogenation. H₂ binding energies will be discussed for both compounds as well as stability against decomposition. The following section, 3, will develop a simple set of two empirical pair potentials, one for the H₂-C interaction and one for the H₂-K interaction. Total energy scans will be taken through each compound and results from the use of the empirical potentials shall be compared with results from DFT in both LDA and GGA-PW91. Slices through the energy landscapes using both the empirical potentials and DFT of each compound will also be compared. The transferability of these potentials and their accurate reproduction of DFT results will allow readers to run rapid classical molecular dynamics simulations. The diffusion of hydrogen between energy minima, the absorption sites, over energy

barriers will be discussed for both KC₁₄ and KC₁₂ in this section and the limitations of the empirical potentials will be considered. Finally §4 will draw conclusions from this work and evaluate and summarise the major findings of this chapter.

2 The differences between KC₁₄ and KC₁₂

The stage-I K-GICs of KC₁₄ and KC₁₂ both have the *P6/mmm* space group. In KC₁₄ the unit cell contains a single K atom residing at the Wyckoff 1 (*a*) site with the C atoms appearing at the same positions as for CaC₁₄ in §3.2.2 on page 66.

In KC₁₂ the structure is more complicated, with a *randomised* in-plane structure fitting experimental data best[96]. This was achieved by taking a one-dimensional liquid-like arrangement of K atoms, superimposing the graphite structure and relaxing the in-plane structure, resulting in K atoms shifting to the nearest hexagonal centre. To simplify the simulations (by reducing the size of the unit cell of KC₁₂) the simplest crystalline structure producing the correct stoichiometry has been used. While this structure does not fit the experimental data well it includes the important aspects of producing *three* different environments for hydrogen (assuming no hydrogen binds to C hexagons containing K atoms), as is seen in the randomised structure that fits experimental data well. This “ideal” KC₁₂ unit cell (modelled as 2(KC₁₂)) contains two K atoms: one at 1 (*a*) and the other at one of the 2 (*c*) sites. Two sets of six C atoms are at the 6 (*k*) sites with one set of six having $x = 1/6$ and the second set using $x = 1/3$. The final twelve C atoms are at the 12 (*q*) sites with $x = 1/6$ and $y = 1/2$. The unit cells viewed down the *c*-axis are shown for both KC₁₄ and KC₁₂ in figure 5.1(a) and 5.1(b) respectively.

To show the difference in the long range in-plane structure, several unit cells are plotted in 5.2, with the different hydrogen environments shown. The long-range structure of KC₁₄ is fully symmetric with only two types of environment present (see 5.2(b)): red hexagons denoting K sites and turquoise showing empty hexagons (with all similarly coloured sites being equivalent). The hexagonal arrangement of K atoms in the idealised KC₁₂ structure produces four different environments (see 5.2(d)): red sites again representing K sites, turquoise, green and yellow showing empty sites with similarly coloured sites being equivalent again.

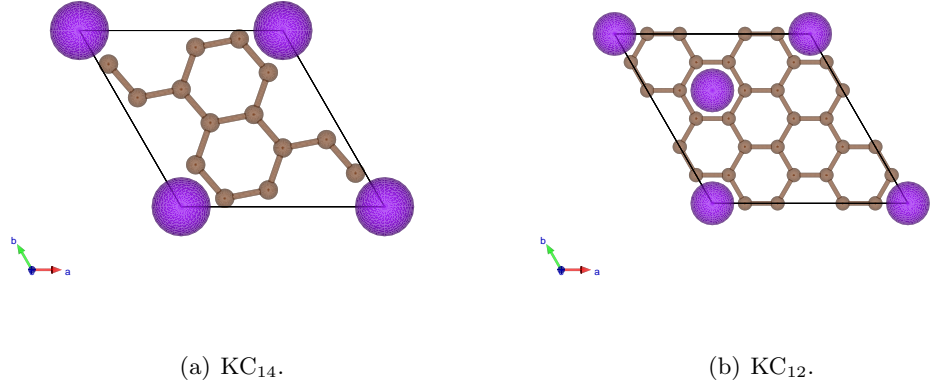


Figure 5.1: The unit cells of (a) KC₁₄ and (b) KC₁₂ (drawn as 2(KC₁₂)) as viewed down the *c*-axis to elucidate the in-plane structure.

2.1 Comparison of the structures of hydrogenated and unhydrogenated KC₁₂ and KC₁₄

The structures of KC₁₂ and KC₁₄ were relaxed using DFT with both the LDA and GGA-PW91 *xc*-functionals in VASP using a similar method as is used for the materials in chapters 3 and 4. The atomic basis was chosen on the merit of symmetry and the unit cell relaxed around it. The in-plane *a*-value was relaxed first and the *c*-axis parameter next. Once an equilibrium *c*-axis value was found the *a*-value was checked to ensure no change had occurred and no changes were seen. The atomic basis was then allowed to vary within the unit cell and no change was found from the symmetric positions reported above in §2. Plane-wave cut-offs and *k*-point grids of sufficient density were used to ensure the total energies were converged to within 0.1 eV. A summary of the simulation details are shown in table 5.1.

The unhydrogenated unit cell *a*- and *c*- parameters are similar for both KC₁₄ and KC₁₂, both exhibiting approximately a 1% increase in the C-C in-plane bond length, *a*, over graphite. The *c*-axis swelled in both compounds from pure graphite by $\sim 55\%$ with LDA and $\sim 60\%$ with GGA-PW91; KC₁₂ gave a smaller *c*-axis separation in all cases compared with KC₁₄. The GGA-PW91 *c*-axis results for KC₁₂ agree extremely well experimental values reported by Lovell et al. [94] of $c = 5.35 \pm 0.01 \text{ \AA}$ for the unhyrdogenated KC₂₄ (GGA-PW91 giving a *c*-value just 0.05 Å larger) and $c = 5.64 \pm 0.01 \text{ \AA}$ for the hydrogenated compound with GGA-PW91 giving a *c*-value 0.14 Å smaller).

Hydrogenated KC₁₂ and KC₁₄ showed little change from the unhydrogenated struc-

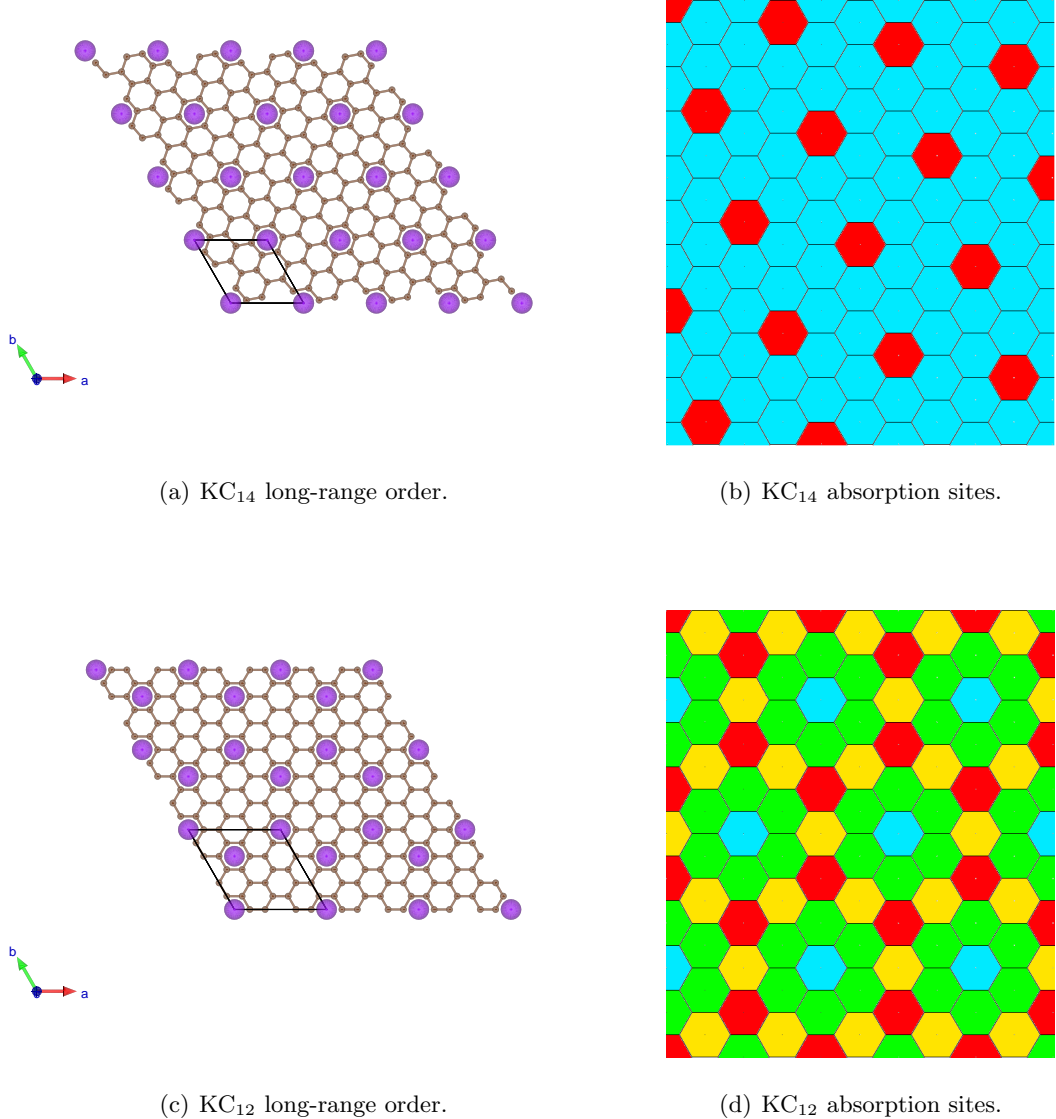


Figure 5.2: The long-range in-plane order of (a) the highly symmetric KC₁₄ and (c) KC₁₂ (unit cells are outlined in black). The different structures leading to different types of absorption environments, or sites, shown for (b) KC₁₄ where every empty site is equivalent, and (d) KC₁₂ where three different types of empty site exist (site A shown in yellow; site B in green and site C in turquoise). Note that similarly coloured sites are equivalent, with red hexagons denoting K sites and green, turquoise and yellow denoting empty sites.

Simulation detail	Value
Calculation type	DFT
<i>xc</i> -functionals	LDA and GGA-PW91
Program	VASP
Basis	Plane wave within PAW scheme
Basis cut-off	800 eV
<i>k</i> -point grid	8 × 8 × 8
Atomic basis	Fixed

Table 5.1: A summary of the DFT simulation details used for modelling KC₁₄ and KC₁₂.

ture with only a slight (1-3%) increase in *c*-axis parameter. The binding energies for H₂ in KC₁₄ are for the single site: between two eclipsing empty C hexagon centres (turquoise sites in figure 5.2(b)), with a slight shift after relaxation away from the K atom, with the H₂ bond axis parallel to the *c*-axis. For the KC₁₂ system the three absorption sites (shown in 5.2(d) in turquoise, green and yellow) offer slightly different binding energies, but exhibit the same structure in all cases. Again, hydrogen positions were found to be centred below C hexagon centres with the H₂ bond axis parallel to the *c*-axis. This orientation was chosen as its fits with experimental evidence found for hydrogenated KC₂₄[94, 96]; calculations performed on hydrogen-metal complexes from §4; electrostatic considerations of bonding mechanisms discussed in §4; and results from hydrogenated Ca-GICs (§3.3) where the orientation of H₂ was varied and found that transverse was most favourable. Absorption energies for KC₁₄ match well with experimental absorption isotherms reported by Purewal [96] of -0.095 eV. The three empty sites in KC₁₂, denoted A, B and C, are shown in figure 5.2(d) as yellow, green and turquoise respectively. Table 5.2 compares the results of relaxing the hydrogenated and unhydrogenated structures of KC₁₄ and KC₁₂.

We can see in table 5.2 that the H₂ absorption sites for KC₁₂ are more favourable (lower in energy) than for KC₁₄ by ∼ 0.1 eV. The single KC₁₄ site shows favourable H₂ binding within the DoE targets and the structure agrees with that found by Lovell et al. [94]. All three sites in KC₁₂ exhibit favourable H₂ binding with LDA (GGA-PW91 shows close to no binding energy for sites B and C and unfavourable binding for site A) with site B (the green site) showing the most favourable absorption, closely followed by site A (the yellow site). All three sites exist within the DoE absorption enthalpy targets.

2 The differences between KC_{14} and KC_{12}

	LDA			GGA-PW91		
	a	c	E_{bind}	a	c	E_{bind}
KC_{14}						
no H_2	1.420	5.20	N/A	1.430	5.50	N/A
+ H_2	1.420	5.20	-0.099	1.430	5.70	-0.026
KC_{12}						
no H_2	1.425	5.15	N/A	1.435	5.40	N/A
+ H_2 (site A)	1.425	5.20	-0.213	1.435	5.50	+0.127
+ H_2 (site B)	1.425	5.20	-0.243	1.435	5.50	+0.044
+ H_2 (site C)	1.425	5.20	-0.192	1.435	5.50	+0.028

Table 5.2: Structure parameters for unhydrogenated (no H_2 rows) and hydrogenated (+ H_2 rows) KC_{14} and KC_{12} with all three non-equivalent sites shown for K_{12} .

As discussed earlier, we expect the true absorption energies to be bracketed by the LDA and GGA-PW91 values, corroborated by the favourable binding of H_2 in KC_{24} seen in experiment[93, 94, 96, 116, 169]. We can see that the three absorption sites presented by KC_{12} have extremely similar binding energies (all within 0.05 eV for LDA and 0.1 eV for GGA-PW91). Upon hydrogenation the sites would be filled approximately equally, assuming no major barriers to filling the sites thus causing the absorption isotherm to smooth (the evidence of a single absorption site) as was seen by Lovell [4]. The small spread of absorption enthalpies over just three sites fits the explanation required by Lindsell [168] to explain the peak splitting seen in experimental neutron diffraction data.

2.2 Comparison of the energy landscapes of hydrogenated KC_{12} and KC_{14}

The H_2 energy landscapes for an H_2 molecule centred mid-plane and vertically oriented (the H_2 bond axis being parallel to the GIC c -axis) have been calculated for KC_{12} and KC_{14} to show how the different structures result in very different landscapes for the absorption of hydrogen. These DFT landscapes agree well with those calculated (for KC_{14}) by Purewal [96]. Landscapes have been calculated using both flavours of DFT, LDA and GGA-PW91, and the unit cell and C and K atomic basis was fixed during the calculation of each data point, i.e. the structure was not relaxed for every given H_2

position in the landscape. These landscapes help to show the structure of each of the absorption sites and the likely pathways to diffusion in each material.

For KC₁₄ 86 data points were used to calculate the energy landscape; for KC₁₂ 126 data points were used. This gives the same data point density as for the CaC_n landscapes given in chapter 3 of $\sim 0.5 \text{ \AA}^2/\text{point}$.

The DFT LDA landscapes are shown in figure 5.3 with (a) showing KC₁₄ and (b) showing KC₁₂. Figure 5.4 shows the DFT GGA-PW91 energy landscapes for (a) KC₁₄ and (b) KC₁₂. In 5.3(a) and 5.4(a) we can see the structure of the KC₁₄ absorption site *a* (the three neighbouring equivalent turquoise sites in 5.2(b)): three small barriers exist separating the site into three equivalent absorption sites (each labelled site 1 later in §3.2.1 figure 5.9). The steep barriers surrounding each intercalant K atom is a feature common to all H₂ GIC landscapes. It is apparent that the two KC₁₄ sites are equivalent to each other and not distinct.

The KC₁₂ landscapes in 5.3(b) and 5.4(b) show more variation than the symmetric KC₁₄ landscapes. It can be immediately seen that the broken symmetry results in different sites in the material. There exists a small local minima near the centre of an empty C hexagon between two hexagons occupied by intercalant K atoms. We can see that an energy barrier exists on the line joining two adjacent K atoms across this site making the H₂ preferentially absorb slightly off-centre in the hexagon (increasing the H₂-K distance slightly). This site (yellow in figure 5.2(d)) is clearly less favourable than the large minima in the lower half of the unit cell, a conglomerate of the green and turquoise sites in 5.2(d). The structure of the green sites is clearly equivalent as we see each of the six symmetric sites, with the turquoise site showing small barriers between it and the neighbouring green sites. Diffusion of H₂ around this area of the unit cell will clearly be favourable to crossing to the yellow site. We can see from the KC₁₂ landscapes and from table 5.2 that site B (green in figure 5.2(d)) is the most favourable as the most symmetric site, C (turquoise in 5.2(d)), is too distant from K atoms to benefit fully from the H₂-K interaction.

3 Diffusion of H₂ in KC₁₄ and KC₁₂

The diffusion of H₂ in these two materials is very different. The extra absorption sites offered by KC₁₂ creating additional barriers to diffusion make the process of H₂ diffusion in the material more complex than that of KC₁₄. The diffusion of H₂ was studied

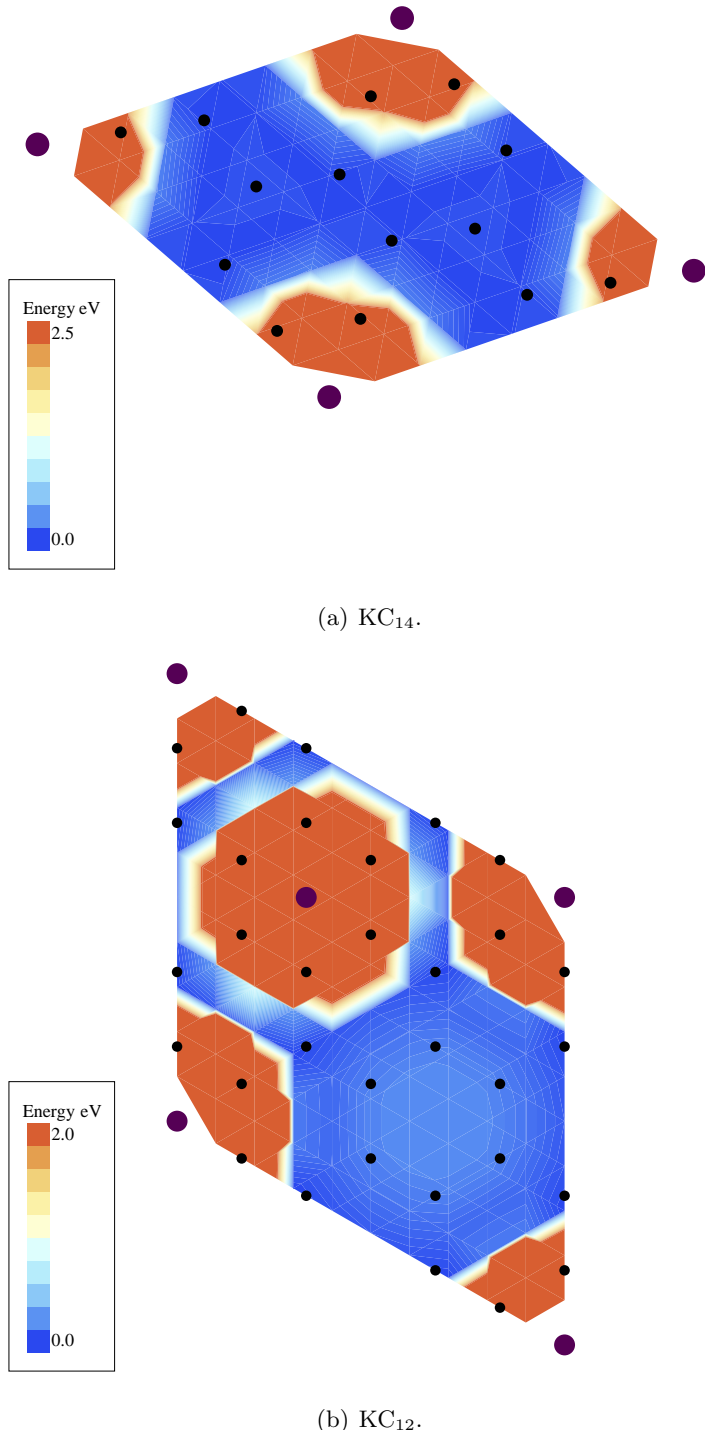
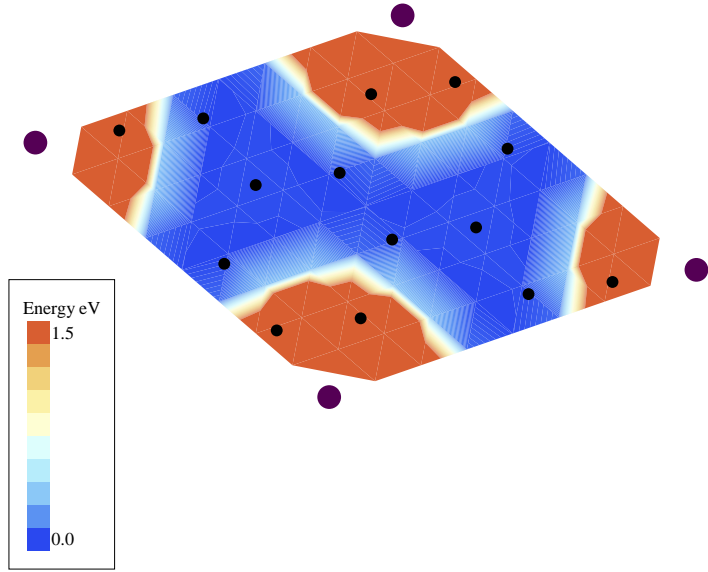
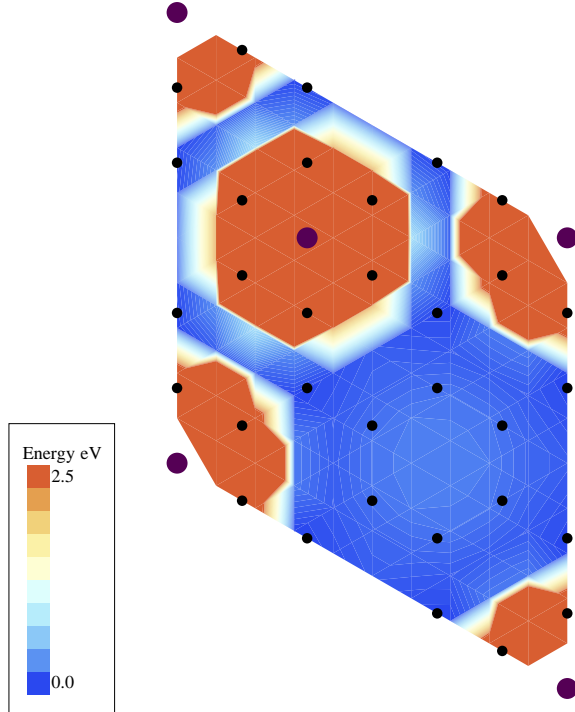


Figure 5.3: DFT LDA H₂ energy landscapes for (a) KC₁₄ and (b) KC₁₂. Note the different energy scales, (a) showing between 0 eV and 2.5 eV while (b) shows between 0 eV and 2.0 eV.



(a) KC₁₄ DFT GGA-PW91 energy landscape.



(b) KC₁₂ DFT GGA-PW91 energy landscape.

Figure 5.4: DFT GGA-PW91 H₂ energy landscapes for (a) KC₁₄ and (b) KC₁₂. Note the different energy scales, (a) showing between 0 eV and 1.5 eV while (b) shows between 0 eV and 2.5 eV.

by examining the energy barriers between absorption sites within the materials. One-dimensional energy scans with high linear data point density were taken through both materials to cover the important energy minima and barriers.

Energy scans were performed using both LDA and GGA-PW91 flavours of DFT in VASP. Again, the same simulation parameters as given in table 5.1 were used. Empirical potentials were also created to allow further work on fast classical molecular dynamics simulations. The energy scans, and thus the energy barriers, produced by the empirical potentials are compared with DFT calculations.

3.1 Empirical potentials for H₂-C and H₂-K

Empirical potentials for the H₂-C and H₂-K interactions were parametrised from DFT calculations of hydrogenated KC₁₄. The H₂ molecule was treated as a spherically symmetric point particle (with the H₂ molecule in the vertical orientation in the DFT calculations) and all distances were measured to the H₂ centre of mass. Thus the energy scans and landscapes presented represent this simplified situation of a point particle H₂ molecule with no rotational aspects included.

The two pair potentials were parametrised to DFT calculations using both LDA and GGA-PW91 *xc*-functionals. The H₂-C interaction was presumed to be purely repulsive. Upon investigating the H₂-C interaction with DFT calculations on K-GICs it was clear that the graphene sheets were strongly repulsive. The H₂-K interaction was given a Lennard-Jones type interaction as the intercalate in the GIC is positively charged (again, see §2.1) and offers favourable binding in the GIC (and agrees with the results of H₂-K⁺ free ion interaction of §4). The two forms of the potentials were,

$$V_{H_2-C}(r) = 4\epsilon \left(\frac{\sigma}{r}\right)^N \quad \text{and} \quad (5.1)$$

$$V_{H_2-K}(r) = 4\epsilon \left[\left(\frac{\sigma}{r}\right)^N - \left(\frac{\sigma}{r}\right)^M \right], \quad (5.2)$$

with σ representing the zero-crossing point of the potential; r representing the distance from the centre of mass of the H₂ point particle and the C or K atom; ϵ representing the depth of the energy well in the H₂-K potential; and the exponents N and M representing the strength of the fall-off of the potentials. The H₂-C potential was chosen of this form to mimic the purely repulsive part of the Lennard-Jones type interaction.

In DFT calculations the H₂ molecule was moved along the *c*-axis in KC₁₄ above (and below) the centre of a graphite hexagon. This resulted in the H₂-K distance barely

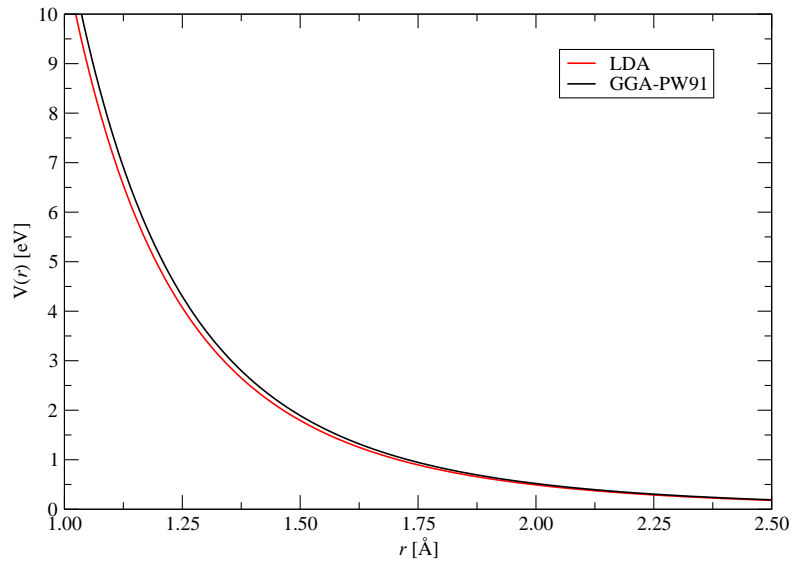
changing (and thus giving minimal energy change from the contribution of the H₂-K interaction) while giving data on the H₂-C interaction. The resultant parabola, giving the minimum configuration midway between the planes of graphite, was then fitted using the form of the potential in 5.1. The fit was performed by considering the nearest neighbour C atoms that existed within a cut-off of 8 Å, which included the sum 144 H₂-C interactions.

To parametrise the H₂-K interaction, the H₂ molecule was moved on a scan through the KC₁₄ compound along the mid-plane of the GIC. The H₂-C empirical potential was then subtracted from every point along the energy scan. This left only the energy due to the interaction of H₂-K, this was then fitted using the form in 5.2. The H₂-C potential was given a cut-off of 10 Å when it was removed from the DFT energy scan. The H₂-K potential was then fitted by inspection using a cut off of 10 Å. The σ parameter was initially chosen to agree with the value from CCSD(T) calculations on H₂-K in the transverse orientation, $\sigma = 2.6$ Å. The quality of the fit was then judged by calculating the mean value of the square error and the ε value changed appropriately. Sets of the exponents N and M were chosen and the fitting procedure within one of these sets performed until the best result achieved. The best fit from each set of exponents was compared and resulted in the values given here. The final value of σ is close to that of the corresponding CCSD(T) calculations of chapter 4. The total potential gave a mean error of 26 meV with LDA and 12 meV with GGA-PW91 (calculated as the square root of the mean square error of the full empirical potential energy and the DFT energy along the KC₁₄ scan).

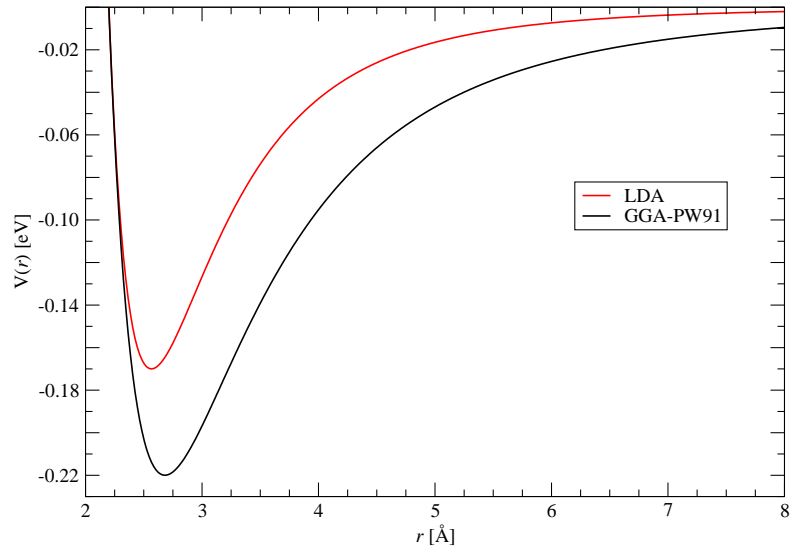
The fitted form of the H₂-C and H₂-K potentials for both LDA and GGA-PW91 *xc*-functionals are shown in figure 5.5 to clarify the difference between the assumed H₂-K and H₂-C interactions, using the final parameters shown in table 5.3. This figure shows the difference the parameters make to the form of the potentials when LDA is used and when GGA-PW91 is used.

3.2 H₂ energy scans through KC₁₂ and KC₁₄

One-dimensional energy scans through the mid-plane of KC₁₄ and KC₁₂ were calculated using DFT (both LDA and GGA-PW91) and compared with the parametrised pair potentials of §3.1. Energy scans were chosen in each material such that all important energy minima and barriers were included. In KC₁₂ this required two distinct paths,



(a) H₂-C potentials.



(b) H₂-K potentials.

Figure 5.5: The functional forms of (a) H₂-C potentials and the (b) H₂-K potentials fitted to DFT data (both LDA and GGA-PW91) from hydrogenated KC₁₄.

Parameter	H ₂ -C		H ₂ -K	
	LDA	GGA-PW91	LDA	GGA-PW91
ε [eV]	0.045	0.0475	0.17	0.22
σ [\AA]	2.5	2.5	2.2	2.2
N	4.5	4.5	9	7
M	N/A	N/A	4.5	3.5

Table 5.3: The fitted parameters for the H₂-C and H₂-K potentials using both LDA and GGA-PW91 *xc*-functionals.

while for KC₁₄ one linear path was sufficient.

Energy scans were performed by placing an H₂ molecule vertically in the K-GIC (bond axis parallel to the GIC *c*-axis) with the H₂ centre of mass at the GIC mid-plane. The GIC was chosen to have the unit cell parameters of the relaxed hydrogenated GIC (table 5.2) and was not allowed to change during the energy scan. Calculations (DFT with LDA and GGA-PW91 and empirical calculations) were then performed with the H₂ molecule fixed at each point along the path. Calculations using the empirical potentials were performed in a bespoke code^a that respected the form of potentials but adjusted them such that they would be force-corrected and energy-corrected (cut-and-shifted)^b with radial cut-offs of 20 \AA for all potentials.

In KC₁₄ it was possible for a single scan to cover the three important energy barriers to H₂ diffusion and the single absorption site. In KC₁₂, two scans were necessary to map the five important energy barriers and three absorption sites. These energy barriers and sites will govern the diffusion of H₂ within the materials.

^aThe code was written by the author and calculates energies from pair potentials with no thermodynamic considerations and respects periodic boundary conditions. No other interactions, beyond H₂-C and H₂-K, were included and the atomic basis was fixed for each point along the path.

^bForce-correction was performed using the simple method given in the DL Poly manual[170]. Given a potential $V(r)$ it can be corrected for a discontinuous change in the potential at the cut-off radius (r_{cut}) by using the force-corrected equivalent potential,

$$V_{\text{F corr.}} = V(r) - V(r_{\text{cut}}) - V'(r_{\text{cut}}) \times (r - r_{\text{cut}}), \quad (5.3)$$

where V' is the derivative dV/dr .

3.2.1 H₂ energy scans through KC₁₄

The path chosen for the energy scan in KC₁₄ is shown in figure 5.6 with distances along the path measured from the K atom at “START” (the path concludes at “FINISH”). The major barriers are labelled with capital letters, A, B and C respectively. The single absorption site is labelled 1.

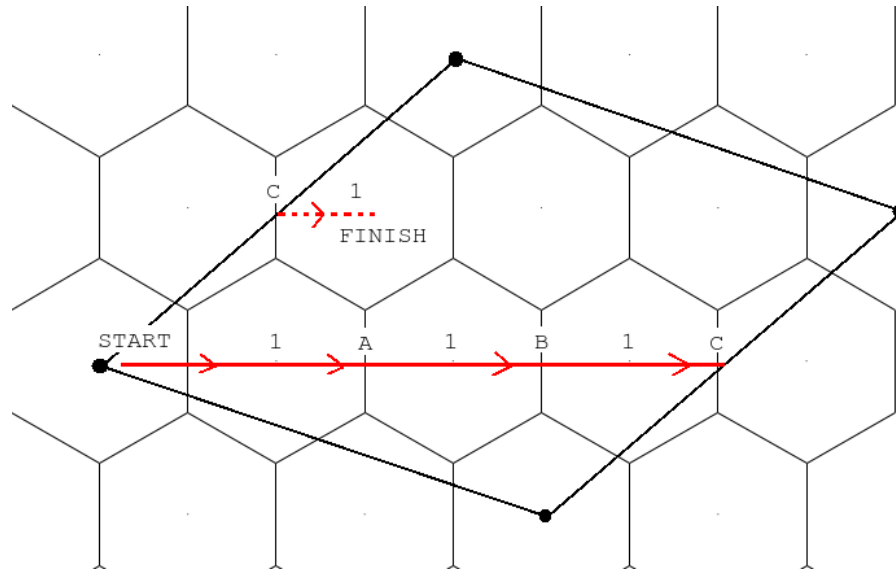


Figure 5.6: The path along which the energy scan in KC₁₄ is plotted. The unit cell is marked in black with the path starting at “START” and following the arrows finishing at “FINISH”. The single absorption site is marked with 1 and the three important energy barriers are marked A, B and C. K positions are denoted with black filled circles and the graphite lattice is shown.

The energy scans through KC₁₄ are shown in figure 5.7 with (a) showing LDA data and (b) showing GGA-PW91 data; both plots compare DFT and data from empirical potentials. Please note that “Empirical LDA” and “Empirical GGA-PW91” mean “Empirical potential fitted to LDA DFT data” and “Empirical potential fitted to DFT-GGA-PW91 data” respectively. Plots are superimposed to allow direct comparison between empirical and DFT data with the ordinate showing relative heights of energy barriers. We can see that the absorption sites that the path passes through all have the same energy minimum, due to the sites being equivalent. The three barriers are clearly distinct with B being more than 5 × higher than A and C. The difference between the energy barriers produced using DFT and those produced using the empirical potential are extremely close with the empirical potentials giving relative barrier heights within 2 % of the DFT relative barrier heights. A classical simulation of H₂ in KC₁₄ would give

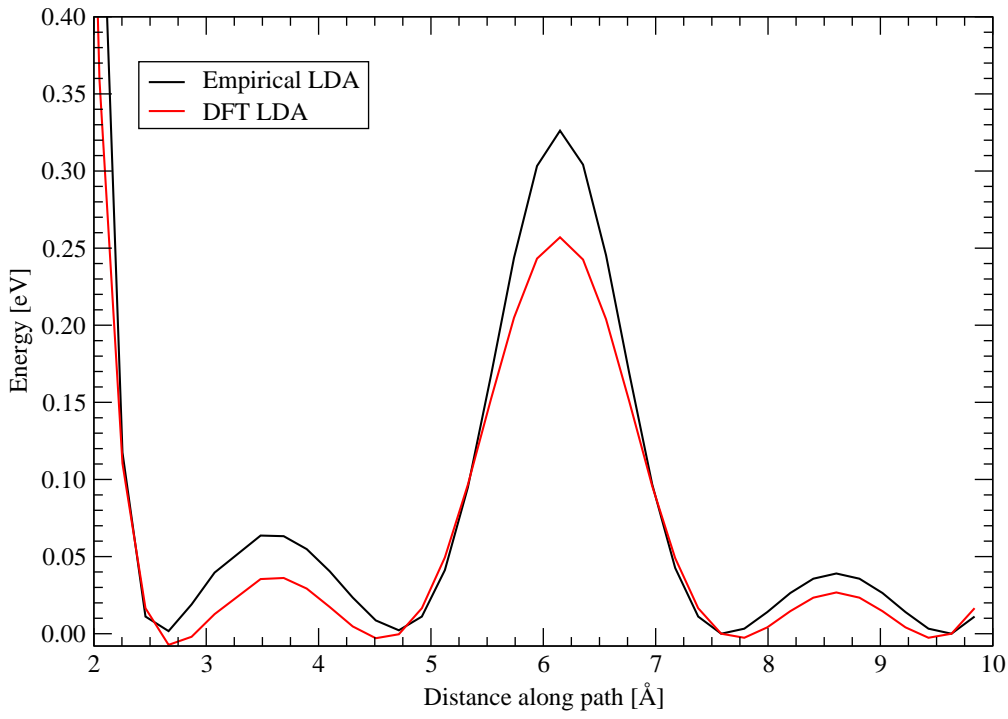
similar results to DFT if the temperature of the simulation was tuned appropriately.

Figure 5.9 shows the example of a H₂ located at the site 1. It faces six likely routes for diffusion consisting of 4 distinct barriers. Two sets of absorption sites are labelled in blue as *a* and *b* with vectors pointing from the centre of each set to the three absorption sites (labelled 1) in each. The H₂ molecule faces two barriers that keep it within the set of absorption sites *a* (barrier A); one barrier that allows it to change between sets of sites (barrier C taking it from set *a* to set *b*); and two high barriers that allow it to change between sets of sites (barrier B taking it again from set *a* to set *b*), which is likely impassable at reasonable temperatures. The dotted path represents a jump that is extremely unlikely given the enormity of this barrier. We can see from the barrier heights given in table 5.4 that of the two barriers of interest, A and C, LDA estimates that A $\sim 1.5 \times$ C (with GGA-PW91 giving A $\sim 4 \times$ C). Given that an H₂ molecule faces twice as many A-barriers as C-barriers it would imply that the molecule is likely to have a measurable residency time at a set of absorption sites with LDA and is more likely to diffuse through the material (jumping between sets of sites) with GGA-PW91. These results are mirrored by the empirical potentials.

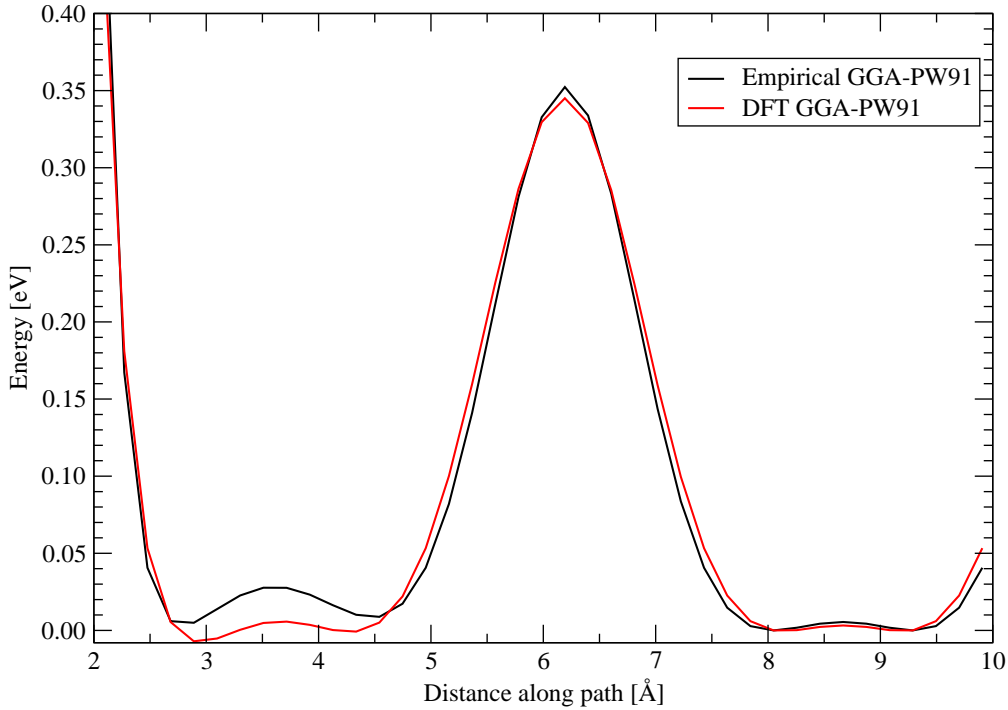
Using an Arrhenius relationship for the thermally activated diffusion of a particle at temperature *T* over a barrier of height *E_b* attempting a jump with a frequency of ν_{att} . (due usually to the thermal vibrations and constriction of the energy well, related to the barrier height) we get a frequency of attempted jumps with sufficient energy to clear the barrier of,

$$\omega = \nu_{\text{att}} e^{-\frac{E_b}{k_B T}}. \quad (5.4)$$

Using the relationship given in 5.4 we can plot the hopping frequency, ω , for a *diffusive* hop over a C-barrier (that leads to diffusion through the material by allowing the H₂ to travel to the next set of absorption sites, *a* \rightarrow *b*) and for a *non-diffusive* hop (over either of the two A barriers that keeps the H₂ localised to particular set of sites, *a* \rightarrow *a*). Figure 5.8 shows this comparison (for (a) LDA data and (b) GGA-PW91 data) by plotting $\omega/\nu_{\text{att}} = e^{-\frac{E_b}{k_B T}}$ against temperature. The temperature where the diffusive jump (C, red in the figure) crosses below the non-diffusive jump (A, black in the figure) is the temperature at which we would expect the H₂ molecule to make fewer set-changing jumps and more non-set changing jumps, thus above this temperature the molecule remains more local to the three binding sites that make up set *a*. The plots show this



(a) MC₁₄ LDA scan.



(b) MC₁₄ GGA-PW91 scan.

Figure 5.7: H₂ energy scans along the path given in 5.6 comparing DFT with empirical data for (a) LDA and (b) GGA-PW91. Note that “Empirical LDA” and “Empirical GGA-PW91” mean “Empirical potential fitted to LDA DFT data” and “Empirical potential fitted to DFT-GGA-PW91 data” respectively

		Barrier height, E _b [eV]			
		LDA		GGA-PW91	
		DFT	Empirical	DFT	Empirical
A		0.04336	0.06195	0.01281	0.02269
B		0.25998	0.32395	0.34577	0.34352
C		0.02937	0.03906	0.00320	0.00546

Table 5.4: The barriers to H₂ diffusion in KC₁₄.

comparison using energy barriers from DFT (solid lines) and energy barriers from the empirical potentials (dashed lines).

We can see that at temperatures above 234 K for DFT LDA (383 K for empirical LDA), and 161 K for DFT GGA-PW91 (288 K for empirical GGA-PW91), we expect the H₂ molecule to make fewer diffusive jumps and more non-diffusive jumps, causing the molecule to appear more localised to one set of absorption sites.

For this compound all barriers are symmetric and so only one value is given for the height of each in table 5.4 (for KC₁₂ the barriers will be asymmetric and so will have a *forward* and *reverse* barrier height).

Using the values for barrier heights in table 5.4 and using an approximation for the attempt frequency, $\nu_{\text{att.}}$, we can predict the jump rates for the diffusive process and for the non-diffusive process and compare with the experimental values. The attempt frequency was taken as the vibration energy of an atom in a harmonic potential approximating the energy potentials at each site by

$$\nu_{\text{att.}} = \frac{1}{2\pi} \sqrt{\frac{1}{m(\text{H}_2)} \frac{1}{x} \frac{dU}{dx}}, \quad (5.5)$$

where x is a linear measure along the potential energy scan and was taken to be as small as possible to allow the best approximation to the actual potential minima using a parabola; $m(\text{H}_2)$ is the mass of a hydrogen molecule; $\frac{dU}{dx}$ is the derivative of the potential, the force, felt at the energy minima. Using values taken from the empirical potential attempt frequencies of 4.70×10^{12} Hz for LDA and 3.44×10^{12} Hz for GGA-PW91 were found.

Quasi-elastic neutron scattering experiments[96] give two diffusion processes, one on a long time scale and one on a short time scale. Converting the quoted residency times to jump rates we can see that the calculated values bracket the experimental values.

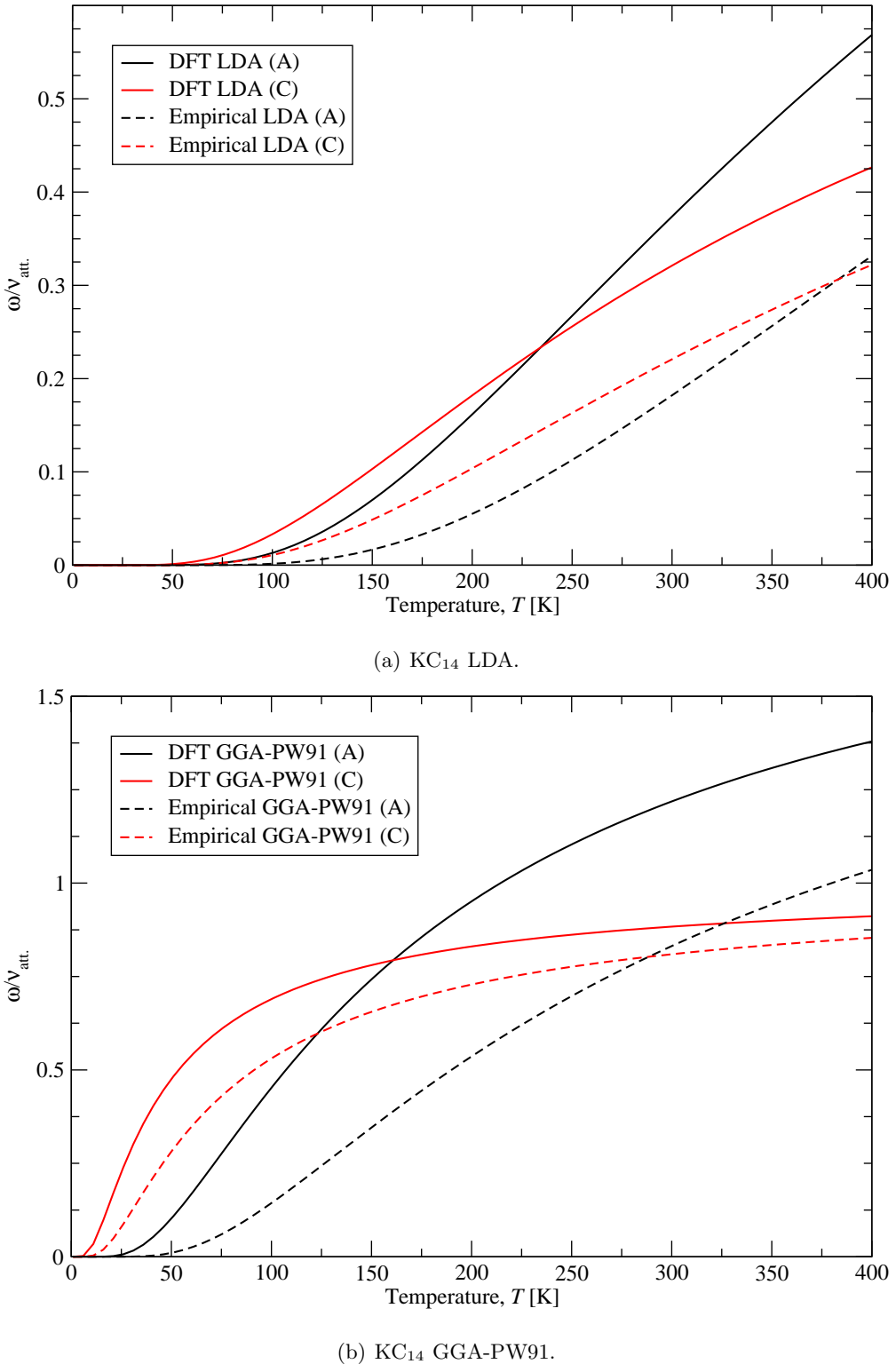


Figure 5.8: Comparison of the jump frequencies (the Boltzmann factors for each jump) for a diffusive jump (red) and a non-diffusive jump (black) of H₂ at a site 1 in set of sites *a* in KC₁₄ (see figure 5.9) with (a) LDA data and (b) GGA-PW91 data. DFT data (solid lines) is compared with empirical data (dashed lines).

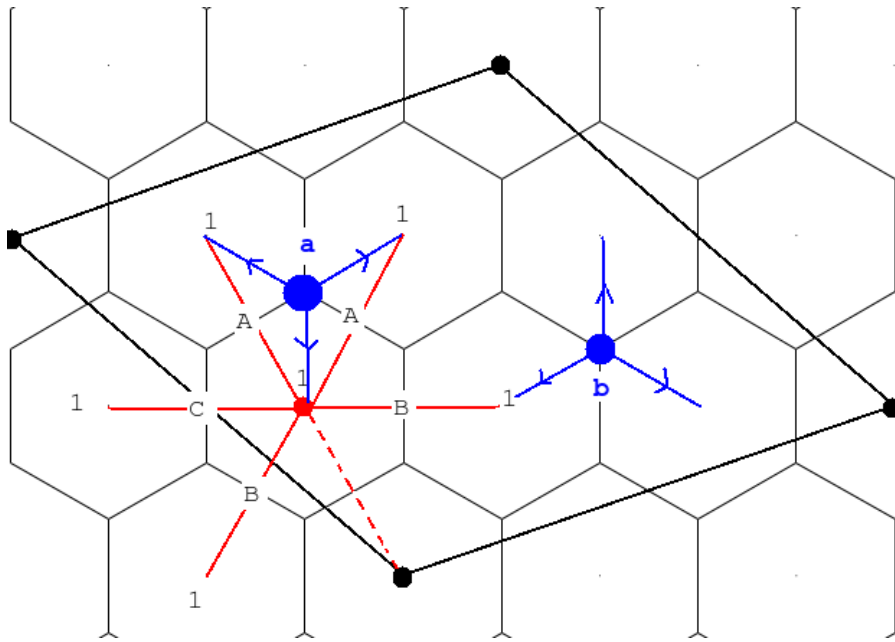


Figure 5.9: An H₂ molecule (filled red circle) located at a site faces six possible routes for diffusion with only three of them likely; two jumps (over barrier A) keep the molecule with the set of sites *a* (*non-diffusive* jumps) and one jump (barrier C) takes it to another set of sites *b* (*diffusive* jump). The two high barriers, B, are unlikely to be traversed at reasonable temperatures and the dotted path represents an impossible jump.

Table 5.5 shows the comparison between experimental jump rates for the fast and slow process and calculated jump rates for the diffusive and non-diffusive processes. The slow process observed in experiment has been associated with the non-diffusive process over barrier A in the model used here; and the fast process seen in experiment with the diffusive process of jumping over barrier C. These crude potentials clearly do not accurately describe the processes on this level, with LDA getting markedly better results for the diffusion processes than GGA-PW91.

The differences between the energy scans performed using the empirical potentials and DFT become evident in the energy-difference landscape, an *energy-error* landscape. Figure 5.10 shows the landscape produced showing the error between the empirical and the DFT landscapes, with (a) showing the LDA energy differences and (b) showing the GGA-PW91 differences. We can see that generally the empirical potentials parametrised to DFT GGA-PW91 calculations fit the landscape better than the LDA parametrised potentials, evidenced from the more accurate barrier representation given by GGA-

Temp	Diff./Fast process ($\times 10^9 \text{ s}^{-1}$)			Non-diff./Slow process ($\times 10^8 \text{ s}^{-1}$)		
	LDA	GGA-PW91	Expt.[96]	LDA	GGA-PW91	Expt.[96]
60 K	16	2530	75	21	7883	7.5
70 K	36	2760	106	71	11230	14
80 K	66	2950	143	172	14640	17

Table 5.5: Jump rates, ω , for H₂ diffusing via the diffusive process (over barrier C) and by the no-diffusive process (either of the A barriers) in KC₁₄ compared with experimental values for the two jump rates of H₂ seen in KC₂₄.

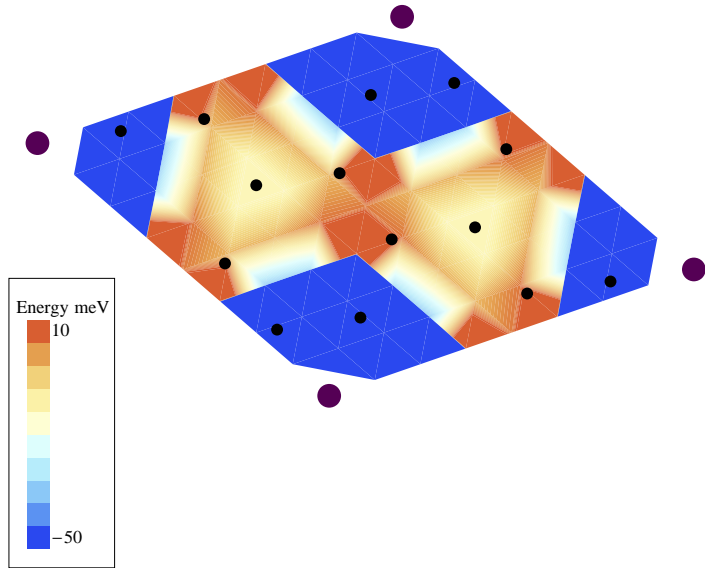
PW91 in 5.7(b). We can see in the LDA calculations in 5.10(a) barrier A is slightly over estimated by the potential and B very overestimated while barrier C is closer to the DFT values. We see a similar pattern in 5.10(b) for the GGA-PW91 landscape with barrier C represented better this with the empirical potential than for LDA.

3.2.2 H₂ energy scans through KC₁₂

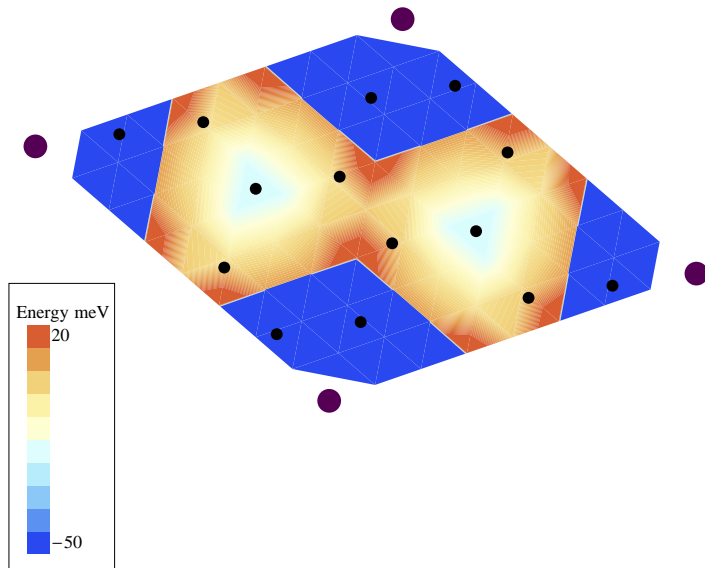
The two paths of the KC₁₂ energy scans are shown in figure 5.11. Scan 1 extends from a type 1 absorption site, over barrier A, then through a K atom (presenting an extremely high energy barrier), over barrier B to a type 2 absorption site, then finally over barrier C and finishing at a type 3 absorption site. Scan 2 starts at a type 2 absorption site, over barrier D to another type 2 absorption site, then over barrier E to finish at a type 1 absorption site.

The energy scans for scan 1 in KC₁₂ are shown in figure 5.12 with LDA results shown in (a) and GGA-PW91 results shown in (b). Energy scans are superimposed for clearer comparison with the ordinate measuring relative barrier heights.

We can see in energy scan 1 in figure 5.12 that barriers A and B have been absorbed by the extremely high barrier due to the H₂ close approach to K. This finally comes back down to meet the absorption site 2 where we see the empirical scan and DFT scans for both LDA and GGA-PW91 meet within 20 meV with DFT predicting the absorption site to be 0.2 Å further along the path than the empirical scan. For barrier C in this scan we can see a large discrepancy between the DFT data and empirical data. The empirical data predicts a much larger forward barrier with LDA giving $E_{\text{emp}} \sim 1.5 \times E_{\text{DFT}}$ and GGA-PW91 giving $E_{\text{emp}} \sim 3 \times E_{\text{DFT}}$. The empirical data also gives a negligible reverse barrier height while DFT predicts the reverse barrier to be approximately a third of



(a) KC₁₄ energy-difference DFT LDA landscape.



(b) KC₁₄ energy-difference DFT GGA-PW91 landscape

Figure 5.10: Energy-error landscapes showing the energy difference between DFT and empirical landscapes for (a) LDA and (b) GGA-PW91 for KC₁₄.

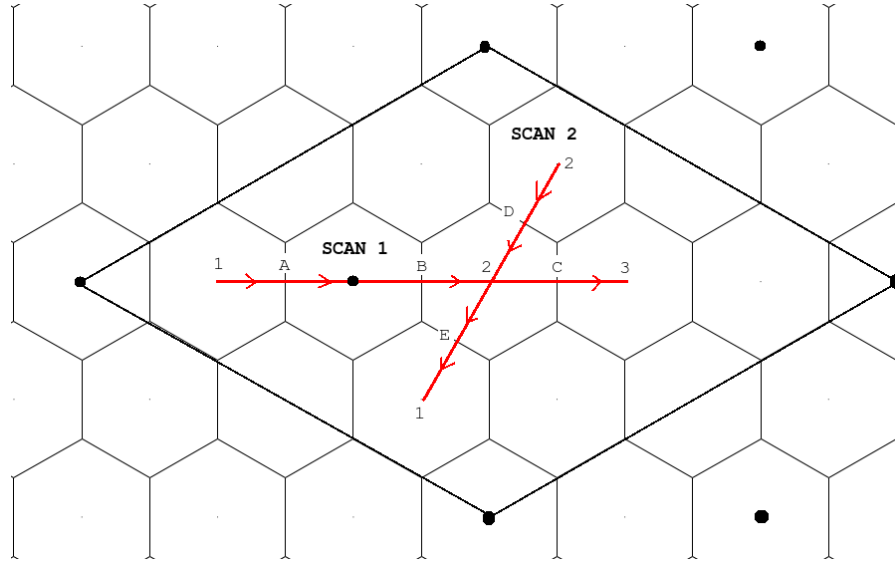
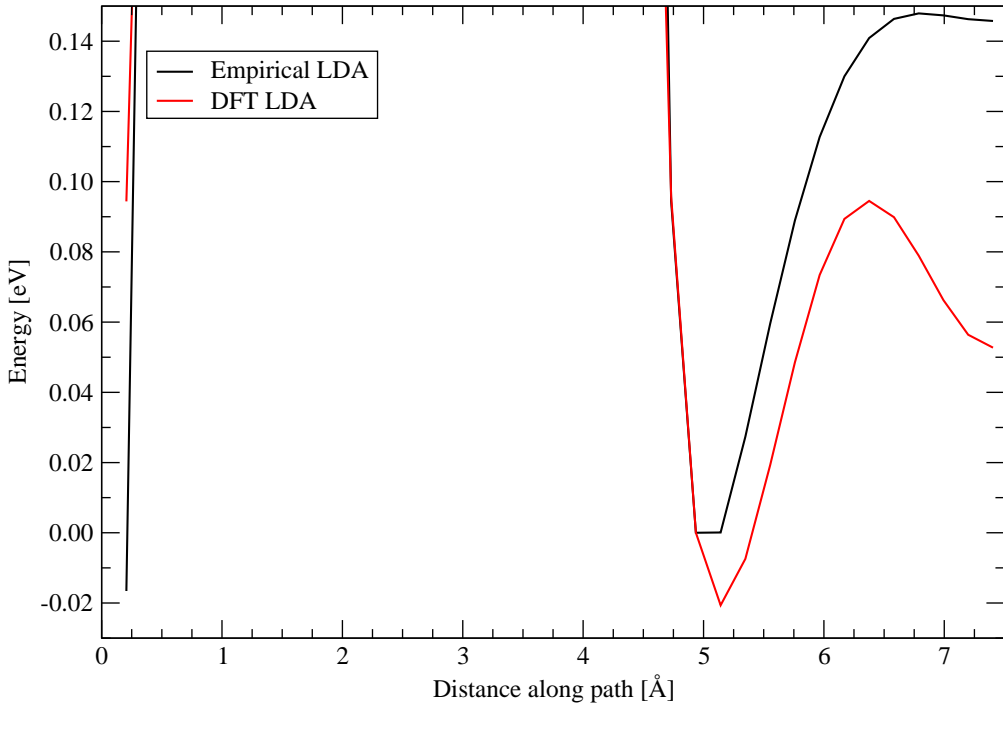


Figure 5.11: The two paths along which the energy scan in KC₁₂ is plotted. The unit cell is marked in black with the paths stretching in the direction of the arrows. The three absorption sites are marked 1, 2 and 3 and the five important energy barriers are marked A, B, C, D and E. K positions are denoted with black filled circles and the graphite lattice is shown.

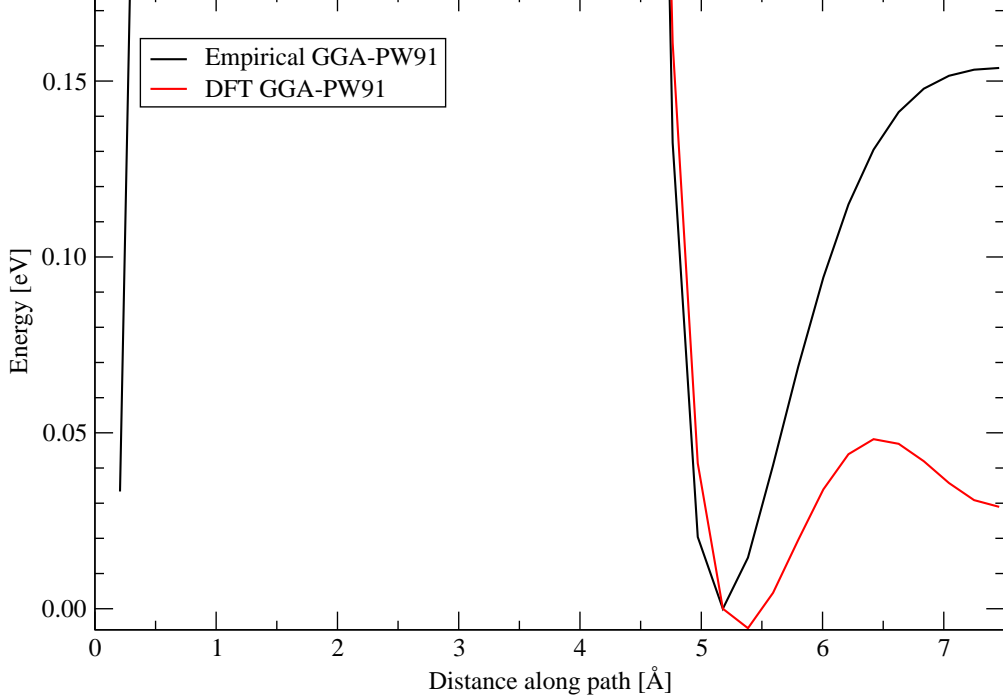
the forward barrier height ($E_{2 \rightarrow 3} \sim 1/3 E_{2 \leftarrow 3}$). These discrepancies will cause a classical simulation using these potentials to pass too easily from site 2 to 3 but find itself trapped in site 3 with the high barriers surrounding it, when compared with DFT molecular dynamic simulations.

In energy scan 2 we can see that empirical potentials are now performing markedly better than for scan 1. Barrier D is reproduced excellently using the empirical data and is within 5 meV of the DFT barrier. The position of both the type 2 absorption sites is also in excellent agreement. The following larger barrier, E, is well produced in the forward trajectory but the disagreement between DFT and the empirical potentials as to the depth of site 1 makes the reverse barrier height nearly a factor of 2 higher than for DFT. Also the empirical potentials predict site 1 to be more favourable than site 2, while DFT predicts the opposite. This disagreement will cause a classical simulation using these potentials in KC₁₂ to find the H₂ molecule trapped at site 1 facing an oversized barrier, when compared with a DFT molecular dynamics simulation. Tuning the temperature to reduce this barrier will make passage over barrier D trivial.

It can clearly be seen that in this material the energy barriers to diffusion are asymmetric and must have a *forward* and *reverse* height. Barriers A and B are indistinguishable from the barrier due to the close approach of H₂ and K and so no useful data

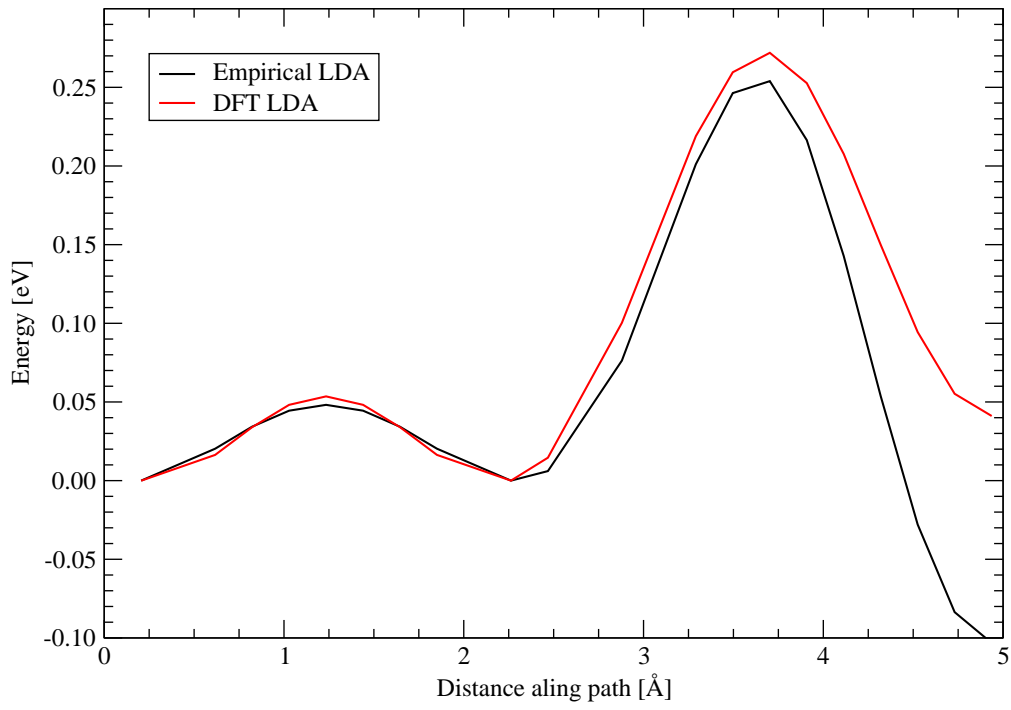


(a) KC₁₂ LDA, scan 1.

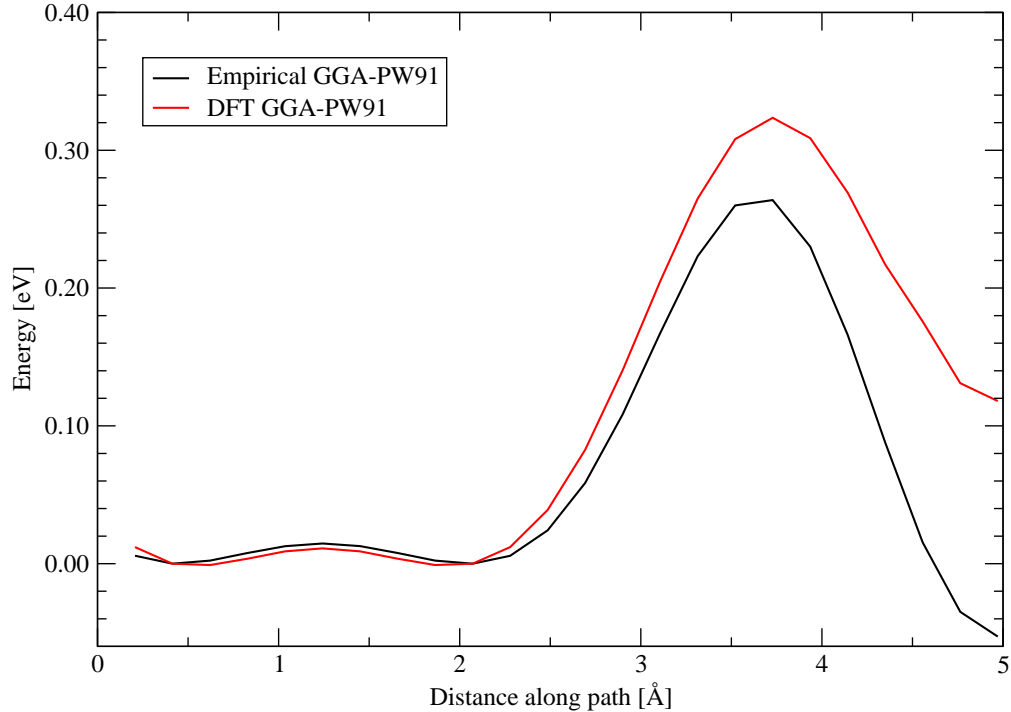


(b) KC₁₂ GGA-PW91, scan 1.

Figure 5.12: H₂ energy scans along scan 1 given in 5.11 comparing DFT with empirical data for (a) LDA and (b) GGA-PW91. The initial extremely large barrier is barriers A and B combined with the path passing through a K atom, the subsequent minima is then site 2 followed by barrier C then finishing at site 3.



(a) KC₁₂ LDA, scan 2.



(b) KC₁₂ GGA-PW91, scan 2.

Figure 5.13: H₂ energy scans along scan 2 given in 5.11 comparing DFT with empirical data for (a) LDA and (b) GGA-PW91. The scan starts at site 2, the first small barrier is D then to the minima for site 2, over barrier E until finally finishing at site 1.

4 Conclusions and discussion

Barrier height, E_b [eV]					
	LDA		GGA-PW91		
	DFT	Empirical	DFT	Empirical	
C					
$2 \rightarrow 3$	0.11516	0.14791	0.05374	0.15372	
$2 \leftarrow 3$	0.04179	0.00214	0.01924	N/A	
D					
$2 \rightarrow 2$	0.05360	0.04818	0.01210	0.01463	
$2 \leftarrow 2$	0.05357	0.04820	0.01210	0.01464	
E					
$2 \rightarrow 1$	0.27195	0.25392	0.32454	0.26384	
$2 \leftarrow 1$	0.23086	0.35712	0.20552	0.31677	

Table 5.6: The barriers to H_2 diffusion in KC_{12} .

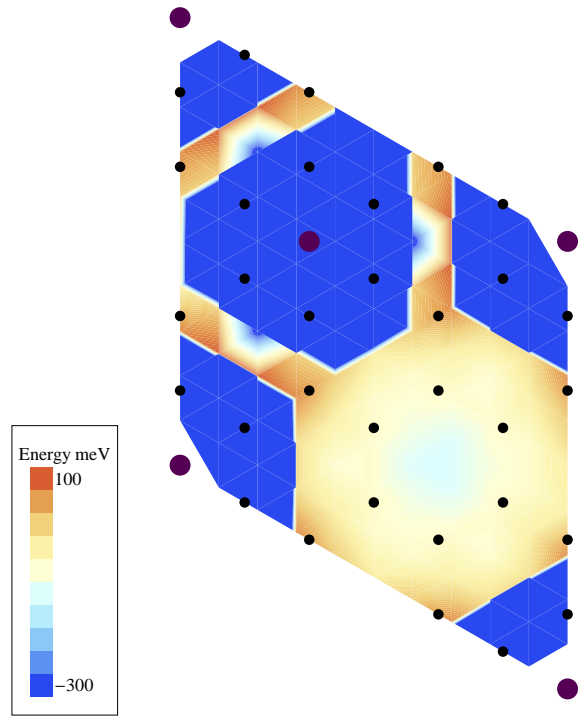
for these barriers is available. The symmetric barrier of C has both forward and reverse heights reported to confirm the symmetry of the barrier. The measurable barrier heights are given in table 5.6.

Energy-difference landscapes are shown for KC_{12} in figure 5.14 with (a) showing LDA and (b) showing GGA-PW91 results. We can see that the effect of the potential overestimating barrier C gives an absorption energy at site 3 that is too small with the empirical potentials, i.e. the energy minima is not low enough. The accurate representation of barrier D with both forms of the empirical potential gives the landscape a clear equality with DFT (shown by the hexagonal white ring in both 5.14(a) and 5.14(b) joining the six equivalent type-2 sites).

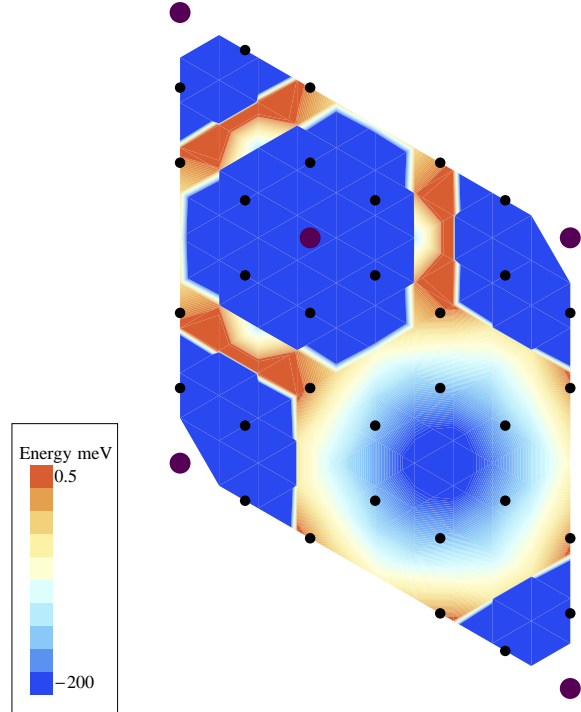
4 Conclusions and discussion

KC_{14} has been shown to favourably absorb hydrogen with LDA and GGA-PW91. KC_{12} has been shown to favourably absorb hydrogen at all three binding sites within the DoE targets with LDA and only marginally unfavourably absorbs H_2 with GGA-PW91. The results for hydrogen binding with LDA are within 0.004 eV of the experimental values reported by Purewal [96].

The stability of KC_{12} and KC_{14} against decomposition into pure graphite and KH is



(a) KC₁₂ energy-difference DFT LDA landscape.



(b) KC₁₂ energy-difference DFT GGA-PW91 landscape

Figure 5.14: Energy-error landscapes between DFT and empirical calculations with (a) showing LDA results and (b) GGA-PW91 results for KC₁₂.

4 Conclusions and discussion

guaranteed (as confirmed by experiments of stable hydrogenated stage-II KC₂₄[93, 94, 96, 116, 169]) with the calculated stability energies, ΔE_{form} (using the equation given in the first paragraph of section 6 on page 133) shown in table 5.7 along with stability energy calculated from the hydrogenated compound, ΔE_{form}^* , using equation 3.3 on page 94. For KC₁₄ ΔE_{form}^* is the energy representing the stability against decomposition into pure graphite, KH and a single H₂ molecule in the gas phase per unit cell.

	ΔE_{form}		ΔE_{form}^*	
	LDA	GGA-PW91	LDA	GGA-PW91
H ₂ +KC ₁₄	-0.203	+0.820	-0.005	+0.872
H ₂ +KC ₁₂	-0.254	+0.515	N/A	N/A
Site A	N/A	N/A	-0.041	0.389
Site B	N/A	N/A	-0.012	0.471
Site C	N/A	N/A	-0.062	0.487

Table 5.7: Stability energies (eV unit), ΔE_{form} , for formation of KC₁₂ and KC₁₄ from free atoms. Stability is calculated against decomposition of the GIC into the metal in its standard state and pure graphite. N.B. stable GICs have positive values for ΔE_{form} .

We can see that ΔE_{form} for both KC₁₄ and KC₁₂ border stability with LDA predicting slightly unstable hydrogenated compounds while GGA-PW91 predicts stable compounds. In KC₁₂ we can see that the stability energies follow the pattern of the absorption energies: those with the most favourable binding show the most stable energy. We see that E_{form}^* , the stability energy taking into account H₂ binding energy, is slightly less stable for KC₁₂ than for KC₁₄.

The diffusion patterns of H₂ within KC₁₄ and KC₁₂ compounds depend strongly upon the barriers to diffusion. We can see from the energy landscapes that these compounds exhibit very different energy landscapes to H₂. The barriers to diffusion of H₂ in KC₁₂ have been shown to be more varied presenting three main absorption sites and three likely crossable barriers, while hydrogenated KC₁₄ has been shown to offer just one absorption site and two crossable barriers. The process of diffusion within the more complex KC₁₂ compound is expected to exhibit on two different time-scales, with two barriers within a factor of 2 while the third barrier is markedly higher in both LDA and GGA-PW91. The presence of three absorption sites with extremely similar predicted binding energies and

4 Conclusions and discussion

the addition of energetic barriers go some way to fulfilling the requirement of Lindsell [168] in order to explain experimental neutron peak-splitting data seen in hydrogenated stage-II KC₂₄. It is hoped that the similar, yet distinct from KC₁₄, KC₁₂ structure can be used in future to fit experimental data from hydrogenating KC₂₄. We see that further refinements to the models are necessary to recover the experimental values for jump rates and associated residency times. In spite of this we notice that the calculated values, while presenting a broad range of jump rates, do bracket the experimental values obtained by Purewal [96] with DFT LDA results performing considerably better than GGA-PW91.

The success of the potentials constructed in this chapter has been shown for KC₁₄ and KC₁₂ with varying degrees of success. It is hoped that these can be further honed and will then be able to fit DFT data accurately and allow rapid classical molecular dynamics simulations to be performed on these compounds. The similarity between the empirical and DFT landscapes, shown in the energy-error plots in §3.2, confirm that the key interactions within these compounds are the H₂-K (dominating the binding of H₂ in the GIC) and a purely repulsive H₂-C interaction that is responsible for most of the small barriers to diffusion.

This chapter has shown that the K-GIC structure used for calculations, KC₁₄, is subtly different from the experimental structure, KC₂₄ (with a KC₁₂ in-plane structure). While the hydrogen absorption properties of each are extremely similar, the diffusion properties of each are markedly different. This small correction to H₂ dynamics on moving from the KC₁₄ to the KC₁₂ structure is shown to help correct the comparison with experiment.

Conclusions and discussion

The dominating question posed by this thesis is whether alkali and alkaline-earth GICs are suitable for hydrogen storage. It has been shown in this thesis that some alkaline-earth metal GICs favourably absorb hydrogen but unfortunately all the alkaline-earth GICs (Be, Mg, Ca, Sr and Ba) are extremely unstable against decomposition into pure graphite and the metal hydride upon hydrogenation. The energetics being dominated by the strong binding of the metal hydride.

The story for the alkali GICs is very different. The thesis shows that they favourably absorb hydrogen with the lower metal concentration GICs (exhibiting high stoichiometries such as MC_{14}) most favourably absorbing hydrogen molecularly. The work showed that the heavier alkali GICs of KC_n , RbC_n and CsC_n are all stable against decomposition into the metal hydride and pure graphite, with stability improving as you descend the alkali series. These calculations agree well with experiments performed on all three of these materials. These heavier alkali GICs are clearly worth extra study and investigation to definitively understand their dynamics of hydrogen absorption. The strength of the binding of the metal to the GIC and the strength of the binding of the metal hydride are the dominant factors determining the stability of the hydrogenated GICs.

Evidence was presented in the thesis that the stability of the GICs, determined by the formation energy, is strongly dependent upon hybridisation of the metal intercalant orbitals with the carbon orbitals of graphite. Intercalants with empty d -orbitals find them shifted below the Fermi energy and broadened as they hybridise and become involved in binding. This mechanism is not present in the lighter alkali and alkaline-earth metals. The involvement of these high angular momentum orbitals improves the formation

energetics greatly, creating a step jump in the outright stability in all GICs studied.

The GICs of Be, Mg and Na are all shown to be energetically unfavourable versus the metal and pure graphite. This resistance to formation agrees well with experiment where these GICs have either never been made or only made in extreme environments or low metal concentrations.

While the bonding of the H₂ molecule in the GICs is of little importance to the stability of the hydrogenated material the mechanisms are still of interest. Calculations presented in the thesis make it clear that the main two contributions to H₂-metal bonding are the charge-quadrupole and charge induced dipole interactions. These two interactions together fully described the binding of H₂ to metal ions at further distances where orbital overlap, and thus chemical bonding, are not taking place. DFT has been shown to produce over-binding, with various success, when compared with more accurate CCSD(T) calculations. For fully ionised systems, close to the environments seen in GICs, DFT was shown to perform markedly better. It would be favourable to calculate all H₂ binding processes with high-level quantum chemistry over DFT to reduce errors.

In depth analysis in the thesis show that the important factors governing the diffusion of hydrogen in K-GICs can be captured with DFT. The energy landscapes and energy barriers produced by DFT bracket the experimental values obtained with LDA performing better than GGA-PW91. The essential barriers to diffusion are shown to be due to C-H₂ interactions while the symmetry is broken by K-H₂ interactions. Molecular dynamics simulations could allow the K-GIC models to be further improved to gain proper insight into the accuracy of DFT for predicting experimental diffusion data, although preliminary indications suggest the important features are included in DFT.

The simple pair potentials developed in this work showed large departures from DFT when used for KC₁₂, for which they were not parametrised. Further refinement of the potentials and the analysis of their performance in long dynamical simulations, again both experiment and DFT, will allow the real deficiencies to become apparent.

Appendices

Appendix **A**

Functional variation

This derivation of functional variation, the more general form of the variational principle, will follow that of Szabo and Ostlund [101] and will be used towards the end of the derivation of the Hartree-Fock method to minimise a single Slater determinant (3).

Consider the expectation value of the Hamiltonian operator with some wave function Φ , such that the energy given is a functional of this wave function,

$$E[\Phi] = \langle \Phi | \hat{\mathbf{H}} | \Phi \rangle, \quad (\text{A.1})$$

where the energy depends upon the form of the wave function rather than on a specific variable and is thus a functional of Φ .

If we wish to vary the energy then we must change the form of Φ by some small amount, $\delta\Phi$, to form a slightly different wave function given by $\tilde{\Phi} = \Phi + \delta\Phi$, and the new energy will be

$$\begin{aligned} E[\tilde{\Phi}] &= E[\Phi + \delta\Phi] \\ &= \langle \Phi + \delta\Phi | \hat{\mathbf{H}} | \Phi + \delta\Phi \rangle. \end{aligned} \quad (\text{A.2})$$

We can now expand A.2 fully to give,

$$\begin{aligned} E[\Phi + \delta\Phi] &= \langle \Phi | \hat{\mathbf{H}} | \Phi \rangle + \underbrace{\left[\langle \delta\Phi | \hat{\mathbf{H}} | \Phi \rangle + \langle \Phi | \hat{\mathbf{H}} | \delta\Phi \rangle \right]}_{\delta E} + \dots \\ \implies \delta E &= \langle \delta\Phi | \hat{\mathbf{H}} | \Phi \rangle + \langle \Phi | \hat{\mathbf{H}} | \delta\Phi \rangle \\ &= \delta \langle \Phi | \hat{\mathbf{H}} | \Phi \rangle, \end{aligned} \quad (\text{A.3})$$

where δ has been treated like the differential operator. The first variation of the energy $E[\tilde{\Phi}]$ is δE and includes all linear terms of the variation. So we can write the *full* variation of $E[\tilde{\Phi}]$ as

$$E[\tilde{\Phi}] = E[\Phi + \delta\Phi] = E[\Phi] + \delta E + \dots \quad (\text{A.4})$$

To find the minimum value of A.4 (to first order) we set the first variation to zero, while this will specify only a stationary point it will generally give the minimal value,

$$\delta E = 0. \quad (\text{A.5})$$

We cannot vary the wave function Φ arbitrarily in order to minimise $E[\tilde{\Phi}]$; it must remain normalised, i.e. $\langle \Phi | \Phi \rangle = 1$. In general the possible parameters affecting Φ and thus E will be complicated and thus there is no simple way to find a minimal value of E . We shall then limit ourselves to only linear variations of Φ , thus we can use the linear superposition ansatz and posit

$$|\Phi\rangle = \sum_{i=1}^N c_i |\phi_i\rangle, \quad (\text{A.6})$$

where $|\Phi\rangle$ is represented on the predetermined *fixed* set of N basis functions, $\{|\phi_N\rangle\}$. The problem of finding the optimal Φ to minimise E then requires finding the optimum set of coefficients, $\{c_N\}$ - a matrix diagonalisation problem.

We cannot simply solve the problem by differentiating A.1 as our coefficients are not independent. Instead we use the method of Lagrange undetermined multipliers with the constraint of Φ remaining normalised. We can then build the Lagrangian and expand it using A.6,

$$\begin{aligned} \mathcal{L} &= \langle \Phi | \hat{\mathbf{H}} | \Phi \rangle - E (\langle \Phi | \Phi \rangle - 1), \\ &= \sum_{i,j} c_i^* c_j \langle \phi_i | \hat{\mathbf{H}} | \phi_j \rangle - E \left(\sum_{i,j} c_i^* c_j \langle \phi_i | \phi_j \rangle - 1 \right), \end{aligned} \quad (\text{A.7})$$

where E is the undetermined multiplier. Using the fact that our basis, $\{\phi_N\}$, is fixed and our flexibility is in our choice of the coefficients, $\{c_N\}$, in the expansion A.6, then setting the first variation of the Langrangian to zero, $\delta\mathcal{L} = 0$, gives

$$\begin{aligned} \delta\mathcal{L} &= \sum_{i,j} \delta c_i^* c_j \langle \phi_i | \hat{\mathbf{H}} | \phi_j \rangle - E \sum_{i,j} \delta c_i^* c_j \langle \phi_i | \phi_j \rangle \\ &\quad + \sum_{i,j} c_i \delta c_j^* \langle \phi_i | \hat{\mathbf{H}} | \phi_j \rangle - E \sum_{i,j} c_i \delta c_j^* \langle \phi_i | \phi_j \rangle = 0, \end{aligned} \quad (\text{A.8})$$

where we have set the first variation to zero just as we did in A.5 to find the minimal value.

Noting that E is real we can then rewrite A.8 by carefully rearranging the summation indices and merging terms. Using the standard notation for the elements of the matrix of the Hamiltonian on the basis $\{\phi_N\}$, i.e. $H_{ij} = \langle \phi_i | \hat{\mathbf{H}} | \phi_j \rangle$, we can write

$$\sum_i \delta c_i^* \left[\sum_j H_{ij} c_j - E S_{ij} c_j \right] + \text{complex conjugate} = 0, \quad (\text{A.9})$$

where we have noted that the basis functions need not be orthonormal but may have an overlap given by the matrix element $S_{ij} = \langle \phi_i | \phi_j \rangle$.

Since our choice of δc_i^* is arbitrary, c_i and c_i^* are both independent variables, the only way A.9 can be zero is if the quantity in square brackets is,

$$\sum_j H_{ij} c_j = E \sum_j S_{ij} c_j, \quad (\text{A.10})$$

or in matrix notation, defining the column vector $\vec{c} = (c_1, c_2, \dots, c_N)$,

$$\hat{\mathbf{H}} \vec{c} = E \hat{\mathbf{S}} \vec{c}. \quad (\text{A.11})$$

This general form of the variational principle will allow us to vary the ansatz wave function when deriving the Hartree-Fock equation in section 1.

Appendix **B**

Hartree-Fock method derivation

The derivation given here for the Hartree-Fock (HF) method shall mirror that of Szabo and Ostlund [101]. The major difference between the two shall be that this derivation will be given in *physicists'* Dirac bracket notation, whereas the work of Szabo and Ostlund [101] is given in chemists' notation. While Dirac notation preserves the concept of the scalar product between two vectors, with the conjugated wave function appearing in the bra and non-conjugated in the ket ($|\chi_i\rangle^* = \langle\chi_i|$), chemists' notation groups spin orbitals by electron so need to be expanded directly to find the conjugated spin orbitals. Table B.1 shows the relationship between the two notations.

One-electron spin orbitals

$$[\chi_i(\vec{x}_1) | h(\vec{r}_1) | \chi_j(\vec{x}_1)] = \langle \chi_i(\vec{x}_1) | h(\vec{r}_1) | \chi_j(\vec{x}_1) \rangle$$

(abbreviated to $[i|h|j] = \langle i|h|j \rangle$)

Two-electron spin orbitals

$$[\chi_i(\vec{x}_1) \chi_j(\vec{x}_1) | \chi_k(\vec{x}_2) \chi_l(\vec{x}_2)] = \langle \chi_i(\vec{x}_1) \chi_k(\vec{x}_2) | \chi_j(\vec{x}_1) \chi_l(\vec{x}_2) \rangle$$

(abbreviated to $[ik|jl] = \langle ij|kl \rangle$)

Table B.1: The relationship between chemists' notation (abbreviated as $[i|h|j]$ and $[ik|jl]$) and physicists' Dirac bracket notation (abbreviated as $\langle i|h|k \rangle$ and $\langle ij|kl \rangle$). Note that the chemists' notation groups electrons together (those orbitals with \vec{x}_1 appear on the left, those with \vec{x}_2 on the right) while physicists' notation groups conjugated spin orbitals together.

1 The Hartree-Fock equations

Hartree-Fock theory will be equated to a single determinant theory, that is it shall be implemented as a method to find the best approximation to the ground state wave function, Ψ_0 , by finding the optimum set of spin orbitals, $\{\chi_N\}$, to find in the determinant,

$$|\Psi_0\rangle = |\chi_1 \chi_2 \dots \chi_a \chi_b \dots \chi_N\rangle. \quad (\text{B.1})$$

The HF method is used to solve the reduced electronic Schrödinger equation of 2.50, $E[\{\chi_N\}] = \langle \Psi | \hat{\mathbf{H}}_e | \Psi \rangle = \langle \chi_1 \chi_2 \dots \chi_N | \hat{\mathbf{H}}_e | \chi_1 \chi_2 \dots \chi_N \rangle$. Using the variational principle we wish to $E[\{\chi_N\}]$ by varying the spin orbitals $\{\chi_N\}$. The variation of the spin orbitals shall be constrained such that any pair of spin orbitals is orthonormal,

$$\begin{aligned} \langle \chi_a | \chi_b \rangle &= \delta_{ab} \\ \implies \langle \chi_a | \chi_b \rangle &= \begin{cases} 0 & \text{if } a \neq b, \\ 1 & \text{if } a = b. \end{cases} \end{aligned} \quad (\text{B.2})$$

Optimisation of this problem under constraint will use the Lagrangian method of undetermined multipliers, we form the Lagrangian,

$$\mathcal{L}[\{\chi_N\}] = E[\{\chi_N\}] - \sum_{a=1}^N \sum_{b=1}^N \varepsilon_{ba} (\langle \chi_a | \chi_b \rangle - \delta_{ab}), \quad (\text{B.3})$$

where the energy functional is given by Schrödinger-type equation including single particle *core-Hamiltonian*, $h(i)$, and the electron-electron interaction term,

$$E[\{\chi_N\}] = \sum_{a=1}^N \langle \chi_a | h | \chi_a \rangle + \frac{1}{2} \sum_{a=1}^N \sum_{b=1}^N (\langle \chi_a \chi_b | \chi_a \chi_b \rangle - \langle \chi_a \chi_b | \chi_b \chi_a \rangle). \quad (\text{B.4})$$

Note that the difference in the last two terms of B.4 is in the order of indices in the last pair of spin-orbitals in the two Dirac brackets. The single-particle core-Hamiltonian for electron 1 is

$$h(1) = -\frac{1}{2} \nabla_1^2 - \sum_{\nu=1}^n \frac{Z_\nu}{r_{1\nu}}, \quad (\text{B.5})$$

where the designation $h(1)$ is shorthand for $h(\vec{x}_1)$ thus denoting the information for electron 1. The first term is the kinetic energy operator for electron 1 (using the Laplacian operator, ∇^2); the second term is the coulomb operator for the electron interacting with the field created by the n nuclei with the ν -th nucleus has charge Z_ν and is at a distance of $r_{1\nu}$ from electron 1.

2 The coulomb and exchange operators

Varying the Lagrangian of B.3, by varying the spin-orbitals of the Slater determinant (as shown in 3), and setting the first variation to zero allows us to find the lowest energy solution. The ground state energy E_0 is found by solving the Hartree-Fock integro-differential equation acting on electron 1 in orbital χ_a ,

$$h(1)\chi_a(1) + \sum_{b \neq a} \left[\int d\vec{x}_2 |\chi_b(2)|^2 \frac{1}{r_{12}} \right] \chi_a(1) - \sum_{b \neq a} \left[\int d\vec{x}_2 \chi_b^*(2) \chi_a(2) \frac{1}{r_{12}} \right] \chi_b(1) = \varepsilon_a \chi_a(1). \quad (\text{B.6})$$

The two terms in B.6 that are not part of the single-particle core-Hamiltonian shall be grouped into the Hartree-Fock field acting on electron 1 in spin-orbital χ_a ,

$$v_{\text{HF}}(1)\chi_a(1) = \sum_{b \neq a} \left[\int d\vec{x}_2 |\chi_b(2)|^2 \frac{1}{r_{12}} \right] \chi_a(1) - \sum_{b \neq a} \left[\int d\vec{x}_2 \chi_b^*(2) \chi_a(2) \frac{1}{r_{12}} \right] \chi_b(1). \quad (\text{B.7})$$

This Hartree-Fock field is the part of B.6 that separates this expression from a set of non-interacting electrons moving in the field of the nuclei to interacting electrons, thus the HF integro-differential equation can be written,

$$h(1)\chi_a(1) + v_{\text{HF}}(1)\chi_a(1) = \varepsilon_a \chi_a(1), \quad (\text{B.8})$$

$$\left[-\frac{1}{2}\nabla_1^2 - \sum_{\nu=1}^n \frac{Z_\nu}{r_{1\nu}} + v_{\text{HF}}(1) \right] \chi_a(1) = \varepsilon_a \chi_a(1). \quad (\text{B.9})$$

We will now decompose the HF field into two components: the coulomb operator and the exchange operator. The coulomb operator will concern pairs of electrons in different spin orbitals, a classical form of operator that could be described as a *local* operator. It is local in the sense that it can be written as a field felt at a given location (and spin) \vec{x}_1 . The exchange operator appears purely because of the choice of an antisymmetric wave function (thus an effect of including the Pauli exclusion principle in the theory). This exchange operator cannot be written as a field at a position \vec{x}_1 as the result of acting with this operator on an orbital depends upon the value of the orbital throughout all space, not just upon its local value at \vec{x}_1 , and is said to be an *non-local* operator.

2 The coulomb and exchange operators

The coulomb and exchange operators making up v_{HF} in B.7 make up the electron-electron interaction terms of the HF equations. This Hartree-Rock field felt by electron

2 The coulomb and exchange operators

1 in orbital χ_a has the form

$$v_{\text{HF}}(1) \chi_a = \underbrace{\sum_{b \neq a} \left[\int d\vec{x}_2 |\chi_b(2)|^2 \frac{1}{r_{12}} \right] \chi_a}_{\text{coulomb operator}} - \underbrace{\sum_{b \neq a} \left[\int d\vec{x}_2 \chi_b^*(2) \chi_a(2) \frac{1}{r_{12}} \right] \chi_b}_{\text{exchange operator}}. \quad (\text{B.10})$$

Without these terms, the HF equation of B.8 would simply become

$$h(1) \chi_a(1) = \varepsilon_a \chi_a(1), \quad (\text{B.11})$$

a single-particle problem. The solution of this equation of non-interacting electrons would be relatively simple; the two terms of the HF field complicate the solution but modify the HF method to represent real electrons.

2.1 The coulomb operator

The classical electrostatic interaction between electrons is included in the coulomb operator term and has the form of a coulomb potential. The exact coulomb interaction between two electrons would be the two-electron operator $1/r_{12}$. In HF theory this two-electron operator is replaced by a one-electron potential felt by electron 1 in spin-orbital χ_a ,

$$v_a^{\text{coul}}(1) = \sum_{b \neq a} \int d\vec{x}_2 |\chi_b(2)|^2 \frac{1}{r_{12}}. \quad (\text{B.12})$$

Interpreting this potential we see that the integral has the effect of averaging the $1/r_{12}$ potential felt by electron 1 in spin-orbital χ_a due to electron 2 in spin-orbital χ_b over all space and spin coordinates weighted by the probability $d\vec{x}_2 |\chi_b(2)|^2$ that electron 2 occupies the volume element $d\vec{x}_2$ centred on \vec{x}_2 . Thus this is the average potential felt by electron 1 in χ_a due to electron 2 with every space and spin coordinate in orbital χ_b . Summing over all the orbitals that electron 1 is not in ($\sum_{b \neq a}$) gives a (space and spin) average potential felt by electron 1 due to the other ($N - 1$) electrons occupying every other orbital. We can now define a one-electron operator that will give the local coulomb potential at \vec{x}_1 ,

$$\mathcal{J}_b(1) = \int d\vec{x}_2 |\chi_b(2)|^2 \frac{1}{r_{12}}. \quad (\text{B.13})$$

2.2 The exchange operator

The second term of the Hartree-Fock field arises purely from the adapting the old Hartree theory to respect the antisymmetry principle and is the exchange term. This term has no classical interpretation; it cannot be written as a field at a given position. We gain a

3 Minimising a single Slater determinant

clearer understanding of the main differences between the coulomb and exchange terms of v_{HF} if we look at them together with the coulomb term rearranged slightly. The two operators acting upon electron 1 in orbital χ_a have the form

$$\mathcal{J}_b(1) \chi_a = \left[\int d\vec{x}_2 \chi_b^*(2) \frac{1}{r_{12}} \chi_b(2) \right] \chi_a(1) \quad (\text{B.14})$$

$$\mathcal{K}_b(1) \chi_a = \left[\int d\vec{x}_2 \chi_b^*(2) \frac{1}{r_{12}} \chi_a(2) \right] \chi_b(1), \quad (\text{B.15})$$

where we have defined the exchange operator to be \mathcal{K}_b and have decomposed $|\chi_b(2)|^2 = \chi_b^*(2) \chi_b(2)$.

We can see the difference between operating with the exchange operator on electron 1 in orbital χ_a ($\mathcal{K}_b \chi_a(1)$) compared with operating with the coulomb operator on the same electron in the same orbital ($\mathcal{J}_b \chi_a(1)$); the former operator exchanges the two orbitals to the right of the $1/r_{12}$. The result of operating with this exchange operator on electron 1 in orbital χ_a then needs the value of the orbital throughout all space and spin coordinates, not just the local value of \vec{x}_1 and is thus a non-local operator.

Taking the difference between B.15 and B.14 and using Dirac notation for the spin-orbitals gives an expression that shall be used later,

$$[\mathcal{J}_b(1) - \mathcal{K}_b(1)] |\chi_a(1)\rangle = \langle \chi_b(2) | \chi_b(2) \chi_a(1) \rangle - \langle \chi_b(2) | \chi_a(2) \chi_b(1) \rangle. \quad (\text{B.16})$$

3 Minimising a single Slater determinant

We are now ready to minimise the Lagrangian of B.3 by varying the spin orbitals a small amount,

$$\chi_a \mapsto \chi_a + \delta \chi_a. \quad (\text{B.17})$$

Taking the first variation of the Lagrangian of B.3, $\delta \mathcal{L}$, and setting to zero gives

$$\delta \mathcal{L} [\{\chi_N\}] = \delta E [\{\chi_N\}] - \sum_{a=1}^N \sum_{b=1}^N \varepsilon_{ba} \delta \langle \chi_a | \chi_b \rangle = 0, \quad (\text{B.18})$$

where we have used δ like a differential operator as we did in chapter A thus acting on the Dirac bracket gives $\delta \langle \chi_a | \chi_b \rangle = \langle \delta \chi_a | \chi_b \rangle + \langle \chi_a | \delta \chi_b \rangle$. Acting with this differential operator on the Kronecker delta of B.3 causes this term to vanish.

Expanding $\delta E [\{\chi_N\}]$ in B.18 using the full expansion in terms of the single-particle Hamiltonian expectation value and electron-electron interaction terms from B.4 and

3 Minimising a single Slater determinant

again applying the same rules for δ , gives

$$\begin{aligned}
\delta E [\{\chi_N\}] &= \sum_{a=1}^N (\langle \delta\chi_a | h | \chi_a \rangle + \langle \chi_a | h | \delta\chi_a \rangle) \\
&\quad + \frac{1}{2} \sum_{a=1}^N \sum_{b=1}^N (\langle \delta\chi_a \chi_b | \chi_a \chi_b \rangle + \langle \chi_a \delta\chi_b | \chi_a \chi_b \rangle \\
&\quad \quad + \langle \chi_a \chi_b | \delta\chi_a \chi_b \rangle + \langle \chi_a \chi_b | \chi_a \delta\chi_b \rangle) \\
&\quad - \frac{1}{2} \sum_{a=1}^N \sum_{b=1}^N (\langle \delta\chi_a \chi_b | \chi_b \chi_a \rangle + \langle \chi_a \delta\chi_b | \chi_b \chi_a \rangle \\
&\quad \quad + \langle \chi_a \chi_b | \delta\chi_b \chi_a \rangle + \langle \chi_a \chi_b | \chi_b \delta\chi_a \rangle) \\
\implies \delta E [\{\chi_N\}] &= \sum_{a=1}^N \langle \delta\chi_a | h | \chi_a \rangle + \sum_{a=1}^N \sum_{b=1}^N (\langle \delta\chi_a \chi_b | \chi_a \chi_b \rangle - \langle \delta\chi_a \chi_b | \chi_b \chi_a \rangle) \\
&\quad + \text{ complex conjugate.} \tag{B.19}
\end{aligned}$$

Expanding the second term of $\delta\mathcal{L}$ from B.18, noting that $\langle \chi_a | \chi_b \rangle = \langle \chi_b | \chi_a \rangle^*$ and the Langragian is real and thus the set of Lagrange multipliers, $\{\varepsilon\}$, forms a Hermitian matrix, i.e. $\varepsilon_{ba} = \varepsilon_{ab}^*$, gives

$$\begin{aligned}
\sum_{a=1}^N \sum_{b=1}^N \varepsilon_{ba} \delta \langle \chi_a | \chi_b \rangle &= \sum_{a=1}^N \sum_{b=1}^N \varepsilon_{ba} (\langle \delta\chi_a | \chi_b \rangle + \langle \chi_a | \delta\chi_b \rangle) \\
&= \sum_{a=1}^N \sum_{b=1}^N \varepsilon_{ba} \langle \delta\chi_a | \chi_b \rangle + \sum_{a=1}^N \sum_{b=1}^N \varepsilon_{ab} \langle \chi_b | \delta\chi_a \rangle \\
&= \sum_{a=1}^N \sum_{b=1}^N \varepsilon_{ba} \langle \delta\chi_a | \chi_b \rangle + \sum_{a=1}^N \sum_{b=1}^N \varepsilon_{ba}^* \langle \delta\chi_a | \chi_b \rangle^* \\
&= \sum_{a=1}^N \sum_{b=1}^N \varepsilon_{ba} \langle \delta\chi_a | \chi_b \rangle + \text{ complex conjugate.} \tag{B.20}
\end{aligned}$$

We can now write the explicit form of the first variation of the Lagrangian in B.18 using the results for the first variation of the energy functional in B.19 and the variation of the electron-electron interaction from B.20 to give

$$\begin{aligned}
\delta\mathcal{L} [\{\chi_N\}] &= \sum_{a=1}^N \langle \delta\chi_a | h | \chi_a \rangle + \sum_{a=1}^N \sum_{b=1}^N (\langle \delta\chi_a \chi_b | \chi_a \chi_b \rangle - \langle \delta\chi_a \chi_b | \chi_b \chi_a \rangle) \\
&\quad + \sum_{a=1}^N \sum_{b=1}^N \varepsilon_{ba} \langle \delta\chi_a | \chi_b \rangle + \text{ complex conjugate} = 0. \tag{B.21}
\end{aligned}$$

Factoring the bra $\langle \delta\chi_a |$ on the left hand side of each term and using the expression for the difference between the exchange and coulomb operators from B.16 and returning

3 Minimising a single Slater determinant

to the full wave mechanics notation to specify the expression more fully gives

$$\delta\mathcal{L} [\{\chi_N\}] = \sum_{a=1}^N \int d\vec{x}_1 \delta\chi_a^*(1) \left[h(1) \chi_a(1) + \sum_{b=1}^N (\mathcal{J}_b(1) - \mathcal{K}_b(1)) \chi_a(1) - \sum_{b=1}^N \varepsilon_{ba} \chi_b(1) \right] + \text{complex conjugate} = 0. \quad (\text{B.22})$$

Our choice of $\delta\chi_a(1)$ in B.22 is arbitrary and thus the contents of the square brackets must be zero, rearranging slightly and defining the *Fock operator*, $f(1)$, then yields

$$\underbrace{\left[h(1) + \sum_{b=1}^N (\mathcal{J}_b(1) - \mathcal{K}_b(1)) \right]}_{\text{Fock operator, } f(1)} \chi_a(1) = \sum_{b=1}^N \varepsilon_{ba} \chi_b(1),$$

$$f |\chi_a\rangle = \sum_{b=1}^N \varepsilon_{ba} |\chi_b\rangle. \quad (\text{B.23})$$

This is the final equation of the HF method that is used in the self-consistent field method, written with the Hartree-Fock field as

$$[h(i) + v_{\text{HF}}(i)] \chi_a(i) = \sum_{b=1}^N \varepsilon_{ba} \chi_b(i). \quad (\text{B.24})$$

Coupled cluster method derivation

This derivation will follow that of Fabian [171] but shall use the nomenclature of Szabo and Ostlund [101] for labelling occupied and unoccupied orbitals. Occupied orbitals shall be denoted χ_a , χ_b , χ_c and χ_d while unoccupied orbitals shall be denoted with χ_r , χ_s , χ_t and χ_u .

The coupled cluster method has resulted in extremely accurate calculations of total energies found from solving the electronic Schrödinger equation. It is widely used for ever larger clusters of atoms but is still computationally expensive compared with DFT, but does lend itself well to parallel computing. It represents an exact solution to the many-body electronic problem if N -clusters can be modelled. In reality we are always limited to fewer than 5-electron clusters, i.e. CCSDTQP.

This derivation will be shown for a system of four electrons. This is a simple, non-trivial case and will allow the full derivation of the cluster expansion of the wave function (1) and the explanation of the cluster operator (2).

1 The cluster expansion

To elucidate the coupled cluster method, electron clusters of three electrons will need to be considered. For this purpose we will consider a four electron system as the simplest non-trivial case. The initial wave function for the system, $|\Phi_0\rangle$, shall be obtained from an SCF calculation such as Hartree-Fock and have the form of a Slater determinant (written explicitly in 2.51, chapter 3),

$$|\Phi_0\rangle = |\chi_a\chi_b\chi_c\chi_d\rangle, \quad (\text{C.1})$$

where, as usual, χ_a represents the a -th occupied one-electron eigenstate from the zeroth-order Hamiltonian, in most cases a single electron spin-orbital.

The first obvious improvement to this initial wave function is to add functions that adapt it to include interactions between pairs of electrons. A function that introduces interaction effects (and thus correlation effects) between the a -th and b -th electron shall be written f_{ab} and modifies the initial wave function to become $|\Phi\rangle$ as

$$|\Phi\rangle = |[\chi_a\chi_a + f_{ab}] \chi_c\chi_d\rangle. \quad (\text{C.2})$$

The *cluster functions*, f_{ab} , are as yet undefined. Clearly our choice of electrons a and b was arbitrary and so the modified wave function to include all electron-pair interactions would be a true improvement. If we include the correlation between all pairs of electrons in our four-electron system we arrive at the full *doubles-correlated* wave function,

$$\begin{aligned} |\Phi\rangle = & |\chi_a\chi_b\chi_c\chi_d + f_{ab}\chi_c\chi_d + \chi_a\chi_bf_{cd} + f_{ab}f_{cd} - f_{ac}\chi_b\chi_d \\ & - \chi_a\chi_cf_{bd} - f_{ac}f_{bd} + f_{ad}\chi_b\chi_c + \chi_af_{bc}\chi_d + f_{ad}f_{bc}\rangle. \end{aligned} \quad (\text{C.3})$$

At this stage clusters of increasing numbers of electrons could be added up to N -electron clusters (for an N electron system) that would produce a modified wave function that would include the full set of electron interactions, but would not produce the exact N -electron wave function. At this stage, single-electron “cluster functions” need to be added to the wave function containing correlations between N -electrons to make the exact wave function. These have the effect of allowing the single-electron spin orbitals to relax due to the correlation effects, i.e. the single-electron basis itself can be manipulated to account for the correlation effects. The unwieldy four-electron wave function including

only single and double electron clusters is

$$\begin{aligned}
 |\Phi\rangle = & |\chi_a\chi_b\chi_c\chi_d + f_a\chi_b\chi_c\chi_d + \chi_a f_b\chi_c\chi_d + \chi_a\chi_b f_c\chi_d + \chi_a\chi_b\chi_c f_d \\
 & + f_a f_b\chi_c\chi_d + f_a\chi_b f_c\chi_d + f_a\chi_b\chi_c f_d + \chi_a f_b f_c\chi_d + \chi_a f_b\chi_c f_d \\
 & + \chi_a\chi_b f_c f_d + f_a f_b f_c\chi_d + f_a f_b\chi_c f_d + f_a\chi_b f_c f_d + \chi_a f_b f_c f_d \\
 & + f_a f_b f_c f_d + f_{ab}\chi_c\chi_d + f_{ab}f_c\chi_d + f_{ab}\chi_c f_d + f_{ab}f_c f_d \\
 & + \chi_a\chi_b f_c d + f_a\chi_b f_c d + \chi_a f_b f_c d + f_a f_b f_c d - f_{ac}\chi_b\chi_d \\
 & - f_{ac}f_b\chi_d - f_{ac}\chi_b f_d - f_{ac}f_b f_d - \chi_a\chi_c f_{bd} - f_a\chi_c f_{bd} \\
 & - \chi_a f_c f_{bd} - f_a f_c f_{bd} - f_{ac}f_{bd} + f_{ad}\chi_b\chi_c + f_{ad}f_j\chi_c \\
 & + f_{ad}\chi_b f_c + f_{ad}f_b f_c + \chi_a f_{bc}\chi_d + f_a f_{bc}\chi_d + \chi_a f_{bc} f_d \\
 & + f_a f_{bc} f_d + f_{ad}f_{bc}\rangle . \quad (\text{C.4})
 \end{aligned}$$

The next step is to narrow down the form of the cluster functions and find a more concise notation. Systems with many electrons and including cluster functions for single, double and cross-term triple interactions would be nearly impossible to manipulate in the current form of notation.

2 The cluster operator

In this section we search for a form for the cluster functions, f . In order to simplify the notation, to avoid wave functions like that of C.4, an object that could generate all the cluster functions up to an arbitrary size of electron clusters when applied to the initial zeroth-order wave function, $|\Phi_0\rangle$, would be ideal; an operator fits this description well. We shall define a *cluster operator* as an object that when applied to a zeroth-order wave function generates the wave function that includes all the cluster functions up to the specified size of electron-cluster.

The cluster functions for electrons need to be antisymmetric under exchange of indices, thus exchanging two electrons will change the sign of the wave function (allowing the wave function to respect the Pauli exclusion/antisymmetry principle). We also require the cluster functions to be strongly orthogonal to the occupied single-electron states, χ_a ,

$$f_{ab} = -f_{ba} \quad (\text{C.5})$$

$$\int \chi_c^*(\vec{x}_1) f_{ab}(\vec{x}_1, \vec{x}_2) d\vec{x}_1 = 0 \quad \forall a, b, c. \quad (\text{C.6})$$

2 The cluster operator

The constraints of C.5 and C.6 lead us to simplest form of the two-electron cluster function to be

$$f_{ab}(\vec{x}_1, \vec{x}_2) = \frac{1}{2} \sum_{r,s}^N t_{ab}^{rs} [\chi_r(\vec{x}_1) \chi_s(\vec{x}_2) - \chi_s(\vec{x}_1) \chi_r(\vec{x}_2)], \quad (\text{C.7})$$

where the summation is over all pairs of orbitals r and s , e.g. in a two-orbital system both pairs $r = 1$ and $s = 2$, $r = 2$ and $s = 1$ would need be counted, the factor of $1/2$ cancels this double-counting. The summation term for the case $r = s$ would vanish. We assert that the prefactors are antisymmetric under exchange of indices,

$$t_{ab}^{rs} = -t_{ba}^{rs} \quad \text{and} \quad t_{ab}^{rs} = -t_{ab}^{sr}.$$

We now define an operator that when applied to the pair of occupied single-electron states, $\chi_a \chi_b$ in a zeroth-order wave function, will replace them with the cluster function f_{ab} from C.7. This operator will then produce the coupled cluster wave function for two-electron clusters. We can represent this as a disturbance which shall excite two electrons from the occupied orbitals a and b and into the virtual unoccupied orbitals r and s . Using the nomenclature of the second quantisation of quantum mechanics, we define this excitation as two electrons annihilated from occupied orbitals a and b and two electrons created in the unoccupied orbitals r and s . We now define the two-electron excitation operator, the two-electron excitation operator $\hat{\mathbf{t}}_{ab}$, as

$$\hat{\mathbf{t}}_{ab} = \frac{1}{2} \sum_{r,s}^N t_{ab}^{rs} \mathbf{a}_r^\dagger \mathbf{a}_s^\dagger \mathbf{a}_b \mathbf{a}_a, \quad (\text{C.8})$$

where \mathbf{a}_r^\dagger represents the creation operator of an electron into orbital r (and the \dagger represents the Hermitian conjugate); \mathbf{a}_a is the annihilation operator for an electron in orbital a ; the prefactor t_{ab}^{rs} now gains the meaning of the probability amplitude for the excitation of a pair of electrons from the orbitals a and b to the orbitals r and s . The creation and annihilation operators are restricted to the occupied and unoccupied orbitals only, such that $\mathbf{a}_a^\dagger |\chi_1 \chi_2 \dots \chi_a \chi_b \dots \chi_r \chi_s\rangle = 0$ and $\mathbf{a}_r |\chi_1 \chi_2 \dots \chi_a \chi_b \dots \chi_s\rangle = 0$, so different excitation operators commute $[\hat{\mathbf{t}}_{ab}, \hat{\mathbf{t}}_{cd}] = 0$.

Operating with the excitation operator of C.8 upon the occupied states $\chi_a(\vec{x}_1)$ and $\chi_b(\vec{x}_2)$ will produce the cluster function $f_{ab}(\vec{x}_1, \vec{x}_2)$,

$$\hat{\mathbf{t}}_{ab} \chi_a(\vec{x}_1) \chi_b(\vec{x}_2) = f_{ab}(\vec{x}_1, \vec{x}_2). \quad (\text{C.9})$$

Successive application of the excitation operator will produce products of cluster functions, thus (returning to Dirac notation),

$$\hat{\mathbf{t}}_{ab} \hat{\mathbf{t}}_{cd} |\chi_a \chi_b \chi_c \chi_d\rangle = |f_{ab} f_{cd}\rangle. \quad (\text{C.10})$$

2 The cluster operator

We can now define a general excitation operator for exciting clusters of m electrons (where $m < N$ and N is the total number of electrons in the system),

$$\hat{\mathbf{t}}_{\{a\}} = \frac{1}{m!} \sum_{\{r\}}^N t_{\{a\}}^{\{r\}} \prod_{p=r, q=a}^m \mathbf{a}_p^\dagger \mathbf{a}_q, \quad (\text{C.11})$$

where $\{a\}$ represents the set of m occupied orbitals that electrons shall be excited from; $\{r\}$ represents the set of m unoccupied virtual orbitals electrons shall be promoted; the sum runs over the N electrons in the system, the product runs over the m electrons within the cluster.

The excitation operator, in its singular form, will produce the single-electron “cluster” functions alluded to in equation C.4

$$\hat{\mathbf{t}}_a = \sum_a^N t_a^r \mathbf{a}_r^\dagger \mathbf{a}_a. \quad (\text{C.12})$$

Using the excitation operators defined in C.11 we can now rewrite the unwieldy four-electron wave function in C.4 in a more compact form as

$$|\Phi\rangle = \left[1 + \sum_a^N \hat{\mathbf{t}}_a + \frac{1}{2} \sum_{a,b}^N \hat{\mathbf{t}}_a \hat{\mathbf{t}}_b + \frac{1}{6} \sum_{a,b,c}^N \hat{\mathbf{t}}_a \hat{\mathbf{t}}_b \hat{\mathbf{t}}_c + \frac{1}{24} \sum_{a,b,c,d}^N \hat{\mathbf{t}}_a \hat{\mathbf{t}}_b \hat{\mathbf{t}}_c \hat{\mathbf{t}}_d \right. \\ \left. + \frac{1}{2} \sum_{a,b}^N \hat{\mathbf{t}}_{ab} + \frac{1}{2} \sum_{a,b,c}^N \hat{\mathbf{t}}_{ab} \hat{\mathbf{t}}_c + \frac{1}{4} \sum_{a,b,c,d}^N \hat{\mathbf{t}}_{ab} \hat{\mathbf{t}}_c \hat{\mathbf{t}}_d + \frac{1}{8} \sum_{a,b,c,d}^N \hat{\mathbf{t}}_{ab} \hat{\mathbf{t}}_{cd} \right] |\Phi_0\rangle, \quad (\text{C.13})$$

where the factors of $1/2$, $1/6$ etc. account for the “ N -tuple” counting in the sum, e.g. for the three-electron sum it accounts for counting abc , acb , bac , bca , acb and cab which produce the same excitation operator since $\hat{\mathbf{t}}_a \hat{\mathbf{t}}_b \hat{\mathbf{t}}_c$ commute.

We can now introduce a final piece of simplifying notation: an umbrella function that will envelope the sums of excitation operators that appear in a coupled cluster wave function (such as the sums of excitation operators in C.13) called the *cluster operators*

$$\hat{\mathbf{T}}_1 = \sum_a^N \hat{\mathbf{t}}_a = \sum_{a,r}^N t_a^r \mathbf{a}_r^\dagger \mathbf{a}_a, \quad (\text{C.14})$$

$$\text{and } \hat{\mathbf{T}}_2 = \frac{1}{2} \sum_{a,b}^N \hat{\mathbf{t}}_{ab} = \frac{1}{4} \sum_{a,b,r,s}^N t_{ab}^{rs} \mathbf{a}_r^\dagger \mathbf{a}_s^\dagger \mathbf{a}_b \mathbf{a}_a. \quad (\text{C.15})$$

Using these two cluster operators in equation C.13 leads to the greatly simplified coupled cluster wave function

$$|\Phi\rangle = \left[1 + \hat{\mathbf{T}}_1 + \frac{1}{2!} \hat{\mathbf{T}}_1^2 + \frac{1}{3!} \hat{\mathbf{T}}_1^3 + \frac{1}{4!} \hat{\mathbf{T}}_1^4 \right. \\ \left. + \hat{\mathbf{T}}_2 + \hat{\mathbf{T}}_2 \hat{\mathbf{T}}_1 + \frac{1}{2!} \hat{\mathbf{T}}_2 \hat{\mathbf{T}}_1^2 + \frac{1}{2!} \hat{\mathbf{T}}_2^2 \right] |\Phi_0\rangle. \quad (\text{C.16})$$

2 The cluster operator

We can see this is a Taylor series for the exponential function raised to the power $(\hat{\mathbf{T}}_1 + \hat{\mathbf{T}}_2)$. The full expansion would be

$$\begin{aligned} e^{\hat{\mathbf{T}}_1 + \hat{\mathbf{T}}_2} = & 1 + \hat{\mathbf{T}}_1 + \hat{\mathbf{T}}_2 + \frac{1}{2!} \hat{\mathbf{T}}_1^2 + \frac{1}{2!} \hat{\mathbf{T}}_2^2 + \hat{\mathbf{T}}_1 \hat{\mathbf{T}}_2 + \frac{1}{3!} \hat{\mathbf{T}}_1^3 \\ & + \frac{1}{3!} \hat{\mathbf{T}}_2^3 + \frac{1}{2!} \hat{\mathbf{T}}_2 \hat{\mathbf{T}}_1^2 + \frac{1}{2!} \hat{\mathbf{T}}_2^2 \hat{\mathbf{T}}_1 + \frac{1}{4!} \hat{\mathbf{T}}_1^4 + \frac{1}{4!} \hat{\mathbf{T}}_2^4 + \frac{1}{3!} \hat{\mathbf{T}}_2^3 \hat{\mathbf{T}}_1 \\ & + \frac{1}{3!} \hat{\mathbf{T}}_2^3 \hat{\mathbf{T}}_1 + \frac{1}{3!} \hat{\mathbf{T}}_2 \hat{\mathbf{T}}_1^3 + \frac{1}{4} \hat{\mathbf{T}}_1^2 \hat{\mathbf{T}}_1 2 + \dots, \end{aligned} \quad (\text{C.17})$$

where we have curtailed the expansion at the $x^4/4!$ level for e^x with $x = \hat{\mathbf{T}}_1 + \hat{\mathbf{T}}_2$. Asserting this *exponential ansatz* we can rewrite the wave function (and include all terms in the exponentiated operator) as

$$|\Phi\rangle = e^{\hat{\mathbf{T}}_1 + \hat{\mathbf{T}}_2} |\Phi_0\rangle, \quad (\text{C.18})$$

which will include all single electron and double electron excitations. Clearly including electron clusters of all sizes, up to N electron cluster operators ($\hat{\mathbf{T}}_N$) would result in an exact wave function,

$$|\Phi_{\text{exact}}\rangle = \exp \sum_m^N \hat{\mathbf{T}}_m |\Phi_0\rangle,$$

where $\hat{\mathbf{T}}_m$ is the m -electron cluster operator, written as

$$\hat{\mathbf{T}}_m = \frac{1}{m!} \sum_{ab\dots rs\dots}^m t_{ab\dots rs\dots}^{rs\dots} \mathbf{a}_r^\dagger \mathbf{a}_r^\dagger \dots \mathbf{a}_a \mathbf{a}_b \dots \quad (\text{C.19})$$

To formulate the CC equations we consider the Schrödinger equation for the system, $\hat{\mathbf{H}}_e |\Phi\rangle = E |\Phi\rangle$, and expanding $|\Phi\rangle$ as in C.18 and projecting left onto $\langle \Phi_0 |$ gives,

$$\begin{aligned} \langle \Phi_0 | \hat{\mathbf{H}}_e e^{\sum_m^N \hat{\mathbf{T}}_m} | \Phi_0 \rangle &= \langle \Phi_0 | E e^{\sum_m^N \hat{\mathbf{T}}_m} | \Phi_0 \rangle, \\ \langle \Phi_0 | \hat{\mathbf{H}}_e e^{\sum_m^N \hat{\mathbf{T}}_m} | \Phi_0 \rangle &= E, \end{aligned} \quad (\text{C.20})$$

noting that the projection $\langle \Phi_0 | E e^{\sum_m^N \hat{\mathbf{T}}_m} | \Phi_0 \rangle = 1$. The second general CC equation is for the set of coefficients and involves projecting the Schrödinger equation onto the excited state $\langle \Phi_{ab\dots}^{rs\dots} |$,

$$\langle \Phi_{ab\dots}^{rs\dots} | \hat{\mathbf{H}}_e e^{\sum_m^N \hat{\mathbf{T}}_m} | \Phi_0 \rangle = E \langle \Phi_{ab\dots}^{rs\dots} | e^{\sum_m^N \hat{\mathbf{T}}_m} | \Phi_0 \rangle. \quad (\text{C.21})$$

These equations, C.20 and C.21, require no particular approximation beyond that of the cluster operator $\hat{\mathbf{T}}_m$ being a form of excitation operator and the wave function used be a single reference wave function constructed on a basis of single-electron basis functions.

Appendix D

Allowable stoichiometries for GICs

GICs can be formed with different metal densities to form compounds of MC_n referred to as GICs with different stoichiometries. If we stipulate that the allowable densities must form a regular lattice within the graphite sheets then we impart two constraints that give the only allowable stoichiometries.

Constraint 1. *The metal lattice must give a homogeneous covering of metal atoms. That is to say that each metal atom experiences the same environment.*

Constraint 2. *Each metal lattice site must sit directly above and below a graphite hexagon centre. This enforces that the metal lattice must be coincident with the graphite triangular lattice.*

Constraint 2 follows since each position under a C hexagon centre is a local minima in energy for the metal and will act as a strong attractor to any unrelaxed metal near it. The lattice for graphite, or for any hexagonal structure, is a triangular lattice with a basis of two points, as shown in figure D.1.

The combination of these two constraints gives an interesting problem and not one that is confined to GIC stoichiometries. The question posed upon the assertion of these constraints is the following.

Question 1. *Given a lattice, what secondary lattice can be overlaid upon it such that each lattice point of the second lattice is perfectly coincident with the primary lattice?*

This is clearly a matter of symmetries, the secondary lattice must contain at least the symmetries of the primary lattice. In the specific case of a graphite lattice, while the structure is hexagonal, the lattice is triangular. This type of lattice has a dihedral point

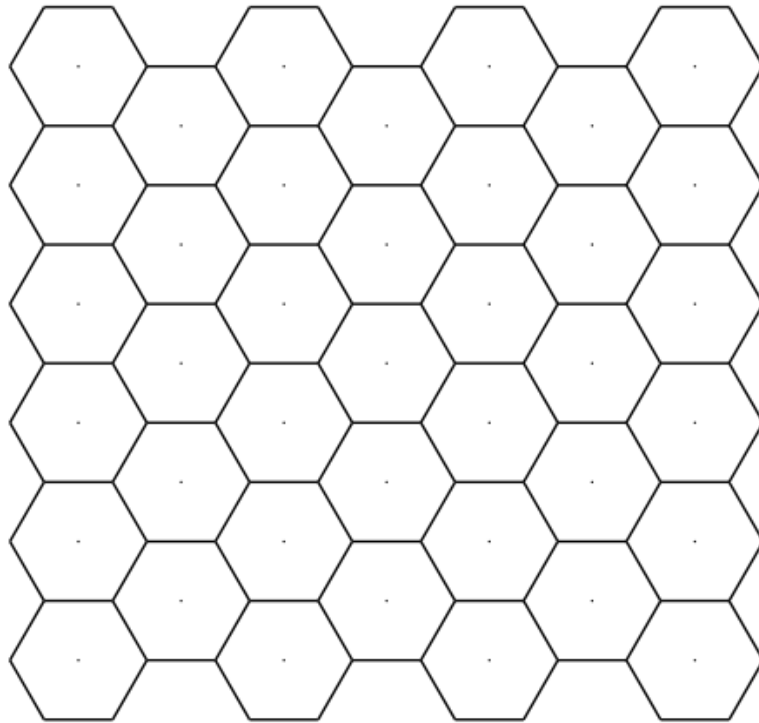


Figure D.1: The hexagonal structure. Lattice points at the centre of each hexagon form a triangular lattice, when a basis of two points is added the hexagonal structure above can be obtained.

group of the third order, D_3 in Schoenflies notation, where a point group of D_n means the lattice has n rotational symmetries by angles of $360/n^\circ$ and n mirror symmetries and is thus the point group of the n -sided regular polygon. Thus any secondary lattice with a point group that is a multiple of the primary lattice will have coincident lattice points given a certain scale.

In the case of the graphite lattice, a secondary lattice (the lattice of metal intercalants) can have any lattice with a dihedral point group of D_{3j} , where j represents some integer, $j = 1, 2, 3, \dots$. The first coincident lattice is the D_3 triangular lattice, the one considered in much of this thesis with stoichiometries such as MC₆, MC₈ and MC₁₄. The second coincident lattice is the D_6 hexagonal lattice and includes regular stoichiometries like that of MC₁₂. The next allowable secondary lattice would be the nonagonal lattice with D_9 point group. The first coincident stoichiometry allowable with this metal lattice would have an extremely low $C : M$ ratio and is not considered here.

From constraint 2 we see that the most dense metal to carbon ratio $C : M$ is 1 : 2, forming an MC₂ GIC. This would give a metal lattice that lies perfectly over each lattice

point of the graphite lattice. Lower density GICs are achieved by stretching out the metal lattice until constraint 2 is met.

Considering the case of a triangular metal lattice (with a basis of one metal atom at the lattice point, i.e. a metal atom at $(0, 0, 0)$) possessing the D_3 point group we have three patterns of increasing metal lattice sizes. We consider that the in-plane unit cell for these structures is a regular rhombus with internal angles of 60° and 120° , thus made with two equilateral triangles. This can then be translated to create a tessellation that is one of the wallpaper group. Since the unit cell is symmetric about the two lines of reflection joining any two opposite vertices and the two lines of reflection joining the centre of two opposing sides, we can consider just half the unit cell: an equilateral triangle. The number of C atoms within this half unit cell will, of course, need to be doubled to obtain the total number of C atoms in the unit cell.

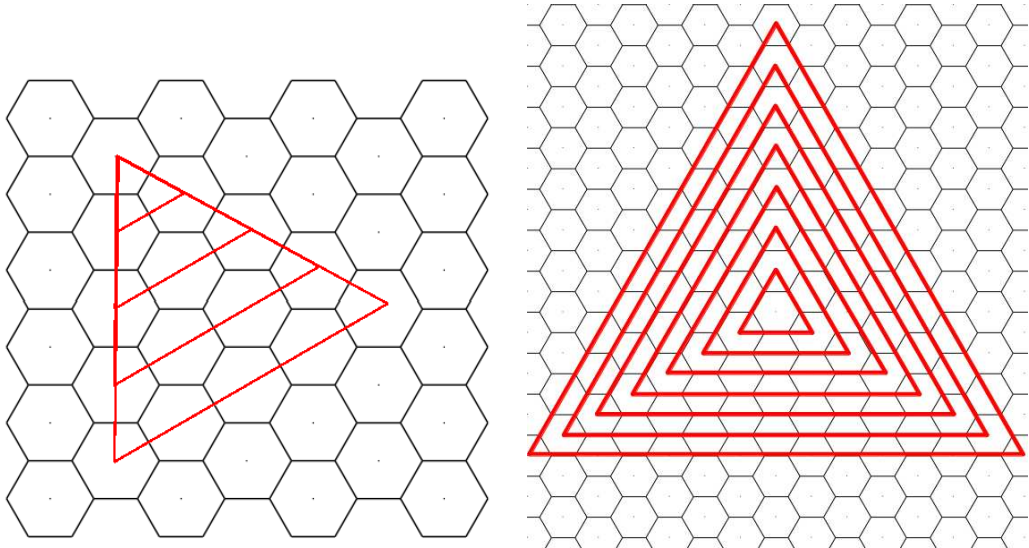
Within this case of a triangular D_3 metal lattice we obtain three geometric patterns of ever decreasing metal densities that obey both constraints. All three are shown in figure D.2 with subfigure (a) showing the case of increasing the scale of the metal lattice (shown in red) while maintaining its orientation until the next graphite lattice point is met, (b) showing the same procedure of expanding the metal lattice until the next lattice point is met but starting with a metal lattice that is orientated by 30° relative to (a). The third geometric pattern, shown in subfigure D.2(c), rotates the stretched metal lattice of pattern (a) by a changing angle. This produces three geometrical patterns for the allowable stoichiometries of a D_3 lattice of metal intercalants. Note that a pattern based on that of figure D.2(b) and rotated and stretched in the manner that figure D.2(c) is a subset of the other two patterns and so is a degenerate case.

Each of these patterns form a geometric pattern for the $C : M$ ratio for a D_3 metal lattice. The two equations describing each pattern, in terms of the stoichiometric label n in the stage-I MC_n GICs are

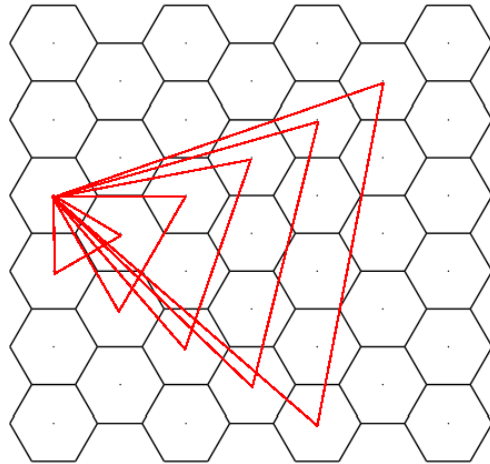
$$n = \begin{cases} 2(k(k+2)+1) & \text{pattern seen in figure D.2(a)} \\ 6(k(k+2)+1) & \text{pattern seen in figure D.2(b)} \\ 2(k(k-1)+1) & \text{pattern seen in figure D.2(c)} \end{cases}, \quad (\text{D.1})$$

where k represents the counter for each successively larger triangle in figure D.2 and can thus be any natural number $0, 1, 2, 3, \dots$

These patterns, and the derived equations, hold true for stage-I GICs and simply



(a) The first D_3 lattice geometric pattern. (b) The second D_3 lattice geometric pattern.



(c) The third D_3 lattice geometric pattern.

Figure D.2: The three in-plane D_3 metal lattices (red) on the graphite structure (black). The lattices are slowly expanded until constraint 2 is met. Subfigure (a) and (a) show the cases of simply stretching the metal lattice from different orientations, subfigure (c) shows the effect of stretching and rotating the metal lattice.

need a factor of m for generalisation to a stage- m GIC, thus

$$n = \begin{cases} 2m(k(k+2)+1) \\ 6m(k(k+2)+1) \\ 2m(k(k-1)+1) \end{cases}. \quad (\text{D.2})$$

For a D_6 metal lattice the pattern of decreasing $C : M$ ratios is more complicated. The same triangular base unit is used (representing half the unit cell) but this time the lattice has a basis of two metal atoms, one on the lattice point and one at the centre

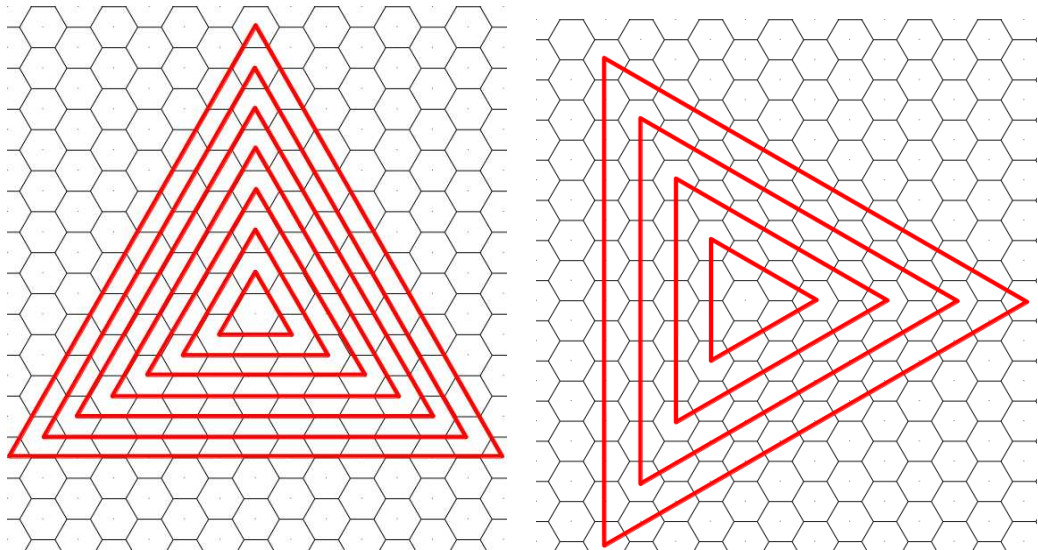
of the triangle, i.e. at $(0, 0, 0)$ and $(1/3, 1/3, 1/3)$ in the coordinates of the cell that these vectors would produce. This form of lattice now exhibits four geometric patterns for each discernible scale of metal lattice. These are shown in figure D.3 with (a) showing the effect of simply expanding the lattice; (b) shows the same effect of expansion but from a different orientation; (c) shows the effect of rotating the pattern seen in (a) by an angle before lattice points coincide; and (d) shows the same rotating effect based on the pattern in (b).

These four geometric patterns for the D_6 metal lattice can be described by four geometric sequences to give the total number of C atoms in the unit cell for the stage- m MC_n GIC thus

$$n = \begin{cases} 3m(k^2 + 2k + 1) & \text{pattern seen in figure D.3(a)} \\ 9m(k^2 + 2k + 1) & \text{pattern seen in figure D.3(b)} \\ 3m(3k^2 + 9k + 7) & \text{pattern seen in figure D.3(c)} \\ \sim 9m(k^2 + 5k + 7) & \text{pattern seen in figure D.3(d)} \end{cases}, \quad (\text{D.3})$$

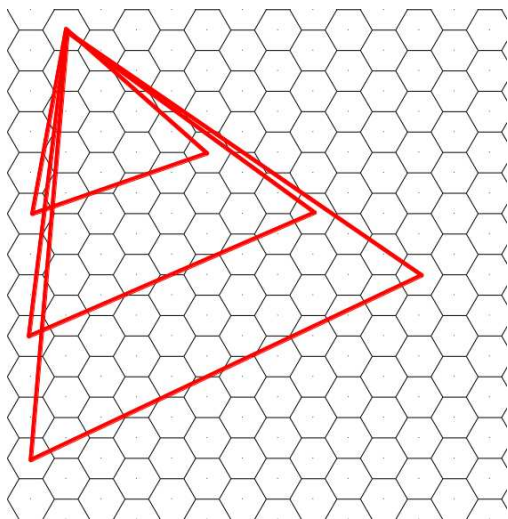
where k can represent the counter for each successively larger triangle in figure D.3 and can thus be any natural number $0, 1, 2, 3, \dots$

Note that the last of the geometric patterns for the D_6 metal lattice is an approximate pattern as the number of C atoms within these unit cells is not geometric as atoms appear on the edge of the unit cell boundary with increasing unit cell sizes.

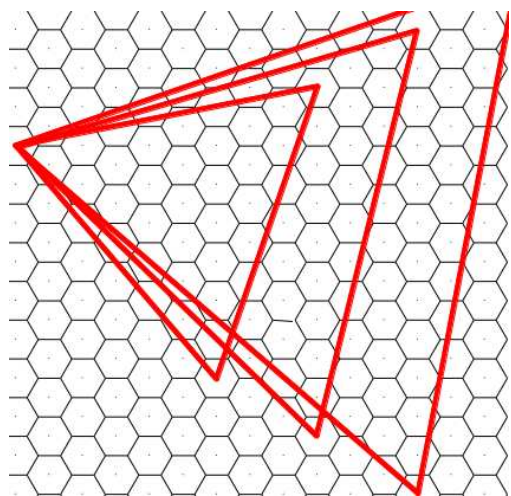


(a) The first D_6 lattice geometric pattern.

(b) The second D_6 lattice geometric pattern.



(c) The third D_6 lattice geometric pattern.



(d) The fourth D_6 lattice geometric pattern.

Figure D.3: The four geometrical patterns of the D_6 lattice allowable under both constraints. Note that the triangles represent half the unit cell (with two sides acting as the cell vectors) and that each triangular lattice has a basis of two metal atoms at the lattice point and the centre of the triangle (at $(0, 0, 0)$ and $(\frac{1}{3}, \frac{1}{3}, \frac{1}{3})$ in the basis of the lattice vectors).

Appendix **E**

Free atom energies

The energies produced by VASP are a version of formation energy but are not directly comparable to experimental formation energies. The results given by VASP are the individual free atom energies within the system subtracted from the total system energy, thus

$$E_{\text{VASP}} = E_{\text{total}}^{\text{DFT}} - \sum_i^{N_{\text{species}}} \sum_j^{N(i)} E_j(i), \quad (\text{E.1})$$

where E_{VASP} is the energy given by VASP; $E_{\text{total}}^{\text{DFT}}$ is the total DFT energy of the system, e.g. the solution to $E_{\text{total}}^{\text{DFT}} = \langle \Psi_0^{\text{DFT}} | \hat{H} | \Psi_0^{\text{DFT}} \rangle$ where Ψ_0^{DFT} is the DFT ground state wavefunction that leads to the ground state electron density $n_0^{\text{DFT}}(r)$; the second term is the sum of the free atom energies for every atom in the simulation with i counting the atomic species with N_{species} the total number of species and j counting the number of atoms of a given species with $N(i)$ the number of atoms of species i ; and $E_j(i)$ is the energy of the free atom of species i .

This energy, E_{VASP} , would be precisely the formation energy from free atoms if the free atom energies $E_j(i)$ were the ground state free atom energies. The VASP reference energy, $E_{\text{ref}}^{\text{VASP}}$, for the free atoms is *not* the energy of the spin-ground state. To arrive at the formation energy from free atoms we need to calculate the spin-polarised ground state for each atom within DFT giving the spin-polarised ground state energy $E_{\text{spin-pol}}$. This can be subtracted from the energy above to give the true formation energy, E_{form} , from free atoms thus

$$\begin{aligned}
E_{\text{form}} &= E_{\text{VASP}} - \sum_i^{N_{\text{species}}} \sum_j^{N(i)} E_{\text{spin-pol}}(i), \\
&= E_{\text{total}}^{\text{DFT}} - \sum_i^{N_{\text{species}}} \sum_j^{N(i)} (E_{\text{spin-pol}}(i) - E_{\text{ref}}^{\text{VASP}}(i)).
\end{aligned} \tag{E.2}$$

The DFT calculations to find the spin-polarised ground state of the atoms relevant to this work (H, C and the alkali and alkaline-earth metals) were performed within VASP using both the LDA and GGA-PW91 *xc*-functionals. The atoms were placed at the centre of a large non-cubic box ($22 \times 24 \times 26 \text{ \AA}$) to break symmetry and a single *k*-point calculation was performed. The magnetic moment of the atom was enforced to ensure convergence to the correct ground state. Occupancies were checked to ensure they were either one or zero. Two arbitrarily high plane-wave cut offs were chosen, 800 eV and 2000 eV, to check the convergence relative to the plane-wave cut off, which was observed to be small (see table E.1). The spin-polarised ground state energies for the alkali and alkaline earth atoms, as well as for carbon and hydrogen, are given below in table E.1.

Values for the formation energy, or bond energy, of H_2 are also included as this is frequently used throughout this work. The molecule was modelled in a $20 \times 20 \times 20 \text{ \AA}$ box with a plane-wave cut-off of 800 eV and a *k*-point grid of $7 \times 7 \times 7 \text{ \AA}$. The total energy of the cell was converged to within 1 meV. The value for the formation enthalpy at 0 K for the atomic H gas from H_2 gas (and thus the closest value for the H_2 bond energy) is given in JANAF Thermochemical tables[127] as -4.478 eV, in good agreement with the calculated values especially with the GGA-PW91 result overestimating the bonding energy by just 2%.

Atom	LDA		GGA-PW91	
	800 eV	2000 eV	800 eV	2000 eV
H	-0.80346	-0.89688	-1.11769	-1.12048
H ₂	-4.903	N/A	-4.558	N/A
C	-1.20653	-1.20692	-1.36889	-1.36955
Li	-0.23567	-0.23567	-0.27427	-0.27298
Na	-0.21040	-0.20823	-0.22670	-0.22567
K	-0.14002	-0.13999	-0.16297	-0.16342
Rb	-0.12562	-0.12549	-0.14751	-0.14764
Cs	-0.11571	-0.11523	-0.13630	-0.13339
Be	0.00868	0.00866	-0.04002	-0.04006
Mg	0.01464	0.01466	-0.00101	0.00025
Ca	0.00896	0.00877	-0.00822	-0.00824
Sr	0.01428	0.01448	-0.01105	-0.01085
Ba	0.01247	0.01254	-0.01749	-0.01797

Table E.1: Differences from the VASP reference state energy of the spin-polarised atomic ground state within DFT using both LDA and GGA-PW91, i.e. $E_{\text{spin-pol}} - E_{\text{ref}}^{\text{VASP}}$.

Appendix **F**

Mode of operation of VASP

To perform a DFT calculation it is necessary to solve the Schrödinger-like Kohn-Sham equation of 2.37, given again for clarity,

$$\left(-\frac{\hbar^2}{2m_e} \nabla_i^2 + v_{\text{eff}}^\sigma(\vec{r}) \right) \phi_i^\sigma(\vec{r}) = \varepsilon_i^\sigma \phi_i^\sigma(\vec{r}), \quad (\text{F.1})$$

where σ labels spin; the first term represents the kinetic energy operator of the i -th non-interacting particle of the Kohn-Sham independent-particle auxiliary system; the effective potential term, v_{eff} , is the Kohn-Sham potential applied to the auxiliary system; the i -th independent-particle spin orbital is given by ϕ_i with a corresponding energy given by the eigenvalue ε_i . The effective potential is chosen to give the same ground state particle density, $n_0(\vec{r})$, for the independent-particle auxiliary system as for the interacting-particle case.

Solving equation F.1 requires an iterative procedure as the density $n(\vec{r})$ is constructed from the orbitals ϕ_i which depend upon v_{eff} which in turn depends upon the density. An iterative loop is started by setting up an effective potential, solving the Kohn-Sham equations, calculating the density, setting up a new potential from this density, viz (where i labels the iteration number)

$$v_i \rightarrow n_i \rightarrow v_{i+1} \rightarrow n_{i+1} \rightarrow v_{i+2} \rightarrow n_{i+2} \rightarrow \dots$$

The procedure for solving this is to iterate until a specified level of self-consistency is obtained, i.e. the change in energy/density between step i and $(i+1)$ is within some tolerance.

In VASP this process is started with a guess for the charge density made by superimposing the atomic charge densities. This initial guess for $n(\vec{r}) = n^\uparrow(\vec{r}) + n^\downarrow(\vec{r})$ is then

used to define the effective potential, v_{eff} , using a given form of the exchange-correlation potential by

$$v_{\text{eff}}^{\sigma}(\vec{r}) = v_{\text{ext}}(\vec{r}) + v_{\text{Hartree}}[n] + v_{xc}^{\sigma}[n^{\uparrow}, n^{\downarrow}]. \quad (\text{F.2})$$

This effective potential can then be used to set up the Hamiltonian and thus the Kohn-Sham equation of F.1. This is then solved using matrix diagonalisation procedures. This is the computationally expensive step and much effort is given in finding efficient methods to diagonalise a matrix. This step is performed iteratively to improve the set of orbitals until they closely matches the exact set of orbitals for the given Hamiltonian.

Once a set of orbitals has been found from the above step, the particle density is found by performing a weighted sum over the square norm of the wave functions,

$$n_{\text{out}}^{\sigma} = \sum_i f_i^{\sigma} |\phi_i^{\sigma}(\vec{r})|^2.$$

This new charge density is not used directly for the next loop but is instead mixed with the input charge density so that large changes in the density are smoothed out. This *charge density mixing* can be done in a number of ways and shall simply be denoted by the operator $(*)$ here,

$$n_{\text{in}}^{\sigma} * n_{\text{out}}^{\sigma} \rightarrow \text{new } n_{\text{in}}^{\sigma}.$$

The Kohn-Sham energy is then computed using

$$E_{\text{KS}} = T_s[n] + \underbrace{\int v_{\text{ext}}(\vec{r}) n(\vec{r}) d\vec{r} + E_{\text{Hartree}}[n] + E_{\text{II}} + E_{xc}[n^{\uparrow}, n^{\downarrow}]}_{E_{\text{pot}}[n]}, \quad (\text{F.3})$$

where $[n]$ denotes that the quantity is a *functional* of the density. T_s is the kinetic energy of the non-interacting auxiliary system; $\int v_{\text{ext}}(\vec{r}) n(\vec{r}) d\vec{r}$ is the interaction of the electrons with the nuclei; E_{Hartree} is the Hartree energy, the classical Coulomb self-interaction energy of the electron density, $n(\vec{r})$; E_{II} is the interaction energy of the positively charged nuclei, with these three terms representing a neutral grouping given a neutral system; and E_{xc} giving the exchange-correlation energy.

This energy is then compared to the energy given in the previous step to give ΔE_{KS} that is then compared with the threshold for self-consistency, E_{break} to see if self-consistency has been found. If self-consistency is not achieved the loop repeats from step two, after the initial guess, until the condition is met. If the condition is met then forces are calculated, atomic positions updated where necessary, eigenvalues given and anything else that requires the resultant ground state density.

This procedure is outlined in the flow diagram given in figure F.1.

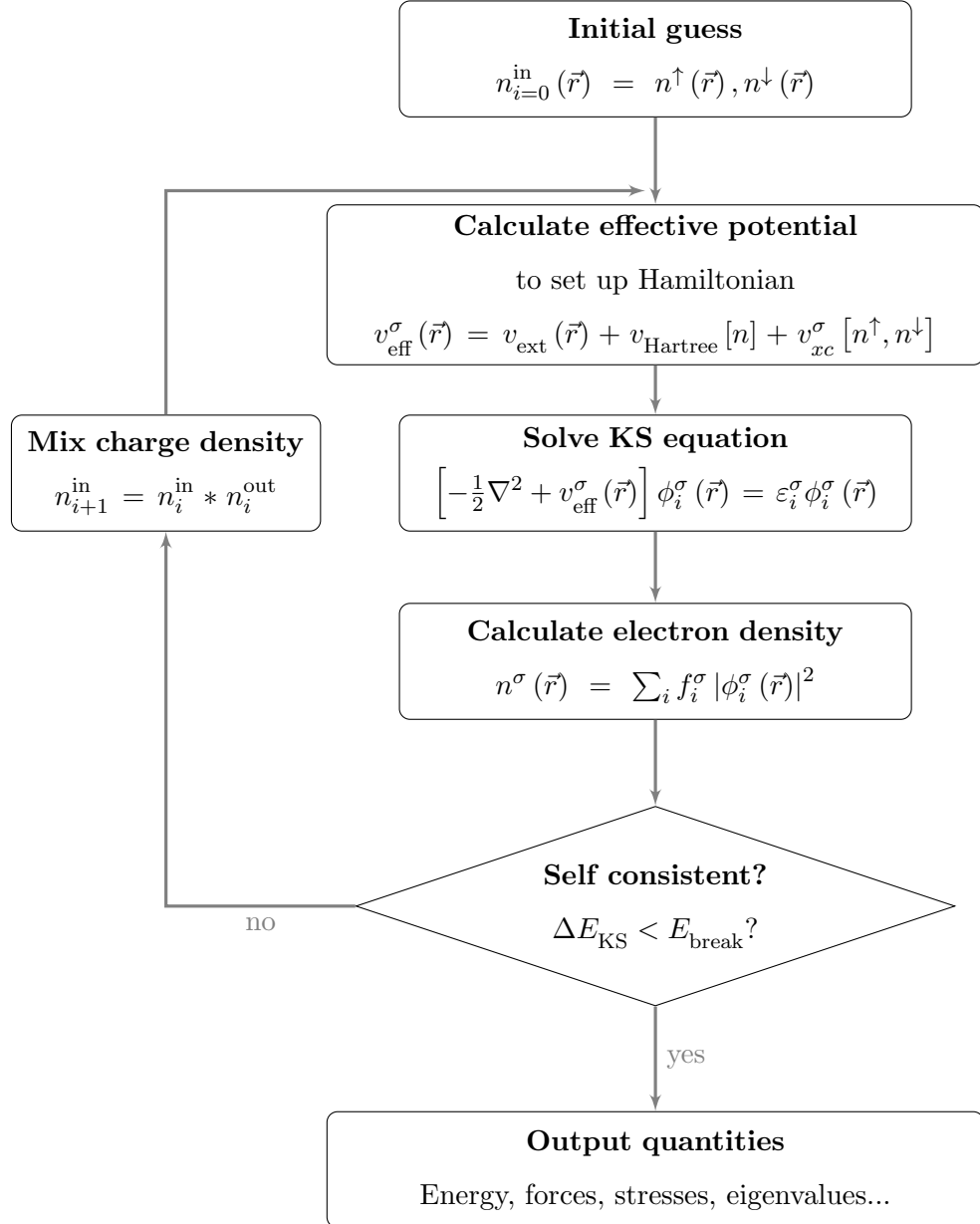


Figure F.1: Flow diagram of the mode of operation of VASP.

1 Achieving self-consistency

In order to achieve self-consistency in the energy it is necessary to integrate over all possible values of \vec{k} in the Brillouin zone of the crystal. Only sampling of the first Brillouin zone is necessary by virtue of Bloch's theorem (see §2.3) making all k -points outside of the first Brillouin zone redundant as they have an equivalent point in the first zone. In principle the problem requires one to find the value of the wave functions at every k -point in the Brillouin zone; in reality one can neglect points that are very

close together as the wave functions vary little between them allowing a finite k -point sampling grid to be used.

The choice of k -point grid should be dense enough to ensure that all variations of the wave functions can be properly mapped and anti-aliasing avoided, but not so dense so as to add excessive computational effort for little gain in accuracy. The convergence of the total energy of a system with ever increasing k -point grid is rarely monotonic and often shows a rapidly varying function that tends to settle down to the actual energy with increasing sample grid size. Figure F.2 shows how the total energy (E) of a CaC₆ unit cell varies with increasing $n \times n \times n$ Monkhorst-Pack k -point mesh. The inset of F.2 shows how the energy difference between successive grid sizes (ΔE) decreases with increasing grid.

Within this thesis k -point grids were chosen so that the change in unit cell energy between two successive grids was always small (less than 0.05 eV). Completely uniform grids were chosen for ease of calculation for the many different unit cell sizes used here and so that no assumption of the electron density was necessary.

Representing the eigenfunctions in F.1 as plane waves and using Bloch's theorem (noted in §2.3) allows us to define out functions as an infinite sum of plane waves (given in equation 2.49 and here for clarity),

$$\phi_{j,\vec{k}}(\vec{r}) = \sum_{\vec{G}} a_{j,(\vec{G}+\vec{k})} e^{i(\vec{G}+\vec{k}) \cdot \vec{r}}.$$

Each member of this sum has a kinetic energy given by $E = \hbar^2 |\vec{k} + \vec{G}|^2 / 2m_e$. Slowly varying functions with low energy contribute most to the representation while quickly varying functions with high energy contribute least. By using a plane wave cut off it is possible to curtail the infinite sum to form a finite basis set to express the orbitals. The basis set limit can be approached by increasing the energy cut off in the sum. The total energy of a crystal tends to the basis set limit monotonically, as can be seen in figure F.3, allowing extrapolation of the total energy at the basis set limit with moderate basis sets. To avoid *wrap around errors* (also called *aliasing errors*), where components of the charge density are wrapped around from the other side of the box, the fast Fourier transform (FFT) grid used in a calculation must contain all wave-vectors up to $2 \times G_{\text{cut}}$ where the cut off wave vector G_{cut} is defined as $E_{\text{cut}} = \frac{\hbar^2}{2m_e} |G_{\text{cut}}|^2$. This requires very large plane wave energy cut-offs and these are used where possible, but since total energies are

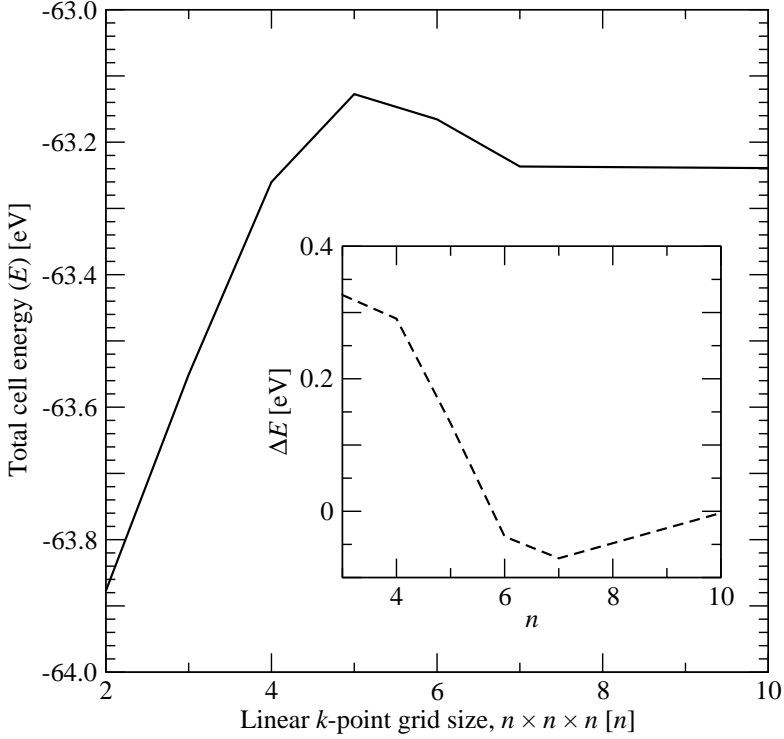


Figure F.2: An example of the non-monotonic behaviour of total energy convergence with k -point grid size. The example shows the total unit cell energy for α -stacked CaC₆ using DFT-LDA in VASP (using a fixed plane wave cut-off) plotted against linear size of an $n \times n \times n$ Monkhorst-Pack k -point mesh. Inset shows how the energy difference (ΔE) between successive k -point grid sizes (n) decreases as the mesh is increased.

compared in this work, systematic errors tend to cancel out during subtraction allowing smaller basis sets to be used.

The particle density at step i is made from mixing the input and output densities from step $(i-1)$. In linear mixing this is done by

$$n_i^{\text{in}} = \alpha n_{i-1}^{\text{out}} + (1 - \alpha) n_{i-1}^{\text{in}}, \quad (\text{F.4})$$

producing a method that essentially follows the steepest descent. Charge density mixing at the end of each iteration is done using the Broyden method in VASP. This is a hybrid method that builds on linear mixing and adds a response function by defining the error in the particle density (from the correct density) at any stage of an iteration as $\delta n_i \equiv n_i - n_{KS}$.

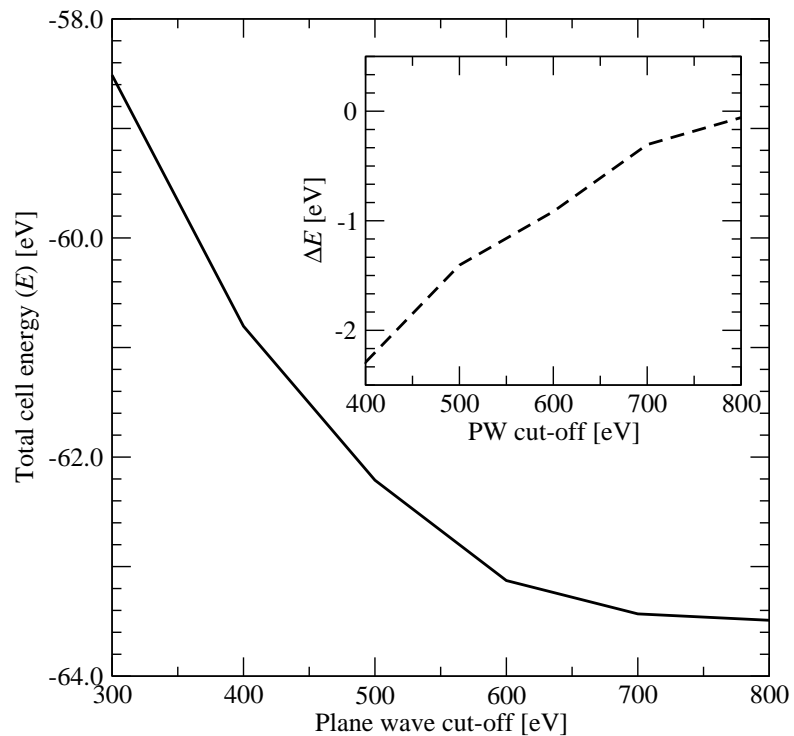


Figure F.3: An example of total energy convergence with plane wave cut-off. The example shows how the unit cell energy of α -stacked CaC₆ converges with increasing plane wave cut-off using DFT-LDA in VASP (using a fixed k -point grid). The inset shows how the difference between each successive plane wave cut-off monotonically decreases allowing extrapolation to the infinite basis set limit.

Bibliography

- [1] M. Cobian and J. Íñiguez. Theoretical investigation of hydrogen storage in metal-intercalated graphitic materials. *J. Phys.-Condens. Matter*, 2:285212, 2008. doi: 10.1088/0953-8984/20/28/285212. URL <http://iopscience.iop.org/0953-8984/20/28/285212>.
- [2] Yong-Hyun Kim, Y. Y. Sun, and S. B. Zhang. *Ab initio* calculations predicting the existence of an oxidized calcium dihydrogen complex to store molecular hydrogen in densities up to 100 g/l. *Phys. Rev. B*, 79:115424, Mar 2009. doi: 10.1103/PhysRevB.79.115424. URL <http://link.aps.org/doi/10.1103/PhysRevB.79.115424>.
- [3] Mina Yoon, Shenyuan Yang, Christian Hicke, Enge Wang, David Geohegan, and Zhenyu Zhang. Calcium as the superior coating metal in functionalization of carbon fullerenes for high-capacity hydrogen storage. *Phys. Rev. Lett.*, 100(20):206806, May 2008. doi: 10.1103/PhysRevLett.100.206806.
- [4] A. Lovell. *Tunable graphite intercalates for hydrogen storage*. PhD thesis, University College London, September 2007. URL <http://eprints.ucl.ac.uk/13806/1/13806.pdf>.
- [5] G. Srinivas, C.A. Howard, N.T. Skipper, S.M. Bennington, and M. Ellerby. High temperature hydrogenation of CaC₆. *Physica C: Superconductivity*, 469(22):2000 – 2002, 2009. ISSN 0921-4534. doi: DOI:10.1016/j.physc.2009.08.004. URL <http://www.sciencedirect.com/science/article/B6TVJ-4X2DD1K-1/2/84eadbe77baa1aaafda844beade48a3c2>.
- [6] The World Bank. Energy usage: kilograms of oil equivalent per capita. (inter-

BIBLIOGRAPHY

- national energy agency statistics). website, 2012. URL <http://www.iea.org/stats/index.asp>.
- [7] H. Shi, J. Barker, M. Y. Saïdi, R. Koksbang, and L. Morris. Graphite structure and lithium intercalation. *J. Power Sources*, 68:291–295, 1997. doi: 10.1016/S0378-7753(96)02562-1.
 - [8] N. Emery, C. Hérald, and P. Lagrange. Structural study and crystal chemistry of the first stage calcium graphite intercalation compound. *J. Solid State Chem.*, 178:2947–2952, 2005. doi: 10.1016/j.jssc.2005.05.031.
 - [9] Bing Li, Yinwei Li, Kaifeng Yang, Qiliang Cui, Yanming Ma, and Guangtian Zou. Raman evidence of a new high-pressure phase in calcium hydride. *J. Phys.-Condens. Matter*, 19:226205, 2007. doi: 10.1088/0953-8984/19/22/226205.
 - [10] C. Wolverton and V. Ozolins. Hydrogen storage in calcium alanate: First-principles thermodynamics and crystal structures. *Phys. Rev. B*, 75:064101, 2007. doi: 10.1103/PhysRevB.75.064101.
 - [11] H. Wu, W. Zhou, T.J. Udovic, J.J. Rush, and T. Yildirim. Structure and vibrational spectra of calcium hydride and deuteride. *J. Alloy. Compd.*, 436:51–55, 2007. doi: 10.1016/j.jallcom.2006.07.042.
 - [12] Russel D. Johnson III. Nist computational chemistry comparison and benchmark databse. Technical Report 101, 15b, NIST, August 2011. URL <http://cccbdb.nist.gov>.
 - [13] Glossary:kilograms of oil equivalent (kgoe). website, February 2013. URL http://epp.eurostat.ec.europa.eu/statistics_explained/index.php/Glossary:Kilograms_of_oil_equivalent_%28kgoe%29.
 - [14] G. Whitney, C. E. Behrens, and C. Glover. U.s. fossil fuel resources: terminology, reporting and summary. Technical report, U.S. Congressional Research Service, 2010.
 - [15] Multiple. 2009 world population data sheet. Technical report, Population Reference Bureau, 2009.
 - [16] David Bodansky. *The Energy Source Book*, chapter Appendix: energy units. New York: American Institute of Physics, 1991.

BIBLIOGRAPHY

- [17] U.N. Population Division. World population prospects: the 2008 revision. Technical report, United Nations, 2008.
- [18] Bradley A. Johnson and Ralph E. White. Characterization of commercially available lithium-ion batteries. *Journal of Power Sources*, 70(1):48 – 54, 1998. ISSN 0378-7753. doi: 10.1016/S0378-7753(97)02659-1. URL <http://www.sciencedirect.com/science/article/pii/S0378775397026591>.
- [19] Encyclopædia Britannica. Hydrogen (h). website, October 2012. URL <http://www.britannica.com/EBchecked/topic/278523/hydrogen-H/80846/Reactivity-of-hydrogen>.
- [20] B. C. H. Steele. Fuell-cell technology: running on natural gas. *Nature*, 400:619–621, August 1999. doi: 10.1038/23144. URL <http://www.nature.com/nature/journal/v400/n6745/full/400619a0.html%3Ffree%3D2>.
- [21] B. C. H. Steele and A. Heinzel. Materials for fuel-cell technologies. *Nature*, 414: 345–352, November 2001. doi: 10.1038/35104620. URL <http://www.nature.com.libproxy.ucl.ac.uk/nature/journal/v414/n6861/abs/414345a0.html>.
- [22] Tesla. Tesla motors. website, Dec 2012. URL <http://www.teslamotors.com/>.
- [23] Toyota. Toyota prius. website, 2012. URL http://www.toyota.co.uk/cgi-bin/toyota/bv/frame_start.jsp?id=CC2-Prius-landing.
- [24] Energy efficiency & renewable energy. Technical report, U.S Department of Energy, February 2011. URL <http://www.hydrogenandfuelcells.energy.gov>.
- [25] J.O'M. Bockris. The origin of ideas on a hydrogen economy and its solution to the decay of the environment. *International Journal of Hydrogen Energy*, 27(7-8):731–740, 2002. ISSN 0360-3199. doi: 10.1016/S0360-3199(01)00154-9. URL <http://www.sciencedirect.com/science/article/pii/S0360319901001549>. Proceedings of the Selected Papers of the Third International Conference on Hydrogen Treatment of Materials, HTM-2001.
- [26] Energy efficiency & renewable energy: fuel cell technologies program. Technical report, U.S. Department of Energy, November 2010.

BIBLIOGRAPHY

- [27] Meyer Steinberg and Hsing C. Cheng. Modern and prospective technologies for hydrogen production from fossil fuels. *International Journal of Hydrogen Energy*, 14(11):797 – 820, 1989. ISSN 0360-3199. doi: 10.1016/0360-3199(89)90018-9.
- [28] Natural gas reforming. website, 08 2011. URL http://www1.eere.energy.gov/hydrogenandfuelcells/production/natural_gas.html.
- [29] Peter Häussinger, Reiner LohmÄller, and Allan M. Watson. *Ullmann's Encyclopedia of Industrial Chemistry*, chapter Hydrogen, 1. Properties and Occurrence. Wiley-VCH Verlag GmbH & Co. KGaA, 2000. ISBN 9783527306732. doi: 10.1002/14356007.a13_297.pub2. URL http://dx.doi.org/10.1002/14356007.a13_297.pub2.
- [30] R. I. George. Hindenburg airship diaster leaves 33 dead. *The Guardian Newsaper*, May 1937. URL <http://www.guardian.co.uk/theguardian/2012/may/08/archive-1937-hindenburg-disaster>.
- [31] A. J. Dessler, D. E. Overs, and W. H. Appleby. The hindenburg fire: hydrogen or incendiary paint? *Buoyant Flight*, 52(2), January 2005.
- [32] R. G. Van Treuren. The hindenburg fire at sixty, part three: what really happened the night of may 6, 1937? *Buoyant Flight*, 44(8), July 1997.
- [33] U. Bossel, B. Eliasson, and G. Taylor. Hydrogen Economy: Bright or Bleak? Technical report, European Fuel Cell Forum, 2003.
- [34] D. Gielen and G. Simbolotti. Prospects for Hydrogen and Fuel Cells. Technical report, International Energy Agency, 2005.
- [35] Targets for onboard hydrogen storage systems for light-duty vehicles. Technical report, U.S. Department of Energy, September 2009.
- [36] Katsuhiko Hirose. Hydrogen as a fuel for today and tomorrow: expectations for advanced hydrogen storage materials/systems research. *Faraday Discuss.*, 151: 11–18, 2011. doi: 10.1039/C1FD00099C. URL <http://dx.doi.org/10.1039/C1FD00099C>.
- [37] Kathleen Zona and Brian Bunbar. Liquid hydrogen—the fuel of choice for space exploration. website, July 2010. URL http://www.nasa.gov/topics/technology/hydrogen/hydrogen_fuel_of_choice.html.

BIBLIOGRAPHY

- [38] William R. Grove. Xxiv. on voltaic series and the combination of gases by platinum. *Philosophical Magazine Series 3*, 14(86):127–130, 1839. doi: 10.1080/14786443908649684. URL <http://www.tandfonline.com/doi/abs/10.1080/14786443908649684>.
- [39] B. Cook. Introduction to fuel cells and hydrogen technology. *Engineering Science and Education Journal*, 11(6):205 – 216, December 2002. ISSN 0963-7346.
- [40] M. A. Weiss, J. B. Haywood, A. Schafer, and V. K. Natarajan. Comparative assessment of fuel cell cars. Technical report, Massachusetts Institute of Technology, 2003.
- [41] Kwi Seong Jeong and Byeong Soo Oh. Fuel economy and life-cycle cost analysis of a fuel cell hybrid vehicle. *Journal of Power Sources*, 105(1):58 – 65, 2002. ISSN 0378-7753. doi: 10.1016/S0378-7753(01)00965-X.
- [42] Naval Technology. U212/u214 submarines, germany. website, October 2005. URL http://www.naval-technology.com/projects/type_212/.
- [43] David Adam. Canal boat charts way to greener ships. *The Gurdian*, June 2008. URL http://www.fuelcellmarkets.com/marine_hydrogen_fuel_cell_association/news_and_information/3,1,12828,1,27286.html.
- [44] Ki-Joon Jeon, Hoi Ri Moon, Anne M. Ruminski, Bin Jiang, Christian Kisielowski, Rizia Bardhan, and Jeffrey J. Urban. Air-stable magnesium nanocomposites provide rapid and high-capacity hydrogen storage without using heavy-metal catalysts. *Nature Materials*, 10:286–290, April 2011. doi: 10.1038/nmat2978. URL <http://ceramics.org/ceramictechtoday/2011/03/23/two-new-mgh2-based-approaches-for-hydrogen-storage-proposed/>.
- [45] B. Bogdanovic and B. Spliethoff. Active MgH₂-Mg-systems for hydrogen storage. *International Journal of Hydrogen Energy*, 12(12):863 – 873, 1987. ISSN 0360-3199. doi: 10.1016/0360-3199(87)90108-X.
- [46] G. Alefeld and J. Völkl. *Hydrogen in Metals II*. Springer-Verlag, 1978.
- [47] L. Schlapbach. *Hydrogen in Intermetallic Compounds II*. Springer-Verlag, 1992.
- [48] Takayuki Ichikawa, Nobuko Hanada, Shigehito Isobe, Haiyan Leng, and Hironobu Fujii. Mechanism of novel reaction from LiNH₂ and LiH to Li₂NH and H₂ as a

BIBLIOGRAPHY

- promising hydrogen storage system. *The Journal of Physical Chemistry B*, 108(23):7887–7892, 2004. doi: 10.1021/jp049968y.
- [49] M. H. Mendelsohn, D. M. Gruen, and A. E. Dwight. LaNi_{5-x}Al_x is a versatile alloy system for metal hydride applications. *Nature*, 269:45 – 47, 1977. doi: 10.1038/269045a0.
- [50] Asbjorn Klerke, Claus Hviid Christensen, Jens K. Norskov, and Tejs Vegge. Ammonia for hydrogen storage: challenges and opportunities. *J. Mater. Chem.*, 18:2304–2310, 2008. doi: 10.1039/B720020J. URL <http://dx.doi.org/10.1039/B720020J>.
- [51] Y.-H. P. Zhang. A sweet out-of-the-box solution to the hydrogen economy: is the sugar powered car science fiction? *Energy & Environmental Science*, 2:272 – 282, 2009. doi: 10.1039/b818694d.
- [52] N.K. Zhevago and V.I. Glebov. Hydrogen storage in capillary arrays. *Energy Conversion and Management*, 48(5):1554 – 1559, 2007. ISSN 0196-8904. doi: DOI:10.1016/j.enconman.2006.11.017.
- [53] Shengqian Ma, Xi-Sen Wang, Daqiang Yuan, and Hong-Cai Zhou. A coordinatively linked yb metal-organic framework demonstrates high thermal stability and uncommon gas-adsorption selectivity. *Angewandte Chemie International Edition*, 47(22):4130–4133, 2008. ISSN 1521-3773. doi: 10.1002/anie.200800312. URL <http://dx.doi.org/10.1002/anie.200800312>.
- [54] Mohamed Eddaoudi, Jaheon Kim, Nathaniel Rosi, David Vodak, Joseph Wachter, Michael O’Keeffe, and Omar M. Yaghi. Systematic design of pore size and functionality in isoreticular mofs and their application in methane storage. *Science*, 295(5554):469–472, 2002. doi: 10.1126/science.1067208. URL <http://www.sciencemag.org/content/295/5554/469.abstract>.
- [55] Dan Zhao, Daren J. Timmons, Daqiang Yuan, and Hong-Cai Zhou. Tuning the topology and functionality of metal-organic frameworks by ligand design. *Accounts of Chemical Research*, 44(2):123–133, 2011. doi: 10.1021/ar100112y. URL <http://pubs.acs.org/doi/abs/10.1021/ar100112y>.

BIBLIOGRAPHY

- [56] David J. Collins and Hong-Cai Zhou. Hydrogen storage in metal-organic frameworks. *J. Mater. Chem.*, 17:3154–3160, 2007. doi: 10.1039/B702858J. URL <http://dx.doi.org/10.1039/B702858J>.
- [57] N. L. Rosi, J. Eckert, M. Eddaoudi, D. T. Vodak, J. Kim, M. O’Keeffe, and O. M. Yaghi. Hydrogen storage in microporous metal-organic frameworks. *Science*, 300(5622):1127–1129, 2003. doi: 10.1126/science.1083440.
- [58] Qiang Sun, Puru Jena, Qian Wang, and Manuel Marquez. First-principles study of hydrogen storage on li₁₂c₆₀. *Journal of the American Chemical Society*, 128(30):9741–9745, 2006. doi: 10.1021/ja058330c. URL <http://pubs.acs.org/doi/abs/10.1021/ja058330c>.
- [59] Yingwei Li and Ralph T. Yang. Significantly enhanced hydrogen storage in metal-organic frameworks via spillover. *Journal of the American Chemical Society*, 128(3):726–727, 2006. doi: 10.1021/ja056831s. URL <http://pubs.acs.org/doi/abs/10.1021/ja056831s>. PMID: 16417355.
- [60] S. M. Lee and Y. H. Lee. Hydrogen storage in single-walled carbon nanotubes. *Applied Physics Letters*, 76(20):2877 – 2879, 2000. doi: 10.1063/1.126503.
- [61] C. Liu, Y. Y. Fan, M. Liu, H. T. Cong, H. M. Cheng, and M. S. Dresselhaus. Hydrogen storage in single-walled carbon nanotubes at room temperature. *Science*, 286(5442):1127–1129, 1999. doi: 10.1126/science.286.5442.1127. URL <http://www.sciencemag.org/content/286/5442/1127.abstract>.
- [62] Gary G Tibbetts, Gregory P Meisner, and Charles H Olk. Hydrogen storage capacity of carbon nanotubes, filaments, and vapor-grown fibers. *Carbon*, 39(15): 2291 – 2301, 2001. ISSN 0008-6223. doi: 10.1016/S0008-6223(01)00051-3. URL <http://www.sciencedirect.com/science/article/pii/S0008622301000513>.
- [63] Alan Chambers, Colin Park, R. Terry K. Baker, and Nelly M. Rodriguez. Hydrogen storage in graphite nanofibers. *The Journal of Physical Chemistry B*, 102(22): 4253–4256, 1998. doi: 10.1021/jp980114l. URL <http://pubs.acs.org/doi/abs/10.1021/jp980114l>.
- [64] C. Park, P. E. Anderson, A. Chambers, C. D. Tan, R. Hidalgo, and N. M. Rodriguez. Further studies of the interaction of hydrogen with graphite nanofibers.

BIBLIOGRAPHY

- The Journal of Physical Chemistry B*, 103(48):10572–10581, 1999. doi: 10.1021/jp990500i. URL <http://pubs.acs.org/doi/abs/10.1021/jp990500i>.
- [65] M. Becher, M. Haluska, M. Hirscher, A. Quintel, V. Skakalova, U. Dettlaff-Weglikovska, X. Chen, M. Hulman, Y. Choi, S. Roth, V. Meregalli, M. Parinello, R. Ströbel, L. Jörissen, M. M. Kappes, J. Fink, A. Züttel, I. Stepanek, and P. Bernier. Hydrogen storage in carbon nanotubes. *Comptes Rendus Physique*, 4 (9):1055 – 1062, 2003. ISSN 1631-0705. doi: DOI:10.1016/S1631-0705(03)00107-5.
- [66] J. O. Sofo, A. S. Chaudhari, and G. D. Barber. Graphane: A two-dimensional hydrocarbon. *Phys. Rev. B*, 75(15):153401, Apr 2007. doi: 10.1103/PhysRevB.75.153401.
- [67] D. C. Elias, R. R. Nair, T. M. G. Mohiuddin, S. V. Morozov, P. Blake, M. P. Halsall, A. C. Ferrari, D. W. Boukhvalov, M. I. Katnelson, A. K. Geim, and K. S. Novoselov. Control of graphene’s properties by reversible hydrogenation: evidence for graphane. *Science*, 323:610–614, 2009. doi: 10.1126/science.1167130.
- [68] Serguei Patchkovskii, John S. Tse, Sergei N. Yurchenko, Lyuben Zhechkov, Thomas Heine, and Gotthard Seifert. Graphene nanostructures as tunable storage media for molecular hydrogen. *Proceedings of the National Academy of Sciences of the United States of America*, 102(30):10439–10444, 2005. doi: 10.1073/pnas.0501030102. URL <http://www.pnas.org/content/102/30/10439.abstract>.
- [69] A. Züttel, P. Sudan, Ph. Mauron, T. Kiyobayashi, Ch. Emmenegger, and L. Schlapbach. Hydrogen storage in carbon nanostructures. *International Journal of Hydrogen Energy*, 27(2):203 – 212, 2002. ISSN 0360-3199. doi: 10.1016/S0360-3199(01)00108-2. URL <http://www.sciencedirect.com/science/article/pii/S0360319901001082>.
- [70] C. Schafhaeutl. Ueber die verbindungen des kohlenstoffes mit silicium, eisen und anderen metallen, welche die verschiedenen gallungen von roheisen, stahl und schmiedeeisen bilden. *Journal für Praktische Chemie*, 21(1):129–157, 1840. ISSN 1521-3897. doi: 10.1002/prac.18400210117. URL <http://dx.doi.org/10.1002/prac.18400210117>.

BIBLIOGRAPHY

- [71] Ulrich Hofmann and Alfred Frenzel. Über permutoide reaktionen des graphits. *Zeitschrift für Elektrochemie und angewandte physikalische Chemie*, 37(8-9):613–618, 1931. ISSN 0005-9021. doi: 10.1002/bbpc.19310370842. URL <http://dx.doi.org/10.1002/bbpc.19310370842>.
- [72] A. Schleede and M. Wellmann. *Zeitschrift für Physikalische Chemie*, 18:1, 1932.
- [73] Vinay Gupta, Peter Scharff, Katrin Risch, Henri Romanus, and Rene MÄller. Synthesis of c_{60} intercalated graphite. *Solid State Communications*, 131(3-4):153 – 155, 2004. ISSN 0038-1098. doi: 10.1016/j.ssc.2004.05.018. URL <http://www.sciencedirect.com/science/article/pii/S0038109804004077>.
- [74] S. Dresselhaus and G. Dresselhaus. Intercalation compounds of graphite. *Adv. Phys.*, 51:1–186, 1980. doi: 10.1080/00018738100101367. URL mgm.mit.edu/historic/w959.pdf.
- [75] N. B. Hannay, T. H. Geballe, B. T. Matthias, K. Andres, P. Schmidt, and D. MacNair. Superconductivity in graphitic compounds. *Phys. Rev. Lett.*, 14:225–226, Feb 1965. doi: 10.1103/PhysRevLett.14.225. URL <http://link.aps.org/doi/10.1103/PhysRevLett.14.225>.
- [76] T. E. Weller, M. Ellerby, S. S. Siddherth, R. P. Smith, and N. T. Skipper. Superconductivity in the intercalated graphite compounds c_6yb and c_6ca . *Nature Physics*, 1(1):39–41, October 2005. doi: 10.1038/nphys0010. URL <http://www.nature.com/nphys/journal/v1/n1/full/nphys0010.html>.
- [77] Seong-Ho Yoon, Chul-Wan Park, Hojung Yang, Yozo Korai, Isao Mochida, R.T.K Baker, and Nelly M Rodriguez. Novel carbon nanofibers of high graphitization as anodic materials for lithium ion secondary batteries. *Carbon*, 42(1):21–32, 2004. ISSN 0008-6223. doi: 10.1016/j.carbon.2003.09.021. URL <http://www.sciencedirect.com/science/article/pii/S0008622303004664>.
- [78] Emily Setzer. Landfills could produce hydrogen and graphite. website, January 2009. URL <http://www.matternetwork.com/2009/1/producing-hydrogen-graphite-from-landfills.cfm>.
- [79] A. Gauzzi, S. Takashima, N. Takeshita, C. Terakura, H. Takagi, N. Emery, C. Hérolde, P. Lagrange, and G. Loupias. Enhancement of superconductivity and

BIBLIOGRAPHY

- evidence of structural instability in intercalated graphite cac_6 under high pressure. *Phys. Rev. Lett.*, 98:067002, Feb 2007. doi: 10.1103/PhysRevLett.98.067002. URL <http://link.aps.org/doi/10.1103/PhysRevLett.98.067002>.
- [80] R. C. Asher and S. A. Wilson. Lamellar compound of sodium with graphite. *Nature*, 181(4606):409–4010, 2 1958. doi: 10.1038/181409a0. URL <http://dx.doi.org/10.1038/181409a0>.
- [81] I.T. Belash, A.D. Bronnikov, O.V. Zharikov, and A.V. Palnichenko. On the superconductivity of graphite intercalation compounds with sodium. *Solid State Communications*, 64(12):1445 – 1447, 1987. ISSN 0038-1098. doi: 10.1016/0038-1098(87)90355-3. URL <http://www.sciencedirect.com/science/article/pii/0038109887903553>.
- [82] I. A. Udod and V. K. Genchel. Synthesis under high pressure and x-rays study graphite intercalation compounds of sodium. *High Pressure Research*, 8(4):581–586, 1992. doi: 10.1080/08957959208203220. URL <http://www.tandfonline.com/doi/abs/10.1080/08957959208203220>.
- [83] I.A. Udod, H.B. Orman, and V.K. Genchel. The sodium-graphite system under high-pressure conditions: The comparison with the lithium-graphite system. *Carbon*, 32(1):101 – 106, 1994. ISSN 0008-6223. doi: 10.1016/0008-6223(94)90014-0. URL <http://www.sciencedirect.com/science/article/pii/0008622394900140>.
- [84] I.A. Udod. Sodium-graphite intercalation compound of the first stage: two-dimensional structure and stability. *Synthetic Metals*, 88(2):127 – 131, 1997. ISSN 0379-6779. doi: DOI:10.1016/S0379-6779(97)80890-9. URL <http://www.sciencedirect.com/science/article/pii/S0379677997808909>.
- [85] Matteo Calandra and Francesco Mauri. Possibility of superconductivity in graphite intercalated with alkaline earths investigated with density functional theory. *Phys. Rev. B*, 74:094507, Sep 2006. doi: 10.1103/PhysRevB.74.094507. URL <http://link.aps.org/doi/10.1103/PhysRevB.74.094507>.
- [86] K. Watanabe, T. Kondow, M. Soma, T. Onishi, and K. Tamari. Molecular-sieve type sorption on alkali graphite intercalation compounds. *Proceedings of the Royal Society of London. Series A, Mathematical and Physical Sciences*, 333(1592):pp.

BIBLIOGRAPHY

- 51–67, 1973. ISSN 00804630. doi: 10.1098/rspa.1973.0047. URL <http://www.jstor.org/stable/78413>.
- [87] Arthur Lovell, Neal T. Skipper, Steve M. Bennington, and Ron I. Smith. A high-resolution neutron scattering study of the hydrogen-driven metal-insulator phase transition in $\text{kc}8\text{hx}$. *Journal of Alloys and Compounds*, 446-447(0):397–401, 2007. ISSN 0925-8388. doi: 10.1016/j.jallcom.2007.01.135. URL <http://www.sciencedirect.com/science/article/pii/S0925838807003398>. *ce:title; Proceedings of the International Symposium on Metal-Hydrogen Systems, Fundamentals and Applications (MH2006);ce:title;*
- [88] T. Enoki, S. Miyajima, M. Sano, and H. Inokuchi. Hydrogen-alkali-metal-graphite ternary intercalation compounds. *Journal of Materials Research*, 5:435–466, February 1990. doi: 10.1557/JMR.1990.0435.
- [89] T. Enoki, M. Endo, and M. Suzuki. *Graphite Intercalation Compounds and Applications*. Oxford Univ. Press, USA, Oxford, 2003. URL http://books.google.co.uk/books?hl=en&lr=&id=pNRSeMZOq5IC&oi=fnd&pg=PA3&dq=Graphite+Intercalation+Compounds+and+Application&ots=niHzXN1_PT&sig=uULx1M4XPDJLiLCo4Pe3pWKpgbI#v=onepage&q=Graphite%20Intercalation%20Compounds%20and%20Application&f=false.
- [90] Wataru Ishida, Hiroki Miyaoka, Takayuki Ichikawa, and Yoshitsugu Kojima. Hydrogenation properties of lithium intercalated graphite. *Carbon*, 46(12):1628 –, 2008. ISSN 0008-6223. doi: 10.1016/j.carbon.2008.06.033. URL <http://www.sciencedirect.com/science/article/pii/S0008622308002996>.
- [91] G. Srinivas, C. A. Howard, S. M. Bennington, N. T. Skipper, and M. Ellerby. Effect of hydrogenation on structure and superconducting properties of CaC_6 . *J. Mater. Chem.*, 19:5239–5243, 2009. doi: 10.1039/b906416h.
- [92] Neal T. Skipper, Jennifer K. Walters, Colin Lobban, Jane McKewn, Robin Mukerji, Gary J. Martin, Michael de Podesta, and Alex. C. Hannon. Neutron diffraction studies of graphite-potassium-methylamine: Staging transitions and structure of new graphite intercalation compounds. *The Journal of Physical Chemistry B*, 104(47):10969–10972, 2000. doi: 10.1021/jp0028960. URL <http://pubs.acs.org/doi/abs/10.1021/jp0028960>.

BIBLIOGRAPHY

- [93] A. Lovell, S. M. Bennington, N. T. Skipper, C. Gejke, H. Thompson, and M. A. Adams. Neutron scattering studies of hydrogen in potassium-graphite intercalates: Towards tunable graphite intercalates for hydrogen storage. *Physica B*, 385–386: 163–165, 2006. doi: 10.1016/j.physb.2006.05.311.
- [94] Arthur Lovell, Felix Fernandez-Alonso, Neal T. Skipper, Keith Refson, Stephen M. Bennington, and Stewart F. Parker. Quantum delocalisation of molecular hydrogen in alkali-graphite intercalates. *Phys. Rev. Lett.*, 101:126101, 2008. doi: 10.1103/PhysRevLett.101.126101.
- [95] G. Srinivas, A. Lovell, C.A. Howard, N.T. Skipper, M. Ellerby, and S.M. Bennington. Structure and phase stability of hydrogenated first-stage alkali- and alkaline-earth metal-graphite intercalation compounds. *Synthetic Metals*, 160(15-16):1631–1635, 2010. ISSN 0379-6779. doi: 10.1016/j.synthmet.2010.05.032. URL <http://www.sciencedirect.com/science/article/pii/S0379677910002250>.
- [96] Justin Purewal. *Hydrogen adsorption by alkali metal graphite intercalation compounds*. Doctor of philosophy, California Institute of Technology, February 2010. URL <http://resolver.caltech.edu/CaltechTHESIS:03042010-183429960>.
- [97] P. Hohenberg and W. Kohn. Inhomogeneous electron gas. *Phys. Rev.*, 136:B864–B871, Nov 1964. doi: 10.1103/PhysRev.136.B864. URL <http://link.aps.org/doi/10.1103/PhysRev.136.B864>.
- [98] G. Vignale and Mark Rasolt. Density-functional theory in strong magnetic fields. *Phys. Rev. Lett.*, 59:2360–2363, Nov 1987. doi: 10.1103/PhysRevLett.59.2360. URL <http://link.aps.org/doi/10.1103/PhysRevLett.59.2360>.
- [99] Mel Levy. Universal variational functionals of electron densities, first-order density matrices, and natural spin-orbitals and solution of the v-representability problem. *Proceedings of the National Academy of Sciences*, 76(12):6062–6065, 1979. doi: 10.1073/pnas.76.12.6062. URL <http://www.pnas.org/content/76/12/6062.abstract>.
- [100] W. Kohn and L. J. Sham. Self-consistent equations including exchange and correlation effects. *Phys. Rev.*, 140:A1133–A1138, Nov 1965. doi: 10.1103/PhysRev.140.A1133. URL <http://link.aps.org/doi/10.1103/PhysRev.140.A1133>.

BIBLIOGRAPHY

- [101] A. Szabo and N. S. Ostlund. *Modern Quantum Chemistry: Introduction to Advanced Electronic Structure Theory*, chapter 3, pages 108–123. Dover, 1996.
- [102] Rohini C. Lochan and Martin Head-Gordon. Computational studies of molecular hydrogen binding affinities: The role of dispersion forces, electrostatics, and orbital interactions. *Phys. Chem. Chem. Phys.*, 8:1357–1370, 2006. doi: 10.1039/B515409J. URL <http://dx.doi.org/10.1039/B515409J>.
- [103] John E. Bushnell, Paul R. Kemper, and Michael T. Bowers. Na⁺/k⁺.cntdot.(h2)1,2 clusters: binding energies from theory and experiment. *The Journal of Physical Chemistry*, 98(8):2044–2049, 1994. doi: 10.1021/j100059a011. URL <http://pubs.acs.org/doi/abs/10.1021/j100059a011>.
- [104] Qiang Sun, Qian Wang, Puru Jena, and Yoshiyuki Kawazoe. Clustering of Ti on a C₆₀ surface and its effect on hydrogen storage. *Journal of the American Chemical Society*, 127(42):14582–14583, 2005. doi: 10.1021/ja0550125. URL <http://pubs.acs.org/doi/abs/10.1021/ja0550125>.
- [105] Walter Kohn, Yigal Meir, and Dmitrii E. Makarov. van der Waals energies in density functional theory. *Phys. Rev. Lett.*, 80:4153–4156, May 1998. doi: 10.1103/PhysRevLett.80.4153. URL <http://link.aps.org/doi/10.1103/PhysRevLett.80.4153>.
- [106] K. R. Kganyago and P. E. Ngope. Structural and electronic properties of lithium intercalated graphite LiC₆. *Phys. Rev. B*, 68:205111, Nov 2003. doi: 10.1103/PhysRevB.68.205111. URL <http://link.aps.org/doi/10.1103/PhysRevB.68.205111>.
- [107] Randolph Q. Hood, M. Y. Chou, A. J. Williamson, G. Rajagopal, and R. J. Needs. Exchange and correlation in silicon. *Phys. Rev. B*, 57:8972–8982, Apr 1998. doi: 10.1103/PhysRevB.57.8972. URL <http://link.aps.org/doi/10.1103/PhysRevB.57.8972>.
- [108] Matteo Calandra and Francesco Mauri. Theoretical explanation of superconductivity in C₆Ca. *Phys. Rev. Lett.*, 95(23):237002, Nov 2005. doi: 10.1103/PhysRevLett.95.237002. URL <http://prl.aps.org/abstract/PRL/v95/i23/e237002>.

BIBLIOGRAPHY

- [109] C. Ataca, E. Aktürk, and S. Ciraci. Hydrogen storage of calcium atoms adsorbed on graphene: First-principles plane wave calculations. *Phys. Rev. B*, 79:041406, Jan 2009. doi: 10.1103/PhysRevB.79.041406. URL <http://link.aps.org/doi/10.1103/PhysRevB.79.041406>.
- [110] D. Guérard and A. Hérold. Intercalation of lithium into graphite and other carbons. *Carbon*, 13(4):337 – 345, 1975. ISSN 0008-6223. doi: 10.1016/0008-6223(75)90040-8. URL <http://www.sciencedirect.com/science/article/pii/0008622375900408>.
- [111] D. Guérard, M. Chaabouni, P. Lagrange, M. El Makrini, and A. Hérold. Insertion de metaux alcalino-terreux dans le graphite. *Carbon*, 18(4):257 – 264, 1980. ISSN 0008-6223. doi: 10.1016/0008-6223(80)90048-2. URL <http://www.sciencedirect.com/science/article/pii/0008622380900482>.
- [112] Mohamed El Makrini, Daniel Guérard, Philippe Lagrange, and Albert Hérold. Insertion de lanthanoides dans le graphite. *Carbon*, 18(3):203 – 209, 1980. ISSN 0008-6223. doi: 10.1016/0008-6223(80)90062-7. URL <http://www.sciencedirect.com/science/article/pii/0008622380900627>.
- [113] R. Hagiwara, M. Ito, and Y. Ito. Graphite intercalation compounds of lanthanide metals prepared in molten chlorides. *Carbon*, 34(12):1591 – 1593, 1996. ISSN 0008-6223. doi: 10.1016/S0008-6223(96)00109-1. URL <http://www.sciencedirect.com/science/article/pii/S0008622396001091>.
- [114] M. Pozzo and D. Alfè. Structural properties and enthalpy of formation of magnesium hydride from quantum Monte Carlo calculations. *Phys. Rev. B*, 77:104103, 2008. doi: 10.1103/PhysRevB.77.104103.
- [115] Hui-Ming Cheng, Quan-Hong Yang, and Chang Liu. Hydrogen storage in carbon nanotubes. *Carbon*, 39(10):1447 – 1454, 2001. ISSN 0008-6223. doi: 10.1016/S0008-6223(00)00306-7.
- [116] Philippe Lagrange, Daniel Guérard, Jean François Mareche, and Albert Hérold. Hydrogen storage and isotopic protium-deuterium exchange in graphite-potassium intercalation compounds. *Journal of the Less Common Metals*, 131(1-2): 371 – 378, 1987. ISSN 0022-5088. doi: DOI:10.1016/0022-5088(87)90536-4.

BIBLIOGRAPHY

- URL <http://www.sciencedirect.com/science/article/B759D-48NC70W-13V/2/0513e4ea0fd09819743001dbe67d5949>.
- [117] C.R. Wood, N.T. Skipper, and M.J. Gillan. Ca-intercalated graphite as a hydrogen storage material: Stability against decomposition into cah₂ and graphite. *Journal of Solid State Chemistry*, 184(6):1561 – 1565, 2011. ISSN 0022-4596. doi: DOI:10.1016/j.jssc.2011.04.013. URL <http://www.sciencedirect.com/science/article/pii/S0022459611001812>.
- [118] C. J. Carlile, G. J. Kearley, G. Lindsell, and J.W. White. Structural and dynamic aspects of the tunnelling of hydrogen in caesium-intercalated graphite. *Physica B*, 341-243:491–494, 1998. doi: 10.1016/S0921-4526(98)80043-4.
- [119] William J. Stead, Peter Meehan, and John W. White. Librations of hydrogen in stage ii caesium graphite, c24cs. *J. Chem. Soc., Faraday Trans. 2*, 84:1655–1668, 1988. doi: 10.1039/F29888401655. URL <http://dx.doi.org/10.1039/F29888401655>.
- [120] Hideoki Murakami, Ikuzo Kanazawa, Mizuka Sano, Toshiaki Enoki, and Hiroo Inokuchi. Hydrogen in a graphite-rubidium intercalation compound rbc8 studied by positron annihilation. *Journal of Physics and Chemistry of Solids*, 49(4):457 – 460, 1988. ISSN 0022-3697. doi: 10.1016/0022-3697(88)90107-2. URL <http://www.sciencedirect.com/science/article/pii/0022369788901072>.
- [121] T. Enoki, M. Suzuki, and M. Endo. *Graphite Intercalation Compounds and Applications*, chapter 2.2.1 Alkali metal with third elements, page 16. Oxford University Press, USA, 2003. ISBN 9780195128277. URL <http://books.google.co.uk/books?id=pNRSemZoq5IC>.
- [122] G. B. Kauffman and J. P. Adolf. *J. P. Educ. Chem.*, pages 135–137, September 1989.
- [123] Eric Scerri. Finding francium. *Nature*, 1:670, November 2009.
- [124] L. A. Orozcom. *Chem. Eng. News*, 2003. URL <http://pubs.acs.org/cen/80th/francium.html>.
- [125] Mme. P. Curie, P. Curie, and G. Bémont. Sur une nouvelle substance fortement radio-active, contenue dans la pechblende. *Comptes rendus de l'AcadÃ©mie des*

BIBLIOGRAPHY

- Sciences*, 127:1215–1217, December 1898. URL <http://www.aip.org/history/curie/discover.htm>.
- [126] EVS Argonne National Laboratory Environmental Science Division. Radium, human health fact sheet. Fact sheet, U.S. Department of Energy, August 2005.
- [127] M.W. Chase. *JANAF thermochemical tables*. Number pt. 1 in Journal of physical and chemical reference data ; v. 14(1985), suppl. no. 1. American Chemical Society, 1986. URL <http://books.google.com.au/books?id=MjZRAAAAMAAJ>.
- [128] J.A.T. Machado. *Nonlinear and Complex Dynamics: Applications In Physical, Biological, and Financial Systems*. SpringerLink : Bücher. Springer New York, 2011. ISBN 9781461402312. URL <http://books.google.co.uk/books?id=8upQiUBtrcIC>.
- [129] Shuiquan Deng, Arndt Simon, and JÃ¶rgen KÃ¶hler. Calcium d states: Chemical bonding of cac6. *Angewandte Chemie International Edition*, 47(35):6703–6706, 2008. ISSN 1521-3773. doi: 10.1002/anie.200801985. URL <http://dx.doi.org/10.1002/anie.200801985>.
- [130] C. Hartwigsen, W. Witschel, and E. Spohr. Charge density and charge transfer in stage-1 alkali-graphite intercalation compounds. *Phys. Rev. B*, 55(8):4953–4959, Feb 1997. doi: 10.1103/PhysRevB.55.4953.
- [131] Hansong Cheng, Guido Pez, Georg Kern, Georg Kresse, and Jürgen Hafner. Hydrogen adsorption in potassium-intercalated graphite of second stage: An ab initio molecular dynamics study. *The Journal of Physical Chemistry B*, 105(3):736–742, 2001. doi: 10.1021/jp0021392. URL <http://pubs.acs.org/doi/abs/10.1021/jp0021392>.
- [132] J.S. Arellano, L.M. Molina, A. Rubio, and J.A. Alonso. Density functional study of adsorption of molecular hydrogen on graphene layers. *Journal of Chemical Physics*, 112:8114–8119, May 2000. doi: 10.1063/1.481411.
- [133] Roger D Amos, Jamie S Andrews, Nicholas C Handy, and Peter J Knowles. Open shell Møller–Plesset perturbation theory. *Chem. Phys. Letters*, 185:256–264, 1991. doi: 10.1016/S0009-2614(91)85057-4.

BIBLIOGRAPHY

- [134] Peter J. Knowles and Nicholas C Handy. A new determinant-based full configuration interaction method. *Chem. Phys. Letters*, 111:315–321, 1984. doi: 10.1016/0009-2614(84)85513-X.
- [135] Peter J. Knowles and H.-J. Werner. An efficient second order MCSCF method for long configuration expansions. *Chem. Phys. Letters*, 115:259–267, 1985. doi: 10.1016/0009-2614(85)80025-7. URL [http://dx.doi.org/10.1016/0009-2614\(85\)80025-7](http://dx.doi.org/10.1016/0009-2614(85)80025-7).
- [136] Peter J. Knowles and H.-J. Werner. An efficient method for the evaluation of coupling coefficients in configuration interaction calculations. *Chem. Phys. Letters*, 145:514–522, 1988. doi: 10.1016/0009-2614(88)87412-8. URL [http://dx.doi.org/10.1016/0009-2614\(88\)87412-8](http://dx.doi.org/10.1016/0009-2614(88)87412-8).
- [137] Peter J. Knowles and Nicholas C Handy. A determinant based full configuration interaction program. *Computer Physics Communications*, 54:75–83, 1989. doi: 10.1016/0010-4655(89)90033-7. URL [http://dx.doi.org/10.1016/0010-4655\(89\)90033-7](http://dx.doi.org/10.1016/0010-4655(89)90033-7).
- [138] Peter J. Knowles, Jamie S. Andrews, Roger D. Amos, Nicholas C. Handy, and John A. Pople. Restricted Møller-Plesset theory for open shell molecules. *Chem. Phys. Letters*, 186:130–136, 1991. doi: 10.1016/S0009-2614(91)85118-G.
- [139] Peter J. Knowles and H.-J. Werner. Internally contracted multiconfiguration reference configuration interaction calculations for excited states. *Theoretical Chemistry Accounts: Theory, Computation, and Modeling*, 84:95–103, 1992. doi: 10.1007/BF01117405.
- [140] Peter J. Knowles, Claudia Hampel, and H.-J. Werner. Coupled cluster theory for high spin open shell reference wavefunctions. *J. Chem. Phys.*, 99:5219–5227, 1993. doi: 10.1063/1.465990. URL <http://dx.doi.org/10.1063/1.465990>.
- [141] Simone Paziani, Saverio Moroni, Paola Gori-Giorgi, and Giovanni B. Bachelet. Local-spin-density functional for multideterminant density functional theory. *Phys. Rev. B*, 73:155111, Apr 2006. doi: 10.1103/PhysRevB.73.155111. URL <http://link.aps.org/doi/10.1103/PhysRevB.73.155111>.
- [142] Robert Polly, Hans-Joachim Werner, Frederick R. Manby, and Peter J. Knowles. Fast hartree-fock theory using local density fitting approximations. *Molecular*

BIBLIOGRAPHY

- Physics*, 102(21-22):2311–2321, 2004. doi: 10.1080/0026897042000274801. URL <http://www.tandfonline.com/doi/abs/10.1080/0026897042000274801>.
- [143] A. Savin. On degeneracy, near-degeneracy and density functional theory. In J.M. Seminario, editor, *Recent Developments and Applications of Modern Density Functional Theory*, volume 4 of *Theoretical and Computational Chemistry*, pages 327 – 357. Elsevier, 1996. doi: 10.1016/S1380-7323(96)80091-4. URL <http://www.sciencedirect.com/science/article/pii/S1380732396800914>.
- [144] H.-J. Werner and Peter J. Knowles. A second order MCSCF method with optimum convergence. *J. Chem. Phys.*, 82:5053, 1985. doi: 10.1063/1.448627. URL <http://dx.doi.org/10.1063/1.448627>.
- [145] H.-J. Werner and Peter J. Knowles. An efficient internally contracted multi-configuration reference CI method. *J. Chem. Phys.*, 89:5803–5814, 1988. doi: 10.1063/1.455556. URL <http://dx.doi.org/10.1063/1.455556>.
- [146] H.-J. Werner, P. J. Knowles, R. Lindh, F. R. Manby, M. Schütz, P. Celani, T. Korrone, A. Mitrushenkov, G. Rauhut, T. B. Adler, R. D. Amos, A. Bernhardsson, A. Berning, D. L. Cooper, M. J. O. Deegan, A. J. Dobbyn, F. Eckert, E. Goll, C. Hampel, G. Hetzer, T. Hrenar, G. Knizia, C. Köppel, Y. Liu, A. W. Lloyd, R. A. Mata, A. J. May, S. J. McNicholas, W. Meyer, M. E. Mura, A. Nicklass, P. Palmieri, K. Pfüger, R. Pitzer, M. Reiher, U. Schumann, H. Stoll, A. J. Stone, R. Tarroni, T. Thorsteinsson, M. Wang, and A. Wolf. Molpro, version 2009.1, a package of ab initio programs, 2009. see <http://www.molpro.net>.
- [147] K. L. Schuchardt, B. T. Didier, T. Elsethagen, L. Sun, V. Gurumoorthi, J. Chase, J. Li, and T. L. Windus. Basis set exchange: a community database for computational sciences. *Journal of Chemical Information and Modeling*, 47(3):1045–1052, 2007. doi: 10.1021/ci600510j.
- [148] D. Feller. The role of databases in support of computational chemistry calculations. *Journal of Computational Chemistry*, 17(13):1571–1586, 1996.
- [149] Mario Barbatti, Ginette Jalbert, and Marco Antonio Chaer Nascimento. Clustering of hydrogen molecules around a molecular cation: The $\text{Li}^3+(\text{H}_2)_n$ clusters ($n = 1 - 6$). *The Journal of Physical Chemistry A*, 106(3):551–555, 2002. doi: 10.1021/jp013159m. URL <http://pubs.acs.org/doi/abs/10.1021/jp013159m>.

BIBLIOGRAPHY

- [150] Randall Davy, Evangelos Skoumbourdis, and Timothy Kompanchenko. Complexation of hydrogen by lithium: structures, energies and vibrational spectra of li+ (h₂)ⁿ (n = 1-4), li-h(h₂)^m and li-h + (h₂)^m (m = 1-3). *Molecular Physics*, 97(12):1263–1271, 1999. doi: 10.1080/00268979909482928. URL <http://www.tandfonline.com/doi/abs/10.1080/00268979909482928>.
- [151] Jenny G. Vitillo, Alessandro Damin, Adriano Zecchina, and Gabriele Ricchiardi. Theoretical characterization of dihydrogen adducts with alkaline cations. *The Journal of Chemical Physics*, 122(11):114311, 2005. doi: 10.1063/1.1869418. URL <http://link.aip.org/link/?JCP/122/114311/1>.
- [152] M. Barbatti, Ginette Jalbert, and M. A. C. Nascimento. The effects of the presence of an alkaline atomic cation in a molecular hydrogen environment. *The Journal of Chemical Physics*, 114(5):2213–2218, 2001. doi: 10.1063/1.1338978. URL <http://link.aip.org/link/?JCP/114/2213/1>.
- [153] Gordon S. Smith, Quintin C. Johnson, Deane K. Smith, D. E. Cox, Robert L. Snyder, Rong-Sheng Zhou, and Allan Zalkin. The crystal and molecular structure of beryllium hydride. *Solid State Communications*, 67(5):491 – 494, 1988. ISSN 0038-1098. doi: DOI:10.1016/0038-1098(84)90168-6. URL <http://www.sciencedirect.com/science/article/pii/0038109884901686>.
- [154] Rici Yu, Pui K. Lam, and John Head. Lattice dynamics of crystalline beryllium hydride. *Solid State Communications*, 70(11):1043 – 1046, 1989. ISSN 0038-1098. doi: DOI:10.1016/0038-1098(89)90189-0. URL <http://www.sciencedirect.com/science/article/pii/0038109889901890>.
- [155] A. El Gridani, R. Drissi El Bouzaidi, and M. El Mouhtadi. Elastic, electronic and crystal structure of srh2 by the method of pseudopotentials. *Journal of Molecular Structure: THEOCHEM*, 531(1-3):193 – 210, 2000. ISSN 0166-1280. doi: DOI:10.1016/S0166-1280(00)00443-7. URL <http://www.sciencedirect.com/science/article/pii/S0166128000004437>.
- [156] W. Bronger, Scha Chi-Chien, and P. MÄller. Crystal structure of barium hydride, determined by neutron diffraction experiments on bad2. *Zeitschrift für anorganische und allgemeine Chemie*, 545(2):69–74, 1987. ISSN 1521-

BIBLIOGRAPHY

3749. doi: 10.1002/zaac.19875450208. URL <http://dx.doi.org/10.1002/zaac.19875450208>.
- [157] Stuart R. Gunn. Heats of formation at 25.degree. of the crystalline hydrides and aqueous hydroxides of rubidium and cesium. *The Journal of Physical Chemistry*, 71(5):1386–1390, 1967. doi: 10.1021/j100864a031. URL <http://pubs.acs.org/doi/abs/10.1021/j100864a031>.
- [158] L. G. Hector, J. F. Herbst, W. Wolf, P. Saxe, and G. Kresse. *Ab Initio* thermodynamic and elastic properties of alkaline-earth metals and their hydrides. *Phys. Rev. B*, 76:014121, Jul 2007. doi: 10.1103/PhysRevB.76.014121. URL <http://link.aps.org/doi/10.1103/PhysRevB.76.014121>.
- [159] M. D. Senin, V. V. Akhachinskii, YU. E. Markushkin, N. A. Chirin, L. M. Kopytin, I. P. Mikhalenko, N. M. Ermolaev, and A. V. Zabrodin. Synthesis, structure and properties of beryllium hydride. *Inorganic Chemistry*, 29:1416, 1993. doi: 10.1002/chin.199419310. URL <http://dx.doi.org/10.1002/chin.199419310>.
- [160] M Bortz, B Bertheville, G BÄ¶ttger, and K Yvon. Structure of the high pressure phase γ -mgh₂ by neutron powder diffraction. *Journal of Alloys and Compounds*, 287(1-2):L4–L6, 1999. ISSN 0925-8388. doi: 10.1016/S0925-8388(99)00028-6. URL <http://www.sciencedirect.com/science/article/pii/S0925838899000286>.
- [161] W. M. Mueller, J. P. Blackledge, and G. G. Libowitz, editors. *Metal Hydrides*. Academic Press, New York, 1968.
- [162] A. El Gridiani and M. El Mouhtadi. Electronic and structural properties of CaH₂: a pseudopotential study. *Journal of Molecular Structure (Theochem)*, 532:183–193, 2000. doi: 10.1016/S0166-1280(00)00512-1.
- [163] T. Sichla and H. Jacobs. Single crystal x-ray structure determinations on calcium and strontium deuteride, cad2 and srd2. *ChemInform*, 27(38), 1996. ISSN 1522-2667. doi: 10.1002/chin.199638004. URL <http://dx.doi.org/10.1002/chin.199638004>.
- [164] G. J. Snyder, H. Borrmann, and A. Simon. Crystal structure of barium dihydride, bah₂. *Zeitschrift fÄr Kristallographie*, 209(5):458–458, January 1994. doi: 10.1524/zkri.1994.209.5.458. URL <http://www.oldenbourg-link.com/doi/abs/10.1524/zkri.1994.209.5.458>.

BIBLIOGRAPHY

- [165] G. Liang, J. Huot, S. Boily, A. Van Neste, and R. Schulz. Hydrogen storage in mechanically milled Mg-LaNi₅ and MgH₂-LaNi₅ composites. *Journal of Alloys and Compounds*, 297(1-2):261 – 265, 2000. ISSN 0925-8388. doi: 10.1016/S0925-8388(99)00592-7.
- [166] K Syassen, R Sonnenschein, M Hanfland, and H.J Beister. Graphite and graphite intercalation compounds under pressure: Raman modes, optical reflectivity, and phase changes. *Synthetic Metals*, 34(1-3):293 – 306, 1990. ISSN 0379-6779. doi: 10.1016/0379-6779(89)90400-1. URL <http://www.sciencedirect.com/science/article/pii/0379677989904001>.
- [167] M. Colin and A. Herold. *Bulletin de la Societe Chimique de France*, page 1598, 1971.
- [168] G. Lindsell. *Structure and dynamics of graphite intercalation compounds*. PhD thesis, Australian National University, 1998.
- [169] Kenji Ichimura, Eichachi Takamura, and Mizuka Sano. Hydrogen in alkali-metal-graphite intercalation compounds. *Synthetic Metals*, 40(3): 355–368, 1991. ISSN 0379-6779. doi: 10.1016/0379-6779(91)92077-U. URL <http://www.sciencedirect.com/science/article/B6TY7-48KF908-7Y/2/8d67db46241d04f86f73eec47ca51bfd>.
- [170] W. Smith and T Forester. Dl poly. *Journal of Molecular Graphics*, 14:136, 1996.
- [171] E. S. Fabian. An introduction to coupled-cluster theory. website, Feb 2001. URL <http://www.ua.es/cuantica/docencia/otros/cc/node1.html>.